UNIVERSITY OF KWAZULU-NATAL

Reconfigurable Intelligent Surface assisted Modulation for Next Generation Networks

Yashil Morar

2023

Reconfigurable Intelligent Surface assisted Modulation for Next Generation Networks

Yashil Morar

218022571

Submitted in fulfilment of the academic requirements of Master of Science in Engineering (Electronic)

Discipline of Electrical, Electronic and Computer Engineering

School of Engineering, College of Agriculture, Engineering and Science

University of KwaZulu-Natal, Durban, South Africa

Supervisor: Prof. Narushan Pillay

Co-Supervisor: Prof. Hongjun Xu

December 2023

PREFACE

The research contained in this dissertation was completed by the candidate while based in the School of Engineering, Discipline of Electrical, Electronic and Computer Engineering, in the College of Agriculture, Engineering and Science, University of Kwazulu-Natal, Howard College, South Africa.

The contents of this work have not been submitted in any form to another university and, except where the work of others is acknowledged in the text, the results reported are due to investigations carried out by the candidate.

As the candidate's supervisor, I agree to the submission of this dissertation.

____

Signed: Prof. Narushan Pillay

Date: _____________________

DECLARATION

I, Yashil Morar, declare that:

i. the research illustrated in this dissertation is my research, except where otherwise indicated;

ii. This dissertation does not contain other people's pictures, diagrams, graphs/graphs or other information unless acknowledged as a source from another person/other people;

iii. This dissertation does not contain other written information belonging to other people unless specifically acknowledged as a source from other researchers. Any information that is the work of others has been re-written, but the general information of their work has been referenced, and any exact words have been placed in quotation marks and referenced;

iv. This dissertation does not contain texts or tables copied from any external sources unless specifically acknowledged and referenced in the dissertation.

I accept full responsibility and accountability for this dissertation.

Yashil Morar: __[redacted]__ **23/11/2023**

signature ***date***

DEDICATION

I would like to dedicate this dissertation to my mother, Mrs Naina B Morar, and my father, Mr Ashwin Morar.

ACKNOWLEDGEMENTS

I would like to express my deepest gratitude and appreciation to Prof. Narushan Pillay for his instructive supervision and his guidance and support throughout the course of my research work. Through his diligent and conscientious mentorship, this work was made possible, and I consider myself so fortunate to have worked under such supervision.

I would like to thank Prof. Hongjun Xu, who not only provided me with a strong foundation upon which I could produce this work, but also imparted upon me many important life lessons which have left an ever-lasting impact on my personal growth and development.

I would like to give thanks to all of the colleagues I have met and had the pleasure of networking with throughout my research.

My heartfelt gratitude goes to my family, whom have, throughout this long journey have given me their continued support and love during the good and tough times.

Last, but not least, I would like to thank the Almighty God, the Absolute Truth, for His blessings, and for helping me to not only advance this far in my academic career, but for also giving me the strength, willpower, perseverance and support to overcome all obstacles that I have encountered during my research.

ABSTRACT

The demand for increased link reliability, higher data rates, improved error performance (EP) and increased spectral efficiency (SE) in wireless communications systems (WCS) is increasing exponentially year after year. Furthermore, the overall data traffic and number of mobile users is growing, and continues to grow, rapidly each year. In theory, multiple-input multiple-output systems can achieve these goals, but not without their drawbacks and challenges. These drawbacks include low energy efficiency, high computational complexity and increased harmful radiation emission. Hence, it is evident that to meet the current and future wireless demands and standards, the next generation of wireless networks can no longer be an extension of the previous generation. Rather, the next generation of wireless networks requires totally novel concepts, implementations and foundations from which to build upon.

As such, reconfigurable intelligent surfaces (RISs) provide a completely new paradigm in this respect. RISs are man-made electromagnetic (EM) surfaces with adjustable parameters capable of modifying the impinging signal to enhance signal strength and quality. In other words, RISs allow control over what was previously assumed to be the uncontrollable wireless propagation environment. The key principle in using the RIS is that its adjustable parameters may be reconfigured to effect a change on the EM wave, thereby improving various aspects of WCS.

RISs hold attractive advantages which make them a key competitor of MIMO systems. Firstly, RISs are nearly passive surfaces, meaning they do not require additional energy sources to operate. Secondly, RISs are cost-effective as they operate on low-power electronics and do not require converters or power amplifiers. Thirdly, they are easily deployable on walls, ceilings, buildings, facades, billboards, vehicles and even clothes. Lastly, RISs are environmentally friendly, and meet the requirements of green communications.

Motivated by this, this dissertation presents a study on RIS-aided WCS. In particular, this dissertation provides an investigation into how RISs may improve the EP of WCS. This dissertation investigates the effect of both passive and active RIS elements on the EP and SE of WCS by considering hybrid RISs to assist data transmission. This dissertation also provides a study on RIS-aided systems in Rician fading channels to investigate the impact of the line-of-sight component of the RIS on the EP of WCS. The theoretical average bit error probability of each scheme is provided and validated by Monte-Carlo simulations. The findings in this dissertation illustrate that hybrid RIS-aided systems can achieve significant improvements in EP over conventional RIS-aided systems, and that Rician fading channels have a distinct impact on the EP of RIS-aided WCS due to the line-of-sight component associated with Rician fading.

(This page is intentionally left blank)

TABLE OF CONTENTS

LIST OF FIGURES

LIST OF TABLES

LIST OF ABBREVIATIONS

Abbreviations	Description
1G	First-generation
2G	Second-generation
3G	Third-generation
4G	Fourth-generation
5G	Fifth-generation
6G	Sixth-generation
ABEP	Average bit error probability
AF	Amplify-and-forward
AMPS	Advanced mobile phone system
AP	Access point
ASEP	Average symbol error probability
ASK	Amplitude shift keying
AWGN	Additive white gaussian noise
BEP	Bit error probability
BER	Bit error ratio
BPSK	Binary phase shift keying
CDF	Cumulative distributive function
CDMA	Code division multiple access
CI-GC	Component-interleaved Golden codeword
CLT	Central limit theorem
CPEP	Conditional pairwise error probability
CSI	Channel state information
DF	Decode-and-forward
DH	Dual-hop
EE	Energy efficiency
EM	Electromagnetic
EP	Error performance
ETACS	European total access communication system
F-HRM	Fully - hybrid reflection modulation
FM	Frequency modulation
GC	Golden codeword
GD	Generalized differential
GPRS	General packet radio service
GSM	Global system for mobile communications
H-RIS	Hybrid reconfigurable intelligent surface
H-RIS-Rx	H-RIS-to-receiver
HRM	Hybrid reflection modulation
HSDPA	High-speed downlink packet access
HSPA+	High speed packet access plus
HSUPA	High-speed uplink packet access
i.i.d.	Independently and identically distributed
IAS	Inter-antenna synchronization
ICI	Inter-channel interference
IM	Index modulation
IoT	Internet-of-things
IRS	Intelligent reflecting surfaces
LIS	Large intelligent surface
LNAs	Low-noise amplifiers

LOS	Line-of-sight
LTE	Long term evolution
m	metre
MBF	Modified Bessel function
MBM	Media-based modulation
MGF	Moment-generating function
MI	Mutual information
MIMO	Multiple-input multiple-output
MISO	Multiple-input single-output
ML	Maximum likelihood
MMSE	Minimum mean-squared-error
mmWave	Millimetre-wave
NLOS	Non-line-of-sight
NMT	Nordic mobile telephone
NOMA	Non-orthogonal multiple access
Non-AP	Non-access point
OAM	Orbital angular momentum
OFDM	Orthogonal frequency division multiplexing
PDF	Probability density function
PEP	Pairwise error probability
PSK	Phase shift keying
QAM	Quadrature amplitude modulation
RF	Radio frequency
RIS	Reconfigurable intelligent surfaces
RIS-MBM	RIS-aided media-based modulation
RIS-Rx	RIS-to-receiver
RIS-SM	RIS-aided spatial modulation
RIS-SSK	RIS-aided space-shift keying
RM	Reflection modulation
RV	Random variable
SD	Sphere decoding
SE	Spectral efficiency
SEP	Symbol error probability
SER	Symbol error ratio
SIMO	Single-input multiple-output
SISO	Single-input single-output
SM	Spatial modulation
SMBM	Spatial media-based modulation
SNR	Signal-to-noise ratio
SSK	Space-shift keying
SSS-SD	Sorted symbol set sphere decoding
STBC	Space-time block code
STLC	Space-time line code
TACS	Total access communication system
TDMA	Time division multiple access
TWR	Two-way relaying
Tx-H-RIS	Transmitter-to-H-RIS
Tx-RIS	Transmitter-to-RIS
UAV	Unmanned aerial vehicles
UMTS	Universal mobile telecommunications systems
VBLAST	Vertical Bell Labs layered space-time
WCS	Wireless communication systems
Wi-Fi	Wireless fidelity

WiMAX	Wireless microwave access
ZF	Zero force
KCS	K-complex symbol

CHAPTER 1

1.1 Introduction

The demands and requirements of mixed-generation wireless networks is rapidly increasing year by year, and although the recent advancements in fifth-generation (5G) networks have been significant, it is evident that more work is needed to meet these ever-increasing demands. Therefore, new technologies in 5G, such as multiple-input multiple-output (MIMO), non-orthogonal multiple access (NOMA) and Golden codeword (GC) modulation, are but a few of the many technologies that have been researched in order to solve these problems. While it may be tempting to design sixth-generation (6G) technologies as mere extensions of 5G, the exponential growth in networked devices and mobile data traffic cannot be ignored. Hence, it is clear that the next mixed-generation network (6G) is required to provide a new paradigm towards wireless communication systems (WCS) in the physical layer.

Figure 1.1.1 illustrates the history of wireless networks and how they have evolved over time. The first first-generation (1G) network to come about was known as the advanced mobile phone system (AMPS), which was invented by Bell Labs and first deployed in 1982 in the United States [1] - [2]. Other 1G networks included the Nordic mobile telephone (NMT), the total access communication system (TACS), and the European total access communication system (ETACS) [2]. The 1G network was characterized by analogue switching technology using frequency division multiple access (FDMA) and operated in the 30kHz bandwidth with frequencies of between 824-894MHz [3]. The 1G network had many disadvantages, namely that it only provided voice calls, was not secure (calls may be decoded using frequency modulation (FM) demodulators), and the number of users and network coverage was extremely limited [1].

The transition from 1G networks to second-generation (2G) networks was characterized by the facilitating of digital communications technology rather than analogue technology. This digital technology became known as the global system for mobile communications (GSM) and was the foundation for further development in WCS standards [2]. GSM allowed for text, picture, and multimedia message services to be developed as the wireless standards could handle data rates of 64 kbps [1]. Later, time division multiple access (TDMA) was developed [4], followed by code division multiple access (CDMA) WCS which were developed by Qualcomm and deployed in the 1990s. These advancements in WCS proved to be successful in improving spectral efficiency (SE), data rate, error performance (EP), and the number of users they could handle compared to its 1G counterpart [2]. Further developments in GSM led to the development of the 2.5G wireless standard, facilitated by general packet radio service (GPRS) technology, producing data rates between 64 kbps and 144 kbps, enabling phone calls, web browsing and email services [4]. Later, enhanced data (EDGE) was developed to improve upon packet switching applications and enable high-speed data applications [4].

The introduction of universal mobile telecommunications systems (UMTS) marked the beginning of the development of third-generation (3G) networks in 2001 [3]. Smartphones became very popular after the deployment of 3G networks due to many new features being enabled by them, such as video calling, email services, gaming, and social media [1]. UMTS technology and protocols made use of features previously seen in 2G but with significant improvements to boost data rates. Later, 3.5G was developed as an advancement to 3G, with two new technologies being developed, namely high speed downlink packet access (HSDPA) and high speed uplink packet access (HSUPA), allowing 3.5G to handle much higher data rates [5]. Further improvements saw 3.75G being deployed with high speed packet access plus (HSPA+) technology, which later developed into 3.9G with long term evolution (LTE) technology being developed [4]. Despite this progress, 3G networks had their drawbacks, namely that they operated on a higher bandwidth to support the increasing data rates, meaning that the infrastructure and equipment needed to implement it was very costly, and so the mobile devices became costly.

The demand for high data rate applications continued to increase, meaning that significant advancements needed to be made to mixed-generation standards. The fourth-generation (4G) standard came about as a continuation of LTE made possible by orthogonal frequency division multiplexing (OFDM) [4]. Features such as cloud computing, internet of things (IoT) and high-definition mobile streaming became possible because of the 4G standard, as it was capable of reaching data rates of between 10Mbps and 1Gbps. Later, MIMO systems were created, which proved to be critical technology in improving SE and signal quality and enabling higher data rates and multi-stream technology [4]. These technologies operated under the IEEE 802.11n, which encompassed wireless fidelity (Wi-Fi), wireless microwave access (WiMAX) and LTE [6].

1G: 1970-1980

AMPS frequency spectrum:

Uplink: 824-845 MHz
Downlink: 869-894 MHz

- **Bandwidth**: 30 kHz
- **Modulation type**: FM
- **Multiplexing**: FDMA
- **Achievable data rate**: 2.4 kbps
- **Switching type**: Circuit
- **Applications**: Voice
- **Key differentiator**: Mobility
- **Weakness**: Poor spectral efficiency & security issues
- **Core Network**: PSTN
- **Technology**: Analogue

2G: 1990-2004

GSM 900 frequency spectrum:

Uplink: 880-915 MHz
Downlink: 925-960 MHz

GSM 1800 frequency spectrum:

Uplink: 1710-1785MHz
Downlink: 1805-1880 MHz

- **Bandwidth**: 200 kHz
- **Modulation type**: GMSK
- **Multiplexing**: TDMA/CDMA
- **Achievable data rate**: 9.6 - 200 kbps
- **Switching type**: Circuit, Packet
- **Applications**: Voice & Data
- **Key differentiator**: Security & Mass adoption
- **Weakness**: Limited data rates, difficulty in email and internet support
- **Core Network**: PSTN
- **Technology**: Digital
- **Latency**: 330 ms
- **EE**: 0.01 ×

Enhancement technologies:

- 2.5G – GPRS
- 2.75G - EDGE

3G: 2004-2010

UMTS frequency spectrum:

Uplink: 1920-1980 MHz
Downlink: 2110-2170 MHz

- **Bandwidth**: 5 MHz
- **Modulation type**: QPSK
- **Multiplexing**: WCDMA
- **Achievable data rate**: 0.3 - 30 Mbps
- **Device per km^2**: 10^4
- **Switching type**: Packet
- **Applications**: Voice, Data, Video call, multimedia
- **Key differentiator**: Better internet
- **Weakness**: Failure of real performance to match type, failure of wireless application protocol for internet access
- **Core Network**: Packet N/W
- **Technology**: CDMA 2000, UMTS, EDGE
- **Latency**: 100 ms
- **EE**: 0.1 ×

Enhancement technologies:

- 3.25G - HSDPA
- 3.5G - HSUPA
- 3.75G - HSPA

4G: 2010-2020

Frequency spectrum:

Uplink: 2500-2570 MHz
Downlink: 2620-2690 MHz

- **Bandwidth**: 1.25-20 MHz
- **Modulation type**: QPSK, QAM
- **Multiplexing**: OFDMA
- **Achievable data rate**: 0.07 - 1 Gbps
- **Device per km^2**: 10^5
- **Switching type**: All Packet
- **Applications**: Voice, Data, Video call, digital video broadcasting, video chat, high definition TV
- **Key differentiator**: Faster Broadband Internet, Lower Latency
- **Weakness**: higher battery usage, hardware is complex and costly
- **Core Network:** Internet
- **Technology:** WiMax, Wi-Fi, LTE
- **Latency**: 10 ms
- **EE**: 1 ×
- **Mobility**: 350 km/h

Enhancement technologies:

- 4G – LTE-A

5G: 2020-present

Frequency spectrum: 3-300 GHz

- **Bandwidth**: 0.25-1 GHz
- **Modulation type**: QPSK, QAM
- **Multiplexing**: OFDMA
- **Achievable data rate**: 20 Gbps
- **Device per km^2**: 10^6
- **Spectral efficiency**: 30 bits/s/Hz
- **Switching type**: All Packet
- **Applications**: Voice, Data, Video call, digital video broadcasting, video chat, high definition TV
- **Key differentiator**: better coverage, better calls, low latency, better performance
- **Core Network**: Internet
- **Technology**: Wireless World Wide Web
- **EE**: ≥10 ×
- **Mobility**: 500 km/h
- **U-plane latency**: 0.5 ms
- **C-plane latency**: 10 ms

Figure 1.1.1: Diagram illustrating the evolution of 1G to 5G networks [1, 2, 4]

The 5G standard has already been deployed in many countries around the world. Many technologies have been implemented, with the main technology being millimetre-wave (mmWave) mobile communications, and some others being massive MIMO and NOMA [7]. However, recent WCS literature has been devoted to technologies that could potentially realise a standard beyond 5G, such as spatial modulation (SM) [8], media-based modulation (MBM) [9], GC modulation [10], orbital angular momentum (OAM) [11] and many other technologies.

Future wireless standards are required to meet the exponentially growing demands for higher data throughput, higher SE, higher capacities, broader network coverages, reduced latencies and improved EPs, all at the lowest cost possible. However, there are several constraints and limitations that need to be addressed to realise such standards, such as hardware requirements, high power consumption and high computational complexity. One of the main challenges in the physical level of WCS is noise, arising from thermal noise from electronic devices used in the construction of WCS, or forms of radiation such as solar radiation. The noise model typically assumed is additive white Gaussian noise (AWGN), which follows a Gaussian distribution [12]. This noise is called 'white' because it is frequency-flat, and it is additive at the received signal [13]. The effects of AWGN may be reduced by increasing the signal power. However, the signal power is limited by various hardware constraints. Other challenges include multiplicative noise and multiplicative fading.

1.1.1 Basic Wireless Communication Scenario

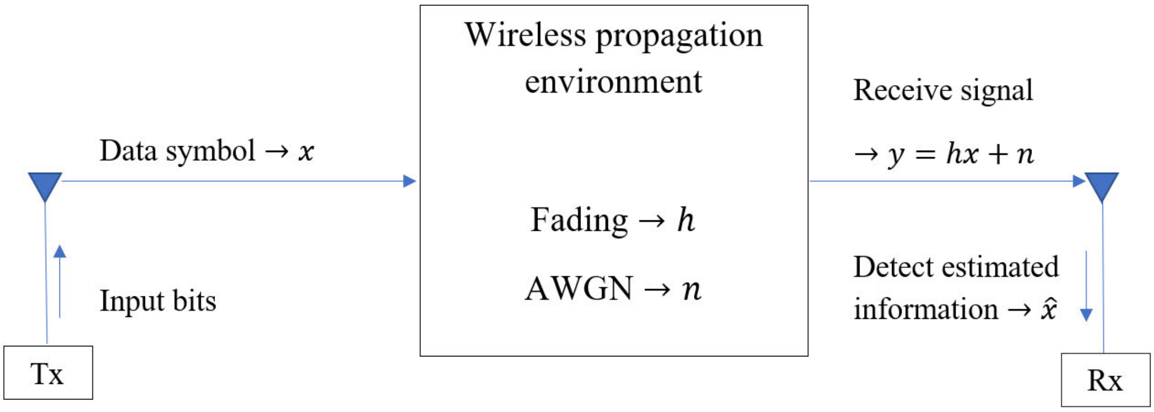

Figure 1.1.2: Diagram illustrating the basic wireless communication scenario

The basic WCS, as illustrated in Figure 1.1.2, consists of a transmitter and receiver, separated by the wireless propagation environment comprising various phenomena that may deteriorate the quality of the wireless signal. The transmitter transmits some digital information, which, in most cases, is mapped to a data symbol, denoted by x, representing the wireless signal. The symbol x is transmitted over the wireless propagation environment, where it experiences two main phenomena. The first phenomenon is fading, denoted by h, and the second is AWGN, denoted by n. The received signal at the receiver is, therefore:

$$y = hx + n. \tag{1.1}$$

The receiver estimates the transmitted information using a specific method of detection. Zero force (ZF) detection is a detection method that nullifies the interference of other symbol constellation layers when detecting in a given symbol layer. Minimum mean-squared-error (MMSE) is another detection method which aims to minimize the mean square error between the transmitted signal and the received signal. The most popular detection method, however, is maximum-likelihood (ML) detection, in which an exhaustive search is carried over the entire solution space to find the estimated symbol to determine the transmitted information, which is given for the receive signal in (1.1) as:

$$\hat{x} = \underset{x\in\Omega}{\operatorname{argmin}} |y - hx|^2, \tag{1.2}$$

where Ω denotes a set of symbols belonging to a particular symbol constellation.

1.1.2 Fading

Fading is a phenomenon in wireless networks defined as the fluctuation, or attenuation, of the strength and quality of a wireless signal over time. Fading accounts for various effects occurring in the wireless channel, namely reflection, refraction, diffraction, multipath propagation, atmospheric conditions, and scattering during radio wave transmission [14]. In WCS, there are many different statistical fading models, and these models are mainly characterized by a cumulative distributive function (CDF) and a probability density function (PDF). Fading causes phase delays and amplitude distortions to a transmitted signal, which is modelled as a complex fading coefficient. This fading coefficient may be expressed in terms of its real and imaginary parts, which are independently and identically distributed (i.i.d.) Gaussian random variables (RVs), as follows:

$$h = Re\{h\} + jIm\{h\}. \tag{1.3}$$

The expression in (1.3) may also be expressed in polar form as:

$$h = \alpha e^{j\theta}, \tag{1.4}$$

where $\alpha = \sqrt{(Re\{h\})^2 + (Im\{h\})^2}$ the magnitude of the fading coefficient, and $\theta = \tan^{-1}\left(\frac{Im\{h\}}{Re\{h\}}\right)$ is the phase of the fading coefficient.

This dissertation will focus on two main models: the Rayleigh fading model and the Rician fading model.

1.1.2.1 Rayleigh Fading Model

The Rayleigh fading model is applied to WCS that assumes a non-line-of-sight (NLOS) path. In other words, there is no direct visible path between the transmitter and the receiver.

Assume that an arbitrary Gaussian RV is given by $r \sim N(\mu, \sigma^2)$, where μ denoes the mean and σ^2 denotes the variance of r.

Rayleigh fading is characterized by a PDF given by [15]:

$$p(r) = \frac{r}{\sigma^2} e^{-\frac{r^2}{2\sigma^2}}, r > 0. \tag{1.5}$$

Integrating the PDF in (1.5) yields the CDF given by [15]:

$$F(r) = 1 - e^{-\frac{r^2}{2\sigma^2}}, r > 0. \tag{1.6}$$

1.1.2.2 Rician Fading Model

The Rician fading model applies to WCS where there exists varying degrees of line-of-sight (LOS) and is characterized by the following PDF [15]:

(1.7)

$$p(r) = \frac{r}{\sigma^2} I_0\left(\frac{rs}{\sigma^2}\right) e^{-\frac{r^2+s^2}{2\sigma^2}}, r > 0,$$

where s is a noncentrality parameter, and $I_0(\cdot)$ is the zero-order of the modified Bessel function (MBF) of the first kind [15]. The Rician distribution may also be characterized by two other parameters, namely the Rician K-factor given by $K = \frac{s^2}{2\sigma^2}$, and a scaling factor $\Omega = s^2 + \sigma^2$ [15].

Integrating the PDF in (1.7) yields the CDF given by [15]:

$$F(r) = 1 - Q_1\left(\frac{s}{\sigma}, \frac{r}{\sigma}\right), r > 0, \tag{1.8}$$

where $Q_m(a, b)$ denotes the m-th order of the generalized Marcum Q-function with inputs a and b.

1.1.2.3 AWGN Model

The mathematical model for an AWGN channel is given by:

$$y = x + n, \tag{1.9}$$

where, similar to (1.1), y is the received signal, x is the transmitted signal, and n represents a zero-mean white Gaussian process with a power spectral density of $\frac{N_0}{2}$ with a PDF given by [15]:

$$p(r) = \frac{1}{\sqrt{\pi N_0}} \exp\left(-\frac{r}{2\sigma^2}\right). \tag{1.10}$$

It may be noted that for an AWGN vector channel given by:

$$\boldsymbol{y} = \boldsymbol{x} + \boldsymbol{n}, \tag{1.11}$$

where $\boldsymbol{y}$, $\boldsymbol{x}$ and $\boldsymbol{n}$ are all of dimension $1 \times m$, the PDF of $\boldsymbol{n}$ may be written, considering that the noise coefficients are i.i.d. Gaussian RVs with zero mean and variance $\frac{N_0}{2}$, as [15]:

$$p(r) = \left(\frac{1}{\sqrt{\pi N_0}}\right)^m \exp\left(-\frac{\|\boldsymbol{n}\|^2}{N_0}\right). \tag{1.12}$$

1.2 Literature Review

Much of the past decade's research in WCS has focused on making the seemingly uncontrollable wireless propagation environment controllable. Various modulation schemes have been designed to utilize reconfigurable antenna technologies in rich scattering environments for the transmission of extra information, including SM, MBM and beam index modulation (IM).

Reconfigurable intelligent surfaces (RISs) have provided a paradigm shift in WCS research. An RIS is an electromagnetic (EM) man-made surface fitted with integrated electronic circuitry capable of intelligently adjusting the amplitude or phase of the incoming wireless signal [16]. This concept allows for control over the strength, as well as the direction, of the wireless signal. Hence, the RIS may enhance the signal-to-noise ratio (SNR), coverage probability, SE, data rate and EP [16]. Previous wireless schemes were limited by the order of modulation and the number of spatial streams, but the RIS provides an entirely new foundation for which the progression in mixed-generation networks may continue.

1.2.1 Use Cases

Use cases of RISs have been documented in [16] and [17]. The RIS can increase channel gains as a centralised beamformer and create paths around major obstacles to create new links or restore existing links in the case of a power outage. It can improve spatial multiplexing capability by emulating a rich scattering environment considering spatially sparse LOS scenarios. Besides being able to scatter and phase-shift the wireless signal, the reflective elements of the RIS can act as an anomalous mirror whose reflection angle may be controlled, and it may contain polarization manipulation capabilities. It can be used to overcome harsh indoor propagation environments and localized coverage holes without increased costs and carbon footprints. RISs can contribute to lowering the overall EM radiation as it does not require the generation of new signals; rather, they can intelligently utilize existing wireless signals.

1.2.2 Advantages

The RIS has the following attractive advantages:

1. RISs are easily deployable, as they are nearly passive devices. Due to their low cost, they may be deployed on indoor walls, furniture, clothing, billboards, vehicles, street poles and even aerial platforms [18].
2. RISs use phase-shift control of their reflective elements to shape the incoming wireless signal, as opposed to using electronic devices such as power amplifiers [18]. Hence, RISs are far more environmentally friendly and energy-efficient than conventional relay systems such as amplify-and-forward (AF) or decode-and-forward (DF). Its passive nature ensures that no additional energy is utilized in RIS-aided WCS.
3. RISs only reflect EM waves. Therefore, they can support full-band and full-duplex transmission. They are also compatible with existing standards and hardware of WCS [16].
4. RISs do not require the use of power amplifiers or analogue-to-digital or digital-to-analogue converters, making them cost-effective [18].

1.2.3 Implementation of RISs

RISs may be implemented in two main ways. The simplest way is by considering the reflect array-based approach, whereby the RIS comprises an array of passive reflective elements whose phase-shifts may be controlled electronically to backscatter and phase-shift the incident wireless signal [19]. This approach enables the use of simpler transmitters and receivers, as much of the complexity lies with the RIS and its controllers. A drawback of this implementation is that it requires a sufficiently large number of elements to effectively manipulate the incident signal, as the effect of each element in the reflect array is limited [20]. Another way to implement RISs is using a metasurface-based approach, which uses metasurfaces made of man-made materials with EM properties which cannot be found in existing natural materials [21]. In this implementation, the RISs are composed of a multitude of ‘tile-shaped’ reconfigurable metasurfaces, and each tile has its own functionality akin to that of a reflect array [21]. This is a much more flexible approach, as each element can reflect the incident wave in a different direction due to the individuality of each tile [17]. Using tuning mechanisms, these metasurfaces may achieve a number of different functionalities at a particular frequency or implement the same functionalities at different frequencies [22]. Reconfigurable metasurfaces can also improve the performance of EM devices such as reflect-array antennas, polarization converters and absorbers [23].

1.2.4 Energy Efficiency of RISs

Energy efficiency (EE) of RIS-aided communications is covered in various literature. In [24], the authors investigate a downlink multiuser communication system considering a base station comprising multiple transmit antennas and focused on the energy-efficient design of the phase shifts of the reflective elements and transmit power allocation under link budget constraints. The authors in [25], consider EE using distributed RISs, where a number of RISs are spatially distributed, and the EE is maximized by the RISs' reflection coefficient matrices and the ON and OFF states of the RISs. The EE of RIS-aided cell-free MIMO systems is covered in [26] using hybrid beamforming methods. The authors of [27], investigate the EE of an RIS-aided mobile edge computing system with a NOMA protocol assumed for communications between users and the base station. The EE is maximized by joint optimization of phase shifters, decoding order, power control and transmission data size, rate and time. Finally, in [28], the EE of RIS-aided wireless base stations is maximized using deep reinforcement learning techniques.

1.2.5 Channel Estimation in RIS systems

The acquisition of channel knowledge in RIS-aided communications has been studied extensively. In [29], an overview is provided of the various fundamental channel estimation problems and acquisition methods, and the authors discuss the advantages, disadvantages and applications of each method. The authors in [30], provide a general overview and framework for the channel estimation for various RIS-aided channel models under various scenarios and cases. In [31], the channel estimation problem is studied for an RIS-aided mmWave MIMO system using compression sensing techniques for cascaded channels. The authors in [32], proposed a channel estimation method based on the two-timescale property in an RIS-aided WCS to reduce the average pilot overhead. Channel estimation of RIS-aided MIMO systems using matrix-calibration is covered in [33]. In [34] and [35], channel acquisition problems are solved using deep learning techniques. The authors of [34], use single-scale and multi-scale enhanced deep residual networks in a RIS-aided mmWave system, while the authors of [35], propose convolutional neural network-based methods to approximate the optimal MMSE channel estimator of an RIS-aided multiple-input single-output (MISO) system.

1.2.6 Path Loss

Path loss is an important factor affecting the performance of RIS-aided WCS. In [36], the fundamental method for calculating path loss in RIS-aided WCS is proposed, assuming passive reflect-array type RISs, and in [37], an improved path loss model is proposed which covers various practical considerations as well, such as the effective received power, reflection phase error, incident and reflection gain and reflection loss of the RIS. In [38], a general formula for the path loss of RIS-aided systems is derived considering EM theory, accounting for the RIS dimensions and radiation patterns of unit cells, and in [39], a refined and more applicable model is proposed and validated using fabricated RISs operating in the mmWave frequency band. The authors in [40], formulate physics-based closed-form expressions to calculate the path loss in RIS-aided systems with respect to distance between the RIS and transmitter/receiver, RIS size and phase transformation applied by the RIS. In [41], path loss models are proposed based on Green's theorem of vector generalization considering metamaterial-based RISs.

1.2.7 Physical Layer security in RIS systems

RISs may also enhance wireless network security against eavesdropping. In [42], the physical layer security of RIS-aided downlink transmission is investigated, and the study evaluates various security metrics such as secrecy outage probability, average secrecy rate and probability of nonzero secrecy capacity. Two studies in [40] and [41], cover the security of unmanned aerial vehicles (UAVs), with the study in [43] covering secure EE for an uplink WCS with a UAV equipped with an RIS by joint optimization of UAV trajectory, transmit power, RIS phase shifts and user association, and the study in [44] proposes a novel RIS-aided UAV communication system to improve communication security against an eavesdropper. The authors of [45] and [46], cover physical layer security in RIS-aided vehicular networks in terms of secrecy capacity and secrecy outage probability. In [47], the physical layer security of the RIS-aided NOMA networks is analysed, and the study considers both internal and external eavesdropping.

1.2.8 Error Performance of RIS-aided systems

From an EP perspective, RISs have been integrated with many existing schemes. In [48], two fundamental configurations of the RIS are considered, the dual-hop (DH) and the access point (AP) scenario and are evaluated in terms of their EPs. In [49], a study of RIS-aided IM schemes is presented, in particular RIS-aided space-shift keying (SSK) and RIS-aided SM, and their EPs are evaluated. In [50] and [51], RISs are integrated with the well-known MBM concept, whilst in [52], an RIS-aided Spatial MBM (SMBM) scheme is proposed and investigated. The RIS-aided NOMA scheme is studied in [53], and RIS-aided two-way relaying (TWR) schemes are investigated in [54] and [55]. The authors in [56], study the performance of RIS-aided mmWave communications systems with respect to channel estimation and tracking. The authors in [57], propose an RIS-aided Alamouti scheme as well as an RIS-aided Vertical Bell Labs layered Space-Time (VBLAST) scheme, and the EP of both schemes is investigated.

1.2.9 Surveys in RIS-aided WCS Research

Finally, there have been many literature survey papers covering the wide evidence-base of RIS research, depending on the application of the RIS. In [58], a survey of implementations of reinforcement learning algorithms in RIS-aided systems is presented, and in [59], a study of artificial intelligence-based implementations in RIS-aided WCS systems is presented. The authors of [60], provide a study of the integration of RISs and NOMA networks. The authors in [61], provide a survey on the existing research on intelligent reflecting surfaces (IRSs), and the survey covers various performance metrics such as capacity, data rate, channel estimation, reliability and deep reinforcement learning. The authors in [62], review RIS-aided WCS from the perspective of hardware architecture, channel modelling and path loss and provide a performance analysis considering various metrics to outline the current improvements in RIS-aided WCS. In [63], a survey is presented on the optimization of specific metrics such as sum rate, EE, secrecy rate and network coverage in RIS-aided WCS. Surveys in [64] and [65], investigate machine learning applications in RIS-aided WCS, and covers various algorithms to reduce computational complexity. A survey in [66], provides a review of concepts, applications and performance metrics of RIS-aided physical layer security. In [67], a survey is presented which reviews the potential of RISs in the context of positioning technologies for 6G networks. In [68], a review of various RIS-aided multi-user communications such as MIMO, NOMA, mmWave, UAVs and Terahertz (THz) is presented. In [69], RIS-aide localization is investigated in terms of current and future developments and challenges. The authors in [70], survey the applications of RISs for underground and underwater environments. In [71], a survey of RIS hardware implementations and machine learning algorithms, along with channel modelling and physical layer design optimization, is presented. In [72], the potential of RISs in rich-scattering channels is investigated using physics-based methods. In [73], a review of RIS-aided railway communications is presented in the context of mmWave frequency bands. In [74], various channel estimation methods are reviewed for semi-passive RIS-aided WCS. The authors in [75], review RIS-aided WCS applications below the 10GHz frequency band. In [76], the potential of RIS-assisted UAV communications is reviewed in terms of its use cases, opportunities, challenges and future research directions.

The key findings of this literature review are summarized in Table 1.2.1:

Table 1.2.1: Table summarizing the key findings of the literature review

Key Findings	
1.	RISs are practically advantageous in comparison to MIMO in terms of cost, complexity and environmental friendliness.
2.	RISs have various use cases and applications, making it a versatile technology.
3.	RISs have been shown to greatly improve various performance metrics in WCS under specific assumptions.
4.	The full potential of RIS-aided WCS is yet to be determined.
5.	There are still many practical challenges of RIS-aided systems that need to be investigated and considered.

The scope of this dissertation in comparison with other literature is summarized in Table 1.2.2:

Table 1.2.2: Table summarizing the scope of this dissertation in contrast to other literature

Reference	Year	Scope of the work							
		EP	RIS-aided scheme	Active Elements	Hybrid RIS	AP RISs	Considers low numbers of RISs	IM	Rician fading
[48]	2019	✓	✓	✗	✗	✓	✗	✗	✗
[49]	2020	✓	✓	✗	✗	✓	✗	✓	✗
[77]	2021	✗	✓	✓	✗	✗	✗	✗	✗
[57]	2021	✓	✓	✗	✗	✓	✗	✓	✗
[78]	2021	✓	✓	✗	✗	✓	✓	✗	✗
[79]	2023	✓	✓	✓	✓	✗	✗	✓	✓
Dissertation	2023	✓	✓	✓	✓	✓	✓	✓	✓

1.3 Research Motivation

The demand for improved reliability, EP and SE in WCS is growing exponentially as the total data traffic and number of mobile users increases. As it stands, MIMO systems appear to be the most favourable solution to achieving these improvements through their ability to achieve higher diversity gains. However, MIMO systems hold significant practical disadvantages. MIMO systems tend to have poor reliability for high modulation orders [14]. A large number of transmit and receive antennas are required for MIMO systems to achieve high diversity gains, which is not only costly but also takes up unnecessary space. This may lead to inter-channel interference (ICI), which degrades the EP significantly, when the distances between the antennas are decreased to accommodate high numbers of antennas. MIMO systems are also physically limited by computational complexity, EE and inter-antenna synchronization (IAS) [14].

Hence, RISs have been proposed as a more cost-effective, energy-efficient and environmentally-friendly alternative to MIMO systems. RIS-aided systems can theoretically achieve significantly improved EP gains over MIMO systems at a low cost, as RISs are low-cost, passive EM surfaces. RISs are easily deployable on almost any surface, such as vehicles, clothes, indoor walls and traffic signs, and can enhance SE by enhancing the signal-to-interference-plus-noise-ratio (SINR) [17]. Furthermore, RISs do not require power amplifiers to shape the wireless signal as in AF or DF; they simply reflect the incoming signal by phase-shifting the reflecting elements; hence, it is a more environmentally friendly option [16]. Due to the number of antennas, MIMO systems emit a lot of radiation, which may be harmful to living organisms, which means that RIS-aided systems can improve societal welfare in this respect [16].

Passive RISs suffer from multiplicative path attenuation, which limits the potential performance of RIS-aided systems when considering strong direct links [36]. Active RIS elements have been proposed to overcome this limitation, with the capability of not only reflecting the incident wave but amplifying it simultaneously at the expense of added power consumption. A study in [80], demonstrated that active RISs can achieve a 67% sum-rate gain, whereas passive RISs only demonstrated a 3% gain. For practically small numbers of reflective elements, active RIS-aided systems have been shown to produce superior performance over passive RIS-aided systems with respect to achievable rate [77].

Fully active RISs consume additional power. Hence, hybrid RISs (H-RISs) have emerged as an attractive research topic for their ability to produce significantly improved performance gains over fully passive RISs at a lower power consumption than fully active systems. More significantly, H-RISs can leverage the benefits of IM and active RISs to increase SE by controlling the number of active and passive elements depending upon additional input bits, as demonstrated in [79], in a scheme called hybrid reflection modulation (HRM). It is also shown in [81] and [82] that H-RIS-aided systems are more energy-efficient than fully active RIS-aided systems for increasing transmit power and reflective elements. In [83], it is shown that H-RISs can provide an improvement in the minimum rate of a multi-user MISO system by 80% in comparison to a fully passive MISO system, which only reported a 27% improvement, under specific settings. A study in [84], showed that for a specific user distribution, H-RISs could provide significant improvements in system capacity over fully active and fully passive systems.

Another avenue of interest and importance is the performance of RIS-aided systems under Rician fading. The implementation of RISs allows for a dominant LOS component compared to the NLOS components, meaning that it is useful when the LOS paths in a wireless channel are either completely blocked, as in NLOS, or weak, as the reflective elements of the RIS create additional transmission paths. The effect of the LOS component has been evaluated in [85] and [86], in which the authors investigate average symbol error probability (ASEP), ergodic capacity and outage performance of RIS-aided networks over Rician fading channels.

1.4 Research Objectives

Following the motivation described, the objectives of this dissertation are outlined as follows:

1. To improve the SE of the conventional HRM scheme, it is proposed that a data symbol is transferred over the channel as opposed to an unmodulated carrier signal, called the HRM non-AP scheme. It is also proposed that the HRM concept may be applied using an AP-based H-RIS called the HRM AP scheme.
2. The EP of RIS-aided systems in Rician fading channels is investigated to evaluate the impact of the LOS component on RIS-aided systems.
3. The formulation of the average bit error probability (ABEP) of the HRM non-AP and HRM AP schemes is provided.
4. The formulation of the exact symbol error probability (SEP) and ABEP of RIS-aided systems in Rician fading channels for low numbers of reflective elements is provided.

1.5 Contributions to the Literature

The following research contributions have been made based on the work documented in this dissertation:

1. Y. Morar, N. Pillay and H. Xu, "Hybrid Reflection Modulated Networks," in *Southern African Telecommunication Networks and Applications Conference (SATNAC)*, Drakensberg, 2023.
2. Y. Morar, N. Pillay and H. Xu, "Hybrid Large Intelligent Surfaces," in *IEEE AFRICON 2023*, Nairobi, 2023.
3. Y. Morar, N. Pillay and H. Xu, "A Study of Large Intelligent Surfaces in Rician Fading Channels," in *International Conference on Electrical, Computer and Energy Technologies (ICECET)*, Cape Town, 2023.

1.6 Overview of the Dissertation Structure

In Chapter 1, a review of the historical evolution of WCS was presented, and the different fading models studied in this dissertation were outlined. An extensive literature survey was conducted to gain an understanding on the current research base on RIS-aided WCS. The research motivations and objectives were stated in Sections 1.3 and 1.4, respectively, and the contributions to the literature were stated in Section 1.5.

In Chapter 2, the non-access-point (non-AP) and AP RIS-aided systems are presented. The system models and the performance analysis of each scheme are presented, and computer simulations are provided to assess the validity of the theoretical analysis of the RIS-aided systems.

Chapter 3 presents the RIS-aided multiple complex symbol GC modulation scheme. The system model, the low-complexity detector and the performance analysis of the scheme are presented. Computer simulation results are presented to validate the theoretical analysis of the scheme.

Chapter 4 investigates the conventional HRM scheme. A discussion of the system model, performance analysis, achievable rate and EE is presented. Computer simulation results are provided to validate the aforementioned metrics.

Chapter 5 introduces two novel HRM-aided schemes. The first is the HRM non-AP scheme, and the second is the HRM AP scheme. The system models are presented for the two schemes, and the performance analysis of the HRM non-AP and HRM AP is presented. Computer simulations are provided to evaluate the EP of the two schemes in comparison to benchmark schemes.

Chapter 6 provides a study of RIS-aided systems in Rician fading channels. The system model and performance analysis for the RIS non-AP and RIS AP scheme is presented. Moreover, the system model and performance analysis of the RIS AP scheme for low numbers of reflective elements is presented. Computer simulation results are provided to assess the validity of the analyses described.

Finally, Chapter 7 concludes the dissertation, and results, observations and key findings are discussed. Possible future work is also outlined.

1.7 Notation used in this Dissertation

The notation used in this dissertation is described in Table 1.7.1:

Table 1.7.1: Table describing notation used throughout the dissertation

Notation	Description
Vectors	bold lowercase symbols/characters
Matrices	bold uppercase symbols/characters
j	$\sqrt{-1}$
$\mathbb{C}^{n\times m}$	Dimensions of vector/matrix containing complex-valued elements – n rows and m columns
$\mathbb{Z}$	Set of integers
$\lvert\cdot\rvert$	Absolute value/Euclidean norm
$\lVert\cdot\rVert_F$	Frobenius norm
$(\cdot)^T$	Transpose operation
$(\cdot)^H$	Hermitian operation
$\max_x \quad y = (\cdot)$	Maximized value of variable y with respect to variable x
$E[\cdot]$	Expectation operator
$Var(\cdot)$	Variance operator
$P(\cdot)$	Probability operator
$Q(\cdot)$	Gaussian Q-function
$Q_m(a,b)$	Marcum Q-function of order m with inputs a and b
$N(\mu,\sigma^2)$	Standard normal distribution of Gaussian RV with mean μ and variance σ^2
$CN(\mu,\sigma^2)$	Complex normal distribution of Gaussian RV with mean μ and variance σ^2
$Re\{\cdot\}$	Real operator
$Im\{\cdot\}$	Imaginary operator
$\underset{x}{\operatorname{argmin}}(\cdot)$	Minimum argument with respect to x
$D_m(\cdot)$	Constellation demodulation function
$diag(\cdot)$	Diagonal matrix operator
$\underset{x}{\operatorname{argmax}}(\cdot)$	Maximum argument with respect to x
$\operatorname{argsort}(\cdot)$	Sort operator
!!	Double factorial

CHAPTER 2

RECONFIGURABLE INTELLIGENT SURFACE-AIDED MODULATION

2.1 Introduction

Many 5G wireless communications networks have been launched around the world, and while it may be tempting to design 6G technologies as mere extensions of 5G, the exponential growth in the number of networked devices and mobile data traffic cannot be ignored. According to [16], the number of network-connectable devices and connections would have increased to 28.5 billion, with around 12 billion of these devices and connections predicted to be fully mobile-ready by the end of 2022. To compound this, the data traffic was predicted to increase by approximately 77 exabytes per month, and this figure is expected to increase further whilst newer use cases, user requirements, and networking trends continue to be developed. These trends indicate that 6G is required to provide a new paradigm towards wireless communications in the physical layer.

In recent literature, many technologies such as SM, MBM and other IM technologies have emerged utilizing the novel idea of making the seemingly uncontrollable wireless propagation environment controllable to improve link reliability, EP and, hence, overall quality of service. RISs have been proposed as a new technology and solution, which are reconfigurable smart devices capable of manipulating the wireless propagation environment to enhance signal strength and quality.

The development of the large intelligent surface (LIS) followed, which is a large contiguous surface comprising a number of passive reflective elements to passively reflect the transmitted signal without the need for any additional power sources. For convenience, the term RIS will be used to describe all instances of intelligent reflective surfaces.

Much work has been devoted to RISs. In an earlier study [87], intelligent walls were proposed to control the wireless propagation environment using active frequency selective surfaces. Following this, the smart reflect array was proposed in [88], which improves the signal quality by adjusting the phase-shifts of each of the reflective elements in the reflective array, without signal processing. In [89], the concept of the LIS, a large surface comprising many RISs, is proposed for aiding the transmission and reception of information. In [89] and [90], the impact of data transmission and positioning in RIS-aided systems is evaluated. In [91], the data rate of a practical RIS-aided scheme is analysed considering channel hardening. In [92] and [93], the uplink SE and data rate of uplink RIS-assisted schemes is studied under channel estimation error and pilot contamination. In [94], the uplink sum rate of a RIS scheme is asymptotically analysed. In [24, 95, 96], the downlink transmission scenario is focused on, and the achievable sum-rate and EE is investigated. Joint active and passive beamforming is analysed in [97] and [98], and the average received power of the user is studied.

From this background, this chapter illustrates two types of RIS-aided WCS [48]. Firstly, the conventional RIS-aided scheme is presented, called the RIS non-AP scheme. The second scheme is the RIS AP scheme, where the RIS functions as an AP, using an RF signal generator to generate an unmodulated carrier signal and reflect it directly towards the receiver. The AP -based RIS has strong motivations. Firstly, it enables simultaneous information transmission and phase shift control. Secondly, less channel state information (CSI) needs to be acquired as there is only a single link existing between the RIS reflective element and the receiver. Lastly, Smaller AP-based RISs may also help overcome many hardware impairments and deployment challenges as they are easily deployable on clothing, traffic signs, vehicles, walls, and furniture.

The chapter is organised as follows. Section 2.2 illustrates the system and mathematical models of the RIS non-AP scheme, as well as the performance analysis of the scheme. Section 2.3 illustrates the system and mathematical models of the RIS AP scheme and the performance analysis of the scheme. Section 2.4 provides computer-simulated results and comparisons of the two systems.

2.2 RIS Non-AP scheme

2.2.1 RIS Non-AP System Model

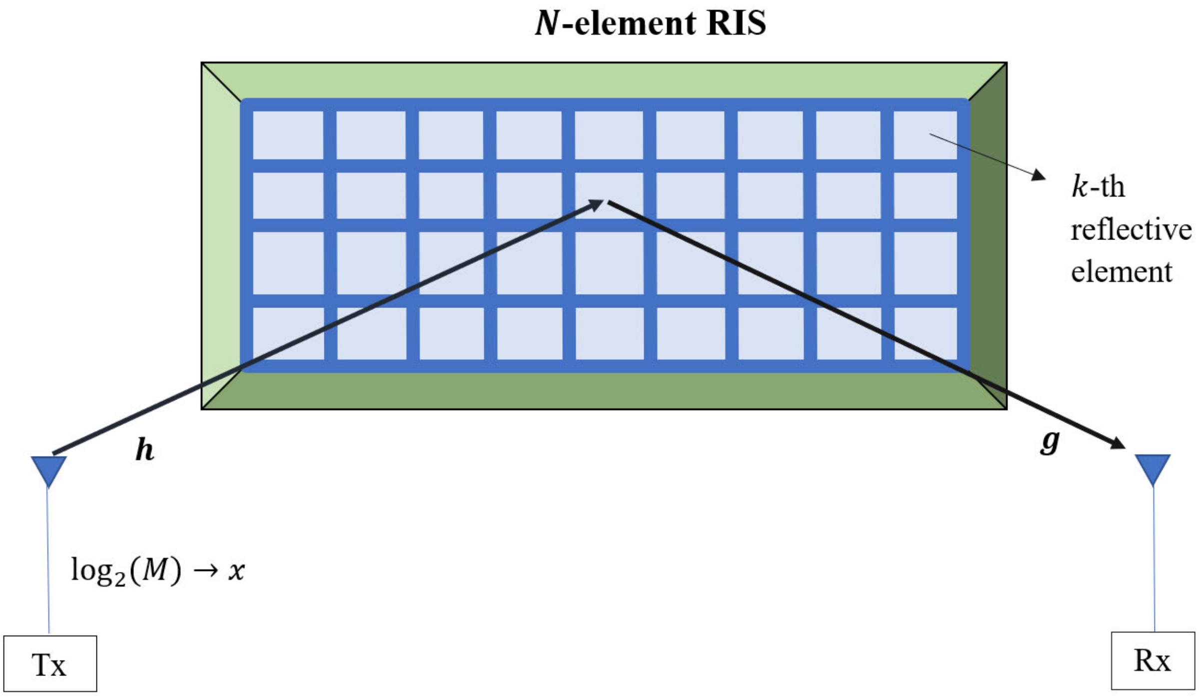

Figure 2.2.1.1: Diagram illustrating the system model of the RIS non-AP scheme

In Figure 2.2.1.1, an illustration of the system model of the conventional RIS-aided scheme is shown. Two Rayleigh frequency-flat fading channels are present, one from the transmitter-to-RIS (Tx-RIS) denoted by $\boldsymbol{h} \in \mathbb{C}^{N\times 1} \sim CN(0,1)$, and the other from the RIS-to-receiver (RIS-Rx) denoted by $\boldsymbol{g} \in \mathbb{C}^{N\times 1} \sim CN(0,1)$. It is assumed that the RIS comprises an array of N reconfigurable reflective elements controlled by communication software. The data symbol is given by x, which may be an M-ary quadrature amplitude modulation (QAM) or M-ary phase shift keying (PSK) symbol.

The SE of the RIS non-AP scheme is given by:

$$\eta_{non-AP} = \log_2(M) \text{ bits/s/Hz}. \tag{2.1}$$

The received signal can be expressed as [48]:

$$r_{non-AP} = A_k x + n, \tag{2.2}$$

where the AWGN is given by $n \sim CN\left(0, \frac{N_\Upsilon}{E_s}\right)$, where E_s denotes the transmitted bit energy per symbol, N_Υ denotes the noise power, and A_k is the RIS channel expressed as [48]:

$$A_k = \sum_{k=1}^{N} h_k g_k e^{j\theta_k}, \tag{2.3}$$

where θ_k represents the phase of the k-th reflective element. To maximise the SNR, the phase shifts are optimized as $\theta_k = -(\varphi_k + \psi_k)$, where the fading channels is written in polar form as $h_k = |h_k|e^{j\varphi_k}$ and $g_k = |g_k|e^{j\psi_k}$.

The instantaneous received SNR can be computed as follows [48]:

$$\gamma = \frac{E[|x|^2]}{E[|n|^2]} = \frac{(A_k)^2}{\left(\frac{N_\Upsilon}{E_s}\right)} = \frac{\left(\sum_{k=1}^{N} |h_k|e^{j\varphi_k}|g_k|e^{j\psi_k}e^{j\theta_k}\right)^2 E_s}{N_\Upsilon}$$
$$= \frac{\left(\sum_{k=1}^{N} |h_k|\,|g_k|e^{j(\theta_k+\varphi_k+\psi_k)}\right)^2 E_s}{N_\Upsilon}. \tag{2.4}$$

It can be observed from (2.4) that by optimising the phase shifts, the phases can be completely eliminated, hence the maximized instantaneous SNR can be written as [48]:

$$\gamma_{max} = \frac{\left(\sum_{k=1}^{N} |h_k|\,|g_k|\right)^2 E_s}{N_\Upsilon} = \epsilon^2 \frac{E_s}{N_\Upsilon}. \tag{2.5}$$

The ML detector is used to estimate x, assuming full channel knowledge, as:

$$\hat{x} = \underset{x\in\Omega}{\operatorname{argmin}} |r_{non-AP} - A_k x|^2, \tag{2.6}$$

where Ω represents the set of M-QAM or M-PSK symbols.

2.2.2 Performance Analysis of RIS Non-AP Scheme

From (2.5), both $|h_k|$ and $|g_k|$ are i.i.d. Rayleigh RVs with $\sigma_{|h_k|} = \sqrt{\frac{1}{2}}$ and $\sigma_{|g_k|} = \sqrt{\frac{1}{2}}$. The means of these RVs are computed as $E[|h_k|] = \sigma_{|h_k|}\sqrt{\frac{\pi}{2}} = \sqrt{\frac{\pi}{4}}$. Similarly, $E[|g_k|] = \sigma_{|g_k|}\sqrt{\frac{1}{2}} = \sqrt{\frac{\pi}{4}}$. The variances can be computed as $Var(|h_k|) = \sigma^2_{|h_k|}\left(2 - \frac{\pi}{2}\right) = \frac{1}{2}\left(2 - \frac{\pi}{2}\right) = \left(1 - \frac{\pi}{4}\right)$ and $Var(|g_k|) = \sigma^2_{|g_k|}\left(2 - \frac{\pi}{2}\right) = \left(1 - \frac{\pi}{4}\right)$. Based on the statistics described, the mean and variance of the product $|h_k||g_k|$ can be computed as $E[|h_k||g_k|] = E[|h_k|]E[|g_k|] = \left(\sqrt{\frac{\pi}{4}}\right)^2 = \frac{\pi}{4}$, and $Var(|h_k||g_k|) = E[(|h_k||g_k|)^2] - E[|h_k||g_k|]^2 = E[|h_k|^2]E[|g_k|^2] - E[|h_k|]^2 E[|g_k|]^2$.

It may be noted that $Var(|h_k|) = E[|h_k|^2] - E[|h_k|]^2$, therefore $E[|h_k|^2] = Var(|h_k|) + E[|h_k|]^2 = 1 - \frac{\pi}{4} + \left(\sqrt{\frac{\pi}{4}}\right)^2 = 1$. Similarly, $E[|g_k|^2] = 1$. Hence, $Var(|h_k||g_k|) = (1)(1) - \left(\sqrt{\frac{\pi}{4}}\right)^2 \left(\sqrt{\frac{\pi}{4}}\right)^2 = 1 - \frac{\pi^2}{16}$.

In this analysis, the central limit theorem (CLT) is applied for increasing N. Therefore, the aforementioned results can be extended to N reflecting elements by noticing that $\mu_\epsilon = E[\epsilon] = \sum_{k=1}^{N} E[|h_k|\,|g_k|] = N\left(\frac{\pi}{4}\right)$, and $\sigma_\epsilon^2 = Var(\epsilon) = \sum_{k=1}^{N} Var(|h_k|\,|g_k|) = N\left(1 - \frac{\pi^2}{16}\right)$.

The average pairwise error probability (PEP) is derived using the moment-generating function (MGF) approach by considering the polar form of the Q-function as $Q(x) = \frac{1}{\pi}\int_0^{\frac{\pi}{2}} \exp\left(-\frac{x^2}{2\sin^2\emptyset}\right) d\emptyset$ [15] with $x = \sqrt{2\gamma}\sin\left(\frac{\pi}{M}\right)$ for PSK signalling [13]. Since γ is a non-central chi-square RV with one degree-of-freedom, the MGF of this variable is given according to [15] as:

$$\mathrm{M}_\gamma(s) = \frac{\exp\left(\frac{\mu_\epsilon^2 s}{1 - 2\sigma_\epsilon^2 s}\right)}{\sqrt{1 - 2\sigma_\epsilon^2 s}}. \tag{2.7}$$

Substituting (2.7) into the integral of the Q-function, the PEP for M-PSK is given as [48]:

$$P_e = \frac{1}{\pi}\int_0^{\frac{\pi}{M}(M-1)} \mathrm{M}_\gamma\left(-\frac{E_s \sin^2\left(\frac{\pi}{M}\right)}{N_\Upsilon \sin^2\emptyset}\right) d\emptyset. \tag{2.8}$$

Note that binary-PSK (BPSK) may be achieved by letting $M = 2$.

By setting $f(\emptyset) = \mathrm{M}_\gamma\left(-\frac{E_s \sin^2\left(\frac{\pi}{M}\right)}{N_\Upsilon \sin^2\emptyset}\right)$, $a \approx 0$ and $b = \frac{\pi}{M}(M-1)$, the trapezoidal rule may be used, such that (2.8) can be approximated as:

$$P_e \approx \left(\frac{1}{\pi}\right)\frac{(b-a)}{n_I}\left[\frac{\left(f(a) + f(b)\right)}{2} + \sum_{k=1}^{n_I - 1} f\left(a + \frac{k(b-a)}{n_I}\right)\right], \tag{2.9}$$

where $n_I = 10$ is the number of iterations used to approximate (2.9).

The PEP for square M-QAM can also be determined by using the general expression as [13]:

$$P_e = 4bQ\left(\sqrt{\frac{3}{M-1}\gamma}\right) - 4b^2Q^2\left(\sqrt{\frac{3}{M-1}\gamma}\right), \tag{2.10}$$

where $b = 1 - \frac{1}{\sqrt{M}}$. Substituting (2.7) into (2.10), the PEP for square M-QAM is [48]:

$$P_e = \frac{4b}{\pi}\int_0^{\frac{\pi}{2}} \mathrm{M}_\gamma\left(-\frac{3E_s}{2(M-1)\,N_\Upsilon \sin^2(\emptyset)}\right) d\emptyset - \frac{4b^2}{\pi}\int_0^{\frac{\pi}{4}} \mathrm{M}_\gamma\left(-\frac{3E_s}{2(M-1)N_\Upsilon \sin^2(\emptyset)}\right) d\emptyset. \tag{2.11}$$

The trapezoidal rule given in (2.9) may also be used to approximate (2.11) by applying it to both integrals.

2.3 RIS AP Scheme

2.3.1 RIS AP System Model

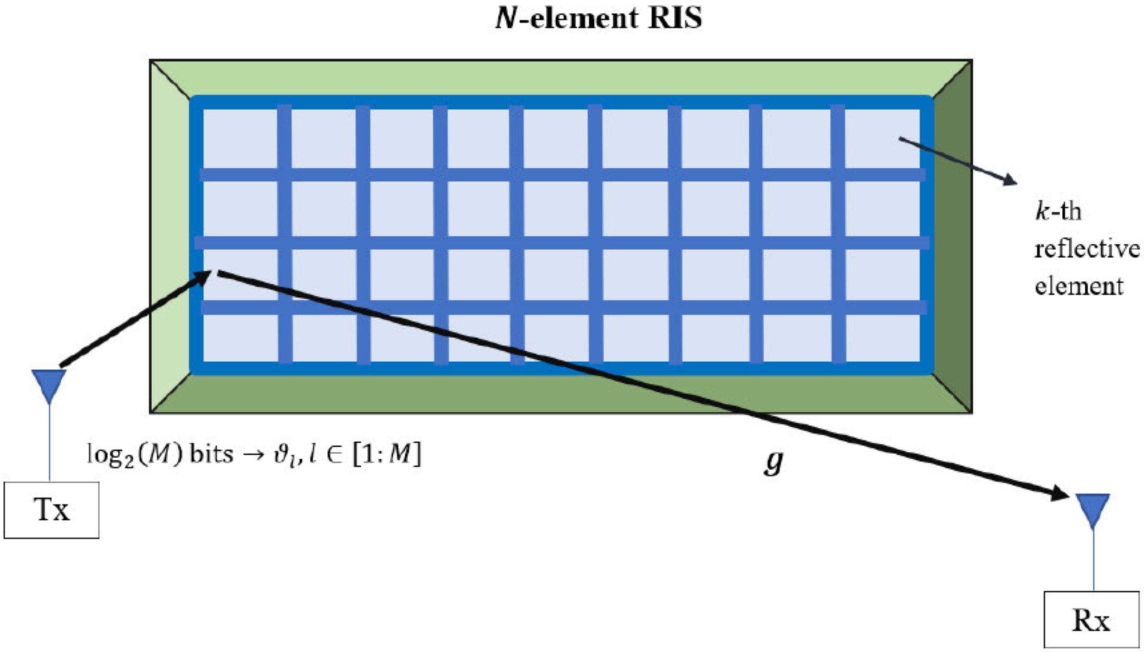

Figure 2.3.1.1: Diagram illustrating the system model of the RIS AP scheme

In the non-AP case, the N-element RIS is placed in the wireless environment to passively reflect the incoming signal from the transmitter to the receiver. However, it has recently been of interest to transmit information from the RIS itself, in other words, to use the RIS as a transmitter of information.

In Figure 2.3.1.1, it can be observed that the RIS is used as an AP source, containing low-cost, passive reflective elements. This configuration entails that there is only one instance of Rayleigh frequency-flat fading, given by $\boldsymbol{g} \in \mathbb{C}^{N\times 1} \sim CN(0,1)$, between the RIS transmitter and the receiver. The RIS can be assisted by either a RF signal generator or any device that can generate an unmodulated carrier signal with a carrier frequency f_c given by $\cos(2\pi f_c t)$ at the RIS. The carrier signal itself can be generated using an RF digital-to-analogue converter containing an internal memory and power amplifier [48]. The information bits are conveyed by adjustment of the phase-shifts of the N reflective elements, unlike the RIS non-AP system which transmits a data symbol.

To further elaborate on the transmission of data in the AP scenario, the RIS-induced phases carry information themselves, and the RIS not only adjusts the phases of its reflective elements to maximize the received SNR, but also aligns all reflected signals to form a 2D virtual constellation [48].

The received signal is given as [48]:

$$r_{AP} = \left[\sum_{k=1}^{N} g_k e^{j\theta_k}\right] + n, \tag{2.12}$$

where θ_k is the optimised reconfigurable phase induced by the k-th reflective element of the RIS, and $n \sim CN\left(0, \sqrt{\frac{N_Y}{E_s}}\right)$ is AWGN. A total of $\log_2 M$ bits are transmitted to select an additional phase term denoted by ϑ_l to adjust the reflector phases as $\theta_k = -\psi_k + \vartheta_l$, $l \in [1{:}M]$. Hence, the SE of the RIS AP scheme is:

$$\eta_{AP} = \log_2(M) \text{ bits/s/Hz.} \tag{2.13}$$

Hence, the received signal can be rewritten as [48]:

$$r_{AP} = \beta e^{j\vartheta_l} + n, \tag{2.14}$$

where $\beta = \sum_{k=1}^{N} |g_k|$. It is observed that this received signal is similar to that of M-PSK signalling over the channel β. Hence, it is recommended that the phases ϑ_l should be selected according to the conventional M-PSK scheme.

The ML detector for the RIS AP scheme is given, assuming full channel knowledge, as [48]:

$$\hat{l} = \underset{l \in [1:M]}{\operatorname{argmin}} \left| r_{AP} - \beta e^{j\vartheta_l} \right|^2. \tag{2.15}$$

2.3.2 Performance Analysis of RIS AP Scheme

The conditional PEP (CPEP) can be derived by assuming that the transmitted message l is erroneously detected as $\hat{l}$. Hence, the CPEP can be calculated as [48]:

$$P\left(l \to \hat{l} | \beta\right) = P\left(\left| r_{AP} - \sqrt{E_s} \beta e^{j\vartheta_l} \right| < \left| r_{AP} - \sqrt{E_s} \beta e^{j\vartheta_{\hat{l}}} \right|\right), \tag{2.16}$$

which is written as [48]:

$$P\left(l \to \hat{l} | \beta\right) = Q\left(\sqrt{\frac{E_s \beta^2}{N_\Upsilon} \left(1 - \cos(\vartheta_l - \vartheta_{\hat{l}})\right)}\right). \tag{2.17}$$

The full derivation of (2.16) can be found in Appendix A.

The instantaneous received SNR can be computed similar to the non-AP case as:

$$\gamma = \frac{\beta^2 E_s}{N_\Upsilon}. \tag{2.18}$$

The variable $|g_k|$ has a mean of $\frac{\sqrt{\pi}}{2}$ and a variance of $\frac{4-\pi}{4}$. A similar analysis given in the non-AP can be used to deduce that the RV β has a mean of $\frac{N\sqrt{\pi}}{2}$ and a variance of $N\left(\frac{4-\pi}{4}\right)$. The MGF of γ for the AP case is based on (2.7), with $\mu_\epsilon^2 = \mu_\beta^2 = E[\beta]^2 = N^2\left(\frac{\pi}{4}\right)$ and $\sigma_\epsilon^2 = \sigma_\beta^2 = Var(\beta) = N\left(\frac{4-\pi}{4}\right)$. The PEP for M-PSK data is expressed as [48]:

$$P_e = \frac{1}{\pi} \int_0^{\frac{\pi}{M}(M-1)} \mathrm{M}_\gamma \left(-\frac{E_s}{N_\Upsilon} \frac{\sin^2\left(\frac{\pi}{M}\right)}{\sin^2 \emptyset} \right) d\emptyset. \tag{2.19}$$

Note that the trapezoidal rule given in (2.9) may be used to approximate (2.19).

2.4 Numerical Results

In this section, numerical results are provided for both the RIS non-AP and RIS AP schemes in the form of symbol error rate (SER) vs SNR graphs, and comparisons are drawn between their EPs. It must be noted that the term $\frac{E_s}{N_Y}$ denotes the SNR of both systems. All theoretical results are based on Equations (2.8), (2.11) and (2.19).

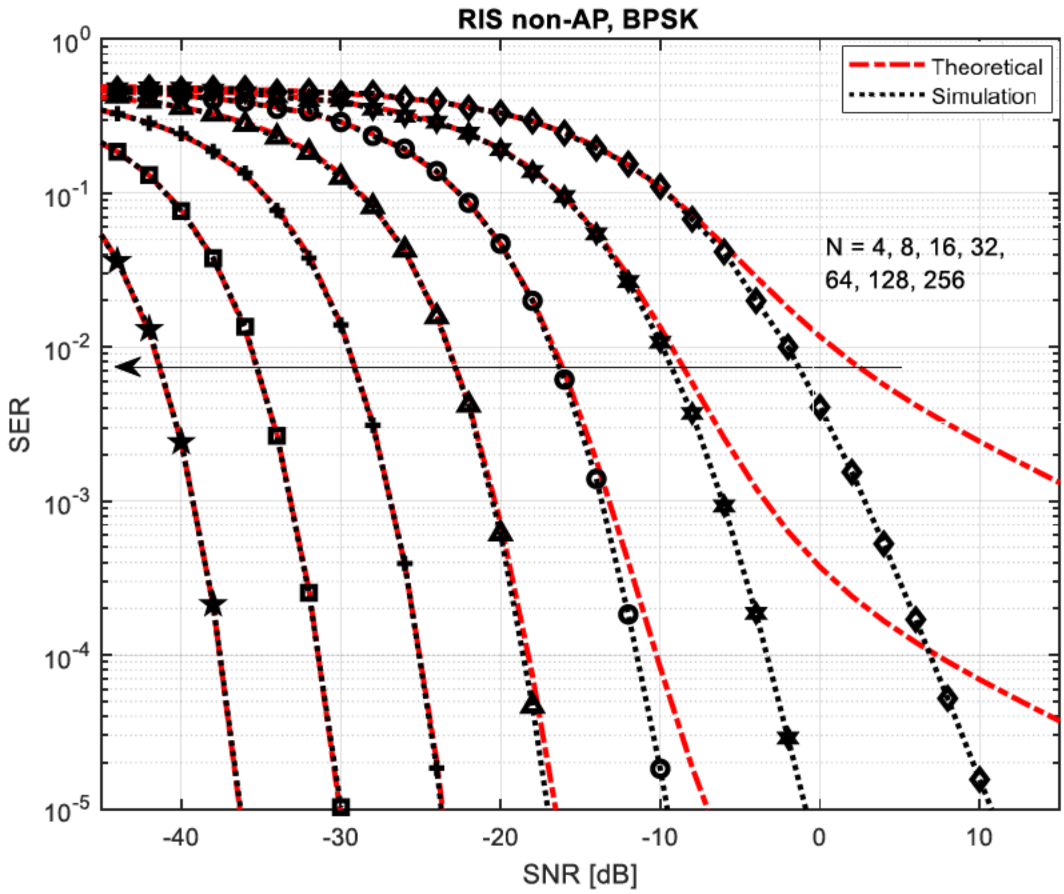

Figure 2.4.1: SER vs SNR graphs of the RIS non-AP for BPSK for various values of N

Figure 2.4.1 shows the EP of the RIS non-AP system for BPSK for varying values of N. The theoretical results are based on (2.8). It is observed that the theoretical results display a tight fit with the simulation results for high N, with an improvement of approximately 5.5 - 6dB for each N value. For low values of N, it is observed that error floors form, which is expected as the CLT is applied assuming high values of N. A different approach is required to evaluate the theoretical performance at low values of N, such as a PDF-based approach for a series of RVs.

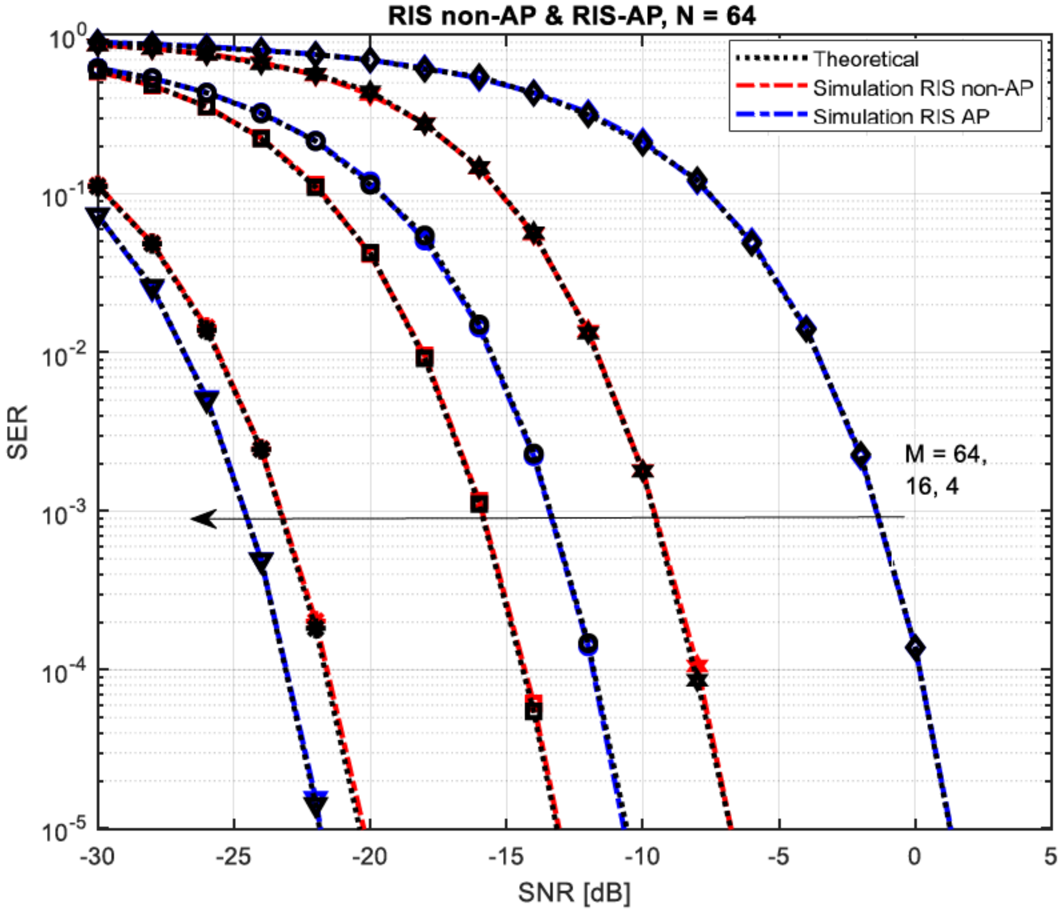

Figure 2.4.2: SER vs SNR graphs of the RIS non-AP and RIS AP for $N = 64$ and various modulation orders M

Figure 2.4.2 shows the EP of the RIS non-AP and RIS AP schemes for varying modulation orders, namely $M = \{4, 16, 64\}$ with a constant number of reflective elements set as $N = 64$. The theoretical results are based on (2.11) and (2.19), meaning that for the RIS non-AP scheme, M-QAM data is considered, and the RIS AP transmits data as previously described. It is quite clear that both systems experience a degradation in EP for increasing M, particularly in the RIS AP as there is a greater SNR loss in M-PSK over M-QAM for $M \geq 16$.

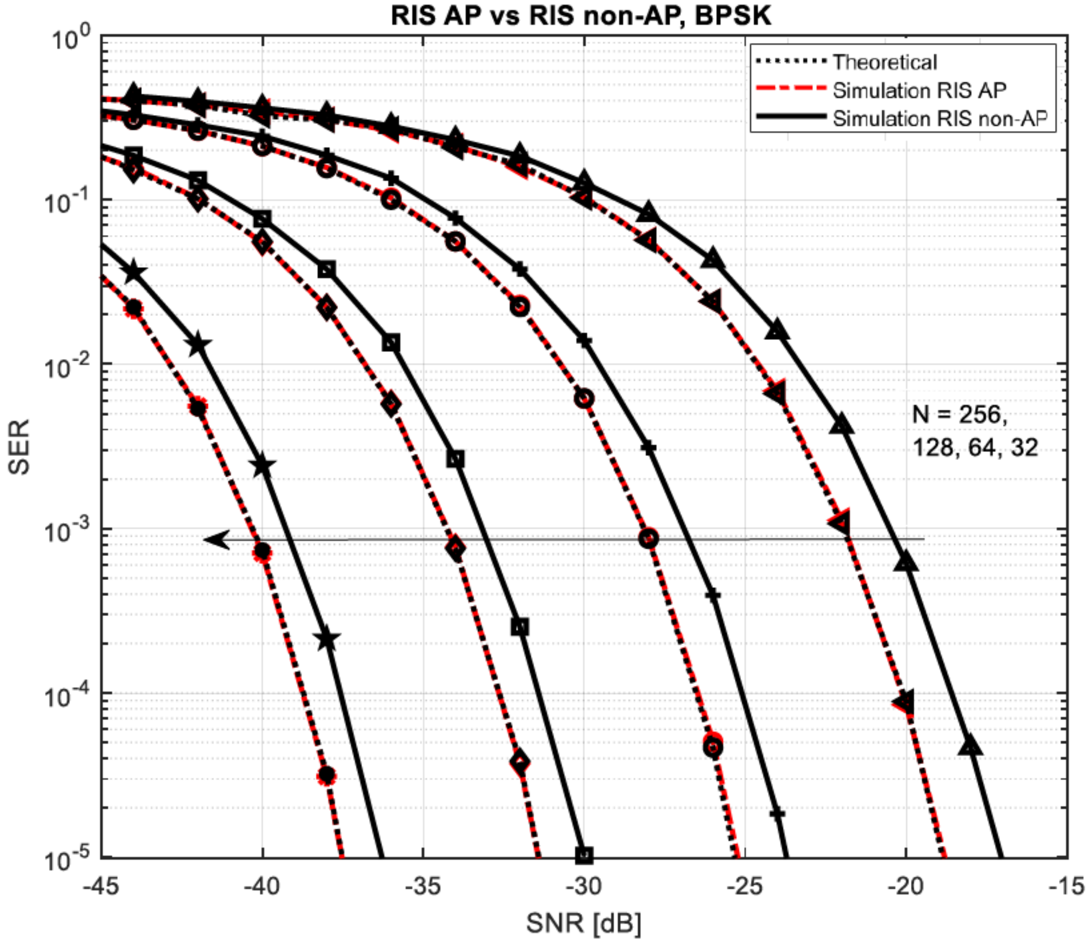

Figure 2.4.3: SER vs SNR graphs of RIS non-AP and RIS AP for various values of N for BPSK

Figure 2.4.3 shows the EP of the RIS non-AP and RIS AP schemes for BPSK modulation for varying N values of $N = \{32, 64, 128, 256\}$. The theoretical results are based on (2.8). The RIS-AP scheme yields significant improvements in EP in comparison to the RIS non-AP scheme of approximately 3dB at a BER of 10^{-5} when doubling N, hence showcasing its superior reliability in wireless communications over the non-AP scheme. In the case that CSI is partially known or absent, the RIS-AP scheme requires less channel knowledge to acquire over the RIS non-AP scheme, as there is only a single fading channel to estimate in comparison to two fading channels for the RIS non-AP scheme.

Chapter Summary

In this chapter, the system models of the RIS non-AP and RIS AP schemes in Rayleigh fading channels were presented, and the performance analysis of each scheme was described. Simulation results in the form of SER vs SNR graphs were provided to evaluate the EP of each scheme, and observations are drawn based on the results. The theoretical framework has been shown to fit tightly with the simulation graphs for high values of N, with error floors present for low values of N. Overall, it may be said that the RIS-AP scheme produces significantly better EP gains over the RIS non-AP scheme and holds other advantages such as reduced CSI acquisition and ease of deployment on flat surfaces. Of course, each configuration of the RIS has its applications.

CHAPTER 3

RECONFIGURABLE INTELLIGENT SURFACE-AIDED GOLDEN CODEWORD BASED MODULATION

3.1 Introduction

The next generation of wireless networks require drastic improvements in EP, SE, link reliability, channel capacity, and many other metrics of performance. Increasing hardware requirements, power consumption and computational complexity are just a few of the many constraints that need to be mitigated to achieve these improvements and, hence, meet the ever-increasing standards of modem WCS. The advancements and progress in mixed-generational wireless networks has been substantial thus far, with 5G networks having already been deployed in many countries around the world. Despite these advancements, research into beyond 5G, or 6G, has been relentlessly pursued, with many promising concepts being proposed such as NOMA, SM, MBM, THz communications, OAM, generalized differential (GD) modulation and many more.

The introduction of RISs has provided a new paradigm, in its ability to reflect the incoming signal by smartly adjusting the phase shifts of the reflective elements, thereby creating a controllable wireless propagation environment [16]. An RIS generally comprises man-made passive reflective elements that are low cost with adjustable parameters, which may include phase, amplitude, frequency or polarisation.

A concept that has proven to be a very attractive solution to improving EP and increasing SE has been GC-based modulation. The GC is based on the Golden ratio and holds some attractive properties in that it is a full-rate and full-diversity space-time block code (STBC). Previous works on the GC is as follows. In [99], GC-based modulation is proposed in a SIMO system, which consider two schemes, the first being the conventional GC system, which considers the transmission of two super-symbols, and the second being the Component-Interleaved GC (CI-GC) system, which considers the transmission of four super-symbols. The CI-GC scheme is further elaborated on in [100], which considers various low-complexity detection algorithms to decode the super-symbols, and an alternative method of encoding the GC is presented in [101]. In [102], the GC has been integrated with GD modulation, and in [103], the GC has been integrated with GD Alamouti modulation. In [104], the GC has been integrated with generalised SM. In [105] - [107], the GC has been integrated with the MBM concept, and in [108], the GC has been used in uplink NOMA. In [109], rotated GCs have been proposed in space-time line code (STLC) systems. The authors in [110], investigate fast ML detection of the GC, and the authors in [111], explore other low-complexity detection algorithms for the GC, such as sphere-decoding (SD), sorted-symbol-set-SD (SSS-SD), and fast essentially ML detection. In [112], the multiple complex symbol GC scheme was proposed, which is the general-order GC scheme.

Due to the attractiveness of GC and RISs, RISs have been integrated with GC-based modulation schemes in [113], where the GC schemes already covered in [99] are integrated with RISs, and consider both the non-AP and AP configurations.

In this chapter, the RIS-aided K-complex symbol (KCS) GC-based modulation scheme documented in [78] is investigated. The system model, the performance analysis and computer simulation results of the scheme is provided. Of particular note in this scheme, the AP configuration is considered. For convenience, the scheme is referred to as the RIS-SISO-KCS-GC scheme, as a SISO configuration is assumed in the scheme.

This chapter is structured as follows. Section 3.2 illustrates the system model of the RIS-SISO-KCS-GC scheme. Section 3.3 describes the SSS-SD of the RIS-SISO-KCS-GC scheme. Section 3.4 details the formulation of the ABEP of the RIS-SISO-KCS-GC scheme. Finally, Section 3.4 provides computer simulation results to validate the EP of the RIS-SISO-KCS-GC scheme.

3.2 RIS-SISO-KCS-GC System Model

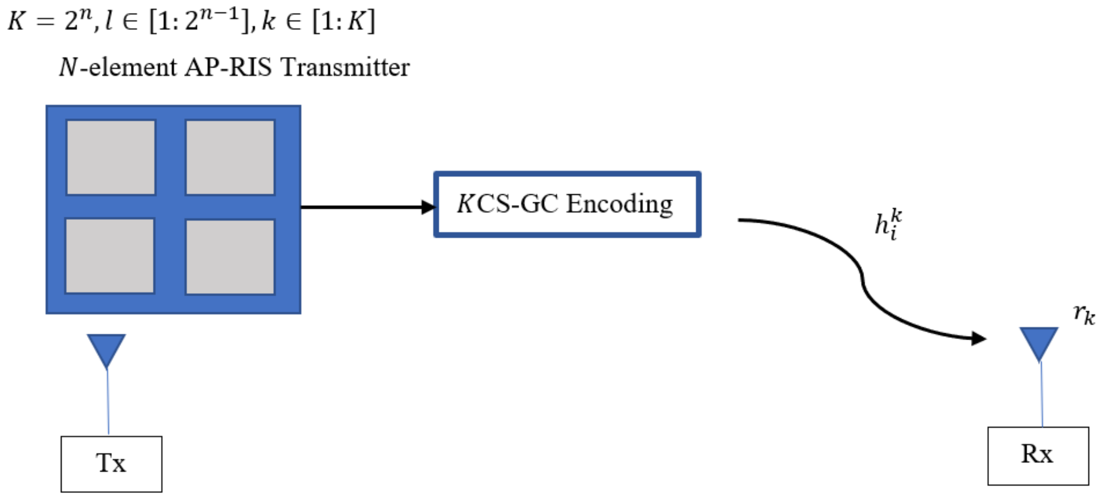

Figure 3.2.1: Diagram illustrating the system model of the RIS-SISO-KCS-GC modulation scheme

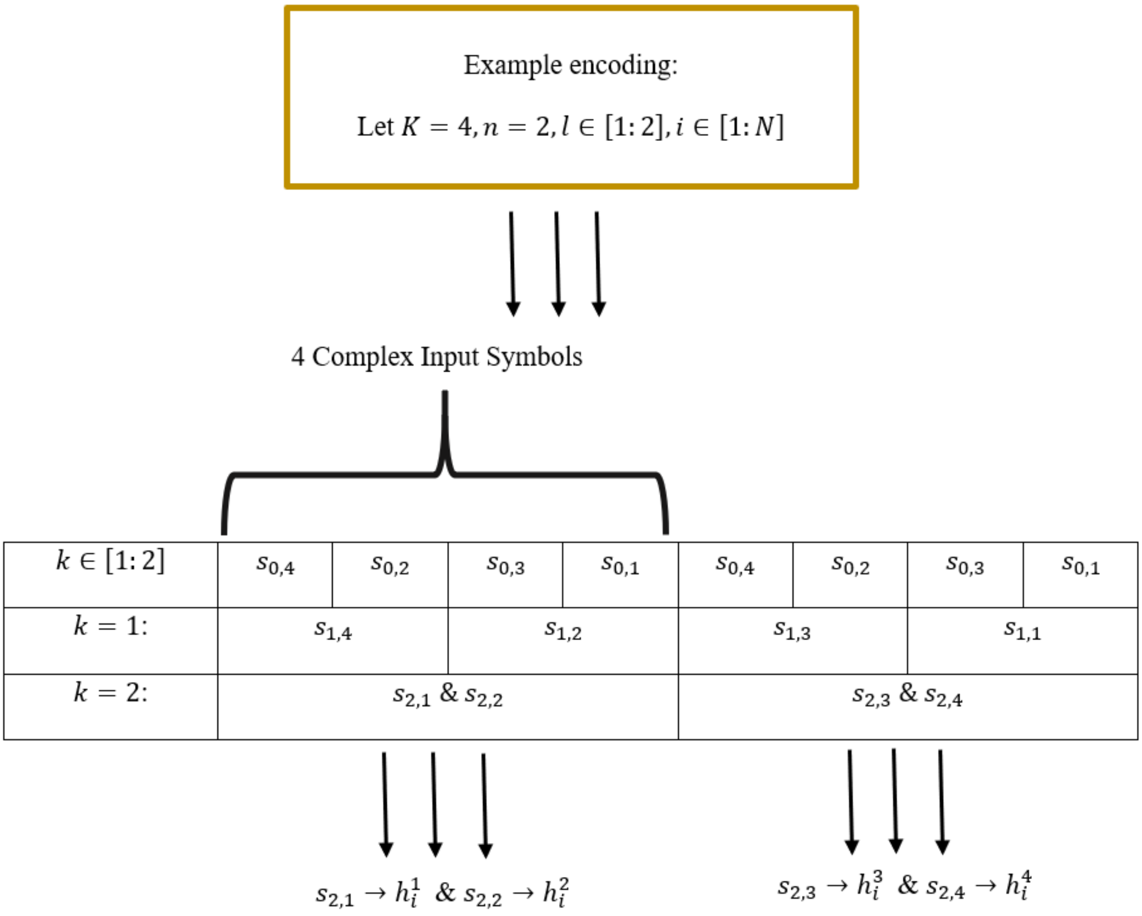

$k \in [1:2]$	$s_{0,4}$	$s_{0,2}$	$s_{0,3}$	$s_{0,1}$	$s_{0,4}$	$s_{0,2}$	$s_{0,3}$	$s_{0,1}$
$k = 1$:	$s_{1,4}$		$s_{1,2}$		$s_{1,3}$		$s_{1,1}$	
$k = 2$:	$s_{2,1}$ & $s_{2,2}$				$s_{2,3}$ & $s_{2,4}$			

Figure 3.2.2: Example encoding of the KCS-GCs

Consider Figure 3.2.1. The N-element RIS acts as an AP transmitter, whereby the RIS is placed close to the transmitter, hence creating a wireless communications scenario where there is only a single link existing, which lies between the RIS and the receiver. Unlike the original multiple complex symbol GC scheme in [112] which considers transmission over multiple transmit and receive antennas, information is transmitted over K timeslots in the RIS-aided KCS GC scheme. In this scheme, a NLOS scenario is assumed.

The input bits are denoted by an l-tuple $\boldsymbol{b}_k = \begin{bmatrix} b_1^k & b_2^k & \cdots & b_m^k \end{bmatrix}$, where $m = \log_2(M)$, and $k \in [1:K]$, where $\{K = 2^n, n \in \mathbb{Z} \geq 1\}$. The parameter n determines the number of GC encodings that the symbols undergo, and K represents the number of GC encoded symbols to be transmitted. The input vector $\boldsymbol{b}_k$ is mapped to a set of M-QAM symbols denoted by $\boldsymbol{\Phi}$, where M is the size of the QAM constellation.

The encoding of the symbols is performed as follows. Assuming p is a variable that indexes the set of integers given by n, the p-th encoded GC is given by:

$$x_{p,2l-1} = \frac{\alpha}{\sqrt{5}}\left(x_{p-1,l} + x_{(p-1,l+2^{n-1})}\theta\right), \tag{3.1}$$

$$x_{p,2l} = \frac{\bar{\alpha}}{\sqrt{5}}\left(x_{p-1,l} + x_{(p-1,l+2^{n-1})}\bar{\theta}\right), \tag{3.2}$$

where $\theta = \frac{1+\sqrt{5}}{2}, \bar{\theta} = \frac{1-\sqrt{5}}{2}, \alpha = 1 + j\bar{\theta}, \bar{\alpha} = 1 + j\theta$, and $l \in [1\colon 2^{n-1}]$. The GCs given by (3.1) and (3.2) are then transmitted via the AP-RIS to the receiver over K timeslots. An example of the GC encoding is given in Figure 3.2.2. The AWGN over each time slot is given by $\eta_k \sim CN\left(0, \frac{1}{\bar{\rho}}\right), k \in [1\colon K]$, where $\bar{\rho}$ is the average received SNR. Rayleigh frequency-flat fading channels are assumed over the k-th timeslot, given by $h_i^k \sim CN(0,1), k \in [1\colon K], i \in [1\colon N]$.

Hence, the k-th receive signal may be written as:

$$r_k = \left(\sum_{i=1}^{N} h_i^k e^{-j\phi_i} \right) x_{n,k} + \eta_k, k \in [1\colon K]. \tag{3.3}$$

The phase shifts of the i-th RIS elements given by ϕ_i may be completely eliminated by writing $h_i^k = \left| h_i^k \right| e^{j\varphi_i}$, and setting $-\phi_i = -\varphi_i$. Hence, the simplified receive signal may be written as:

$$r_k = t_k x_{n,k} + \eta_k, k \in [1\colon K], \tag{3.4}$$

where $t_k = \sum_{i=1}^{N} \left| h_i^k \right|$.

3.3 Sorted Symbol Set – Sphere Decoding of the RIS-SISO-*K*CS-GC scheme

The receive signal in (3.4) may be written in vector notation in terms of the M-QAM symbols themselves. Let $\boldsymbol{x} = \left[x_{0,1}, x_{0,2}, \cdots, x_{0,K} \right]$ be the vector containing the K M-QAM symbols, $\boldsymbol{\eta} = [\eta_1, \eta_2, \cdots, \eta_K]$ the vector of AWGN terms in each timeslot, and $\boldsymbol{H}$ the fading channel matrix of dimension $K \times K$, the receive can be written as:

$$\boldsymbol{r} = \boldsymbol{Hx} + \boldsymbol{\eta}, \tag{3.5}$$

where $\boldsymbol{H}$ is defined for each K below:

$$\boldsymbol{H} = \frac{1}{\sqrt{5}} \begin{bmatrix} t_1\alpha & t_1\alpha\theta \\ t_2\bar{\alpha} & t_2\bar{\alpha}\bar{\theta} \end{bmatrix}, \text{if } K = 2 \tag{3.6.1}$$

$$\boldsymbol{H} = \frac{1}{5} \begin{bmatrix} t_1\alpha^2 & t_1\alpha^2\theta & t_1\alpha^2\theta & t_1\alpha^2\theta^2 \\ t_2\alpha\bar{\alpha} & t_2\alpha\bar{\alpha}\bar{\theta} & t_2\alpha\bar{\alpha}\theta & t_2\alpha\bar{\alpha}\theta\bar{\theta} \\ t_3\alpha\bar{\alpha} & t_3\alpha\bar{\alpha}\theta & t_3\alpha\bar{\alpha}\bar{\theta} & t_3\alpha\bar{\alpha}\theta\bar{\theta} \\ t_4\bar{\alpha}^2 & t_4\bar{\alpha}^2\bar{\theta} & t_4\bar{\alpha}^2\bar{\theta} & t_4\bar{\alpha}^2\bar{\theta}^2 \end{bmatrix}, \text{if } K = 4 \tag{3.6.2}$$

$$\boldsymbol{H} = \frac{1}{5\sqrt{5}} \begin{bmatrix} t_1\alpha^3 & t_1\alpha^3\theta & t_1\alpha^3\theta & t_1\alpha^3\theta^2 & t_1\alpha^3\theta & t_1\alpha^3\theta^2 & t_1\alpha^3\theta^2 & t_1\alpha^3\theta^3 \\ t_2\alpha^2\bar{\alpha} & t_2\alpha^2\bar{\alpha}\bar{\theta} & t_2\alpha^2\bar{\alpha}\theta & t_2\alpha^2\bar{\alpha}\theta\bar{\theta} & t_2\alpha^2\bar{\alpha}\theta & t_2\alpha^2\bar{\alpha}\theta\bar{\theta} & t_2\alpha^2\bar{\alpha}\theta^2 & t_2\alpha^2\bar{\alpha}\theta^2\bar{\theta} \\ t_3\alpha^2\bar{\alpha} & t_3\alpha^2\bar{\alpha}\theta & t_3\alpha^2\bar{\alpha}\bar{\theta} & t_3\alpha^2\bar{\alpha}\theta\bar{\theta} & t_3\alpha^2\bar{\alpha}\theta & t_3\alpha^2\bar{\alpha}\theta^2 & t_3\alpha^2\bar{\alpha}\theta\bar{\theta} & t_3\alpha^2\bar{\alpha}\theta^2\bar{\theta} \\ t_4\alpha\bar{\alpha}^2 & t_4\alpha\bar{\alpha}^2\bar{\theta} & t_4\alpha\bar{\alpha}^2\bar{\theta} & t_4\alpha\bar{\alpha}^2\bar{\theta}^2 & t_4\alpha\bar{\alpha}^2\theta & t_4\alpha\bar{\alpha}^2\theta\bar{\theta} & t_4\alpha\bar{\alpha}^2\theta\bar{\theta} & t_4\alpha\bar{\alpha}^2\theta\bar{\theta}^2 \\ t_5\alpha^2\bar{\alpha} & t_5\alpha^2\bar{\alpha}\theta & t_5\alpha^2\bar{\alpha}\theta & t_5\alpha^2\bar{\alpha}\theta^2 & t_5\alpha^2\bar{\alpha}\bar{\theta} & t_5\alpha^2\bar{\alpha}\theta\bar{\theta} & t_5\alpha^2\bar{\alpha}\theta\bar{\theta} & t_5\alpha^2\bar{\alpha}\theta^2\bar{\theta} \\ t_6\alpha\bar{\alpha}^2 & t_6\alpha\bar{\alpha}^2\bar{\theta} & t_6\alpha\bar{\alpha}^2\theta & t_6\alpha\bar{\alpha}^2\theta\bar{\theta} & t_6\alpha\bar{\alpha}^2\bar{\theta} & t_6\alpha\bar{\alpha}^2\bar{\theta}^2 & t_6\alpha\bar{\alpha}^2\theta\bar{\theta} & t_6\alpha\bar{\alpha}^2\theta\bar{\theta}^2 \\ t_7\alpha\bar{\alpha}^2 & t_7\alpha\bar{\alpha}^2\theta & t_7\alpha\bar{\alpha}^2\bar{\theta} & t_7\alpha\bar{\alpha}^2\theta\bar{\theta} & t_7\alpha\bar{\alpha}^2\bar{\theta} & t_7\alpha\bar{\alpha}^2\theta\bar{\theta} & t_7\alpha\bar{\alpha}^2\bar{\theta}^2 & t_7\alpha\bar{\alpha}^2\theta\bar{\theta}^2 \\ t_8\bar{\alpha}^3 & t_8\bar{\alpha}^3\bar{\theta} & t_8\bar{\alpha}^3\bar{\theta} & t_8\bar{\alpha}^3\bar{\theta}^2 & t_8\bar{\alpha}^3\bar{\theta} & t_8\bar{\alpha}^3\bar{\theta}^2 & t_8\bar{\alpha}^3\bar{\theta}^2 & t_8\bar{\alpha}^3\bar{\theta}^3 \end{bmatrix}, \text{if } K = 8 \tag{3.6.3}$$

The full derivation of (3.6.1) - (3.6.3) is given in Appendix B.

The receive signal in (3.5) is decoded using the SSS-SD method in [112] as follows.

First, QR decomposition is employed for $\boldsymbol{H}$, such that $\boldsymbol{H} = \boldsymbol{QR}$, where $\boldsymbol{Q} \in \mathbb{C}^{K \times K}$ is a unitary matrix, and $\boldsymbol{R} \in \mathbb{C}^{K \times K}$ is an upper-triangular matrix with entries $r(a, b)$, where a indexes the row and b indexes the column of $\boldsymbol{R}$.

Then, (3.5) is multiplied by $\boldsymbol{Q}^H$ as follows:

$$\tilde{\boldsymbol{z}} = \boldsymbol{Q}^H \boldsymbol{r} = \boldsymbol{Q}^H(\boldsymbol{Hx} + \boldsymbol{\eta}) = (\boldsymbol{Q}^H \boldsymbol{H})\boldsymbol{x} + \boldsymbol{Q}^H \boldsymbol{\eta} = \boldsymbol{Rx} + \overline{\boldsymbol{\eta}} = [\tilde{z}(1) \quad \tilde{z}(2) \quad \cdots \quad \tilde{z}(K)], \tag{3.7}$$

where $\tilde{\boldsymbol{z}} \in \mathbb{C}^{K \times 1}$.

Next, SSS-SD is performed to detect the estimated M-QAM symbols as follows.

The SSS-SD is based on the constraint $\|\tilde{\boldsymbol{z}} - \boldsymbol{Rx}\|_F^2 \leq d^2$, where d is the radius chosen for sphere decoding based on [114], hence after determining $\tilde{\boldsymbol{z}}$ from (3.7), the estimated symbols are detected in reverse order as follows:

$$\tilde{x}_{0,K} = D_m\left(\tilde{\xi}_K = \frac{\tilde{z}(K)}{r(K, K)}\right), \tag{3.8.1}$$

$$\tilde{x}_{0,k} = D_m\left(\tilde{\xi}_k = \frac{\tilde{z}(k) - \sum_{i=1}^{K} r(k, i)\tilde{x}_{0,i}}{r(k, k)}\right), k \in [1\colon K - 1], \tag{3.8.2}$$

where $D_m(\,\cdot\,)$ denotes the constellation demodulation function. Next, the estimated symbols are sorted from most to least probable for each $k \in [1\colon K]$ with respect to the M-QAM symbol set $\boldsymbol{\Phi}$ as:

$$\left[\tilde{x}_{0,k}^1 \quad \tilde{x}_{0,k}^2 \quad \cdots \quad \tilde{x}_{0,k}^M\right] = \boldsymbol{\Phi}\left(\operatorname{argsort}\left(v_1^k, v_2^k, \cdots, v_M^k\right)\right), \tag{3.9}$$

where $v_m^k = \left|\tilde{\xi}_k - x_0^m\right|^2, m \in [1\colon M], x_0^m \in \boldsymbol{\Phi}$.

Now that the sorted sets have been obtained, SD can be performed using these sets. The K-th symbol is estimated in accordance with the following SD constraint:

$$\left|\tilde{z}(K) - r(K, K)\tilde{x}_{0,K}^{\breve{m}}\right|^2 \leq d^2, \tag{3.10}$$

where $\breve{m} \in [1\colon \mathrm{T}]$, and T denotes the symbols with highest probability of transmission for any given SNR value, where $1 < \mathrm{T} \leq M$.

The remaining symbols are detected in reverse order using the k-th SD constraint given by:

$$\left|\wp_k\left(x_{0,k}^{\breve{m}}\right)\right|^2 \leq d^2 - \sum_{i=k+1}^{K} \left|\wp_i\left(\hat{x}_{0,i}\right)\right|^2, \tag{3.11}$$

where $\wp_K\left(\hat{x}_{0,K}\right) = \tilde{z}(K) - r(K, K)\tilde{x}_{0,K}$ and $\wp_k(s) = \tilde{z}(K) - r(k, k)s - \sum_{i=k+1}^{K} r(k, i)\hat{x}_{0,i}, k \in [1\colon K - 1]$.

3.4 Performance Analysis of the RIS-SISO-*K*CS-GC scheme

The ABEP is calculated by assuming that only one M-QAM symbol given by $x_{0,1}$ is detected erroneously, whilst the remaining symbols are detected without any error [78].

The k-th receive signal based on (3.4) may be expressed as:

$$r_k = \varepsilon_k t_k x_{0,1} + \eta_k, k \in [1\colon K], \tag{3.12}$$

where ε_k represents an array of the GCs constants for $K = 2, 4,$ and 8 as follows:

$$[\varepsilon_1 \quad \varepsilon_2 \quad \cdots \quad \varepsilon_K]^T = \begin{cases} \frac{1}{\sqrt{5}}[\alpha \quad \bar{\alpha}]^T, & \text{if } K = 2. \\ \frac{1}{5}[\alpha^2 \quad \alpha\bar{\alpha} \quad \alpha\bar{\alpha} \quad \bar{\alpha}^2]^T, & \text{if } K = 4. \\ \frac{1}{5\sqrt{5}}\left[\alpha^3 \quad \alpha^2\bar{\alpha} \quad \alpha^2\bar{\alpha} \quad \alpha\bar{\alpha}^2 \quad \alpha^2\bar{\alpha} \quad \alpha\bar{\alpha}^2 \quad \alpha\bar{\alpha}^2 \quad \bar{\alpha}^3\right]^T, & \text{if } K = 8. \end{cases} \tag{3.13}$$

The proof of (3.13) is found in Appendix B.

It is observed that, based on the assumptions made, the expression in (3.12) translates to transmitting $x_{0,1}$ over K identical Rayleigh fading channels, with a channel gain of $|\varepsilon_k|^2$.

The ABEP may be calculated using the following expression [78]:

$$P_e \approx \frac{4a}{\pi \log_2(M)} \int_0^{\frac{\pi}{2}} \mathrm{M}_\rho(g_\phi)\, d\phi - \frac{4a^2}{\pi \log_2(M)} \int_0^{\frac{\pi}{4}} \mathrm{M}_\rho(g_\phi)\, d\phi, \tag{3.14}$$

where $\mathrm{M}_\rho(s) = \prod_{k=1}^{K} \mathrm{M}_{\rho_k}(s)$, where $\mathrm{M}_{\rho_k}(\,\cdot\,)$ denotes the MGF of the instantaneous SNR given by ρ_k in the k-th fading channel, $g_\phi = -\frac{3}{2(M-1)\sin^2(\phi)}$, and $a = 1 - \frac{1}{\sqrt{M}}$.

In this performance analysis, the PDF of a series of Rayleigh-distributed RVs given in [115] is employed to calculate a bound on the ABEP of the RIS-SISO-KCS-GC scheme as follows.

The PDF is given in [115] as:

$$f_Z(r) = \frac{r^{2N-1} \exp\left(-\frac{r^2}{2b}\right)}{2^{N-1} b^N (N-1)!}, \tag{3.15}$$

where $b = \frac{1}{2N}[(2N-1)!!]^{\frac{1}{N}}$.

Using this PDF and employing a transformation of RVs, the variable $\rho_k = g(T_k)$ is defined, where $T_k = \frac{t_k}{\sqrt{N}}$ and $\rho_k = \bar{\rho}|\varepsilon_k|^2 T_k N$, formulated from (3.12). The transformation of RVs may be performed by rearranging $g^{-1}(\rho_k) = \sqrt{\frac{\rho_k}{\bar{\rho}|\varepsilon_k|^2 N}}$ and taking the derivative $\frac{\mathrm{d}T_k}{\mathrm{d}\rho_k} = \frac{1}{2\bar{\rho}|\varepsilon_k|^2 T_k N}$. Based on these results, the PDF in (3.15) may now be written as [78]:

$$f_{\rho_k}(\rho_k) = f_{T_k}\left(g^{-1}(\rho_k)\right)\left|\frac{\mathrm{d}T_k}{\mathrm{d}\rho_k}\right| = \frac{\rho_k^{N-1} \exp\left(-\frac{\rho_k}{2bN\bar{\rho}|\varepsilon_k|^2}\right)}{(2bN|\varepsilon_k|^2\bar{\rho})^N (N-1)!}. \tag{3.16}$$

The MGF of ρ_k may be calculated as:

$$\mathrm{M}_{\rho_k}(s) = \int_0^\infty f_{\rho_k}(\rho_k) e^{\rho_k s} d\rho_k = \frac{\Gamma(N)}{(N-1)!\,(1 - 2bN|\varepsilon_k|^2\bar{\rho}s)^N}. \tag{3.17}$$

The full proof of (3.17) is given in Appendix B.

Hence, the ABEP may be written as:

$$\begin{aligned} P_e \approx & \frac{4a}{\pi \log_2(M)} \int_0^{\frac{\pi}{2}} \mathrm{M}_\rho \left(-\frac{3}{2(M-1)\sin^2\theta}\right) d\theta \\ & - \frac{4a^2}{\pi \log_2(M)} \int_0^{\frac{\pi}{4}} \mathrm{M}_\rho \left(-\frac{3}{2(M-1)\sin^2\theta}\right) d\theta. \end{aligned} \tag{3.18}$$

The trapezoidal rule may be used to approximate (3.18) as [78]:

$$\begin{aligned} P_e \approx & \frac{2a\Gamma(N)}{\pi n(N-1)!\log_2(M)} \left[\prod_{k=1}^{K}\left(\frac{\pi}{2}F\left(\frac{\pi}{2}\right)+\pi\sum_{i=1}^{n-1}F\left(\frac{i\pi}{2n}\right)\right)\right. \\ & \left. - a\prod_{k=1}^{K}\left(\frac{\pi}{4}F\left(\frac{\pi}{4}\right)+\frac{\pi}{2}\sum_{i=1}^{n-1}F\left(\frac{i\pi}{4n}\right)\right)\right], \end{aligned} \tag{3.19}$$

where $F(\theta) = \left(\frac{1}{1-2bN|\varepsilon_k|^2\bar{\rho}g_\phi}\right)^N$, and $n = 10$ is the number of iterations used in (3.19).

The expression in (3.18) may be approximated by assuming high SNR and may be upper-bounded by setting $\phi = \frac{\pi}{2}$. Therefore, (3.18) may be written as:

$$P_e \approx \frac{2a\Gamma(N)}{(N-1)!\log_2(M)}\left[\prod_{k=1}^{K}\left(\frac{1}{|\varepsilon_k|^2}\right)^N\right]\left(\frac{3bN\bar{\rho}}{M-1}\right)^{-KN}, \tag{3.20}$$

where the diversity order is given by KN. This is a significant observation, as it means that each symbol experiences a K number of different fading instances. Hence, the diversity order of the RIS-SISO-KCS-GC scheme increases by a factor of K.

3.5 Numerical Results

In this section, numerical results are presented for the RIS-SISO-KCS-GC scheme for $K = \{2, 4, 8\}$, $M = \{16, 64\}$ and $N = \{2, 4, 8, 16\}$. The numerical results are presented in the form of bit error ratio (BER) vs SNR graphs, and the EP analyses are drawn at a BER of 10^{-5}. The theoretical bound given in (3.19) is also included to validate the correctness of the simulation result. The simulation settings for the schemes when using the SSS-SD detection are tabulated in Tables 3.5.1 – 3.5.4 based on [78]. Each range of SNR values corresponds to an T value in the T-array.

Table 3.5.1: Simulation settings of the RIS-SISO-KCS-GC scheme for $N = 2$

M	K	RIS-SISO-KCS-GC scheme, $N = 2$	
		SNR	T
16	2	[-6:2:12, 14, 16:2:18, 20:2:22]	[2, 4, 8, 16]
	4	[-6:2:8, 10, 12, 14:2:16, 18:2:20]	[2, 4, 12, 14, 16]
	8	[-6:2:8, 10, 12:2:14, 16:2:18]	[2, 4, 10, 16]
64	2	[0:2:16, 18, 20, 22, 24, 26:2:28, 30]	[2, 4, 8, 30, 50, 60, 64]
	4	[0:2:8, 10:2:14, 16, 18:2:20, 22, 24, 26]	[2, 16, 20, 30, 40, 60, 64]
	8	[0:2:14, 16, 18, 20, 22, 24]	[2, 4, 10, 30, 60, 64]

Table 3.5.2: Simulation settings of the RIS-SISO-KCS-GC scheme for $N = 4$

M	K	RIS-SISO-KCS-GC scheme, $N = 4$	
		SNR	T
16	2	[-10:2:2, 4, 6:2:8, 10:2:12]	[2, 4, 8, 16]
	4	[-10:2:2, 4:2:6, 8, 10:2:12]	[2, 4, 14, 16]
	8	[-10:2:0, 2, 4, 6, 8:2:10]	[2, 4, 8, 10, 16]
64	2	[-4:2:14, 16, 18, 20, 22:2:24, 26]	[2, 4, 10, 30, 60, 64]
	4	[-4:2:8, 10, 12:2:14, 16, 18]	[2, 4, 16, 50, 64]
	8	[-4:2:6, 8, 10:2:14, 16]	[2, 4, 10, 64]

Table 3.5.3: Simulation settings of the RIS-SISO-KCS-GC scheme for $N = 8$

M	K	RIS-SISO-KCS-GC scheme, $N = 8$	
		SNR	T
16	2	[-16:2:-6, -4, -2:2:0, 2:2:4]	[2, 4, 8, 16]
	4	[-16:2:-4, -2, 0, 2:2:4]	[2, 4, 12, 16]
	8	[-16:2:-8, -6:2:-4, -2, 0:2:4]	[2, 4, 12, 16]
64	2	[-8:2:2, 4:2:8, 10, 12]	[2, 4, 30, 64]
	4	[-8:2:8, 10]	[2, 60]
	8	[-8:2:4, 6, 8, 10]	[2, 10, 60, 64]

Table 3.5.4: Simulation settings of the RIS-SISO-KCS-GC scheme for $N = 16$

M	K	RIS-SISO-KCS-GC scheme, $N = 16$	
		SNR	T
16	2	[-22:2:-8, -6, -4:2:-2]	[2, 14, 16]
	4	[-22:2:-8, -6, -4, -2]	[2, 4, 12, 16]
	8	[-22:2:-10, -8, -6, -4:2:-2]	[2, 4, 12, 16]
64	2	[-16:2:-4, -2, 0, 2:2:4]	[2, 8, 60, 64]
	4	[-16:2:-4, -2, 0:2:4]	[2, 50, 64]
	8	[-16:2:-2, 0:2:2, 4]	[2, 30, 64]

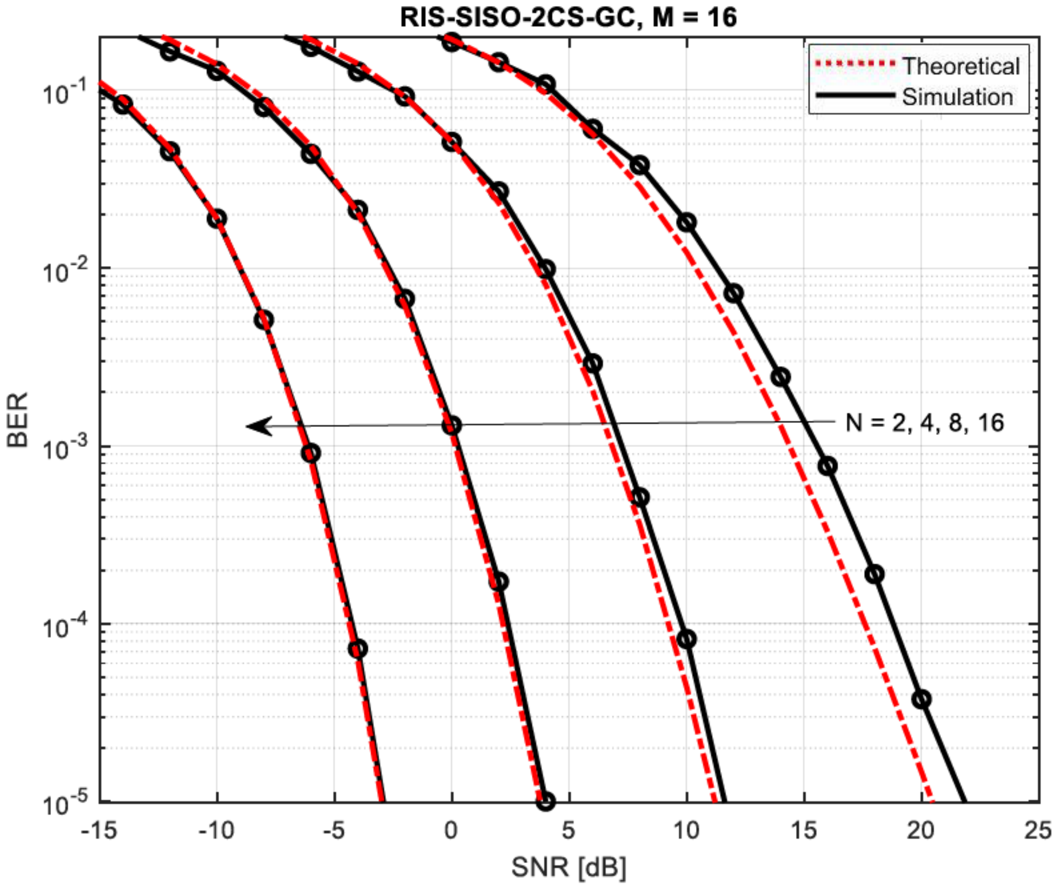

Figure 3.5.1: BER vs SNR graphs of RIS-SISO-2CS-GC scheme for $M = 16$ and varying N

Figure 3.5.1 shows the EP of the RIS-SISO-2CS-GC scheme for $M = 16$ and varying $N \in \{2, 4, 8, 16\}$. It can be observed that for $N = 2, 4, 8, 16$, the SNR values are 22dB, 12dB, 4dB and -3dB, respectively, for a BER of 10^{-5}. It is also observed that for $N = 2$ and $N = 4$, the theoretical bound is not as tight, whereas for $N = 8$ and $N = 16$, the bound fits tightly with the simulation graphs. This can be explained by observing Equation 3.19. As N increases, the tightness of the approximation increases as $F(\theta) \rightarrow 0$, meaning that higher values of N will yield a tighter approximation as opposed to lower N. Here, the diversity orders that are achieved for increasing N are 4, 8, 16 and 32.

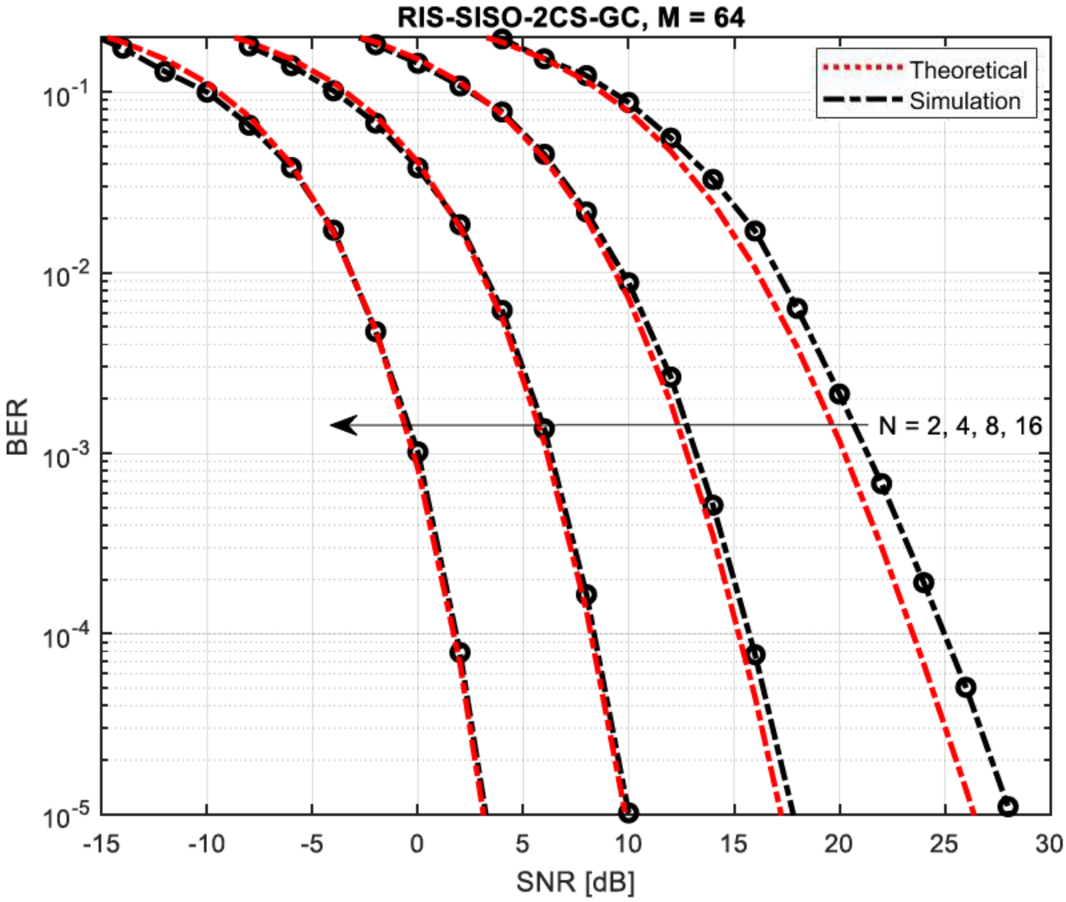

Figure 3.5.2: BER vs SNR graphs of RIS-SISO-2CS-GC scheme for $M = 64$ and varying N

Figure 3.5.2 shows the EP of the RIS-SISO-2CS-GC scheme for $M = 64$ and varying $N \in \{2, 4, 8, 16\}$. It can be observed that for $N = 2, 4, 8, 16$, the SNR values are 28dB, 17.5dB, 10dB and 3dB, respectively, at a BER of 10^{-5}. Similar to Figure 3.5.1, it is observed that for $N = 2$ and $N = 4$, the theoretical bound is not as tight, whereas for $N = 8$ and $N = 16$, the bound demonstrates a tight match with the simulation graphs. When comparing the EP of the RIS-SISO-2CS-GC shown in Figure 3.5.1 for $M = 16$ with that of Figure 3.5.2 for $M = 64$, it is observed that a 5-6dB deterioration in EP occurs for each corresponding N value. Note that the diversity orders and the theoretical bound observations are the same as that mentioned in Figure 3.5.1.

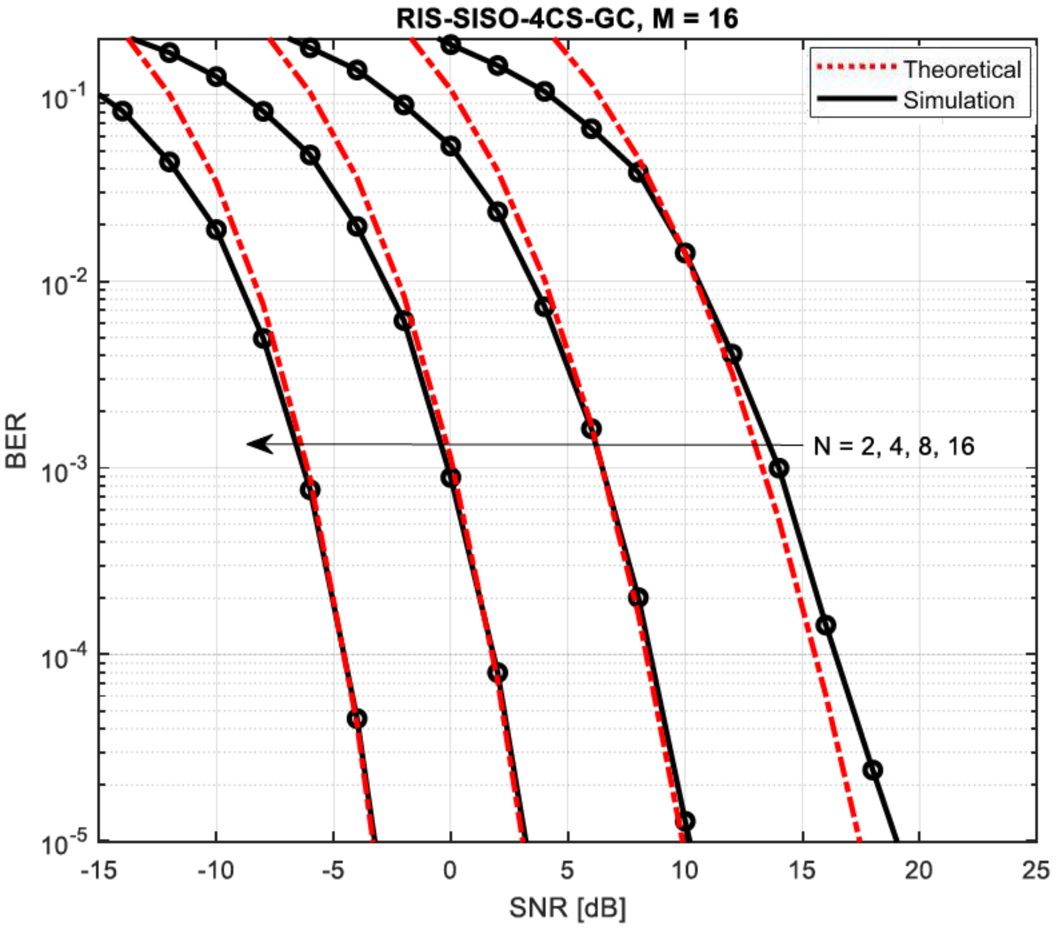

Figure 3.5.3: BER vs SNR graphs of RIS-SISO-4CS-GC scheme for $M = 16$ and varying N

Figure 3.5.3 shows the EP of the RIS-SISO-4CS-GC scheme for $M = 16$ and varying $N \in \{2, 4, 8, 16\}$. It can be observed that for $N = 2, 4, 8, 16$, the SNR values are 18.5dB, 10dB, 3dB and -3.5dB, respectively, at a BER of 10^{-5}. It is also observed that for $N = 2$, the theoretical bound fails, whereas for $N = 4, N = 8$ and $N = 16$, the theoretical bound fits tightly with the simulation graphs in the high SNR range. When comparing the RIS-SISO-4CS-GC to the RIS-SISO-2CS-GC scheme in Figure 3.5.1 for $M = 16$, it may be observed that there is an improvement of 4.5dB at $N = 2$, a 2dB improvement at $N = 4$, a 1dB improvement at $N = 8$ and an improvement of 0.5dB at $N = 16$. In this case, the diversity orders for increasing N are 8, 16, 32, 64. It is also noted that the bound does not fit the curves at high SNR. This can be explained by looking at Equation 3.20, whereby the diversity order influences the tightness of the curve for high SNRs. In this case, K increases the diversity order, meaning that the theoretical curve forms an upper bound at high SNRs. When comparing this to the RIS-SISO-2CS-GC scheme in Figure 3.5.1, it is observed that identical diversity orders of 8, 16 and 32 may be produced.

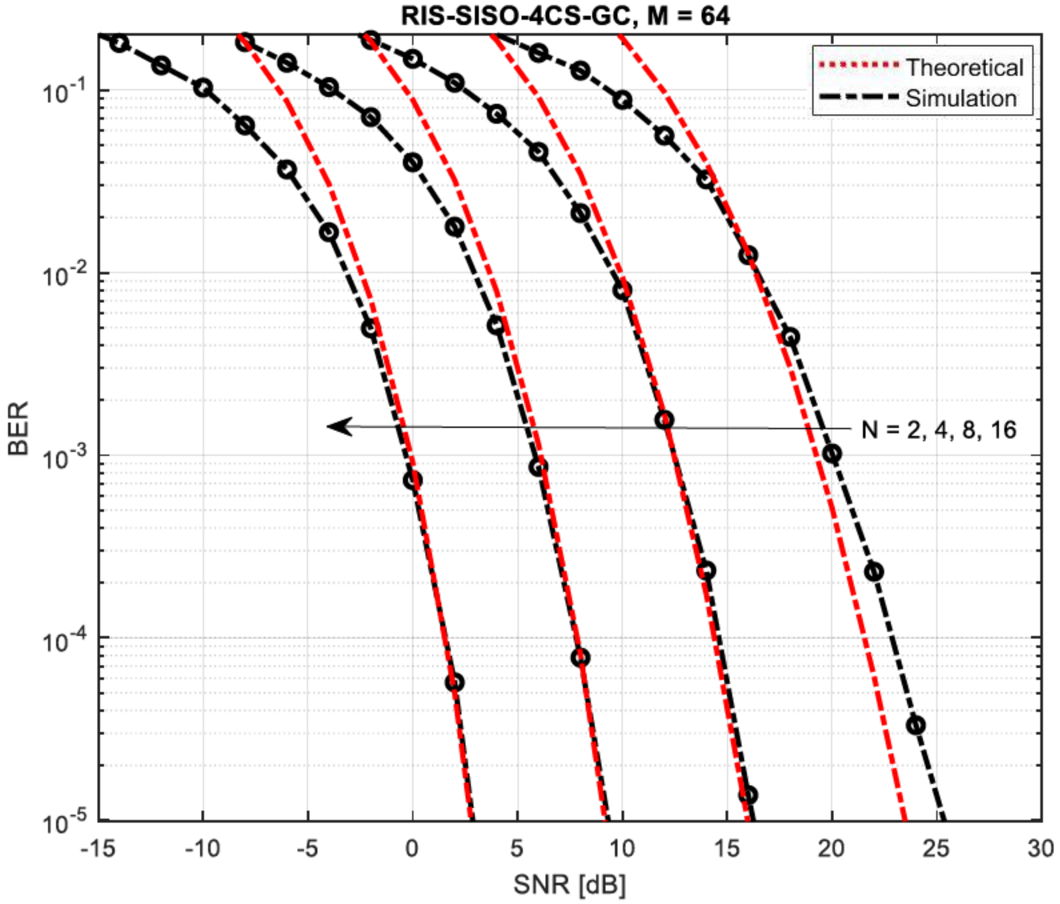

Figure 3.5.4: BER vs SNR graphs of RIS-SISO-4CS-GC scheme for $M = 64$ and varying N

Figure 3.5.4 shows the EP of the RIS-SISO-4CS-GC scheme for $M = 64$ and varying $N \in \{2, 4, 8, 16\}$. It can be observed that for $N = 2, 4, 8, 16$, the SNR values are 25.5dB, 16dB, 9dB and 2.5dB, respectively, at a BER of 10^{-5}. It is also observed that for $N = 2$, the theoretical bound fails, whereas for $N = 4, N = 8$ and $N = 16$, the theoretical bound fits tightly with the simulation graphs in the high SNR range. Comparing the RIS-SISO-4CS-GC to the RIS-SISO-2CS-GC scheme in Figure 3.5.2 for $M = 64$, it may be observed that there is an improvement of 2.5dB at $N = 2$, a 1.5dB improvement at $N = 4$, a 1dB improvement at $N = 8$ and an improvement of 0.5dB at $N = 16$. The same observations seen in Figure 3.5.3 regarding the theoretical bound at high SNRs is observed here. Again, it is observed that the RIS-SISO-4CS-GC scheme is able to maintain similar diversity orders to the RIS-SISO-2CS-GC scheme. The same observations with respect to diversity order are seen as in Figure 3.5.3.

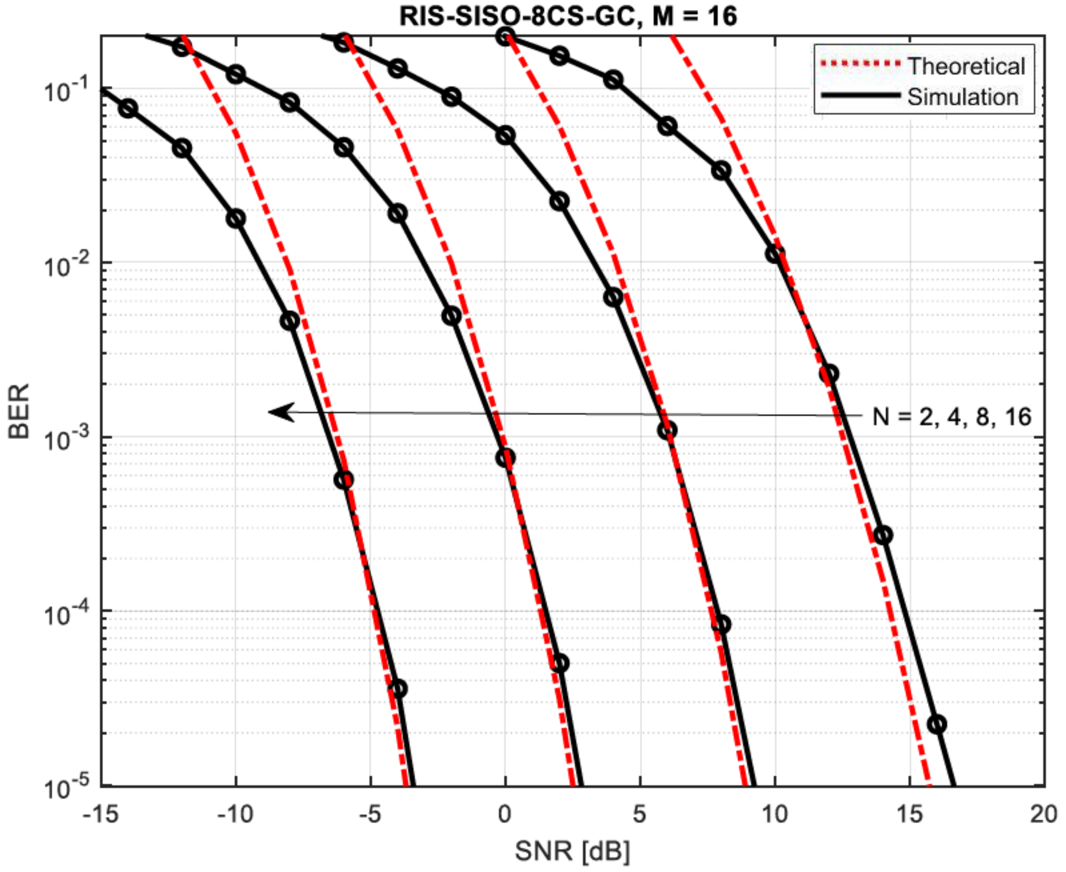

Figure 3.5.5: BER vs SNR graphs of RIS-SISO-8CS-GC scheme for $M = 16$ and varying N

Figure 3.5.5 shows the EP of the RIS-SISO-8CS-GC scheme for $M = 16$ and varying $N \in \{2, 4, 8, 16\}$. It can be observed that for $N = 2, 4, 8, 16$, the SNR values are 17dB, 9dB, 2.5dB and -3.75dB, respectively, for a BER of 10^{-5}. It is also observed that for $N = 2$, the theoretical bound fails, whereas for $N = 4, N = 8$ and $N = 16$, the theoretical bound fits tightly with the simulation graphs for high SNR. When comparing the RIS-SISO-8CS-GC scheme to the RIS-SISO-4CS-GC and RIS-SISO-2CS-GC schemes in Figure 3.5.3 and Figure 3.5.1 for $M = 16$, it may be observed that the RIS-SISO-8CS-GC scheme shows an improvement of 1.5dB at $N = 2$, a 1dB improvement at $N = 4$, a 0.5dB improvement at $N = 8$ and an improvement of 0.25dB at $N = 16$ over the RIS-SISO-4CS-GC scheme, and shows an improvement of 5dB at $N = 2$, a 3dB improvement at $N = 4$, a 1.5dB improvement at $N = 8$ and an improvement of 0.75dB at $N = 16$ over the RIS-SISO-2CS-GC scheme. Here, the diversity orders for increasing N are 16, 32, 64 and 128. When comparing the diversity orders of the RIS-SISO-4CS-GC, identical diversity orders of 16, 32 and 64 are seen, and when comparing to the RIS-SISO-2CS-GC, identical diversity orders of 16 and 32 are seen. Lastly, it is observed that for $K = 8$, the theoretical bound forms a steeper upper bound at high SNRs, which confirms the observation in Figure 3.5.3.

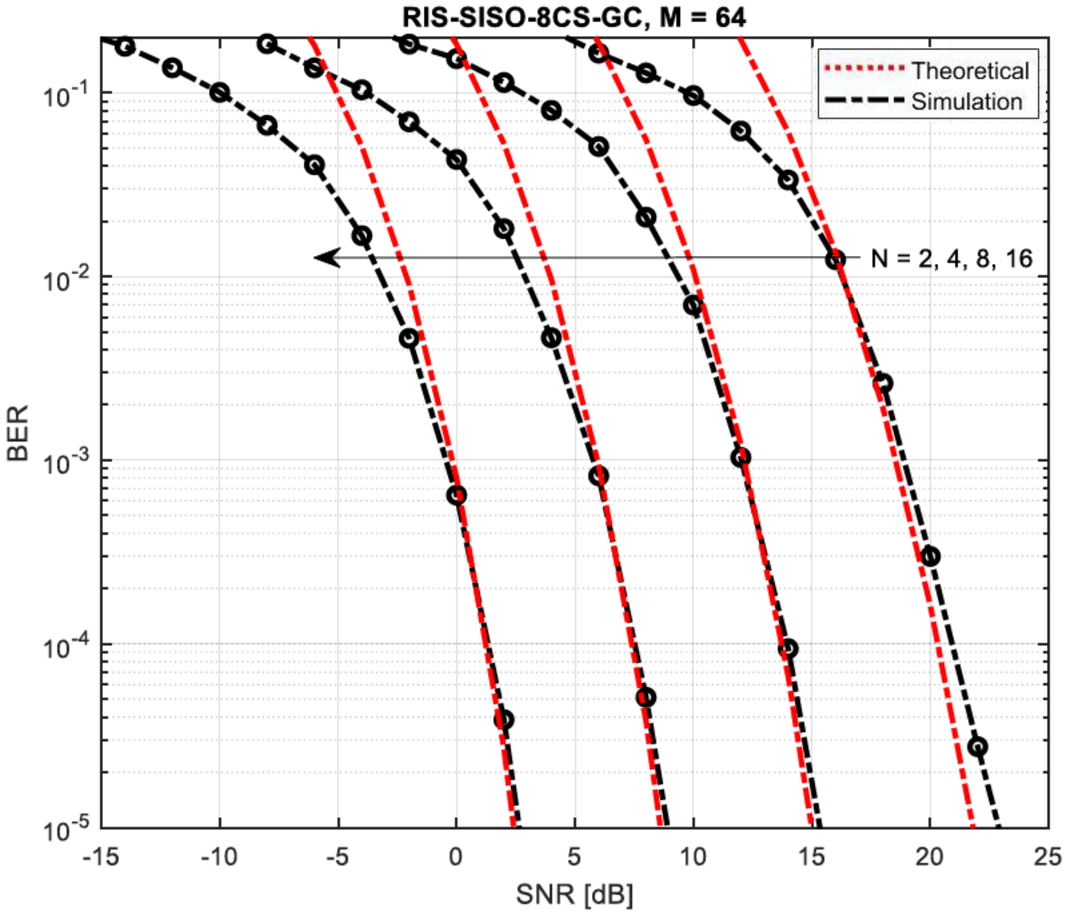

Figure 3.5.6: BER vs SNR graphs of RIS-SISO-8CS-GC scheme for $M = 64$ and varying N

Figure 3.5.6 shows the EP of the RIS-SISO-8CS-GC scheme for $M = 64$ and varying $N \in \{2, 4, 8, 16\}$. It can be observed that for $N = 2, 4, 8, 16$, the SNR values of 22.8dB, 15.3dB, 8.4dB and 2.4dB, respectively, at a BER of 10^{-5}. It is also observed that for $N = 2$, the theoretical bound fails, whereas for $N = 4, N = 8$ and $N = 16$, the theoretical bound fits tightly with the simulation graphs for high SNR. When comparing the RIS-SISO-8CS-GC scheme to the RIS-SISO-4CS-GC and RIS-SISO-2CS-GC schemes in Figures 3.5.4 and 3.5.2 for $M = 64$, it may be observed that the RIS-SISO-8CS-GC scheme shows an improvement of 3.3dB at $N = 2$, a 0.7dB improvement at $N = 4$, a 0.6dB improvement at $N = 8$ and an improvement of 0.1dB at $N = 16$ over the RIS-SISO-4CS-GC scheme, and shows an improvement of 5.2dB at $N = 2$, a 2.2dB improvement at $N = 4$, a 1.6dB improvement at $N = 8$ and an improvement of 0.6dB at $N = 16$ over the RIS-SISO-2CS-GC scheme. The same observations with respect to diversity order and the theoretical bound steepness are seen as in Figure 3.5.5.

Chapter Summary

In this chapter, the system model of the RIS-aided-SISO-KCS-GC scheme in Rayleigh fading channels was presented. The SSS-SD method of detecting K GCs as well as the performance analysis of the RIS-aided SISO KCS-GC scheme was also provided. The theoretical analysis has been shown to fit tightly with the simulation graphs for $N = 8$ and $N = 16$, but not as tight for $N = 2$ and $N = 4$. It was also observed that as K increases, the theoretical steepness at high SNRs increases, forming an upper bound at high SNRs. It was noted that as N increases, the EP gains decrease. Therefore, smaller values of N are more suited for varying K. It was observed that the RIS-SISO-KCS-GC is able to effectively maintain diversity order by virtue of the K-fold increase in diversity order.

CHAPTER 4

HYBRID REFLECTION MODULATION

4.1 Introduction

RIS elements are nearly passive in nature [16, 17, 66], meaning it simply reflects the incoming signal to a desired direction by optimizing the adjustable phase shifts of the RIS elements without an allocated source of energy. Much of the existing research on RISs focuses on these passive reflecting elements, with emphasis on improving EP and the SE of existing schemes [48, 53, 78, 113], optimizing EE [24, 116], and achievable rate [117] - [119].

In recent literature, RISs have been integrated with the popular IM concept. IM refers to a family of modulation techniques characterized by the transmission of additional information bits to alter the ON/OFF states of transmit antennas [120], RF mirrors [121] and various other transmission entities. It has been shown that the IM concept can increase SE and improve data rates significantly. The integration of RISs and IM has been performed in [49], which covers RIS-aided Spatial Modulation (RIS-SM) and RIS-aided Space Shift Keying (RIS-SSK). It has also been performed in [50], which integrates RISs with the popular emerging IM technique, Media-Based Modulation, called RIS-aided Media-Based Modulation (RIS-MBM).

A novel IM concept has been proposed in RIS literature [122] and [123] called Reflection Modulation (RM). RM entails that the passive RIS elements themselves can be used to generate reflection patterns which can transmit information. According to [124], this is achieved by switching between the ON/OFF states of the reflective elements using both passive beamforming and keying mechanisms to transmit information via reflection simultaneously.

Active reflecting elements have emerged as a solution to overcoming the multiplicative path fading described in [36], for passive RIS-aided systems assuming strong direct links. They have provided a new foundation for RIS research, as they can overcome path loss by reflecting and amplifying the wireless signal simultaneously. In [80], the channel capacity of an active RIS-aided SISO system is investigated, where power amplifiers are used to facilitate the active elements. In [77], the channel capacity of an active RIS-aided active RISs is applied to a single-input multiple-output (SIMO) system, to maximize SNR and improve the EE and SE using active elements. Further studies such as [125] and [126] followed showcasing the superior performance of active RISs compared to passive RISs. Despite its advantages, fully active RISs require greater power consumptions to be facilitated in comparison to that of passive RISs.

From this background, an H-RIS-aided scheme was proposed in [79] which utilizes the principle of IM and active reflective elements, called HRM. This chapter, hence, covers the HRM system model, its theoretical ABEP as well as other metrics of performance such as achievable rate and EE.

In this scheme, an unmodulated carrier signal is transmitted via an N-element H-RIS in a SISO system. The H-RIS is equipped with adjustable power amplifiers to enable active reflecting elements and a controller to adjust both the phase shifts of the reflecting elements and amplification gain of the active elements. They are also equipped with phase shifters corresponding to each reflective element to yield the optimal phase shift which maximizes the SNR. The RIS can either be split into subgroups comprising of active and passive elements or can operate as a fully passive RIS depending on whether the reflective power amplifiers are dynamically switched ON or OFF [79].

The motivation for the HRM scheme is that it integrates IM and active reflective elements into a scheme whereby the H-RIS aids in the transmitter of information. The H-RIS is equipped with integrated electronics which allows for both reflection and amplification functionality. Each element may be switched ON or OFF depending on the incoming bits, thereby significantly decreasing power consumption over fully active RISs, and improving the EP and SE over fully passive RIS-aided systems.

The chapter is structured as follows: In Section 4.2, the system model and mathematical model for HRM is presented. In Section 4.3, a special case of HRM, namely fully-HRM (F-HRM) is discussed, and its system model presented. In Section 4.4, the performance analysis of the HRM scheme is presented which includes the ABEP and an upper bounded approximation of the theoretical result. Section 4.5 covers the achievable rate of the HRM scheme, and Section 4.6 covers the EE of the HRM scheme. In Section 4.7, simulation results are provided covering the EP, achievable rate and EE of the HRM system.

4.2 HRM system model

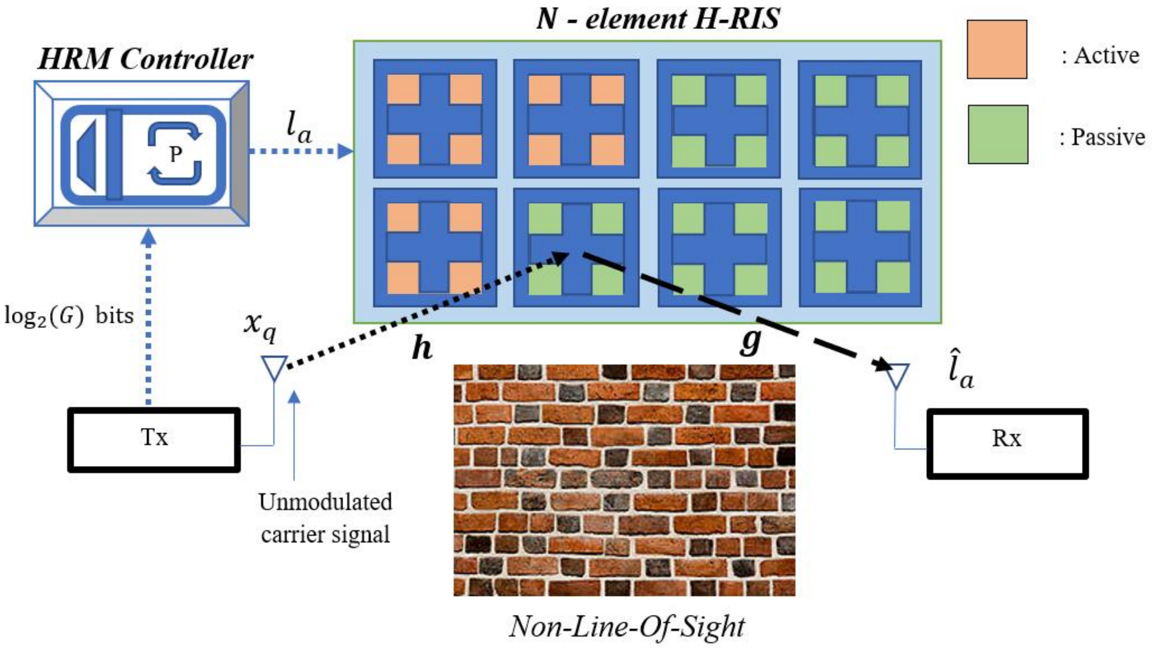

Figure 4.2.1: Diagram illustrating the system model of the HRM scheme

Consider Figure 4.2.1. The H-RIS has a total of N reflecting elements that are divided into sub-groups, denoted by G. Therefore, the variable $S_G = {}^{N}/_{G}$ denotes the number of reflective elements present in each subgroup.

The HRM scheme transmits a total of $\log_2(G)$ bits which selects an index, denoted as $\ell_a \in [0: G-1]$, which selects the number of active and passive elements on the H-RIS as $N_a = \ell_a S_G$ and $N_p = N - N_a$, respectively. For $\ell_a = 0$, the H-RIS functions as a fully passive RIS.

The SE of the HRM system is therefore given as:

$$m = \log_2(G) \text{ bits/s/Hz}. \tag{4.1}$$

As an example, the transmission of information in the HRM scheme can be described as follows:

Table 4.2.1: Table illustrating example mapping of HRM scheme

	Assume $N = 16, G = 4, S_G = {}^{16}/_{4} = 4$			
Parameters determining HRM state	Transmission of $\log_2(4) = 2$ bits per index with $\ell_a \in [0 : 3]$			
Information Bits	$\{00\}$	$\{01\}$	$\{10\}$	$\{11\}$
Index (ℓ_a)	0	1	2	3
Number of active elements (N_a)	0	4	8	12
Number of passive elements (N_p)	16	12	8	4
HRM symbol (H_{ℓ_a})	H_0	H_1	H_2	H_3

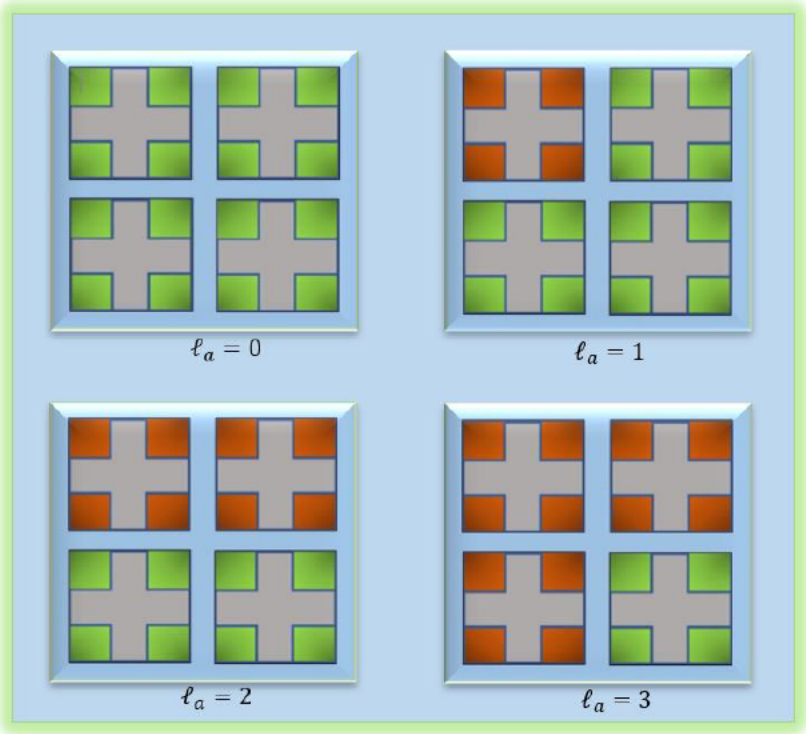

Figure 4.2.2: Example of possible H-RIS configurations in HRM scheme for $N = 16$ & $G = 4$

In Table 4.2.1, a possible HRM mapping scheme is considered for $N = 16$ and $G = 4$. The number of reflective elements in each subgroup of the H-RIS can be determined by $S_G = {}^{N}/_{G} = {}^{16}/_{4} = 4$. For $G = 4$, the SE of the HRM scheme is $m = \log_2(G) = \log_2(4) = 2$ bits/s/Hz. Since there are 2 bits being transmitted, there are 4 different bit combinations: $\{00\}, \{01\}, \{10\}$, and $\{11\}$. Considering Figure 4.2.2, if the information bits are $\{00\}$, the index $\ell_a = \ell_0 = 0$ is selected, the number of active elements is $N_a = \ell_0 S_G = (0)(4) = 0$, and the H-RIS is configured to contain only passive reflective elements, and act as a fully passive RIS. Similarly, for $\{01\}$, $\ell_a = \ell_1 = 1$, $N_a = \ell_1 S_G = (1)(4) = 4$, and the H-RIS is configured to contain 1 group of 4 active reflective elements and 3 groups of 4 passive elements, 4 passive elements in each group. For $\{10\}, \ell_a = \ell_2 = 2$, $N_a = \ell_2 S_G = (2)(4) = 8$, and the RIS is configured to contain 2 groups of 4 active reflective elements and 2 groups of 4 passive elements. Finally, for $\{11\}, \ell_a = \ell_3 = 3, N_a = \ell_3 S_G = (3)(4) = 12$, and the H-RIS is configured to contain 3 groups of 4 active reflective elements and 1 group of 4 passive elements. The different bit configurations can be considered as a means to select corresponding HRM symbols denoted by H_{ℓ_a} depending on ℓ_a, therefore it can be said that $\{00\}$ selects H_0, $\{01\}$ selects H_1, $\{10\}$ selects H_2, and $\{11\}$ selects H_3. The computation of these HRM symbols will be discussed later on in this chapter.

Each RIS reflection coefficient can be described in polar form as:

$$\varrho_k = |\varrho_k| e^{j\theta_k}, k \in [1{:}N], \tag{4.2}$$

where $|\varrho_k|$ is the magnitude of the k-th reflective elements and $\theta_k \in [-\pi, \pi]$ is the phase of the k-th reflective elements. The reflection coefficient of a passive RIS has a unit magnitude ($|\varrho_k| = 1$) which means that the passive element reflects the signal only, whereas active elements both amplify and reflect the signal simultaneously. Therefore, each reflection co-efficient of the active element has an amplification gain given by $|\varrho_k| = \alpha_k > 1$.

Hence, the reflection co-efficients of active RIS elements is given as [79]:

$$\varrho_k = \alpha_k e^{j\theta_k}, k \in [1{:}\, N_a], \tag{4.3}$$

and the reflection co-efficients of passive RISs is given as [79]:

$$\varrho_k = e^{j\theta_k}, k \in [(N_a + 1){:}N]. \tag{4.4}$$

In this analysis, it is assumed that the amplification gain of each active element is equal, in other words, $\alpha_k = \alpha$ for all active elements.

Based on this analysis, the active and passive phase reflection matrices can be computed as [79]:

$$\boldsymbol{\phi} = \begin{bmatrix} e^{j\theta_1} & 0 & 0 & \cdots & 0 \\ 0 & e^{j\theta_2} & 0 & \cdots & 0 \\ \vdots & 0 & \ddots & \cdots & 0 \\ \vdots & \vdots & \vdots & \ddots & \vdots \\ 0 & 0 & 0 & \cdots & e^{j\theta_{N_a}} \end{bmatrix}, \tag{4.5.1}$$

$$\boldsymbol{\psi} = \begin{bmatrix} e^{j\theta_{N_a+1}} & 0 & 0 & \cdots & 0 \\ 0 & e^{j\theta_{N_a+2}} & 0 & \cdots & 0 \\ \vdots & 0 & \ddots & \cdots & 0 \\ \vdots & \vdots & \vdots & \ddots & \vdots \\ 0 & 0 & 0 & \cdots & e^{j\theta_N} \end{bmatrix}, \tag{4.5.2}$$

where $\boldsymbol{\phi} \in \mathbb{C}^{N_a \times N_a}$ is the active reflection diagonal matrix based on the number of active reflective elements, and $\boldsymbol{\psi} \in \mathbb{C}^{N_p \times N_p}$ is the passive reflection diagonal matrix based on the number of passive reflective elements.

The HRM scheme is analysed under slow frequency-flat Rayleigh fading channels. There are two distinct fading paths, the first being in the transmitter-to-H-RIS (Tx-H-RIS) path, and the second being the H-RIS-to-receiver (H-RIS-Rx) path. The path losses in each fading path are defined as follows [79]:

$$\mathcal{L}_t = \mathrm{K}_{\mathrm{pl}} d_t^{-\omega_t}, \tag{4.6.1}$$

$$\mathcal{L}_r = \mathrm{K}_{\mathrm{pl}} d_r^{-\omega_r}, \tag{4.6.2}$$

where $\mathcal{L}_t$ denotes the path loss in the Tx-H-RIS path, $\mathcal{L}_r$ denotes the path loss in the H-RIS-Rx path. K_{pl} is the reference path loss for a 1-metre (m) distance [79], d_t and d_r represent the Tx-H-RIS and H-RIS-Rx path distances respectively, and $\omega_t, \omega_r > 1$ denote the path loss exponents at the Tx-H-RIS and H-RIS-Rx paths respectively.

The Rayleigh fading channel vectors can now be defined in terms of (4.6.1) and (4.6.2) by i.i.d. RVs as $\boldsymbol{h} \in \mathbb{C}^{N\times 1} \sim \mathcal{CN}(0,\mathcal{L}_t)$, and $\boldsymbol{g} \in \mathbb{C}^{1\times N} \sim \mathcal{CN}(0,\mathcal{L}_r)$, where $\boldsymbol{h}$ is the channel vector in the Tx-H-RIS path, and $\boldsymbol{g}$ is the channel vector in the H-RIS-Rx path. These fading vectors may be expressed as $\boldsymbol{h} = [\boldsymbol{h}_a\ \boldsymbol{h}_p]^T$ and $\boldsymbol{g} = [\boldsymbol{g}_a\ \boldsymbol{g}_p]$, where $\boldsymbol{h}_a, \boldsymbol{g}_a \in \mathbb{C}^{1\times N_a}$ represent the fading subvectors corresponding with active RIS elements, and $\boldsymbol{h}_p, \boldsymbol{g}_p \in \mathbb{C}^{1\times N_p}$ represent the fading subvectors corresponding with passive RIS elements.

The receive signal for a given transmit power, P_{tx}, can therefore be written as [79]:

$$r = \left(\sqrt{\mathrm{P}_{tx}}\alpha\boldsymbol{g}_a\boldsymbol{\phi}\boldsymbol{h}_a^T + \alpha\boldsymbol{g}_a\boldsymbol{\phi}\boldsymbol{w}^T\right) + \left(\sqrt{\mathrm{P}_{tx}}\boldsymbol{g}_p\boldsymbol{\psi}\boldsymbol{h}_p^T + n_{stc}\right), \tag{4.7}$$

where the term $\left(\sqrt{\mathrm{P}_{tx}}\alpha\boldsymbol{g}_a\boldsymbol{\phi}\boldsymbol{h}_a^T + \alpha\boldsymbol{g}_a\boldsymbol{\phi}\boldsymbol{w}^T\right)$ denotes that part of the received signal corresponding to the active RIS elements, and the term $\left(\sqrt{\mathrm{P}_{tx}}\boldsymbol{g}_p\boldsymbol{\psi}\boldsymbol{h}_p^T + n_{stc}\right)$ denotes that part of the received signal corresponding to the passive RIS elements. The static noise present in the channel is denoted by $n_{stc} \sim \mathcal{CN}(0,\sigma_{stc}^2)$. The active portion of the received signal includes a thermal noise term $\alpha\boldsymbol{g}_a\boldsymbol{\phi}\boldsymbol{w}^T, \boldsymbol{w} \in \mathbb{C}^{1\times N_a} \sim \mathcal{CN}\left(0,\boldsymbol{I}_{N_a}\sigma_{dyn}^2\right)$ which is non-negligible because of the power dissipated by the power amplifiers of the active RIS elements.

The maximum instantaneous received SNR can be derived by rewriting the received signal in (4.7) as:

$$r = \left(\sqrt{\mathrm{P}_{tx}}\alpha\boldsymbol{g}_a\boldsymbol{\phi}\boldsymbol{h}_a^T + \sqrt{\mathrm{P}_{tx}}\boldsymbol{g}_p\boldsymbol{\psi}\boldsymbol{h}_p^T\right) + \left(\alpha\boldsymbol{g}_a\boldsymbol{\phi}\boldsymbol{w}^T + n_{stc}\right). \tag{4.8}$$

Note that in (4.8), the signal parts $\left(\sqrt{\mathrm{P}_{tx}}\alpha\boldsymbol{g}_a\boldsymbol{\phi}\boldsymbol{h}_a^T + \sqrt{\mathrm{P}_{tx}}\boldsymbol{g}_p\boldsymbol{\psi}\boldsymbol{h}_p^T\right)$ and noise parts $(\alpha\boldsymbol{g}_a\boldsymbol{\phi}\boldsymbol{w}^T + n_{stc})$ have been grouped together to write the maximum SNR as [79]:

$$\max_{\alpha,\boldsymbol{\phi},\boldsymbol{\psi}} \quad \rho = \frac{signal\ power}{noise\ power} = \frac{\left\|\sqrt{\mathrm{P}_{tx}}\alpha\boldsymbol{g}_a\boldsymbol{\phi}\boldsymbol{h}_a^T + \sqrt{\mathrm{P}_{tx}}\boldsymbol{g}_p\boldsymbol{\psi}\boldsymbol{h}_p^T\right\|_F^2}{\alpha^2\|\boldsymbol{g}_a\boldsymbol{\phi}\|_F^2\sigma_{dyn}^2 + \sigma_{stc}^2}. \tag{4.9}$$

The expression in (4.9) simplifies to:

$$\max_{p,\boldsymbol{\phi},\boldsymbol{\psi}} \quad \rho = \mathrm{P}_{tx}\frac{\left\|\alpha\boldsymbol{g}_a\boldsymbol{\phi}\boldsymbol{h}_a^T + \boldsymbol{g}_p\boldsymbol{\psi}\boldsymbol{h}_p^T\right\|_F^2}{\alpha^2\|\boldsymbol{g}_a\boldsymbol{\phi}\|_F^2\sigma_{dyn}^2 + \sigma_{stc}^2}, \tag{4.10}$$

$$\text{Such that:} \qquad \mathrm{P}_a \geq \alpha^2\left(\mathrm{P}_{tx}\|\boldsymbol{\phi}\boldsymbol{h}_a^T\|_F^2 + \|\boldsymbol{\phi}\|_F^2\sigma_{dyn}^2\right), \tag{4.11}$$

where P_a is the maximum reflection power constraint.

It is clear from (4.7) that the HRM receive signal is very complex to compute. To simplify (4.7), a similar analysis in [113] can be used. The aim is to maximise the received SNR by optimising the phase θ_k. Hence, given that $\boldsymbol{h}$ and $\boldsymbol{g}$ can be expressed in polar form as $h_k = |h_k|e^{j\Phi_k}$ and $g_k = |g_k|e^{j\xi_k}$, the optimum phase shift which maximises the received SNR is [79]:

$$\theta_k = -(\Phi_k + \xi_k). \tag{4.12}$$

The amplification gain α can also be written based on the constraint given in (4.11) as [79]:

$$\alpha \leq \sqrt{\frac{\mathrm{P}_A}{\mathrm{P}_{tx}\|\boldsymbol{h}_a^T\|_F^2 + \sigma_{dyn}^2}}. \tag{4.13}$$

The power consumption of the passive RIS elements is considered negligible and is, therefore, ignored.

It can be noted that from (4.13), the active reflection diagonal matrix $\boldsymbol{\phi}$ has been eliminated from the expression. This is because by optimising θ_k, the SNR is maximized and the phases are eliminated from the expression [79], implying that (4.7) can be rewritten solely in terms of the magnitudes of the channel components as:

$$r = \left(\sqrt{\mathrm{P}_{tx}}\alpha \sum_{k=1}^{N_a} |h_k||g_k| + \alpha \sum_{k=1}^{N_a} |g_k|\breve{w}_k\right) + \left(\sqrt{\mathrm{P}_{tx}} \sum_{k=N_a+1}^{N} |h_k||g_k| + n_{stc}\right). \tag{4.14}$$

To simplify further, (4.14) can be rewritten as:

$$r = \sqrt{\mathrm{P}_{tx}}\left(\alpha \sum_{k=1}^{N_a} |h_k||g_k| + \sum_{k=N_a+1}^{N} |h_k||g_k|\right) + \left(\alpha \sum_{k=1}^{N_a} |g_k|\breve{w}_k + n_{stc}\right). \tag{4.15}$$

where $\breve{w}_k = w_k e^{-j\xi_k}$, and w_k corresponds to the k-th complex element of $\boldsymbol{w}$.

The signal part of (4.15) can be expressed as HRM symbols computed as:

$$H_{\ell_a} = \alpha \sum_{k=1}^{N_a} |h_k||g_k| + \sum_{k=N_a+1}^{N} |h_k||g_k|. \tag{4.16}$$

It can be observed clearly from (4.16) how the channel realisations depend on the amplification gain and number of active and passive elements.

By employing the CLT, the noise part of (4.15) is approximated as a complex-valued Gaussian RV [79]. Hence, it can be written as:

$$\alpha \sum_{k=1}^{N_a} |g_k|\breve{w}_k + n_{stc} \approx \eta \sim CN\left(0, \mathrm{N}_{\Upsilon}^2\right), \tag{4.17}$$

where $\mathrm{N}_{\Upsilon}^2 \approx \alpha^2 N_a \mathcal{L}_r \sigma_{dyn}^2 + \sigma_{stc}^2$ [79].

The receive signal may now be written, based on the analysis above, as [79]:

$$r = \sqrt{\mathrm{P}_{tx}} H_{\ell_a} + \eta. \tag{4.18}$$

The HRM receiver assumes full knowledge of the CSI, and the optimal detection of the estimated index $\hat{\ell}_a$ can be performed using ML detection by considering all signal levels to estimate ℓ_a. This is performed as follows [79]:

$$\hat{\ell}_a = \underset{\ell_a \in [0:G-1]}{\operatorname{argmax}}\, p\left(r|H_{\ell_a}\right). \tag{4.19}$$

The expression in (4.19) considers the conditional PDF of received signal r given any HRM symbol in (4.16). The PDF is given in [79] as:

$$p\left(r|H_{\ell_a}\right) = \frac{1}{\pi N_{\Upsilon}^2} \exp\left(-\frac{\left|r - \sqrt{\mathrm{P}_{tx}} H_{\ell_a}\right|^2}{N_{\Upsilon}^2}\right). \tag{4.20}$$

It can be pointed out that the effect of the noise variance N_{Υ}^2 varies as the number of active elements N_a varies, but this effect on the decision metric in (4.19) is negligible because of the path attenuation $\mathcal{L}_r$ that each active element experiences.

Hence, the final ML detection expression which estimates ℓ_a is [79]:

$$\hat{\ell}_a = \underset{\ell_a \in [0:G-1]}{\operatorname{argmin}} \left|r - \sqrt{\mathrm{P}_{tx}} H_{\ell_a}\right|^2. \tag{4.21}$$

In (4.21), it is evident that all possible combinations of active and passive RIS elements are considered in the detection, and the detector selects the combination yielding the smallest argument with respect to the virtual HRM constellation for the receive signal in (4.18).

4.3 Fully-HRM

As established in the previous section, the H-RIS is partitioned into various subgroups to determine how many elements can be either active or passive to manipulate the carrier signal in the HRM scheme. However, a special case exists where the H-RIS can actually be utilized as either a fully active RIS or a fully passive RIS, without having to divide the H-RIS into groups.

In the F-HRM scheme, a single bit ($m = 1$ bit/s/Hz) of information to control the states of all reflecting elements in the H-RIS. If the information bit is $\{0\}$, the H-RIS operates as a fully passive RIS which simply reflects the incoming signal with the optimal phase shifts given in (4.12). If the information bit is $\{1\}$, all reflecting elements are configured as active, with the optimal phase shifts in (4.12), the amplification gain α and the additional dynamic/thermal noise.

It is important to note that the H-RIS of the F-HRM scheme can be fully active at any point, whereas the H-RIS for the HRM scheme for $G = 2$ can only be half-active. Therefore, more elements can become active in the F-HRM scheme, thereby yielding a better EP over the HRM scheme for $G = 2$, which is a key advantage of the scheme. A drawback, however, is that the SE is fixed to $m = 1$ bit/s/Hz, which takes away the advantages of IM from the scheme.

It is clear to see that in this scheme, all reflective elements are configured in the same manner, and the number of active elements on the H-RIS is determined by $N_a = \ell_a N$, where $\ell_a \in [0\!:1]$.

The receive signal of F-HRM is based on (4.18) as:

$$r_f = \sqrt{\mathrm{P}_{tx}} H_{\ell_a} + \eta, \tag{4.22}$$

where $H_{\ell_a}^{F_{HRM}}$ denotes one of two possible F-HRM symbols given by:

$$H_0 = \sum_{k=1}^{N} |h_k||g_k|, \text{ if } \ell_a = 0, \tag{4.23.1}$$

$$H_1 = \alpha \sum_{k=1}^{N} |h_k||g_k|, \text{ if } \ell_a = 1. \tag{4.23.2}$$

The optimal ML detector is based on (4.21), assuming full knowledge of the CSI as:

$$\hat{\ell}_a = \underset{\ell_a \in [0:1]}{\operatorname{argmin}} \left| r_f - \sqrt{\mathrm{P}_{tx}} H_{\ell_a} \right|^2. \tag{4.24}$$

The maximum received instantaneous SNR is based on (4.10), and can be written as:

$$\max_{p,\boldsymbol{\phi},\boldsymbol{\psi}} \quad \rho = \mathrm{P}_{tx} \frac{\left\| \boldsymbol{g}_p \boldsymbol{\psi} h_p^T \right\|_F^2}{\sigma_{stc}^2}, \text{ if } \ell_a = 0, \tag{4.25}$$

$$\max_{p,\boldsymbol{\phi},\boldsymbol{\psi}} \quad \rho = \mathrm{P}_{tx} \frac{\left\| \alpha \boldsymbol{g}_a \boldsymbol{\phi} \boldsymbol{h}_a^T \right\|_F^2}{\alpha^2 \left\| \boldsymbol{g}_a \boldsymbol{\phi} \right\|_F^2 \sigma_{dyn}^2 + \sigma_{stc}^2}, \text{ if } \ell_a = 1. \tag{4.26}$$

The power constraint for (4.26) is based on (4.11), and the optimal phase shifts and amplification gain are based on (4.12) and (4.13).

4.4 Performance Analysis of HRM scheme

First, it is assumed that the ℓ_a along with corresponding number of active reflective elements $N_a = \ell_a S_G$ is incorrectly detected as $\hat{\ell}_a$ and $\widehat{N}_a = \hat{\ell}_a S_G$. The CPEP can be written as [79]:

$$P\left(\ell_a \rightarrow \hat{\ell}_a | \boldsymbol{h}, \boldsymbol{g}, \boldsymbol{\phi}, \boldsymbol{\psi}\right) = P\left(\left|r - \sqrt{\mathrm{P}_{tx}} H_{\ell_a}\right|^2 > \left|r - \sqrt{\mathrm{P}_{tx}} H_{\hat{\ell}_a}\right|^2\right). \tag{4.27}$$

The expression in (4.27) is written by employing the Q-function as follows [79]:

$$P\left(\ell_a \rightarrow \hat{\ell}_a | \boldsymbol{h}, \boldsymbol{g}, \boldsymbol{\phi}, \boldsymbol{\psi}\right) = Q\left(\sqrt{\frac{\mathrm{P}_{tx}\left|H_{\ell_a} - H_{\hat{\ell}_a}\right|^2}{2\mathrm{N}_{\Upsilon}^2}}\right). \tag{4.28}$$

The full derivation of (4.28) can be found in Appendix C.

The channel magnitudes $|h_k|$ and $|g_k|$ are i.i.d. Rayleigh RVs with $\sigma_{|h_k|} = \sqrt{\frac{\mathcal{L}_t}{2}}$ and $\sigma_{|g_k|} = \sqrt{\frac{\mathcal{L}_r}{2}}$. These RVs have means of $E[|h_k|] = \sigma_{|h_k|}\sqrt{\frac{\pi}{2}} = \sqrt{\mathcal{L}_t}\sqrt{\frac{\pi}{4}}$ and $E[|g_k|] = \sigma_{|g_k|}\sqrt{\frac{\pi}{2}} = \sqrt{\mathcal{L}_r}\sqrt{\frac{\pi}{4}}$ respectively; and variances of $Var(|h_k|) = \sigma_{|h_k|}^2\left(2 - \frac{\pi}{2}\right) = \mathcal{L}_t\left(1 - \frac{\pi}{4}\right)$ and $Var(|g_k|) = \sigma_{|g_k|}^2\left(2 - \frac{\pi}{2}\right) = \mathcal{L}_r\left(1 - \frac{\pi}{4}\right)$.

The variable $\mathrm{T} = H_{\ell_a} - H_{\hat{\ell}_a}$ is a Gaussian RV, where the mean and variance of T is written as [79]:

$$\mu_{\mathrm{T}} = \left(\frac{\pi}{4}\right)\sqrt{\mathcal{L}_t\mathcal{L}_r}\left(\alpha\left(N_a - \widehat{N}_a\right) - \left(N_a - \widehat{N}_a\right)\right), \tag{4.29.1}$$

$$\sigma_{\mathrm{T}}^2 = \mathcal{L}_t\mathcal{L}_r\left(1 - \frac{\pi^2}{16}\right)\left[\alpha^2\left(N_a - \widehat{N}_a\right) + \left(N_a - \widehat{N}_a\right)\right]. \tag{4.29.2}$$

The full derivation (4.29.1) and (4.29.2) can be found in Appendix D.

The average PEP is derived using the MGF approach by considering the polar form of the Q-function as $Q(x) = \frac{1}{\pi}\int_0^{\frac{\pi}{2}} \exp\left(-\frac{x^2}{2\sin^2\emptyset}\right) d\emptyset$ [79], where $x = \sqrt{\frac{\mathrm{P}_{tx}\left|H_{\ell_a} - H_{\hat{\ell}_a}\right|^2}{2\mathrm{N}_{\Upsilon}^2}}$. To use the MGF, the variable $\mathrm{Z} = |\mathrm{T}|^2$ is defined as a non-central chi-squared distributed RV for the following MGF given in [15] as:

$$\mathrm{M}_{\mathrm{Z}}(s) = \frac{\exp\left(\frac{\mu_{\mathrm{T}}^2 s}{1 - 2\sigma_{\mathrm{T}}^2 s}\right)}{\sqrt{1 - 2\sigma_{\mathrm{T}}^2 s}}. \tag{4.30}$$

The average PEP for $s = -\frac{\mathrm{P}_{tx}}{4N_{\Upsilon}^2\sin^2\emptyset}$ can hence be expressed as [79]:

$$P\left(\ell_a \rightarrow \hat{\ell}_a\right) = \frac{1}{\pi}\int_0^{\frac{\pi}{2}} \frac{\exp\left(\frac{p_1}{p_2}\right)}{\sqrt{p_2}} d\emptyset, \tag{4.31}$$

where $p_1 = -\frac{\mu_{\mathrm{T}}^2\mathrm{P}_{tx}}{4N_{\Upsilon}^2\sin^2\emptyset}$, and $p_2 = 1 + \frac{\sigma_{\mathrm{T}}^2\mathrm{P}_{tx}}{4N_{\Upsilon}^2\sin^2\emptyset}$.

By letting $f(\emptyset) = \frac{\exp\left(\frac{p_1}{p_2}\right)}{\sqrt{p_2}}$, $a \approx 0$ and $b = \frac{\pi}{2}$, the trapezoidal rule may be used, such that (4.31) can be approximated as:

$$P\left(\ell_a \to \hat{\ell}_a\right) \approx \left(\frac{1}{\pi}\right)\frac{(b-a)}{n}\left[\frac{\left(f(a)+f(b)\right)}{2} + \sum_{k=1}^{n-1} f\left(a + \frac{k(b-a)}{n}\right)\right], \qquad (4.32)$$

where $n = 10$ is the number of iterations selected to approximate (4.32).

The average PEP in (4.31) results in the ABEP for $G = 2, m = 1$ bits/s/Hz, for $\zeta = N_a - \hat{N}_a$.

For higher SEs ($G > 2$), the upper bound in [79] is given as:

$$P_e \leq \frac{1}{r2^r}\sum_{\ell_a}\sum_{\hat{\ell}_a} P\left(\ell_a \to \hat{\ell}_a\right) N\left(\ell_a \to \hat{\ell}_a\right), \qquad (4.33)$$

where $N\left(\ell_a \to \hat{\ell}_a\right)$ denotes the number of bit errors per associated PEP event. It is useful to note that (4.31) can be upper-bounded by setting $\emptyset = \frac{\pi}{2}$ as:

$$P\left(\ell_a \to \hat{\ell}_a\right) \leq \frac{\exp\left(\frac{s_1}{s_2}\right)}{2\sqrt{s_2}}, \qquad (4.34)$$

where $s_1 = -\frac{\mu_{\mathrm{T}}^2 \mathrm{P}_{tx}}{4N_{\Upsilon}^2}$, $s_2 = 1 + \frac{\sigma_{\mathrm{T}}^2 \mathrm{P}_{tx}}{4N_{\Upsilon}^2}$, and $r = \log_2(G)$.

4.5 Achievable Rate of the HRM scheme

The achievable rate of the HRM system is computed by considering a receive signal vector space denoted by $\boldsymbol{R}$ and a spatial constellation H [79]. The constellation H is derived by considering the transmission of an unmodulated carrier signal. Since the information bits are modulated into symbols denoted by H_{ℓ_a}, H denotes the spatial constellation upon which all symbols H_{ℓ_a} can be mapped.

The achievable rate of the HRM scheme can be computed by considering the mutual information (MI) between the transmitted and received signals of the HRM scheme as [79]:

$$A_r(H;\,\boldsymbol{R}) = \int_{-\infty}^{\infty} p\left(r|H_{\ell_a}\right)p\left(H_{\ell_a}\right)\log_2\left(\frac{p\left(r|H_{\ell_a}\right)}{\sum_{\hat{\ell}_a} p\left(r|H_{\hat{\ell}_a}\right)p\left(H_{\ell_a}\right)}\right)dr, \qquad (4.35)$$

where $p\left(r|H_{\ell_a}\right)$ denotes the conditional PDF given in (4.20), $p\left(H_{\ell_a}\right)$ denotes the probability of each HRM symbol being transmitted. Note that since the HRM symbols are dependent on index ℓ_a, there are a total of G HRM symbols. It is assumed that all symbols are equally likely to be transmitted, implying that $p\left(H_{\ell_a}\right) = {}^{1}/_{G}$.

By substituting (4.20) into (4.35) and simplifying, the final expression of the achievable rate is [79]:

$$A_r(H;\,\boldsymbol{R}) = \log_2(G) - \left(\log_2(e) + \frac{1}{G}\sum_{\ell_a} E\left\{\log_2\left(\sum_{\hat{\ell}_a}\exp\left(-\frac{\left|\sqrt{\mathrm{P}_{tx}}\left(H_{\ell_a}-H_{\hat{\ell}_a}\right)+\eta\right|^2}{N_{\Upsilon}^2}\right)\right)\right\}\right). \qquad (4.36)$$

The full derivation of (4.36) can be found in Appendix E.

4.6 Energy Efficiency of HRM scheme

The EE can be found with respect to the maximum instantaneous received SNR ρ in (4.10) as follows [79]:

$$\mathrm{E_P} = \frac{\mathrm{B}\log_2(1+\ \rho)}{\mathrm{P_T}}, \tag{4.37}$$

where B is the bandwidth of the HRM system, and $\mathrm{P_T}$ is the average power consumption for a given transmit power efficiency η_{T} as [79]:

$$\mathrm{P_T} = \frac{\mathrm{P}_{tx}}{\eta_{\mathrm{T}}} + \mathrm{P}_{\mathbb{C}} + \mathrm{P}_{RIS}, \tag{4.38}$$

where P_{tx} is total transmit power, $\mathrm{P}_{\mathbb{C}}$ is the overall power dissipated at both the transmitter and receiver, and P_{RIS} denotes the total power consumption of the RIS.

For the HRM scheme, P_{RIS} is expressed as [79]:

$$\mathrm{P}_{RIS} = \frac{\mathrm{P}_a}{\eta_a} +\ \mathcal{E}_1\mathrm{P}_{dyn} + \mathcal{E}_2\mathrm{P}_p + \mathrm{P}_{stc}, \tag{4.39}$$

where P_a is the maximum reflection power constraint, η_a is the amplifier efficiency of the active reflecting elements, $\mathcal{E}_1$ & $\mathcal{E}_2$ respectively, denotes the average number of active and passive reflecting elements, P_{dyn} and P_{stc} correspond to the dynamic and static power consumptions, P_p is the required power per passive RIS element. Note that for F-HRM, $\mathcal{E}_1 = \mathcal{E}_2 = \frac{N}{2}$.

For fully active RISs, the total power consumption of the RIS is [79]:

$$\mathrm{P}_{RIS} = \frac{\mathrm{P}_a}{\eta_a} + N\mathrm{P}_{dyn} + \mathrm{P}_{stc}. \tag{4.40}$$

For fully passive RISs, the total power consumption of the RIS is [79]:

$$\mathrm{P}_{RIS} = N\mathrm{P}_p. \tag{4.41}$$

4.7 Numerical Results

In this section, numerical results are provided in the form of graphs with respect to BER, achievable rate and EE as a function of P_{tx} or N to investigate the performance of the HRM scheme. The F-HRM scheme is also investigated in this section. Comparisons are drawn with the fully active and fully passive RIS-aided schemes to illustrate the superiority of HRM. All simulation parameters used in all simulations have been tabulated in Table 4.7.1.

Table 4.7.1: Table of simulation parameters for HRM scheme

HRM & Achievable Rate		EE	
Parameter	Value	Parameter	Value
d_t	20m	P_{dyn}	35dBm
d_r	50m	P_{stc}	35dBm
ω_t	2.2	$P_{\mathbb{C}}$	75dBm
ω_r	2.8	P_p	5mW
σ^2_{dyn}	−90dBm	$\daleth_a$	0.5
σ^2_{stc}	−90dBm	$\daleth_T$	0.5
K_{pl}	−30dB	B	10MHz

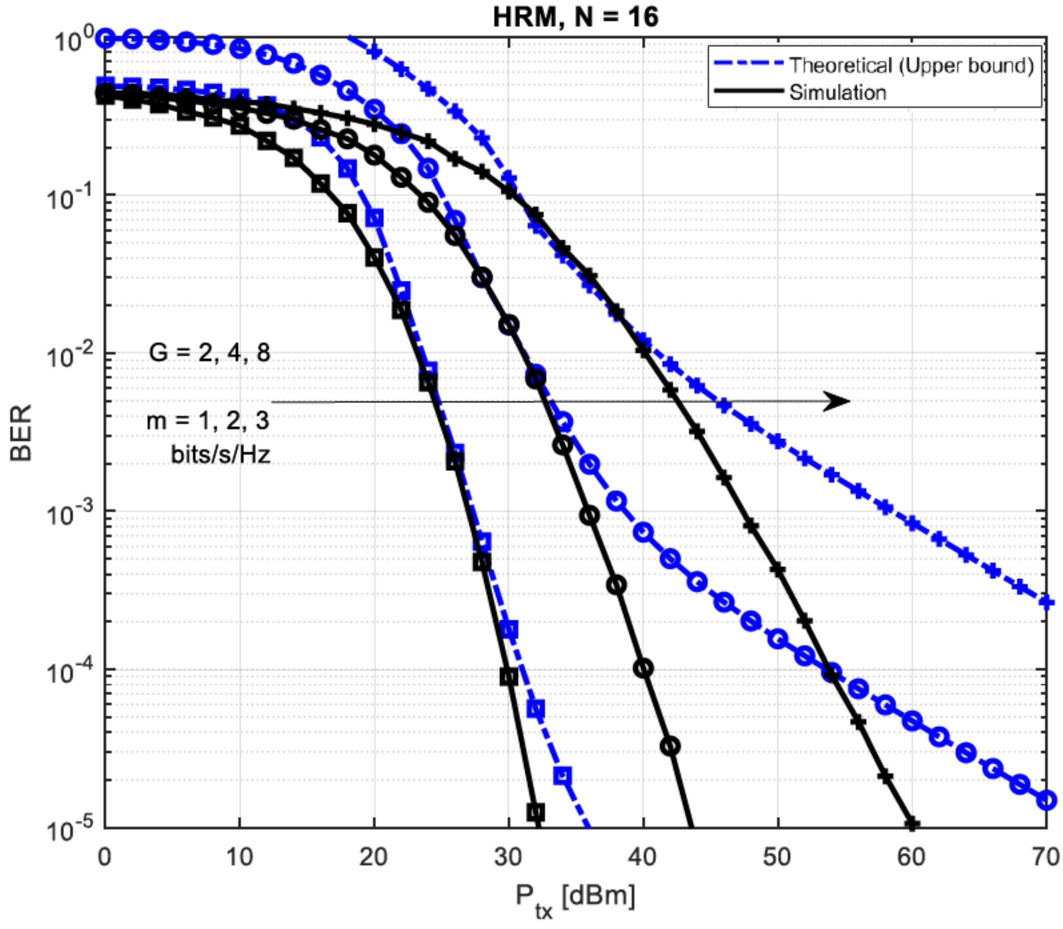

Figure 4.7.1: BER vs P_{tx} graphs of the HRM scheme − $N = 16$, varying G

Figure 4.7.1 shows the EP of the HRM scheme with $N = 16$ for $G = 2, 4$ and 8, yielding SEs of $m = 1, 2$ and 3 bits/s/Hz, with the CLT being applied. The theoretical result is based on the upper bound in (4.33) and (4.34). It can be observed that the EP is poor for increasing G, but it is also seen that error floors form as G increases. This can be explained as follows. As G increases, the number of reflective elements per subgroup S_G decreases, creating a similar effect applying the CLT assuming high values of N, whereby error floors form at higher G. A noteworthy drawback with this scheme is that the SE is limited by N, since G is dependent on the total number of reflective elements. Hence, for small N, the HRM scheme can only achieve small SEs.

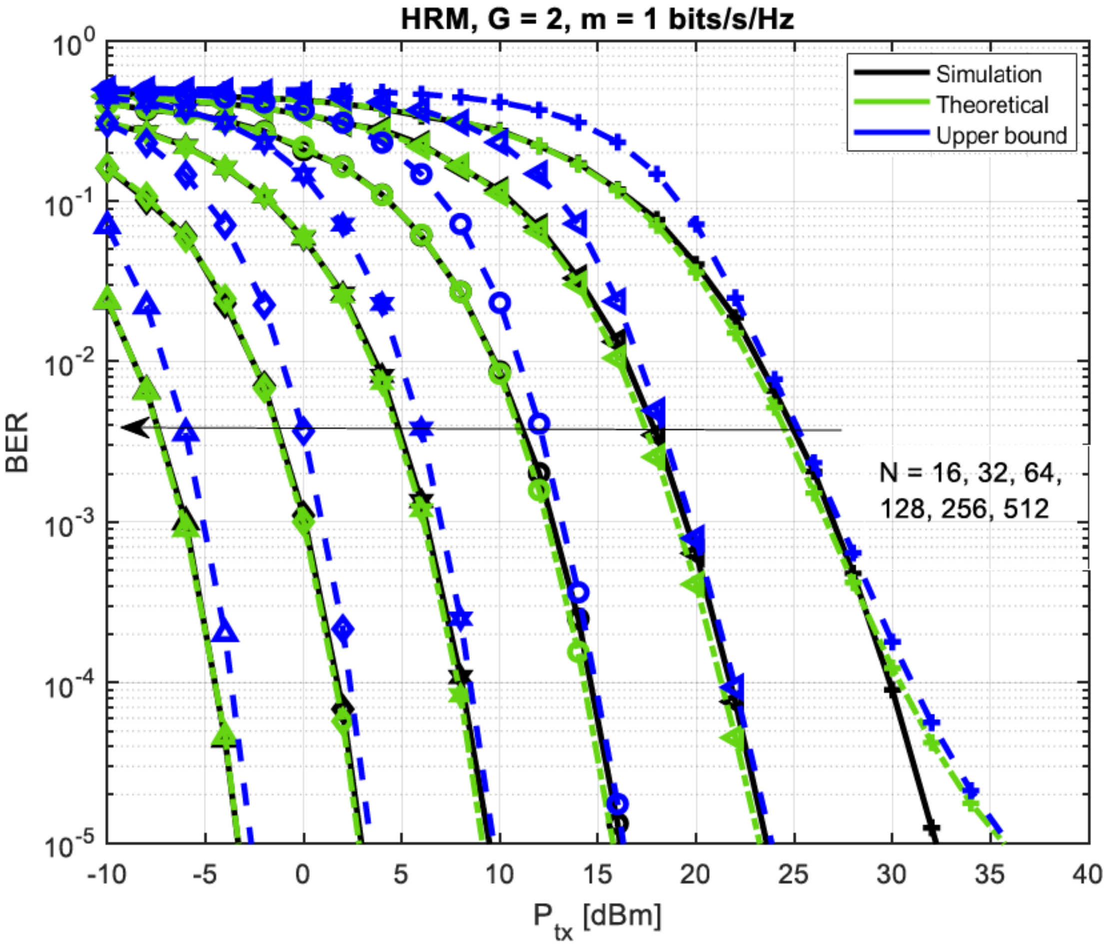

Figure 4.7.2: BER vs P_{tx} graphs of the HRM scheme - $G = 2$, varying N

Figure 4.7.2 shows the EP of the HRM scheme with a SE of $m = 1$ bit/s/Hz, achieved by setting $G = 2$. The amplification gain is set to be $\alpha = 10$. It is assumed that the CLT is applied for all simulations, and the theoretical result is based on Equation (4.31), the upper bound based on (4.33) and (4.34). It can be observed that the simulation results demonstrate a tight fit to the theoretical bound for varying values of N, with the exception being $N = 16$. This is expected as, similar to Figure 4.7.1, large values of N are required to apply the CLT. It is also seen that with double the reflective elements in each instance, an EP gain of approximately 6.5dBm – 7dBm is achieved.

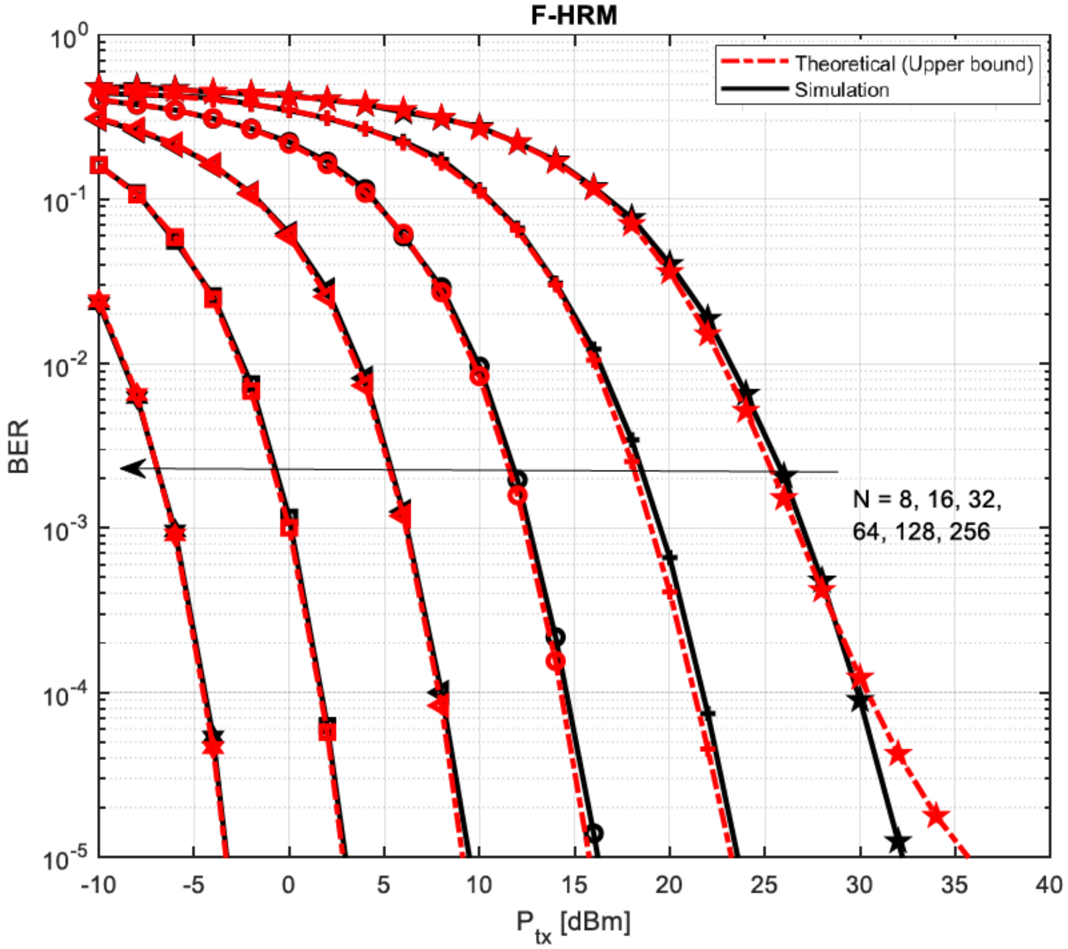

Figure 4.7.3: BER vs P_{tx} graphs of the F-HRM scheme, varying N

Figure 4.7.3 shows the EP of the F-HRM scheme for $N = 8, 16, 32, 64, 128$ and 256, and Figure 4.7.4 draws a comparison between the HRM scheme for $G = 2$ and the F-HRM scheme. The amplification gain is assumed to be $\alpha = 10$, and the CLT is assumed for all simulations. The theoretical result is based on (4.31). A very interesting observation can be seen when comparing the two figures. It is observed that the F-HRM achieves the same EP as the HRM scheme with $G = 2$, with only half the reflecting elements. This shows that for a SE of $m = 1$ bit/s/Hz, the F-HRM is favoured over the HRM scheme for $G = 2$ as, based on the discussions in Section 4.3, the F-HRM allows for a fully active H-RIS in comparison to the HRM scheme for $G = 2$ which only enables a half-active H-RIS. Therefore, the F-HRM scheme allows for more active elements to be facilitated to amplify and reflect the wireless signal.

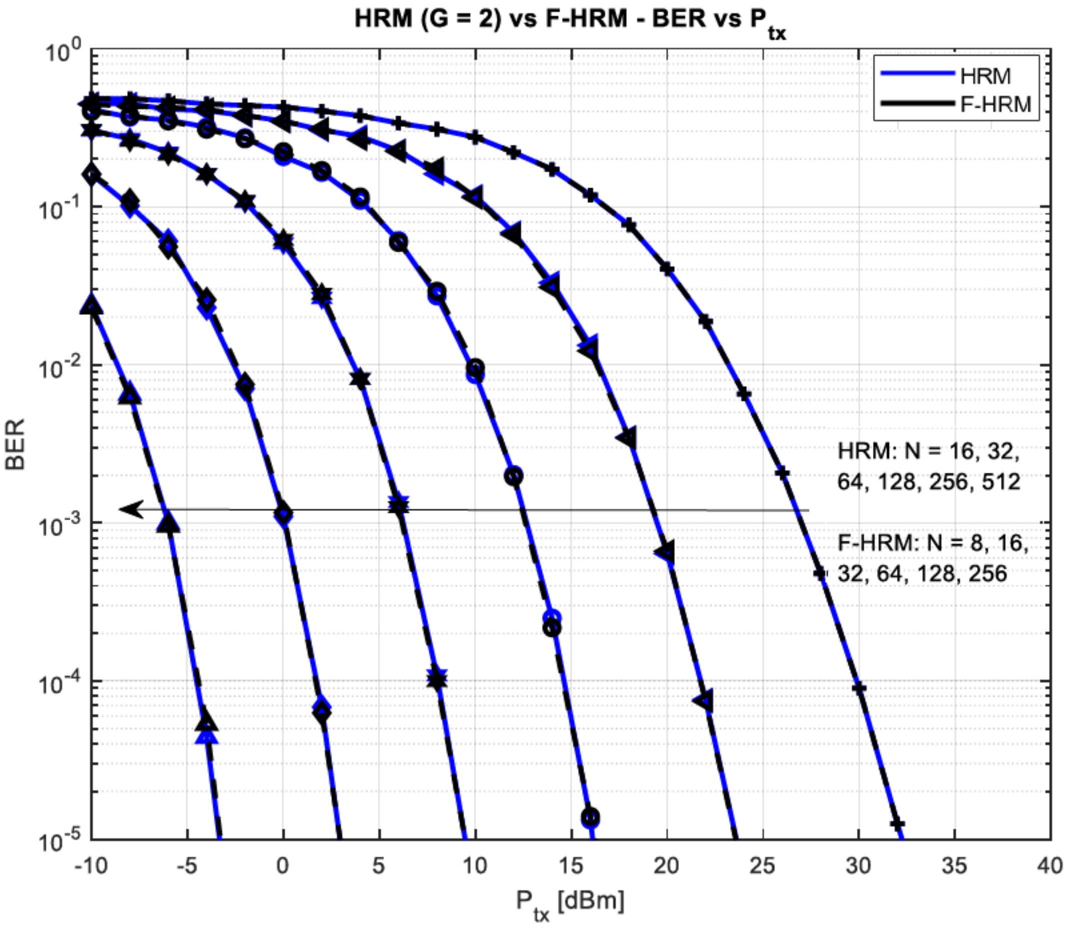

Figure 4.7.4: BER vs P_{tx} graphs of the HRM ($G = 2$) scheme compared to F-HRM scheme

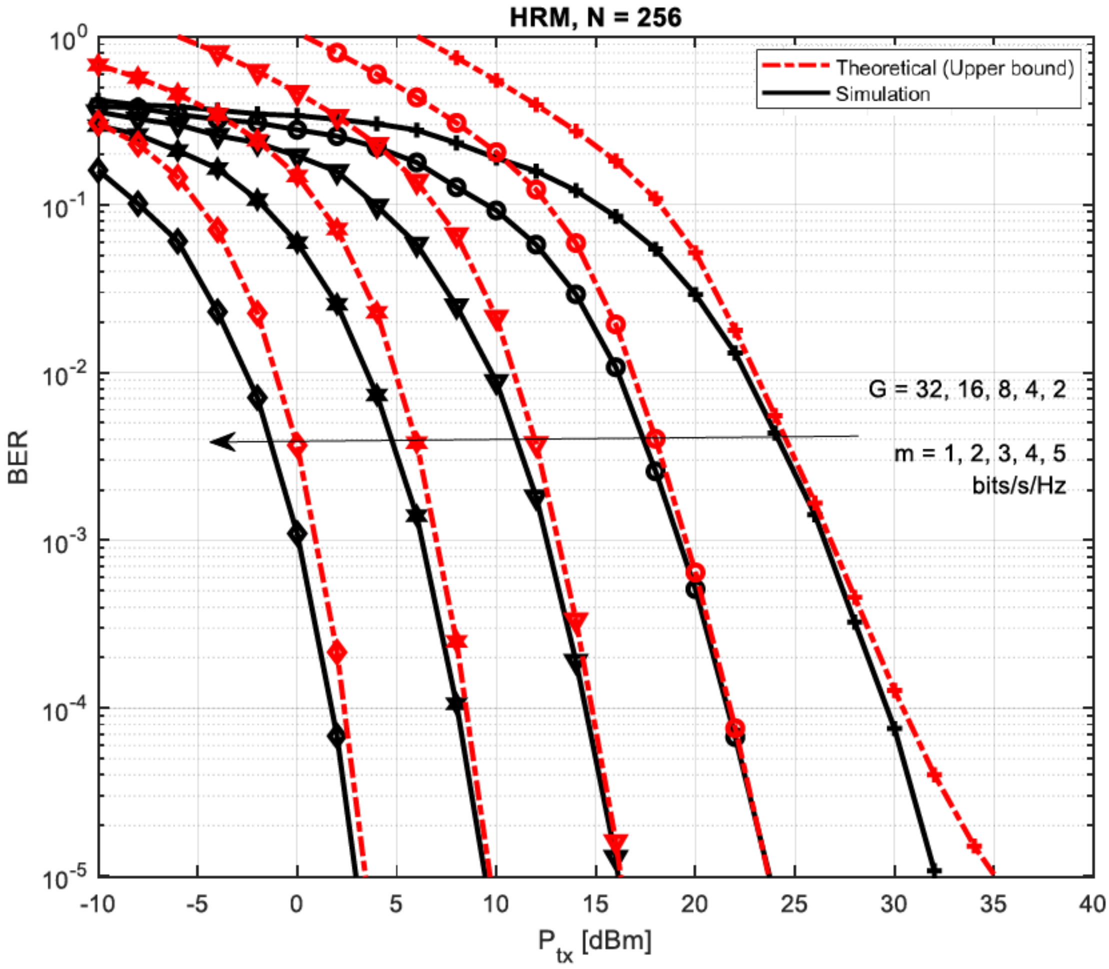

Figure 4.7.5: BER vs P_{tx} graphs of the HRM scheme - $N = 256$, varying G

Figure 4.7.5 shows the EP of the HRM scheme for $N = 256$, and the SE is varied by varying the number of subgroups G, namely for $G = \{2, 4, 8, 16, 32\}$. The theoretical bound is based on the upper bound in (4.33) and (4.34), whereby the upper bound demonstrates a tight fit at low SNRs only. It can be observed that as the SE is increased, the EP becomes worse, particularly for $G = 32$, or a SE of $m = 5$ bits/s/Hz, the EP deteriorates significantly. Moreover, the high SE causes a similar effect as that experienced for low values of N in Figure 4.7.1. This can be explained as follows. As G increases, S_G decreases, hence the overall number of active and passive elements available in any given subgroup decreases. This results in a less accurate approximation when applying the CLT assuming high N, as there is always a trade-off in quantity between the number of active and passive elements.

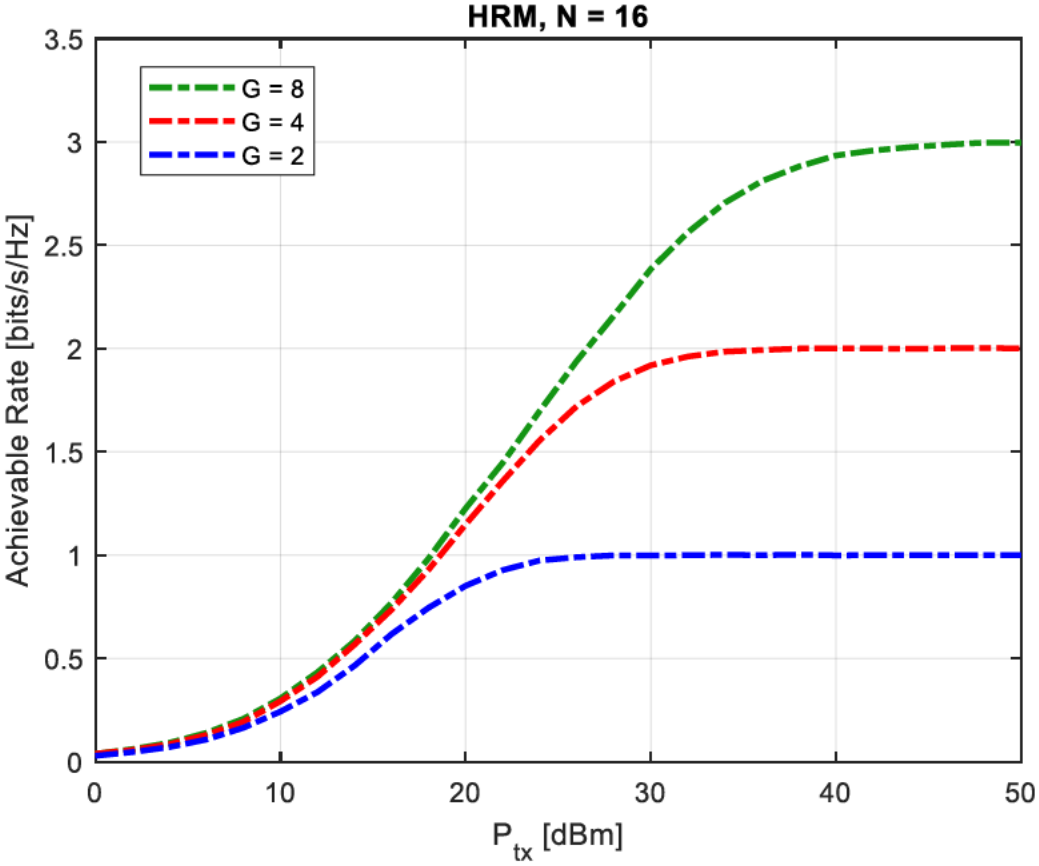

Figure 4.7.6: Achievable Rate vs P_{tx} graphs of the HRM scheme - $N = 16$

Figure 4.7.6 shows the achievable rate of the HRM scheme for $G = 2, 4$ and 8 for $N = 16$ based on (4.36). It can be observed that the HRM scheme requires a significantly higher transmit power to achieve the target data rates for low values of N. Namely, for $G = 2$, 25dBm is required to achieve the data rate of 1 bit/s/Hz, for $G = 4$, 35dBm is required to reach the data rate of 2 bits/s/Hz, and for $G = 8$, 46dBm is required for an achievable rate of 3 bits/s/Hz.

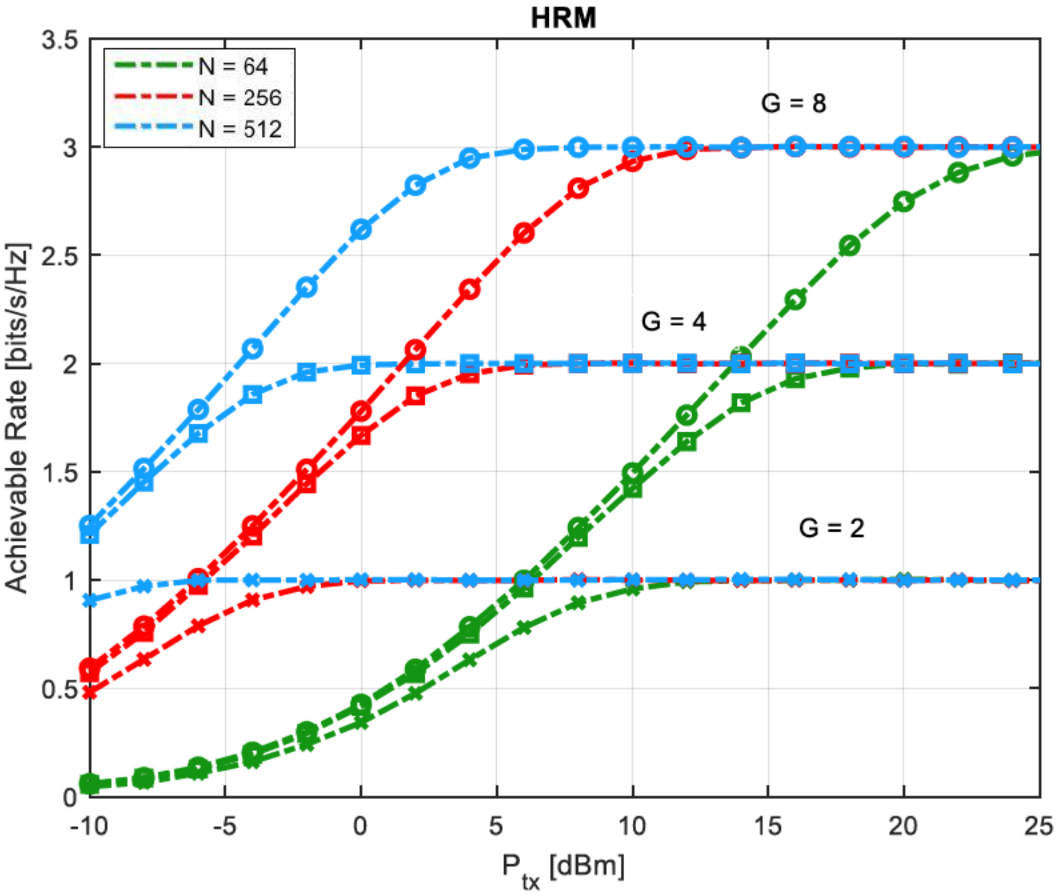

Figure 4.7.7: Achievable Rate vs P_{tx} graphs of the HRM scheme for varying N and G

Figure 4.7.7 shows the achievable rate of the HRM scheme based on (4.36) for $G = 2, 4$ and 8, an amplification gain of $\alpha = 10$, and with the number of reflecting elements being set to $N = 64, 256$ and 512. It can be observed that as N increases, less transmit power is required to reach the achievable rate for all G, hence there is a quicker convergence to the required rate.

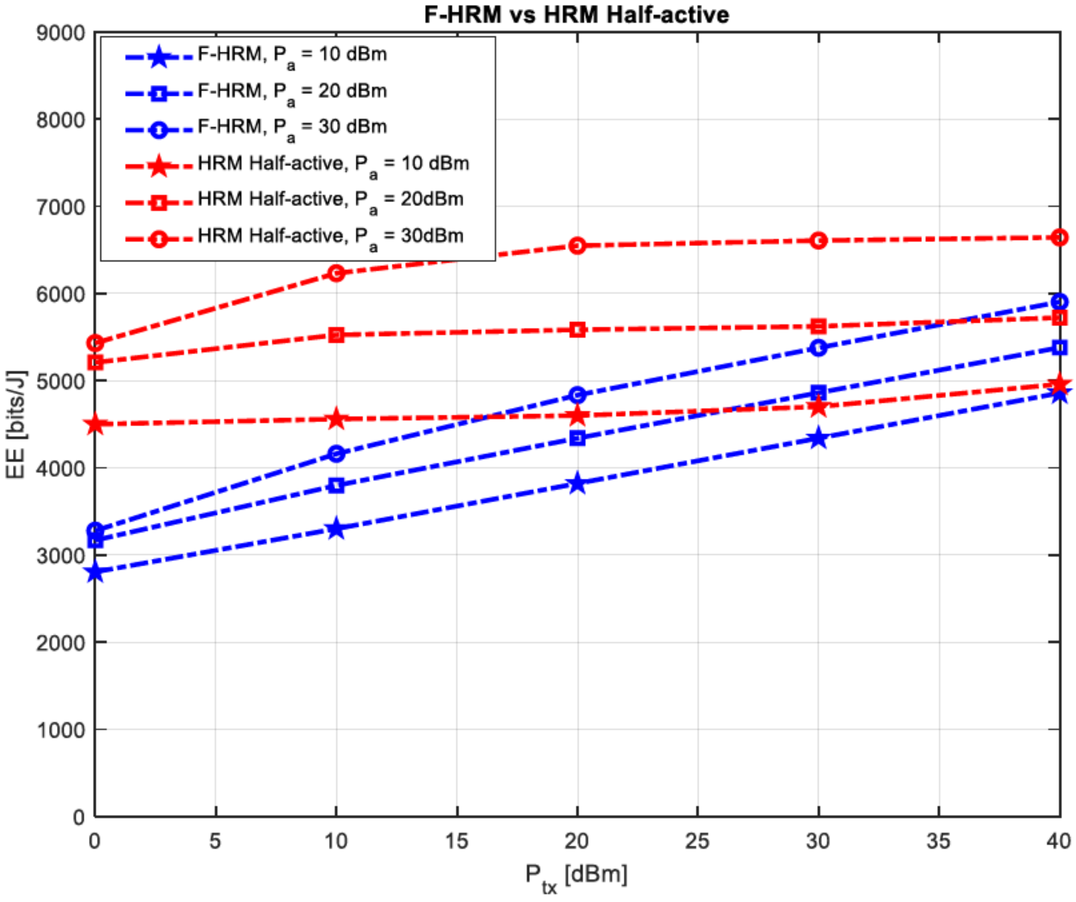

Figure 4.7.8: EE vs P_{tx} graphs of the F-HRM scheme, varying P_a

Figure 4.7.8 shows the EE of the F-HRM scheme and the HRM half-active scheme (half of the reflective elements are constantly active, whilst the other half are constantly passive) as a function of P_{tx} for various values of P_a calculated over 10^6 iterations using (4.37). Note that whilst an unmodulated carrier is considered for F-HRM, BPSK signalling is considered for the HRM half-active scheme. It can be observed that the HRM half-active scheme is more energy efficient than the F-HRM scheme for lower values of P_{tx}, and almost equals the EE of the F-HRM scheme for higher P_{tx} values. As P_a increases, however, the difference in EE between the two systems becomes more prominent.

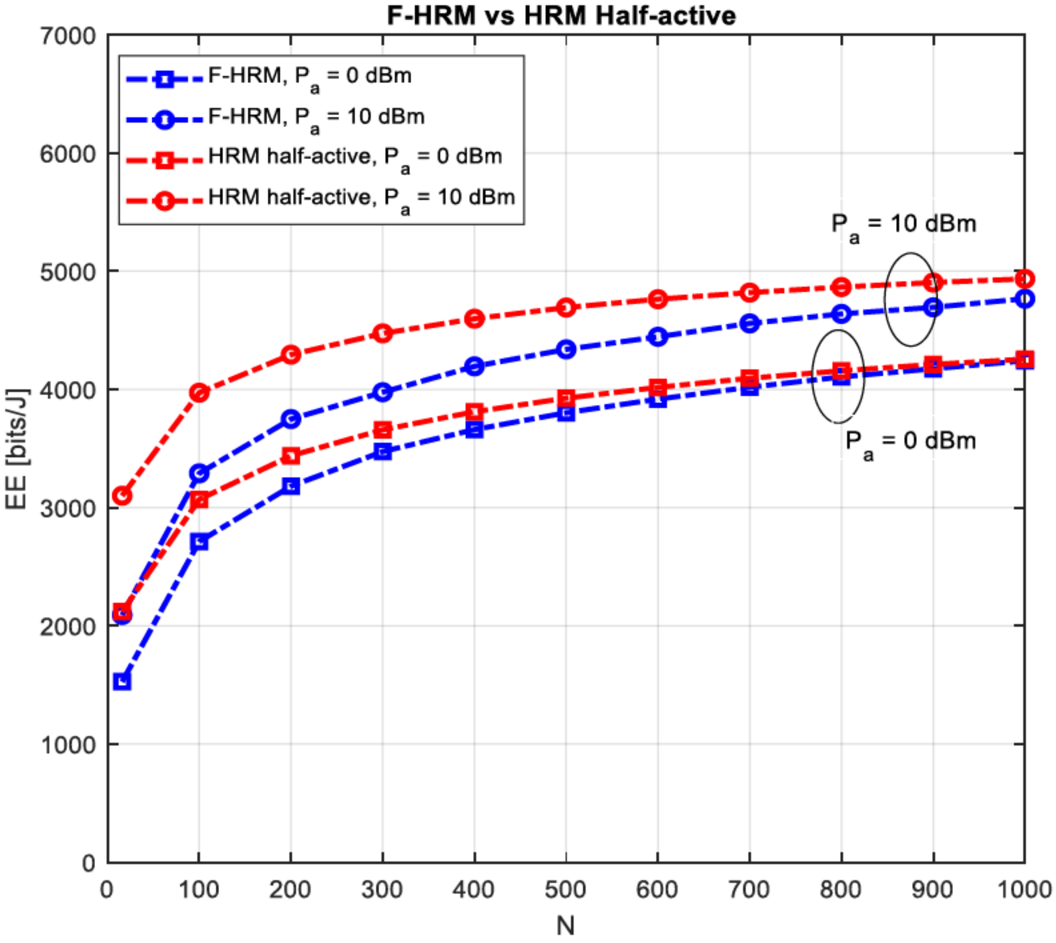

Figure 4.7.9: EE vs N graphs of the HRM half-active scheme vs F-HRM scheme

Figure 4.7.9 shows the EE of the F-HRM scheme and an HRM half-active scheme as a function of N for various values of P_a, calculated over 10^6 iterations using (4.37). It can be observed that the HRM scheme is significantly more energy efficient for lower values of N, and approaches the EE of the F-HRM scheme for higher N values. As P_a increases, however, the HRM half-active scheme proves to be more energy efficient than the F-HRM scheme.

Both Figure 4.7.8 and Figure 4.7.9 illustrate the fact that having a scheme of half-active and passive elements is more energy efficient than having a full hybrid of reflective elements (fully active or fully passive), as the number of active elements in the exact hybrid is only half that of the fully active, hence saving more energy and reducing the total amount of radiation generated, and is therefore a more environmentally-friendly, cost-effective option over the F-HRM scheme.

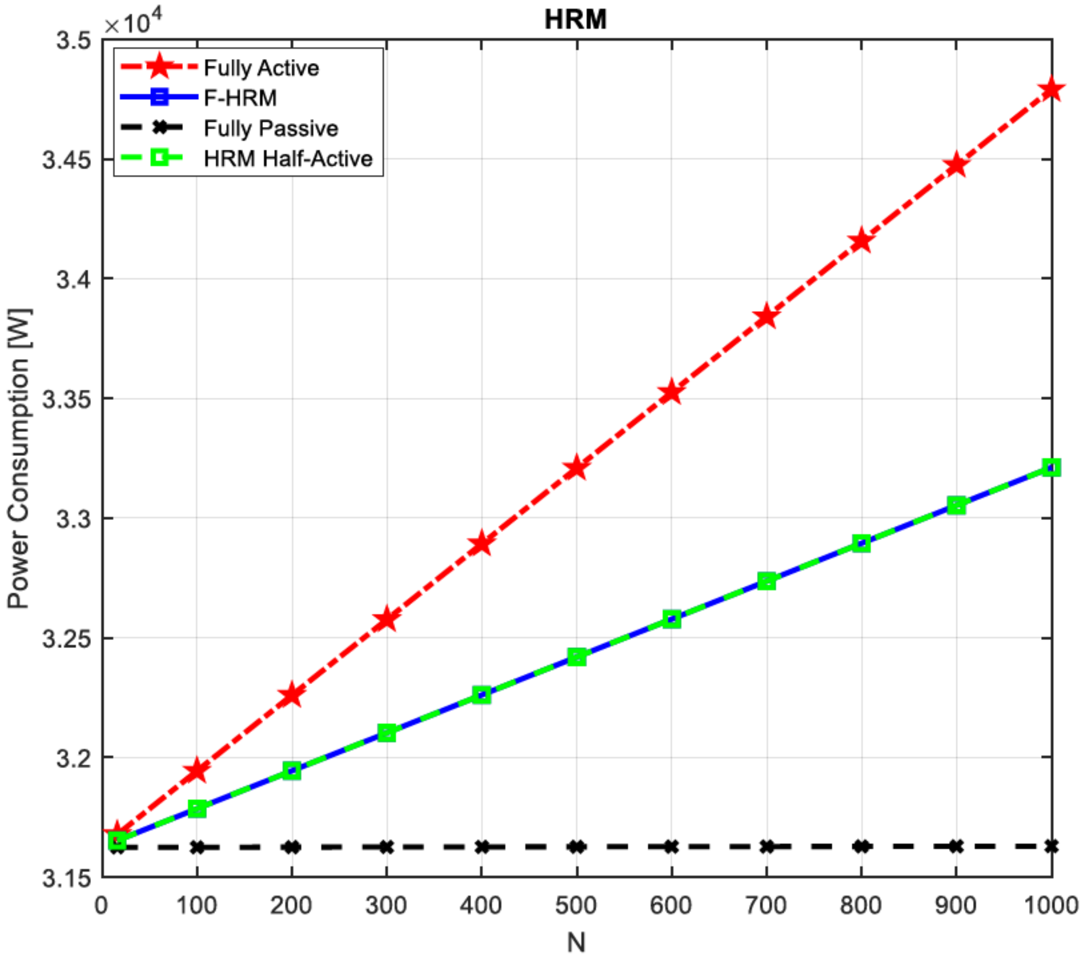

Figure 4.7.10: F-HRM Power Consumption vs N

Figure 4.7.10 shows the power consumption of the F-HRM scheme in comparison to the HRM half-active, fully active and fully passive RIS-aided schemes as a function of N reflective elements, with $\mathrm{P}_a = 10$ dBm and $\mathrm{P}_{tx} = 30$ dBm, using (4.38) - (4.41). It is clear that the F-HRM and HRM half-active scheme consumes the same amount of power and uses considerably less power in comparison with the fully active scheme for increasing N, hence illustrating that the F-HRM scheme is a more cost-effective and environmentally-friendly option over the fully active scheme. Note that increasing N hardly affects the power consumption of the fully passive scheme.

Chapter Summary

In this chapter, the system model of the HRM scheme in Rayleigh fading channels were presented, and the performance analysis of the HRM scheme was described. In addition to this, the mathematical frameworks of the achievable rate and EE of the HRM scheme were also presented. Simulation results in the form of BER vs P_{tx} graphs were provided, and observations were drawn based on the results. The theoretical analysis validated the simulation results for high values of N, with error floors present for low values of N. It was also observed that for low G, the theoretical analysis matches tightly with the simulation graphs, but errors floors form for high G. The achievable rate and EE analyses show that the HRM scheme is very energy efficient in comparison to fully active RISs. Overall, it may be said that the HRM scheme produces greater EP gains than fully passive RIS-aided schemes, whilst reducing power consumption and, therefore, demonstrates greater EE over fully active RIS-aided schemes.

CHAPTER 5

HYBRID REFLECTION MODULATION-AIDED SCHEMES

5.1 Introduction

RISs are man-made EM surfaces capable of creating a controllable wireless environment to improve signal quality at the receiver [16], and have emerged as an attractive solution for meeting the current and future demands of mixed-generation wireless networks. In particular, RISs are metasurfaces which enable control over what was previously assumed to be the uncontrollable wireless propagation environment by performing various functions such as reflection, absorption and amplification to improve signal strength, mitigate ICI and, therefore, significantly enhance performance metrics such as channel capacity.

This idea has led to the concept of using a number of RISs on a large surface for transmission and reception of information [89]. In [24] and [96], the RIS-assisted downlink scenario is focused on, and the maximization of EE and sum-rate is investigated. Performance analyses of RIS-aided schemes are covered in [91] and [92], which focus on uplink data rate and SE under practical impairments of the system. In [48] and [49], the transmission of data using an RIS is investigated in both generic RIS schemes and RIS-based IM schemes to improve EP and SE.

An important contribution proposed in [48] is the AP configuration of the RIS, described in Chapters 2 and 3, and was formulated considering an unmodulated carrier signal, and its EP is evaluated both with and without knowledge of the channel phases. Another study in [49], used an AP-based RIS to assist SSK modulation and SM. Two studies in [78] and [113], used an AP-based RIS to assist various GC modulation schemes, including CI-GC and KCS GC modulation, with promising results. As mentioned in Chapter 2, the AP-based RIS has three main motivations, namely simultaneous data transmission and phase control of the reflective elements, less CSI to be acquired and ease of deployment on various surfaces.

In [36], it has been shown that the performance of WCS assisted by fully passive RISs is limited by multiplicative path loss. Active reflecting elements have been proposed to enhance signal power and overcome the effect of path loss by simultaneously reflecting and amplifying the wireless signal. The idea of the active RIS has first been documented on in [80], where a SISO WCS is assisted by an active RIS facilitated by controllable power amplifiers to enhance channel capacity. Another two studies [77] and [125], demonstrated that fully active, or even partially active, RIS-aided systems enhanced channel capacity and EE. Whilst active RISs may improve various performance metrics, it comes at the cost of additional power consumption [80, 125].

H-RISs have been proposed to mitigate the negative drawbacks of both active and passive elements, whilst also reaping most of the benefits of the active elements at a lower power consumption. The current literature dedicated to H-RISs is described as follows. H-RISs were first documented on in [127], which provides a discussion on its working principles, use cases and challenges. In [83], the sum rate of a MISO system assisted by an H-RIS is investigated and considered fairness-orientated design in its analysis. The authors in [84], compare the sum rates of downlink systems aided by fully active, fully passive and H-RISs, and a study in [128], provides an analysis of channel estimation in H-RIS-aided systems. In [129], joint user localization of an H-RIS is investigated.

The HRM concept has been proposed in [79], where an H-RIS in the non-AP configuration is used to aid the transmission of an unmodulated carrier signal, and the principle of IM is employed to transmit additional information control the state of the H-RIS. The active elements are facilitated using power amplifier circuitry such as tunnel diodes or low-noise amplifiers (LNAs), and a phase shift controller is employed to adjust the phases of the reflective elements.

In this chapter, two novel HRM-aided schemes are investigated. The first is the HRM non-AP scheme, which considers the transmission of a data symbol through the wireless propagation environment in the presence of an H-RIS. The second is the HRM AP scheme, which considers the transmission of a data symbol using an AP configuration of the H-RIS. The ABEP analysis for the HRM non-AP and AP schemes is also presented in this chapter.

The contributions of this chapter are as follows:

1. Two novel HRM-aided schemes are presented as solutions for enhancing SE and EP. The first is the HRM non-AP scheme, and the second is the HRM AP scheme.
2. The ABEP analysis of the HRM non-AP and HRM AP schemes are provided.

This chapter is structured as follows. Section 5.2 covers the system model and performance analysis of the HRM non-AP scheme, Section 5.3 covers the system model and performance analysis of the HRM AP scheme and Section 5.4 provides numerical results of the two HRM-aided schemes.

5.2 HRM non-AP scheme

5.2.1 HRM non-AP system model

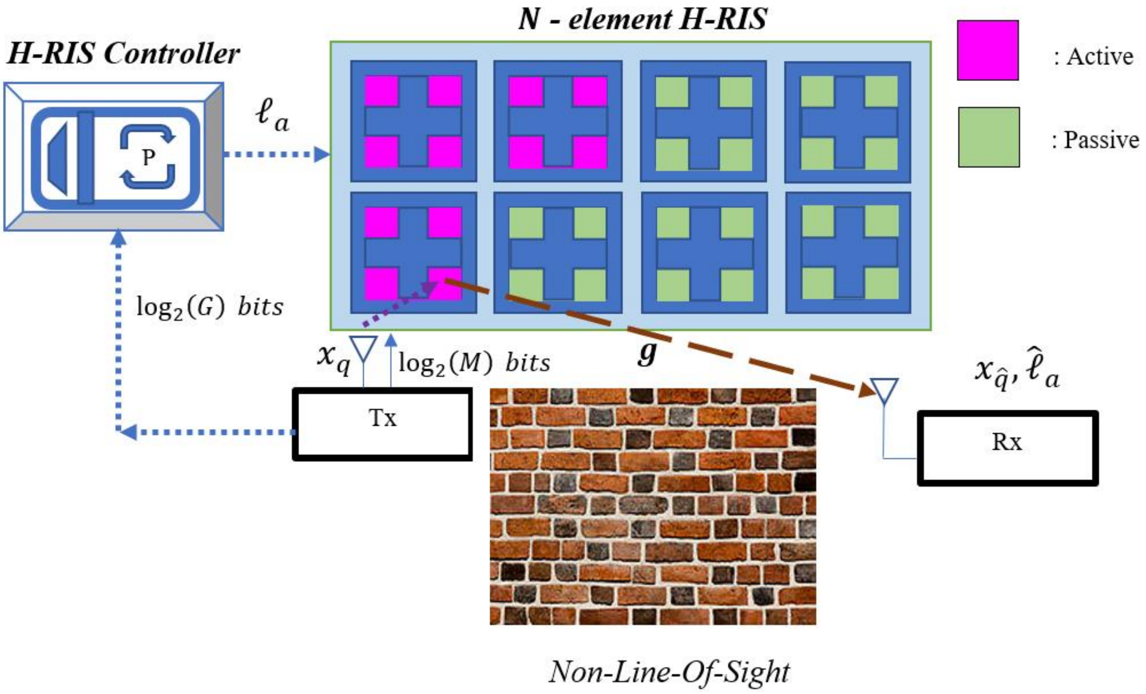

Figure 5.2.1.1: Diagram illustrating the system model of HRM non-AP scheme

Consider Figure 5.2.1.1. The H-RIS is placed in the centre of the wireless channel, where it intelligently reflects the information from the transmitter to the receiver. It consists of N reflective elements, each connected to a power amplifier and a controller. The power amplifiers, when switched ON, causes the reflective elements to become active, and the impinging wave is both amplified and reflected simultaneously to the receiver according to an amplification gain, at the expense of additional power consumption. When switched OFF, the reflective elements become passive, and simply reflect the signal without any amplification. The controller controls both the number of active and passive elements on the H-RIS and how they are grouped together in the H-RIS, depending on the transmitted data. In this scheme, a NLOS path is assumed.

The transmitter transmits a bit vector $\boldsymbol{b} = \left[b_1\ b_2 \cdots b_\eta\right]$, which is split into two sub-vectors $\boldsymbol{b}_A = \left[b_1\ b_2 \cdots b_{\log_2(M)}\right]$ and $\boldsymbol{b}_B = \left[b_1\ b_2 \cdots b_{\log_2(G)}\right]$. The first vector $\boldsymbol{b}_A$ is mapped onto an M-PSK symbol denoted by x_q, where $q \in [1{:}\,M]$, and where M is the size of the PSK constellation. The second vector $\boldsymbol{b}_B$ is transmitted to the H-RIS controller, where it is processed to select an H-RIS index which determines the state of the H-RIS as described below.

The N-element H-RIS is partitioned into sub-groups, denoted by G, such that the number of reflective elements in each subgroup is $\mathrm{S_G} = {}^{N}\!/_{G}$. The $\log_2(G)$ bits select an HRM index, notated as $l_a \in [0{:}\,G - 1]$. This index alters the H-RIS state such that some subgroups contain active reflective elements, with the remainder of the subgroups containing passive reflective elements. The active and passive elements on the H-RIS are calculated by $N_a = l_a S_G$ and $N_p = N - N_a$, respectively. For $l_a = 0$, $N_a = 0$, therefore the H-RIS contains only passive elements. Each unique configuration of the H-RIS produces a different channel realisation, which can be mapped to unique data symbols, called H-RIS symbols denoted by H_{l_a}.

The mapping of the HRM symbols follows the same process as illustrated in Chapter 4, Table 4.2.1.

The HRM non-AP scheme has a SE of:

$$\eta = \log_2(G) + \log_2(M) \text{ bits/s/Hz.} \tag{5.1}$$

Each reflective element has a reflection co-efficient denoted in polar form as:

$$a_k = |a_k| e^{j\theta_k}, k \in [1{:}\,N], \tag{5.2}$$

where $|a_k|$ is the magnitude of the k-th reflective element and $\theta_k \in [-\pi, \pi]$ is the phase of the k-th reflective element. Passive elements have a unit magnitude given by $|a_k| = 1$, hence they simply reflect the incoming signal towards the receiver. However, facilitating active elements means that this gain is non-unitary, that is $|a_k| = \alpha_k > 1$, to allow the amplification of the incoming signal as well as the reflection of it towards the receiver. For all analyses, it is assumed that all active elements hold a common amplification gain $\alpha_k = \alpha$.

Based on this analysis, the active and passive phase reflection matrices can be computed depending on the number of active and passive elements as:

$$\boldsymbol{\Phi} = diag\left(e^{j\theta_1}, e^{j\theta_2}, \dots, e^{j\theta_{N_a}}\right), \tag{5.3.1}$$

$$\boldsymbol{\psi} = diag\left(e^{j\theta_{N_a+1}}, e^{j\theta_{N_a+2}}, \dots, e^{j\theta_N}\right), \tag{5.3.2}$$

where $\boldsymbol{\Phi}$ is the active reflection diagonal matrix based on the number of active reflective elements, and $\boldsymbol{\psi}$ is the passive reflection diagonal matrix based on the number of passive reflective elements.

The path losses are given according to [79] as:

$$L_T = m_\kappa r_T^{-\delta_T}, \tag{5.4.1}$$

$$L_R = m_\kappa r_R^{-\delta_R}, \tag{5.4.2}$$

where r_T and r_R is the distances in metres separating the transmitter and the H-RIS, and the H-RIS and the receiver, respectively, δ_T, $\delta_R > 1$ are the path loss exponents, and m_κ is the reference path loss per metre.

Rayleigh frequency-flat fading channels are assumed, denoted by $\boldsymbol{h} \in \mathbb{C}^{N\times 1} \sim CN(0, L_T)$, and $\boldsymbol{g} \in \mathbb{C}^{1\times N} \sim CN(0, L_R)$, where L_T and L_R are the path losses of each respective fading vector. The instance of fading given by $\boldsymbol{h}$ occurs in the Tx-H-RIS path, while the instance $\boldsymbol{g}$ occurs in the H-RIS-Rx path.

The two fading vectors $\boldsymbol{h}$ and $\boldsymbol{g}$ can further be expressed as combinations of active elements and passive elements, as $\boldsymbol{h} = \left[\boldsymbol{h}_a \ \boldsymbol{h}_p\right]^T$ and $\boldsymbol{g} = \left[\boldsymbol{g}_a \ \boldsymbol{g}_p\right]^T$, where $\boldsymbol{h}_a, \boldsymbol{g}_a \in \mathbb{C}^{1\times N_a}$ denote the fading associated with active elements, and $\boldsymbol{h}_p, \boldsymbol{g}_p \in \mathbb{C}^{1\times N_p}$ denote the fading associated with passive elements.

The static noise is given as $n_{stc} \sim CN(0, \sigma_{stc}^2)$. The dynamic thermal noise is given as $n_{dyn} = \alpha \boldsymbol{g}_a \boldsymbol{\Phi}\, \mathbf{w}^T$, where $\mathbf{w} \in \mathbb{C}^{1\times N_a} \sim CN\left(0, \boldsymbol{I}_{N_a}\sigma_{dyn}^2\right)$ is the dynamic noise vector [79]. As mentioned in Chapter 4, this dynamic noise component is non-negligible, and is dependent on the number of active elements of the H-RIS, resulting from the thermal noise generated by the power amplifiers of the active elements.

The receive signal is written for a given transmit power P_{tx} as:

$$r = \sqrt{P_{tx}}\left(\alpha \boldsymbol{g}_a \boldsymbol{\Phi} \boldsymbol{h}_a^T + \boldsymbol{g}_p \boldsymbol{\psi} \boldsymbol{h}_p^T\right) x_q + \alpha \boldsymbol{g}_a \boldsymbol{\Phi} \boldsymbol{w}^T + n_{stc}. \tag{5.5}$$

The maximum instantaneous received SNR is written as:

$$\max_{\alpha,\boldsymbol{\phi},\boldsymbol{\psi}} \quad \rho = \frac{signal\ power}{noise\ power} = \frac{\left\|\sqrt{P_{tx}}\left(\alpha \boldsymbol{g}_a \boldsymbol{\Phi} \boldsymbol{h}_a^T + \boldsymbol{g}_p \boldsymbol{\psi} \boldsymbol{h}_p^T\right) x_q\right\|_F^2}{\alpha^2 \|\boldsymbol{g}_a \boldsymbol{\phi}\|_F^2 \sigma_{dyn}^2 + \sigma_{stc}^2}. \tag{5.6}$$

The expression in (5.6) simplifies to:

$$\max_{p,\boldsymbol{\phi},\boldsymbol{\psi}} \quad \rho = P_{tx}\left|x_q\right|^2 \frac{\left\|\alpha \boldsymbol{g}_a \boldsymbol{\phi} \boldsymbol{h}_a^T + \boldsymbol{g}_p \boldsymbol{\psi} \boldsymbol{h}_p^T\right\|_F^2}{\alpha^2 \|\boldsymbol{g}_a \boldsymbol{\phi}\|^2 \sigma_{dyn}^2 + \sigma_{stc}^2}, \tag{5.7}$$

$$\text{Such that:} \qquad \mathrm{P}_a \geq \alpha^2\left(P_{tx}\|\boldsymbol{\phi}\boldsymbol{h}_a^T\|_F^2 + \|\boldsymbol{\phi}\|_F^2 \sigma_{dyn}^2\right). \tag{5.8}$$

Note that for M-PSK symbols, $\left|x_q\right|^2 = 1$, hence the received SNR is identical to the conventional HRM scheme in Chapter 4.

To simplify the receive signal in (5.5), the fading vectors are written in terms of their magnitudes and phases as $h_k = |h_k|e^{j\varphi_k}$ and $g_k = |g_k|e^{j\xi_k}$, where $k \in [1\colon N]$. The phase shifts of the H-RIS reflective elements given by θ_k may be optimized to maximise the SNR as $\theta_k = -(\varphi_k + \xi_k)$, thereby completely eliminating the channel phases from the computation. The amplification gain may be expressed by rearranging (5.8) to produce:

$$\alpha \leq \sqrt{\frac{\mathrm{P}_a}{\mathrm{P}_{tx}\|\boldsymbol{h}_a^T\|^2 + \sigma_{dyn}^2}}. \tag{5.9}$$

Hence, the receive signal given in (5.5) is simplified according to the above analysis as:

$$r = \sqrt{P_{tx}}\left(\alpha\sum_{k=1}^{N_a}|h_k||g_k| + \sum_{k=N_a+1}^{N}|h_k||g_k|\right)x_q + \alpha\sum_{k=1}^{N_a}|g_k|\,\overline{w}_k + n_{stc}. \tag{5.10}$$

The quantity $H_{l_a} = \alpha\sum_{k=1}^{N_a}|h_k||g_k| + \sum_{k=N_a+1}^{N}|h_k||g_k|$ is the HRM symbol. The noise part is simplified further by applying the CLT to the quantity $\alpha\sum_{k=1}^{N_a}|g_k|\,\overline{w}_k + n_{stc}$ by assuming high N, as seen in Chapter 4. Therefore, the noise is approximated to a Gaussian RV $n \sim CN(0, N_v)$, where $N_v = \alpha^2 L_R N_a \sigma_{dyn}^2 + \sigma_{stc}^2$.

Hence, the final receive signal is written as:

$$r = \sqrt{P_{tx}}H_{l_a}x_q + n. \tag{5.11}$$

The ML detector for (5.11) is given, assuming full channel knowledge, as:

$$[x_{\hat{q}}, \hat{l}_a] = \underset{q\in[1:M],\, l_a\in[0:G-1]}{\operatorname{argmin}} \left|r - \sqrt{\mathrm{P}_{tx}}H_{l_a}x_q\right|^2. \tag{5.12}$$

5.2.2 Performance Analysis of the HRM non-AP scheme

The ABEP is calculated by considering the lower-bounded analytical approximation given in [14] as:

$$P_e \geq P_s + P_{l_a} - P_s P_{l_a}, \tag{5.13}$$

where P_s denotes the probability of M-PSK symbol error, P_{l_a} denotes the probability of HRM index error, and P_e denotes the ABEP. This approach was first documented in [130], where the authors proposed a method in which the SEP, or bit error probability (BEP), and the index probability of the SM scheme may be evaluated independently, using a lower-bounded analytical approach. It was then used in [14] to evaluate the ABEP of other IM schemes such as SIMO-MBM. This approach is used to reduce the complexity of the analysis that would otherwise be encountered if the probabilities of both sets of data were to be evaluated jointly. In this approach, P_s is calculated first by assuming that l_a is estimated perfectly and x_q is estimated erroneously as $x_{\hat{q}}$. Then, P_{l_a} is calculated assuming that the data symbol x_q is estimated perfectly, and of l_a is estimated erroneously as $\hat{l}_a$. Finally, P_e is calculated using (5.13), which yields a tight approximation for medium-to-high P_{tx}.

5.2.2.1 Calculation of P_s

The union-bound for P_s is formulated as:

$$P_s \leq \sum_{l_a=0}^{G-1}\sum_{q=1}^{M}\sum_{\hat{q}=1}^{M}\frac{N\left(x_{q,l_a} \to x_{\hat{q},l_a}\right)P\left(x_{q,l_a} \to x_{\hat{q},l_a}\right)}{GM\eta}, \tag{5.14}$$

where $P\left(x_{q,l_a} \to x_{\hat{q},l_a}\right)$ is the PEP, and $N\left(x_{q,l_a} \to x_{\hat{q},l_a}\right)$ is the number of bit errors per associated PEP event.

The CPEP is given as:

$$P\left(x_{q,l_a} \to x_{\hat{q},l_a}|H_{l_a}, l_a\right) = P\left(\left|r - \sqrt{P_{tx}}H_{l_a}x_q\right|^2 > \left|r - \sqrt{P_{tx}}H_{l_a}x_{\hat{q}}\right|^2\right), \tag{5.15}$$

which is simplified to:

$$P\left(x_{q,l_a} \rightarrow x_{\hat{q},l_a} | H_{l_a}, l_a\right) = Q\left(\sqrt{\frac{P_{tx}\left|H_{l_a}\right|^2 \left|x_q - x_{\hat{q}}\right|^2}{2N_v}}\right). \tag{5.16}$$

The full derivation of (5.16) may be found in Appendix F.

Equation (5.16) is further evaluated using the exponential form of the Q-function as [15]:

$$Q\left(\sqrt{x}\right) \cong \frac{e^{-\frac{x}{2}}}{12} + \frac{e^{-\frac{2x}{3}}}{4}. \tag{5.17}$$

The instantaneous received SNR of this scheme is given as:

$$\rho = \frac{P_{tx}}{N_v}\left|x_q\right|^2\left|H_{l_a}\right|^2 = \frac{P_{tx}}{N_v}\epsilon^2. \tag{5.18}$$

The channel magnitudes $|h_k|$ and $|g_k|$ are i.i.d. Rayleigh RVs with $\sigma_{|h_k|} = \sqrt{\frac{L_t}{2}}$ and $\sigma_{|g_k|} = \sqrt{\frac{L_r}{2}}$. These RVs have means of $E[|h_k|] = \sigma_{|h_k|}\sqrt{\frac{\pi}{2}} = \sqrt{L_t}\sqrt{\frac{\pi}{4}}$ and $E[|g_k|\,] = \sigma_{|g_k|}\sqrt{\frac{\pi}{2}} = \sqrt{L_r}\sqrt{\frac{\pi}{4}}$ respectively; and variances of $Var(|h_k|) = \sigma_{|h_k|}^2\left(2 - \frac{\pi}{2}\right) = L_t\left(1 - \frac{\pi}{4}\right)$ and $Var(|g_k|) = \sigma_{|g_k|}^2\left(2 - \frac{\pi}{2}\right) = L_r\left(1 - \frac{\pi}{4}\right)$.

Hence, the statistics of ϵ are:

$$\mu_\epsilon = E\left[H_{l_a}\right] = \sqrt{L_T L_R}\left(\frac{\pi}{4}\right)(\alpha N_a - N_a + N), \tag{5.19.1}$$

$$\sigma_\epsilon^2 = E\left[\left|H_{l_a}\right|^2\right] = \frac{1}{16}L_T L_R(16 - \pi^2)(\alpha^2 N_a + N - N_a). \tag{5.19.2}$$

A proof of these statistics can be found in Appendix F.

The MGF approach is employed, where ρ is a non-central chi-squared RV with one degree-of-freedom. Therefore, ρ has the following MGF [15]:

$$\mathrm{M}_\rho(s) = \frac{1}{\sqrt{1 - 2\sigma_\epsilon^2 s}}\exp\left(\frac{\mu_\epsilon^2 s}{1 - 2\sigma_\epsilon^2 s}\right). \tag{5.20}$$

Finally, the PEP can be written as:

$$P\left(x_q \rightarrow x_{\hat{q}}\right) \cong \frac{1}{12}\mathrm{M}_\rho\left(-\frac{P_{tx}\left|x_q - x_{\hat{q}}\right|^2}{4N_v}\right) + \frac{1}{4}\mathrm{M}_\rho\left(-\frac{P_{tx}\left|x_q - x_{\hat{q}}\right|^2}{3N_v}\right). \tag{5.21}$$

5.2.2.2 Calculation of P_{l_a}

The union-bound for P_{l_a} is formulated as:

$$P_{l_a} \leq \sum_{q=1}^{M} \sum_{l_a=0}^{G-1} \sum_{\hat{l}_a=0}^{G-1} \frac{N\left(l_{a,q} \to l_{a,q}\right) P\left(l_{a,q} \to \hat{l}_{a,q}\right)}{GM\eta}, \tag{5.22}$$

where $P\left(l_{a,q} \to \hat{l}_{a,q}\right)$ is the PEP, and $N\left(l_{a,q} \to \hat{l}_{a,q}\right)$ is the number of bit errors per associated PEP event. In this case, it is assumed that x_q is detected correctly, and l_a is detected erroneously as $\hat{l}_a$. The CPEP is given as:

$$P\left(l_{a,q} \to \hat{l}_{a,q} | H_{l_a}, H_{\hat{l}_a}, x_q\right) = P\left(\left|r - \sqrt{P_{tx}} H_{l_a} x_q\right|^2 > \left|r - \sqrt{P_{tx}} H_{\hat{l}_a} x_q\right|^2\right). \tag{5.23}$$

The CPEP can be written, noting that $\left|x_q\right|^2 = 1$, as:

$$P\left(l_{a,q} \to \hat{l}_{a,q} | H_{l_a}, H_{\hat{l}_a}\right) = Q\left(\sqrt{\frac{P_{tx}\left|H_{l_a} - H_{\hat{l}_a}\right|^2}{2N_v}}\right). \tag{5.24}$$

The derivation of (5.24) may be found in Appendix F. It is observed that (5.24) is the same expression yielded chapter 4, Equation (4.28).

To evaluate (5.24), the exponential form of the Q-function is considered in (5.17), and by declaring a RV $\Psi = H_{l_a} - H_{\hat{l}_a}$. Using the same statistics of $|h_k|$ and $|g_k|$, Ψ has the following mean and variance [79]:

$$\mu_\Psi = \frac{\sqrt{L_T L_R}(\alpha X - X)\pi}{4}, \tag{5.25.1}$$

$$\sigma_\Psi^2 = \frac{L_T L_R (16 - \pi^2)}{16}(\alpha^2 X + X), \tag{5.25.2}$$

where $X = N_a - \hat{N}_a$. Now, another RV may be defined as $\mathrm{Z} = |\Psi|^2$, which is a non-central chi-squared distribution with the MGF written as [15]:

$$\mathrm{M_Z}(s) = \frac{1}{\sqrt{1 - 2\sigma_\Psi^2 s}} \exp\left(\frac{\mu_\Psi^2 s}{1 - 2\sigma_\Psi^2 s}\right). \tag{5.26}$$

Hence, the CPEP can be written as:

$$P\left(l_a \to \hat{l}_a\right) \cong \frac{1}{12}\mathrm{M_Z}\left(-\frac{P_{tx}}{4N_v}\right) + \frac{1}{4}\mathrm{M_Z}\left(-\frac{P_{tx}}{3N_v}\right). \tag{5.27}$$

5.3 HRM AP scheme

5.3.1 HRM AP system model

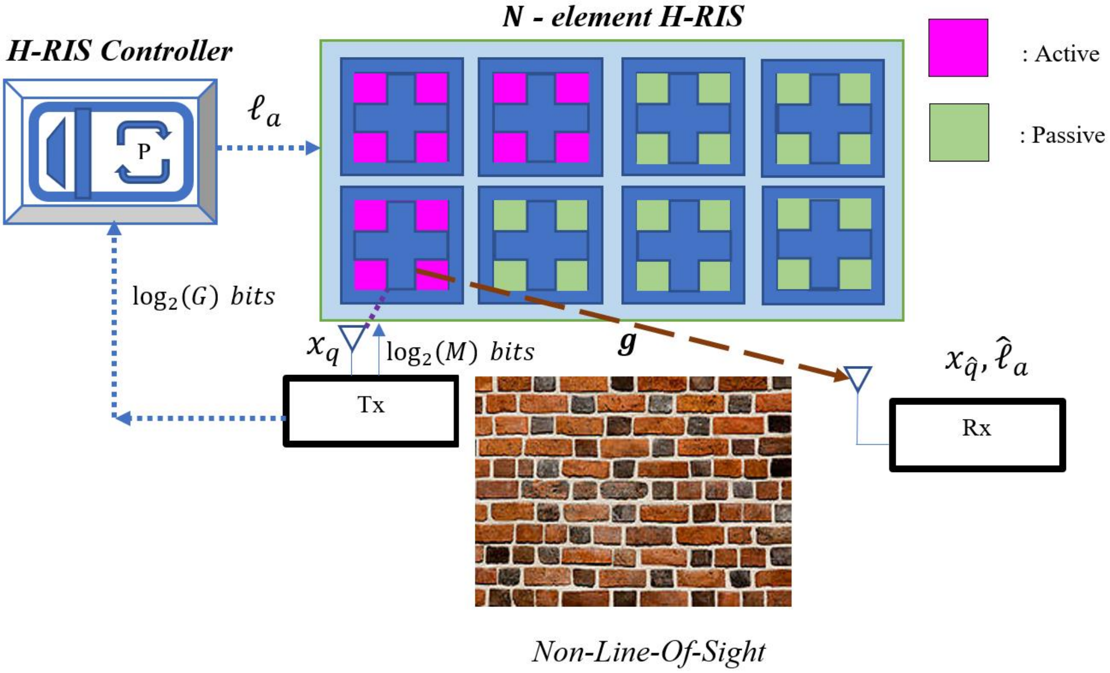

Figure 5.3.1.1: Diagram illustrating the system model of HRM AP scheme

Now consider Figure 5.3.1.1. In this configuration, the H-RIS is positioned next to the transmitter, such that the H-RIS acts as the virtual transmitter of the wireless signal. Similarly to the non-AP scheme, a NLOS path is assumed.

Similar to the HRM non-AP scheme, the information bits of length $\log_2(M)$ bits is mapped to an M-PSK data symbol denoted by $x_q, q \in [1\colon M]$, where M is the size of the PSK constellation, and the H-RIS index ℓ_a to manipulate the state of the H-RIS. The remaining $\log_2(G)$ bits select the index by dividing the N-element H-RIS into G subgroups and using the calculation $\mathrm{S_G} = {}^{N}\!/_{G}$ to determine the number of elements per subgroup. The $\log_2(G)$ information bits select $\ell_a \in [0\colon G-1]$ to select the number of active and passive elements on the H-RIS as $N_a = \ell_a S_G$ and $N_p = N - N_a$. Note that the H-RIS is fully passive for $\ell_a = 0$. Different channel realisations are formed depending on the state of the H-RIS. Therefore, the fading coefficients are mapped to HRM symbols denoted by H_{ℓ_a}.

The mapping of the HRM symbols in the HRM AP scheme follows the same procedure as outlined in Chapter 4, Table 4.2.1.

Based on the above, the SE of the HRM-aided AP scheme is:

$$\eta = \log_2(GM) \text{ bits/s/Hz}. \tag{5.29}$$

The reflection co-efficients of each reflective element in the H-RIS may be written depending on their active/passive status as follows:

$$\varrho_k^a = \alpha_k e^{j\theta_k^a}, k \in [1\colon N_a], \tag{5.30.1}$$

$$\varrho_k^p = e^{j\theta_k^p}, k \in \left[(N_a + 1)\colon N\right]. \tag{5.30.2}$$

Each reflective element has a coefficient $\varrho_k^{a(p)}$, where a denotes 'active' element and p denotes 'passive' elements. As can be observed, the passive reflection coefficients have unit magnitudes, whereas active reflection coefficients have magnitudes $\alpha_k > 1$, thereby facilitating amplification of the wireless signal. It is assumed that $\alpha_k = \alpha$ for all active reflection coefficients.

The Rayleigh fading channel vector is given by $\boldsymbol{g} \in \mathbb{C}^{1\times N} \sim CN(0, L_r)$, where L_r denotes the path loss in [79] as:

$$L_R = m_\kappa r_R^{-\delta_R}, \tag{5.31}$$

where m_κ denotes the reference path loss per metre, r_R denotes the distance in metres from the H-RIS to the receiver, and $\delta_R > 1$ denotes the path loss exponent.

The fading coefficients may be expressed as $\boldsymbol{g} = [\boldsymbol{g}^a\ \boldsymbol{g}^p]^T$, where $\boldsymbol{g}^a \in \mathbb{C}^{1\times N_a}$ denotes the fading vector associated with active elements, and $\boldsymbol{g}^p \in \mathbb{C}^{1\times N_p}$ denotes the fading vector associated with passive elements.

The noise present is comprised of static and dynamic noise. The static noise is expressed as $n_{stc} \sim CN(0, \sigma_{stc}^2)$, and the dynamic noise is denoted by $n_{dyn} = \alpha \sum_{k=1}^{N_a} g_k^a e^{j\theta_k} w_k$, where w_k is the k-th element of $\boldsymbol{w} \in \mathbb{C}^{1\times N_a} \sim CN\left(0, \boldsymbol{I}_{N_a}\sigma_{dyn}^2\right)$ representing the dynamic noise vector [79].

Based on this, the received signal of the HRM AP scheme can be written for a given transmit power P_{tx} as:

$$r = \sqrt{P_{tx}}\left(\alpha \sum_{k=1}^{N_a} g_k^a e^{j\theta_k^a} + \sum_{k=N_a+1}^{N} g_k^p e^{j\theta_k^p}\right) x_q + n_t, \tag{5.32}$$

where $n_t = n_{dyn} + n_{stc}$.

Based on (5.32), the maximum instantaneous received SNR, given symbol x_q, is computed as [79]:

$$\max_{\alpha,\theta} \rho = \frac{E\left[\left|\sqrt{P_{tx}}\left(\alpha \sum_{k=1}^{N_a} g_k^a e^{j\theta_k^a} + \sum_{k=N_a+1}^{N} g_k^p e^{j\theta_k^p}\right) x_q\right|^2\right]}{E[|n_t|^2]}$$

$$= P_{tx}\left|x_q\right|^2 \frac{\left|\alpha \sum_{k=1}^{N_a} g_k^a e^{j\theta_k^a} + \sum_{k=N_a+1}^{N} g_k^p e^{j\theta_k^p}\right|^2}{\alpha^2\left|\sum_{k=1}^{N_a} g_k^a e^{j\theta_k^a}\right|^2 \sigma_{dyn}^2 + \sigma_{stc}^2}, \tag{5.33}$$

$$\text{Such that: } \mathrm{P}_a \geq \alpha^2\left(\mathrm{P}_{tx}\left|\sum_{k=1}^{N_a} e^{j\theta_k^a}\right|^2 + \left|\sum_{k=1}^{N_a} e^{j\theta_k^a}\right|^2 \sigma_{dyn}^2\right), \tag{5.34}$$

where P_a is the maximum reflection power constraint.

Considering $\boldsymbol{g}^a$ and $\boldsymbol{g}^p$ in polar form as $g_k^{a(p)} = \left|g_k^{a(p)}\right| e^{j\xi_k^{a(p)}}$, and optimising the corresponding phase shifts as $\theta_k^{a(p)} = -\left(\xi_k^{a(p)}\right)$, (5.32) may be simplified by noticing that the channel phases are completely eliminated after phase shifting the reflective elements, and the channel gain is written as the HRM symbol given by:

$$H_{\ell_a} = \alpha \sum_{k=1}^{N_a} |g_k^a| + \sum_{k=N_a+1}^{N} |g_k^p|. \tag{5.35}$$

The total noise n_t may be written as:

$$n_t = \alpha \sum_{k=1}^{N_a} |g_k^a| w_k + n_{stc}, \tag{5.36}$$

which is approximated using the CLT as $n \sim CN\left(0, \mathrm{N}_{\mathrm{Y}}^2\right)$, where $\mathrm{N}_{\mathrm{Y}}^2 \approx \alpha^2 N_a L_R \sigma_{dyn}^2 + \sigma_{stc}^2$ [79].

The simplified receive signal in (5.32) is now written as:

$$r = \sqrt{P_{tx}} H_{\ell_a} x_q + n, \tag{5.37}$$

where the ML detector for (5.37) is written, assuming full channel knowledge, as:

$$\left[x_{\hat{q}}, \hat{\ell}_a\right] = \underset{q\in[1:M],\ell_a\in[0:G-1]}{\operatorname{argmin}} \left|r - \sqrt{\mathrm{P}_{tx}} H_{\ell_a} x_q\right|^2. \tag{5.38}$$

5.3.2 Performance Analysis of HRM AP scheme

In the ABEP formulation of the HRM scheme, the approach in (5.13) is employed according to [14] as:

$$P_e \geq P_s + P_{\ell_a} - P_s P_{\ell_a}, \tag{5.39}$$

where P_e is the ABEP, P_s denotes the probability of M-PSK symbol error and P_{l_a} denotes the probability of HRM index error, as mentioned earlier. Similarly to the HRM non-AP scheme, this method is used to reduce the complexity of the analysis. First, P_s is formulated, assuming that and x_q is estimated erroneously as $x_{\hat{q}}$ given that ℓ_a is estimated perfectly. Next, P_{ℓ_a} is formulated, assuming that ℓ_a is estimated erroneously as $\hat{\ell}_a$ given that x_q is estimated perfectly. Based on P_s and P_{ℓ_a}, P_e is evaluated using (5.39), yielding a tight fit for medium-to-high P_{tx}.

5.3.2.1 Calculation of P_s

The union-bound for P_s is given by:

$$P_s \leq \sum_{\ell_a=0}^{G-1} \sum_{q=1}^{M} \sum_{\hat{q}=1}^{M} \frac{P\left(x_{q,l_a} \rightarrow x_{\hat{q},l_a}\right) N\left(x_{q,l_a}, x_{\hat{q},l_a}\right)}{GM\eta}, \tag{5.40}$$

where $P\left(x_{q,l_a} \rightarrow x_{\hat{q},l_a}\right)$ is the PEP, and $N\left(x_{q,l_a}, x_{\hat{q},l_a}\right)$ is the number of bit errors between x_q and $x_{\hat{q}}$.

The CPEP is given as:

$$P\left(x_{q,l_a} \rightarrow x_{\hat{q},l_a} | H_{\ell_a}, \ell_a\right) = P\left(\left|r - \sqrt{P_{tx}} H_{\ell_a} x_q\right|^2 > \left|r - \sqrt{P_{tx}} H_{\ell_a} x_{\hat{q}}\right|^2\right), \tag{5.41}$$

which can be simplified as:

$$P\left(x_{q,l_a} \to x_{\hat{q},l_a} | H_{\ell_a}, \ell_a\right) = Q\left(\sqrt{\frac{P_{tx}\left|H_{\ell_a}\right|^2\left|x_q - x_{\hat{q}}\right|^2}{2N_\Upsilon^2}}\right). \tag{5.42}$$

The full derivation of (5.42) may be found in Appendix F.

The expression in (5.42) can be evaluated by employing (5.17).

Noting that $\left|x_q\right|^2 = 1$ for M-PSK symbols, the instantaneous received SNR is rewritten based on (5.37) as:

$$\rho = \frac{P_{tx}}{N_\Upsilon^2}\left|x_q\right|^2\left|H_{\ell_a}\right|^2 = \frac{P_{tx}}{N_\Upsilon^2}\left|H_{\ell_a}\right|^2 = \frac{P_{tx}}{N_\Upsilon^2}\epsilon^2, \tag{5.43}$$

where ϵ is a Gaussian RV with mean $\mu_\epsilon = E[|g_k|\,] = \sqrt{L_R}\sqrt{\frac{\pi}{4}}$ and variance $\sigma_\epsilon^2 = Var(|g_k|) = L_R\left(1 - \frac{\pi}{4}\right)$.

Hence, the statistics of ϵ are:

$$\mu_\epsilon = \sqrt{\frac{L_r\pi}{4}}(\alpha N_a + N - N_a), \tag{5.44.1}$$

$$\sigma_\epsilon^2 = L_r\left(1 - \frac{\pi}{4}\right)(\alpha^2 N_a + N - N_a), \tag{5.44.2}$$

the full derivation of which may be found in Appendix F. It is observed that ρ is a non-central chi-squared RV with one degree-of-freedom, with the MGF given by [15]:

$$\mathrm{M}_\rho(s) = \frac{\exp\left(\frac{\mu_\epsilon^2 s}{1 - 2\sigma_\epsilon^2 s}\right)}{\sqrt{1 - 2\sigma_\epsilon^2 s}}. \tag{5.45}$$

Finally, $P\left(x_q \to x_{\hat{q}}\right)$ is written as:

$$P\left(x_q \to x_{\hat{q}}\right) \cong \frac{1}{12}\mathrm{M}_\rho\left(-\frac{P_{tx}\left|x_q - x_{\hat{q}}\right|^2}{4N_\Upsilon^2}\right) + \frac{1}{4}\mathrm{M}_\rho\left(-\frac{P_{tx}\left|x_q - x_{\hat{q}}\right|^2}{3N_\Upsilon^2}\right). \tag{5.46}$$

5.3.2.2 Calculation of P_{ℓ_a}

The union-bound for P_{ℓ_a} is given by:

$$P_{\ell_a} \leq \sum_{q=1}^{M}\sum_{\ell_a=0}^{G-1}\sum_{\hat{\ell}_a=0}^{G-1}\frac{P\left(\ell_{a,q} \to \hat{\ell}_{a,q}\right)N\left(\ell_{a,q}, \hat{\ell}_{a,q}\right)}{GM\eta}, \tag{5.47}$$

where $P\left(\ell_{a,q} \to \hat{\ell}_{a,q}\right)$ is the PEP, and $N\left(\ell_{a,q}, \hat{\ell}_{a,q}\right)$ is the number of bit errors between ℓ_a and $\hat{\ell}_a$.

The CPEP is given as:

$$P\left(\ell_{a,q} \to \hat{\ell}_{a,q} | H_{\ell_a}, H_{\hat{\ell}_a}, x_q\right) = P\left(\left|r - \sqrt{P_{tx}} H_{\ell_a} x_q\right|^2 > \left|r - \sqrt{P_{tx}} H_{\hat{\ell}_a} x_q\right|^2\right), \tag{5.48}$$

which can be written, noting that $\left|x_q\right|^2 = 1$ for M-PSK symbols, as:

$$P\left(\ell_{a,q} \to \hat{\ell}_{a,q} | H_{\ell_a}, H_{\hat{\ell}_a}\right) = Q\left(\sqrt{\frac{P_{tx}\left|H_{\ell_a} - H_{\hat{\ell}_a}\right|^2}{2N_\Upsilon^2}}\right). \tag{5.49}$$

The full derivation of (5.49) may be found in Appendix F.

Equation (5.49) is further evaluated using the Q-function approximation in (5.17). The statistics may be found by using the given statistics of $|g_k|$ previously described.

A RV defined as $\Psi = H_{\ell_a} - H_{\hat{\ell}_a}$ is considered, where the given statistics of $|g_k|$ previously described are used to calculate the mean and variance of Ψ as [79]:

$$\mu_\Psi = \sqrt{\frac{L_r \pi}{4}}\,(\alpha\tau - \tau), \tag{5.50.1}$$

$$\sigma_\Psi^2 = L_r\left(1 - \frac{\pi}{4}\right)(\alpha^2\tau + \tau), \tag{5.50.2}$$

where $\tau = N_a - \widehat{N}_a$. The derivation of (5.50a) – (5.50b) may be found in Appendix F.

Furthermore, a RV $\mathrm{Z} = |\Psi|^2$ is defined, such that Z follows a non-central chi-squared distribution with the following MGF [15]:

$$\mathrm{M_Z}(s) = \frac{\exp\left(\frac{\mu_\Psi^2 s}{1 - 2\sigma_\Psi^2 s}\right)}{\sqrt{1 - 2\sigma_\Psi^2 s}}. \tag{5.51}$$

Hence, $P\left(\ell_a \to \hat{\ell}_a\right)$ is written as:

$$P\left(\ell_a \to \hat{\ell}_a\right) \cong \frac{1}{12}\mathrm{M_Z}\left(-\frac{P_{tx}}{4N_\Upsilon^2}\right) + \frac{1}{4}\mathrm{M_Z}\left(-\frac{P_{tx}}{3N_\Upsilon^2}\right). \tag{5.52}$$

5.4 Numerical Results

In this section, the EP of the HRM non-AP and HRM AP is presented for varying M, G and N, and comparisons are made between the HRM-aided schemes and the conventional HRM [79] and RIS-aided [48] schemes. All results are presented in the form of BER vs P_{tx} graphs, and all results are drawn at a BER of 10^{-6}.

The simulation settings are given in Table 5.5.1:

Table 5.4.1: Simulation settings for HRM non-AP and HRM AP schemes

Parameter	r_T	r_R	δ_T	δ_R	$\sigma_{dyn}^2 = \sigma_{stc}^2$	m_κ	α
Value	20m	50m	2.2	2.8	-90dBm	-30dB	10

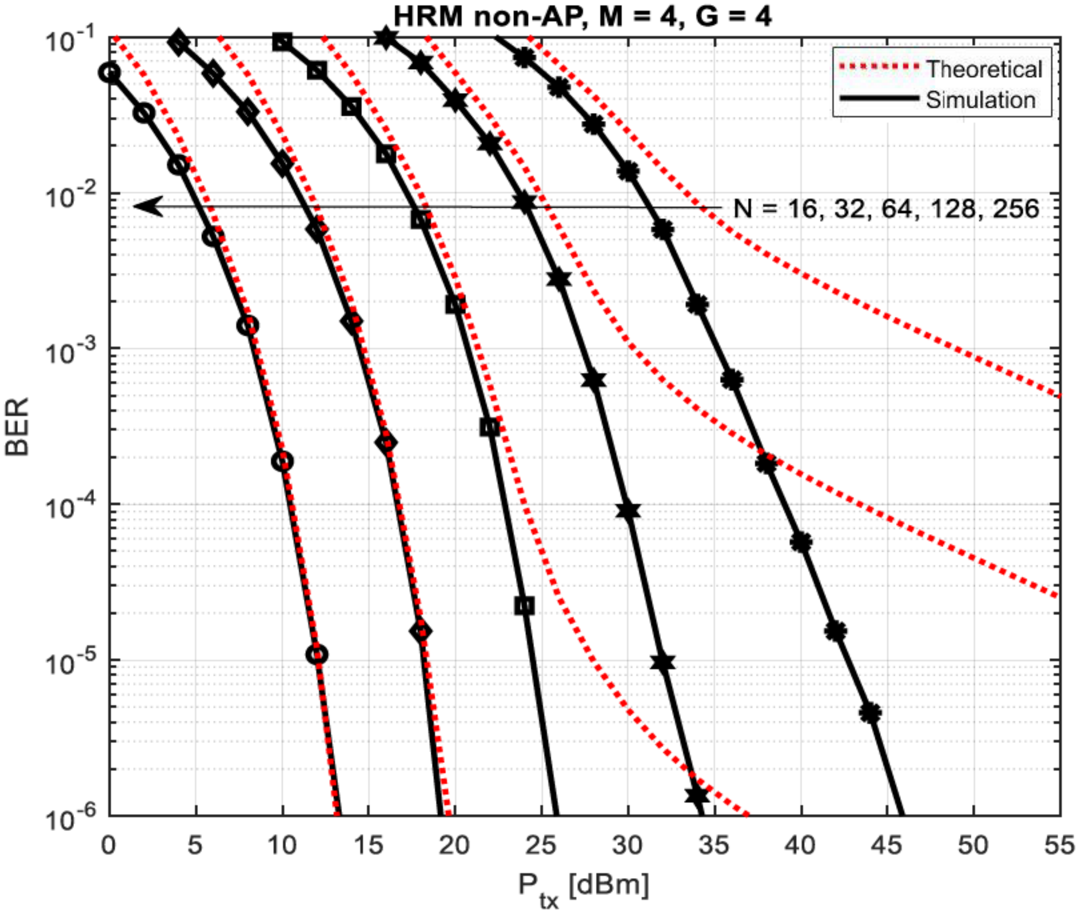

Figure 5.4.1: BER vs P_{tx} graphs of the HRM non-AP scheme for increasing N

Figure 5.4.1 shows the EP of the HRM non-AP scheme for $M = 4$, $G = 4$ and increasing $N \in \{16, 32, 64, 128, 256\}$. It is observed that doubling N improves the EP significantly, particularly in the lower range of N. It is observed that for high N, the theoretical results fit tightly with the simulation results for medium-to-high P_{tx}, as discussed in Section 5.2.2, but for moderate-to-low N, error floors form at higher P_{tx}. As seen in earlier chapters, this phenomenon is due to the CLT being applied assuming high values of N, such that N_a is high enough for the approximation to work, meaning that for low-to-moderate N, N_a is not approximated well, hence large error floors form.

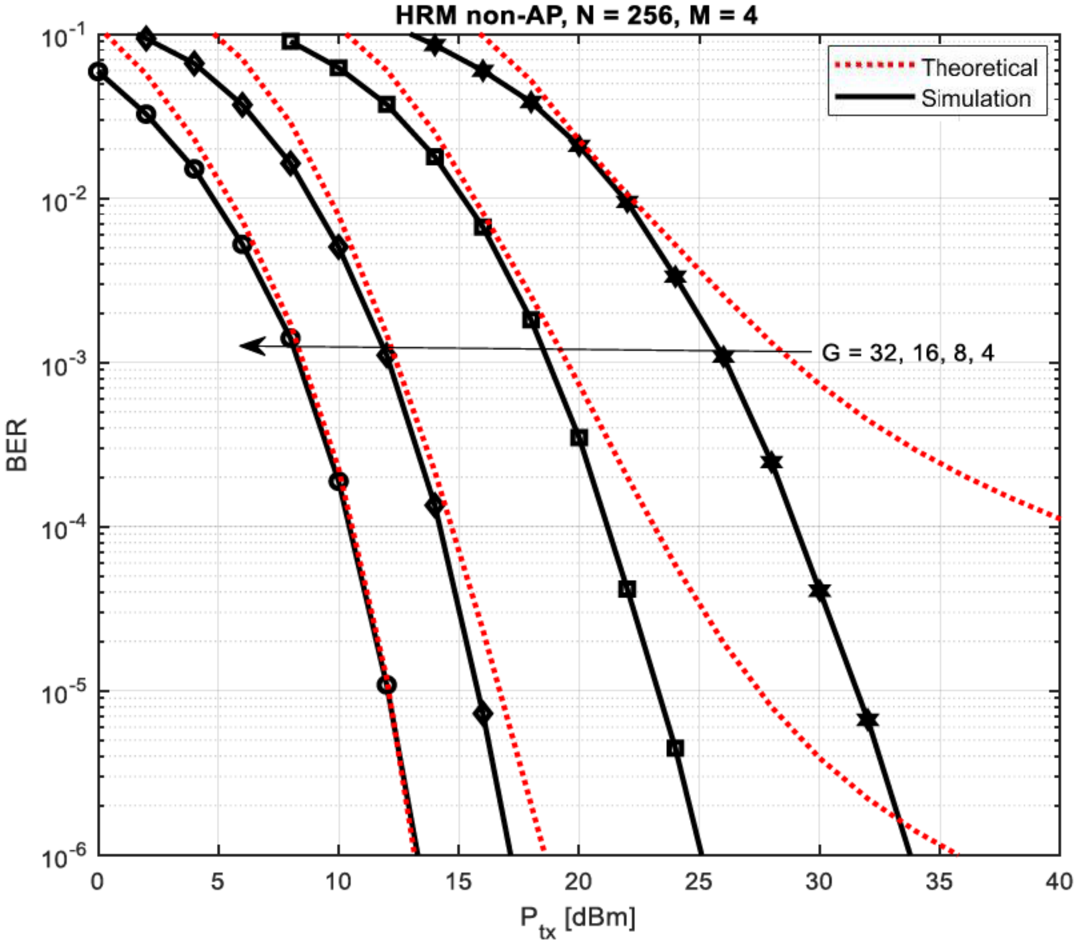

Figure 5.4.2: BER vs P_{tx} graphs of the HRM non-AP scheme for increasing G

Figure 5.4.2 shows the EP of the HRM non-AP scheme for $M = 4$, $N = 256$ and increasing $G \in \{4, 8, 16, 32\}$. It can be observed that increasing the SE by doubling G deteriorates the EP significantly, suggesting that at high G, the EP worsens greatly. Another observation made is that large error floors form as G increases, which is a similar effect observed in Chapter 4, Figure 4.7.5. The CLT being applied assuming high N, such that N_a and N_p is well approximated. In this case, increasing G decreases the number of active and passive elements in each subgroup, hence N_a and N_p is not approximated well for high G.

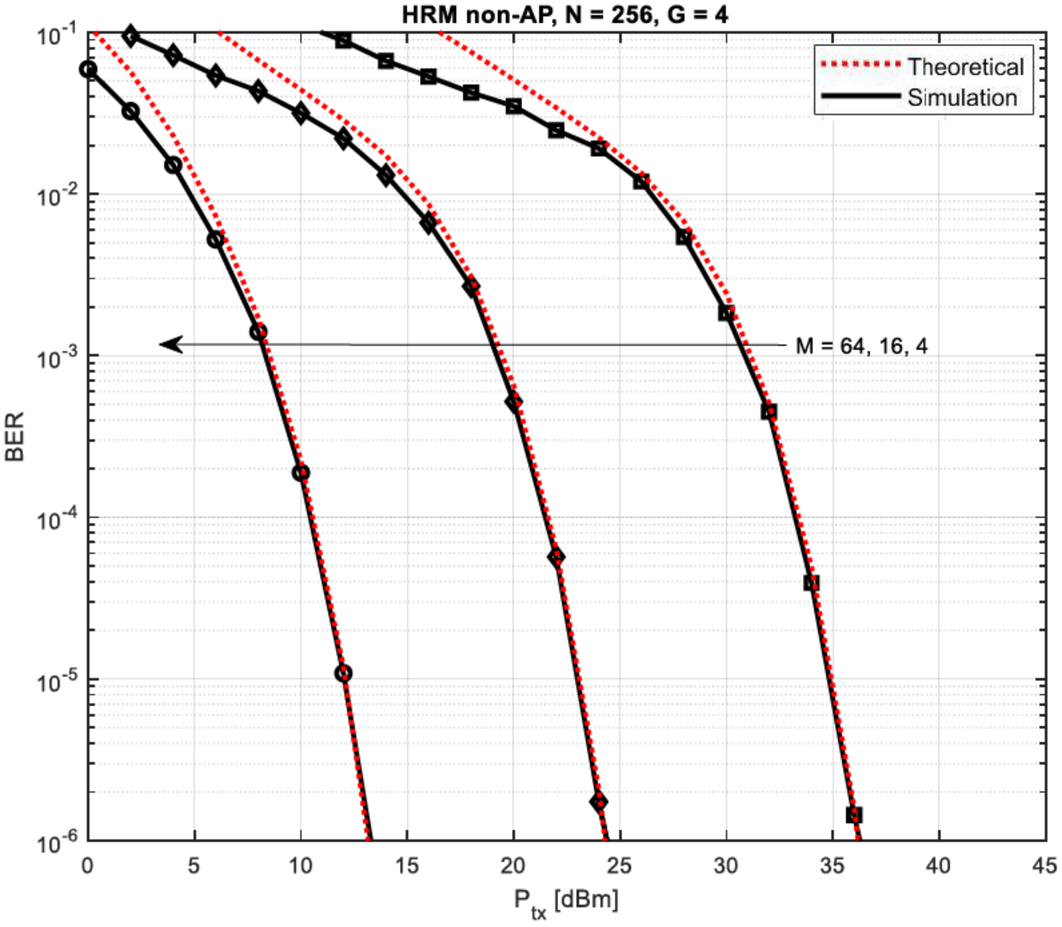

Figure 5.4.3: BER vs P_{tx} graphs of the HRM non-AP scheme for increasing M

Figure 5.4.3 shows the EP of the HRM non-AP scheme for $G = 4, N = 256$ and increasing $M \in \{4, 16, 64\}$. It is observed that as the modulation order increases, the EP deteriorates by 11-12dBm, in other words, the EP deteriorates at a constant rate as opposed to increasing N or G. It is also observed that the theoretical graphs demonstrate a tight approximation for moderate-to-high P_{tx}, hence demonstrating the validity of the approach proposed in Section 5.2.2 for varying M.

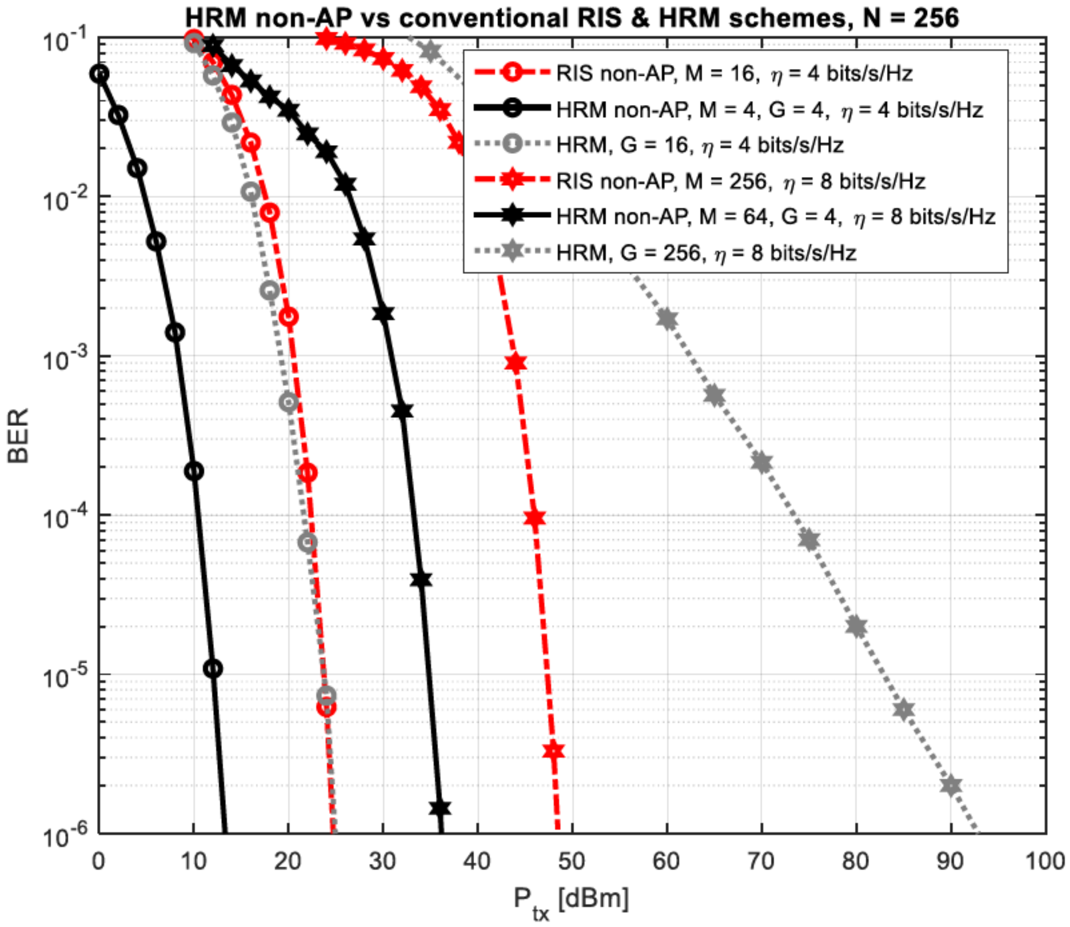

Figure 5.4.4: BER vs P_{tx} graphs of the HRM non-AP compared to conventional RIS non-AP and HRM schemes for $\eta = \{4,8\}$ bits/s/Hz

Figure 5.4.4 shows the EP of the HRM non-AP scheme in comparison to that of the conventional non-AP scheme [48], as well as the conventional HRM scheme [79] for $\eta = 4$ bits/s/Hz and $\eta = 8$ bits/s/Hz. The conventional RIS schemes are assumed to have a fully passive RIS, with the same parameters given in Table 5.4.1. It is seen that for $\eta = 4$ bits/s/Hz, the HRM non-AP scheme demonstrates a 12dBm gain over the conventional schemes, whilst for $\eta = 8$ bits/s/Hz, an improvement of 12dBm and 57dBm is seen over the RIS non-AP scheme and HRM scheme, respectively. A notable observation is that where the SE of the conventional HRM scheme is limited by G, the HRM non-AP scheme overcomes this limitation by increasing M.

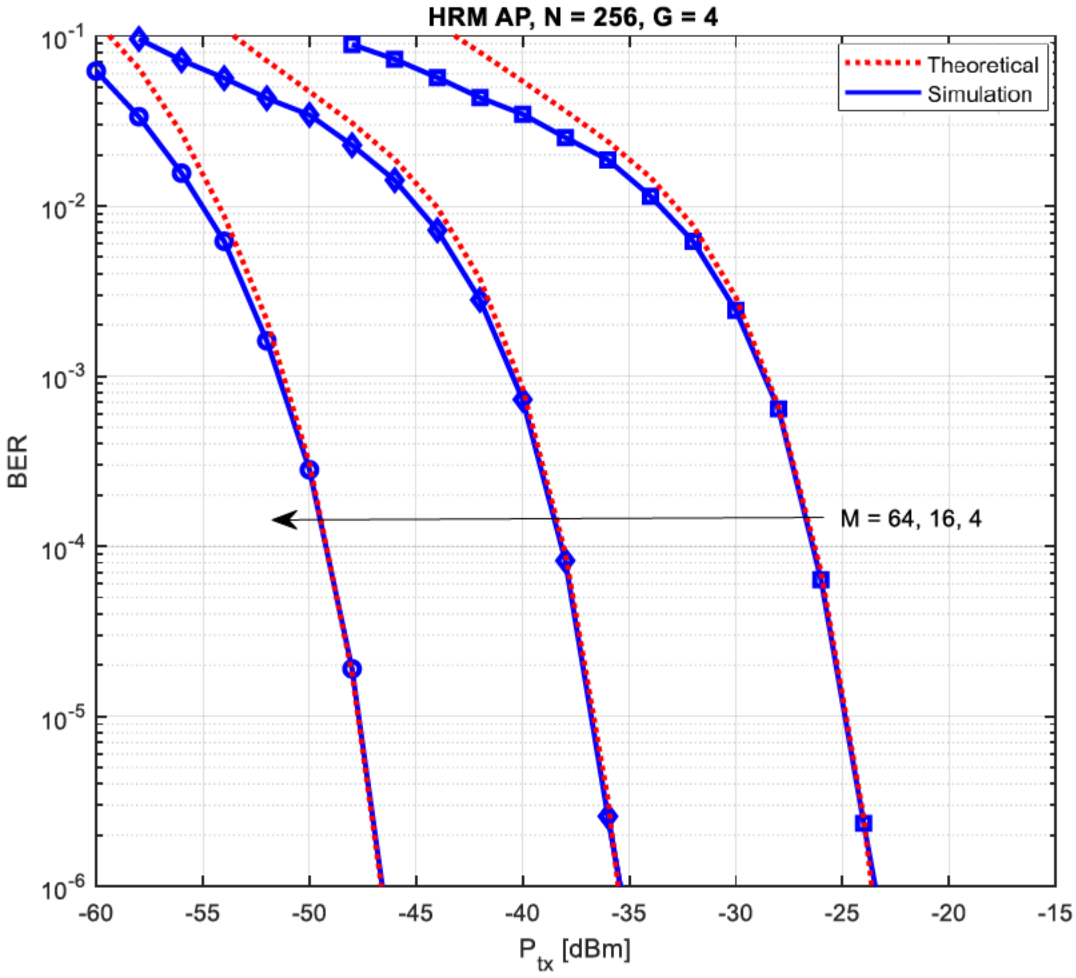

Figure 5.4.5: BER vs P_{tx} graphs of the HRM AP scheme for increasing M

Figure 5.4.5 shows the EP of the HRM AP scheme for $G = 4$ and $N = 256$ with increasing $M \in \{4, 16, 64\}$ with respect to P_{tx}. As discussed in Section 5.3.2, the theoretical curve matches the simulation curve for medium-to-high P_{tx}. For increasing M, it is observed that very low P_{tx} is required to achieve a BER of 10^{-6}, which clearly demonstrates the superiority of the AP-based H-RIS. It is also observed that like the HRM non-AP scheme, the theoretical curve matches the simulation curve at moderate-to-high P_{tx}, further demonstrating the validity of the approach in Section 5.3.2 for increasing M.

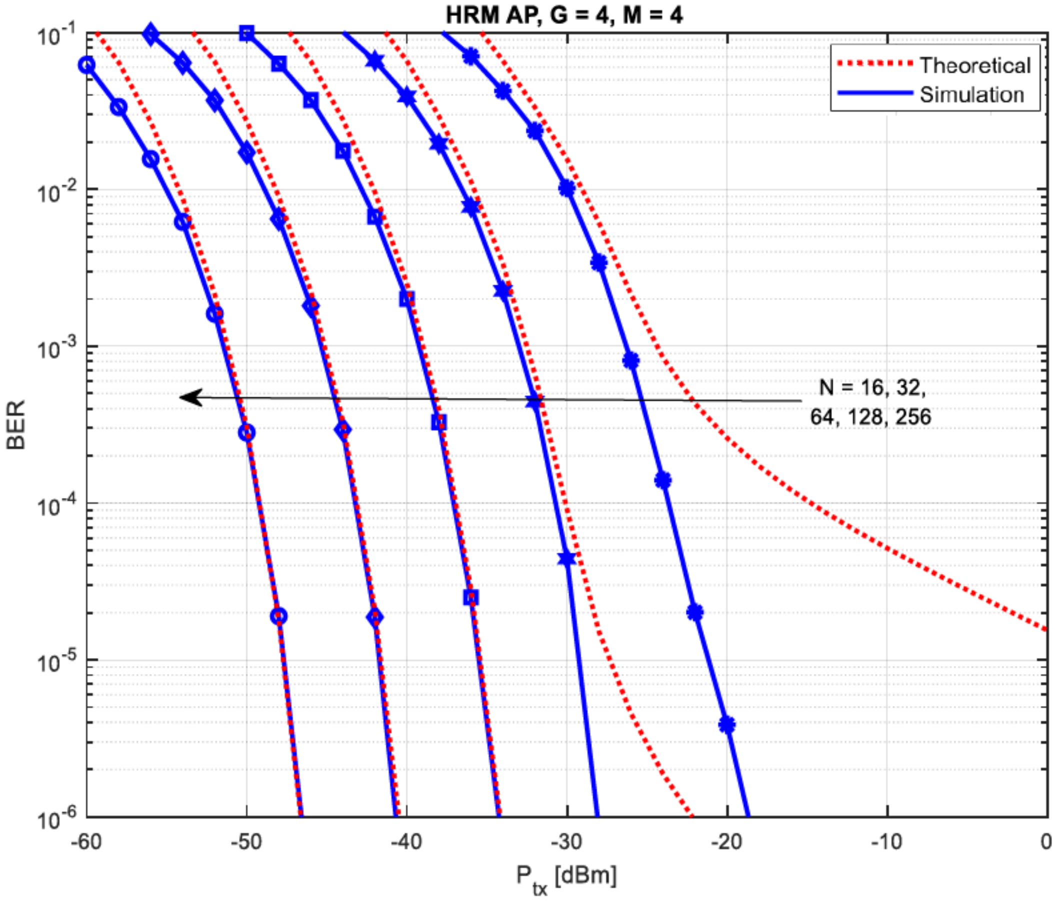

Figure 5.4.6: BER vs P_{tx} graphs of the HRM AP scheme for increasing N

Figure 5.4.6 shows the EP of the HRM AP scheme for $M = 4$ and $G = 4$ with increasing $N \in \{16, 32, 64, 128, 256\}$. It is seen that the simulation graphs match the theoretical results for moderate-to-high N, but errors floors are present for small values of N. As seen earlier, this is expected, due to the employment of the CLT assuming high N, as seen in previous chapters. It may be noted that the effect of the CLT on this scheme is not as profound as in the HRM non-AP scheme. This is because the non-AP scheme considers the product of channel magnitudes, whereas the HRM AP scheme only considers the single channel magnitude. Hence, the CLT can be used to approximate the sum of a single channel magnitude more accurately than it can a product of RVs. It can also be observed that a 6dBm gain in P_{tx} is seen when increasing N in the moderate-to-high range, and a 10-12dBm improvement is seen for low values of N. This trend is very similar to the HRM non-AP scheme, in which the EP greatly improves when doubling N in the low range.

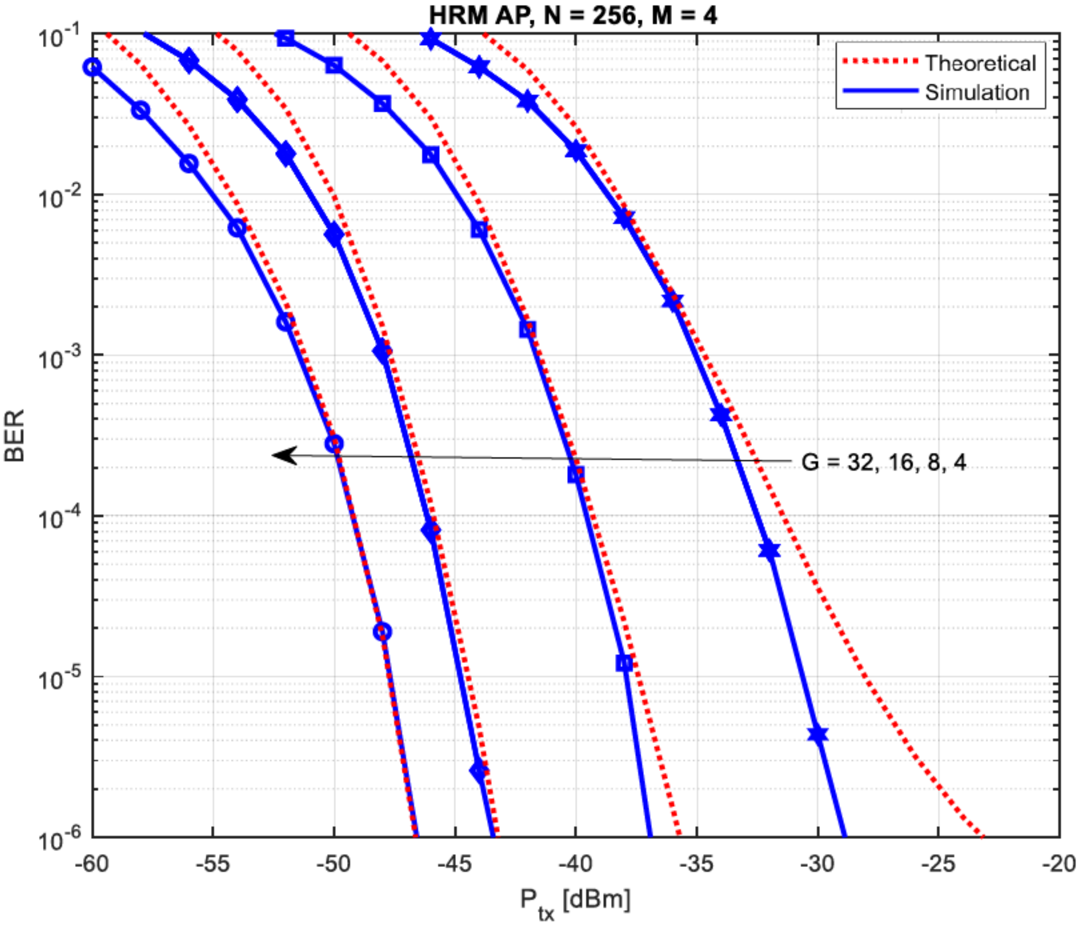

Figure 5.4.7: BER vs P_{tx} graphs of the HRM AP scheme for increasing G

Figure 5.4.7 shows the EP of the HRM AP scheme for $M = 4$ and $N = 256$ with increasing $G \in \{4, 8, 16, 32\}$. It can be observed that the EP deteriorates greatly when G is increased. It is also observed that for increasing G, errors floors form, which is a similar phenomenon observed in Figure 5.4.6, and the reasons for this phenomenon are the same as discussed in Figure 5.4.2. Again, it is evident that in comparison to the HRM non-AP scheme, the error floors are not as large, hence the ABEP formulation in (5.13) and (5.39) is far more accurate for the HRM AP scheme.

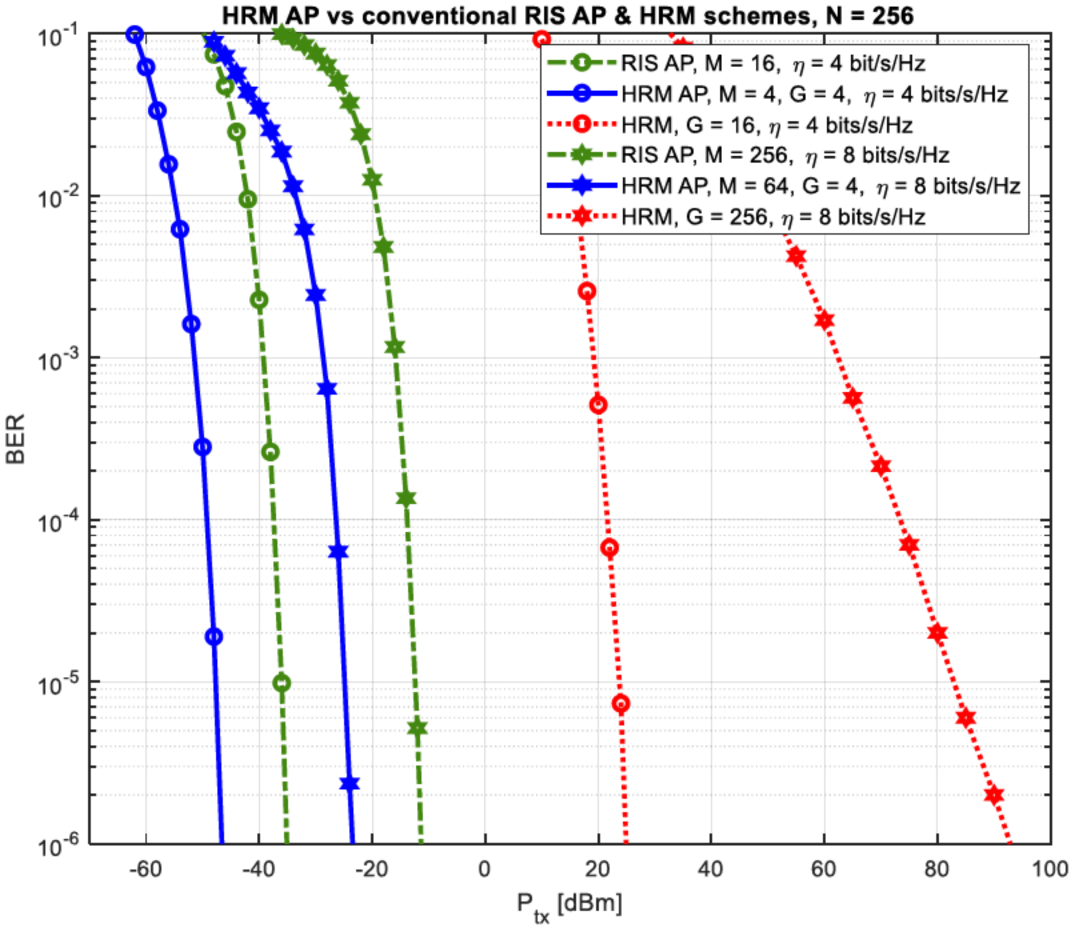

Figure 5.4.8: BER vs P_{tx} graphs of the HRM AP schemes compared to conventional RIS and HRM schemes for $\eta = \{4,8\}$ bits/s/Hz

Figure 5.4.8 shows the EP of the HRM AP scheme in comparison to that of the conventional AP RIS scheme [48] and conventional HRM scheme [79] for SEs of $\eta = \{4,8\}$ bits/s/Hz. For fair comparison, it is assumed that the RIS AP scheme contains a fully passive RIS with the same parameters given in Table 5.4.1. It is seen that for $\eta = 4$ bits/s/Hz, the HRM AP scheme demonstrates gains of 11dBm and 72dBm compared to the RIS AP scheme and the conventional HRM scheme, respectively. For $\eta = 8$ bits/s/Hz, the HRM AP scheme demonstrates gains of 13dBm and 116dBm over the RIS AP scheme and conventional HRM scheme, respectively. These results demonstrate that using the IM concept to transmit additional data using the H-RIS in the AP configuration increases SE and improves EP significantly.

Chapter Summary

In this chapter, two novel HRM-aided schemes were presented, namely the HRM non-AP scheme and the HRM AP scheme. The mathematical frameworks of the ABEP of both HRM-aided schemes were also presented. Simulation results in the form of BER vs P_{tx} graphs were provided, and observations were drawn based on the results. The theoretical framework fits tightly with the simulation graphs for high values of N, and error floors and present for low values of N. Another observation was that the HRM-aided schemes can significantly improve upon the SE and EP of the conventional HRM and RIS schemes. Lastly, it was seen that the HRM AP schemes boasts superior EP over the HRM non-AP scheme. Overall, it may be said that the proposed schemes were able to effectively improve upon the EP and SE using the HRM concept and the AP configuration.

CHAPTER 6

RECONFIGURABLE INTELLIGENT SURFACE-AIDED MODULATION IN RICIAN CHANNELS

6.1 Introduction

The developments made in 5G networks have been significant thus far, with many networks having already being either launched, in deployment or in development in many countries across the globe. Despite these developments, it has been established that no single enabling technology can address all of the challenges and application requirements. Hence, much of the recent research has been dedicated to beyond 5G, or 6G, wireless networks; and due to new use cases, trends and user requirements, it is clear that a drastic change in the design of future wireless communication schemes is required.

One such idea that has received much attention in the research world is the concept of being able to control the seemingly 'uncontrollable' wireless propagation environment. This idea has led to the development of the RIS which is a surface made of man-made EM material used to intelligently reflect the incoming signal towards the receiver.

Some existing RIS literature includes the following. In [89], it was proposed that a number of RISs could be grouped together on a large surface for data transmission and reception. The authors in [24, 96, 131] focus on maximising EE and sum rate in downlink systems aided by RISs. In [91] and [92], performance analyses were carried out under practical impairments, with an emphasis on uplink SE and data rate. The authors in [48] and [49], formulated RIS-assisted wireless networks, which cover generic RIS-assisted schemes and RIS-based IM schemes, with the aim of improving EP and SE. The author of [48] then proposed the AP-based RIS scheme and also considered the effects of blind channel phases on the EP of the scheme. A study in [49], applied the AP configuration with RIS-SSK modulation and RIS-SM. The authors of [78] and [113] then applied the AP configuration in both the RIS-aided SISO GC modulation scheme and the K-complex symbol GC modulation scheme, which boasted significant EP gains.

Rician fading in RIS-aided systems has recently emerged as a topic of interest, as the RIS provides a dominant LOS component in comparison to NLOS components in the propagation environment, and the impact of the dominant LOS component on the performance of RIS-aided systems is documented on in [85] and [86]. The LOS dominant component is an important characteristic of the RIS, as one of the advantages of implementing an RIS is that it can provide additional paths via its reflective elements when the LOS is weak or blocked [132]. No general closed-form of the Rician distribution exists, as it is expressed in terms of the MBF of the first kind. However, closed-form approximations of the Rician distribution for sums of RVs have been proposed in [133].

In this chapter, the EP of the RIS non-AP and AP schemes is evaluated under Rician fading channels, and the formulation of the ABEP of both schemes is presented assuming Rician fading. Furthermore, the EP of the RIS M-QAM AP system in Rician fading for a low number of reflective elements is investigated and formulate a closed-form approximation of the ABEP of the scheme.

The contributions of this chapter are stated as follows:

- The EP of the RIS non-AP and RIS AP schemes are investigated in Rician fading channels.
- The formulation of the theoretical SEPs of the RIS non-AP and RIS AP schemes in Rician fading channels is presented.

- The EP of the RIS M-QAM AP scheme is investigated for low numbers of reflective elements in Rician fading channels.
- The mathematical formulation of the ABEP of the RIS M-QAM AP is derived.

This chapter is organized as follows. In Section 6.2, the system model of the RIS non-AP scheme in Rician fading channels is presented, and in Section 6.3, the system model of the RIS AP scheme in Rician fading channels is presented. In Section 6.4, the formulation of the ABEP of both schemes is presented. In Section 6.5, the system model of the RIS M-QAM AP scheme in Rician fading channels is presented, and in Section 6.6, the formulation of the ABEP of the RIS M-QAM AP scheme in Rician fading channels is presented.

6.2 RIS non-AP system model

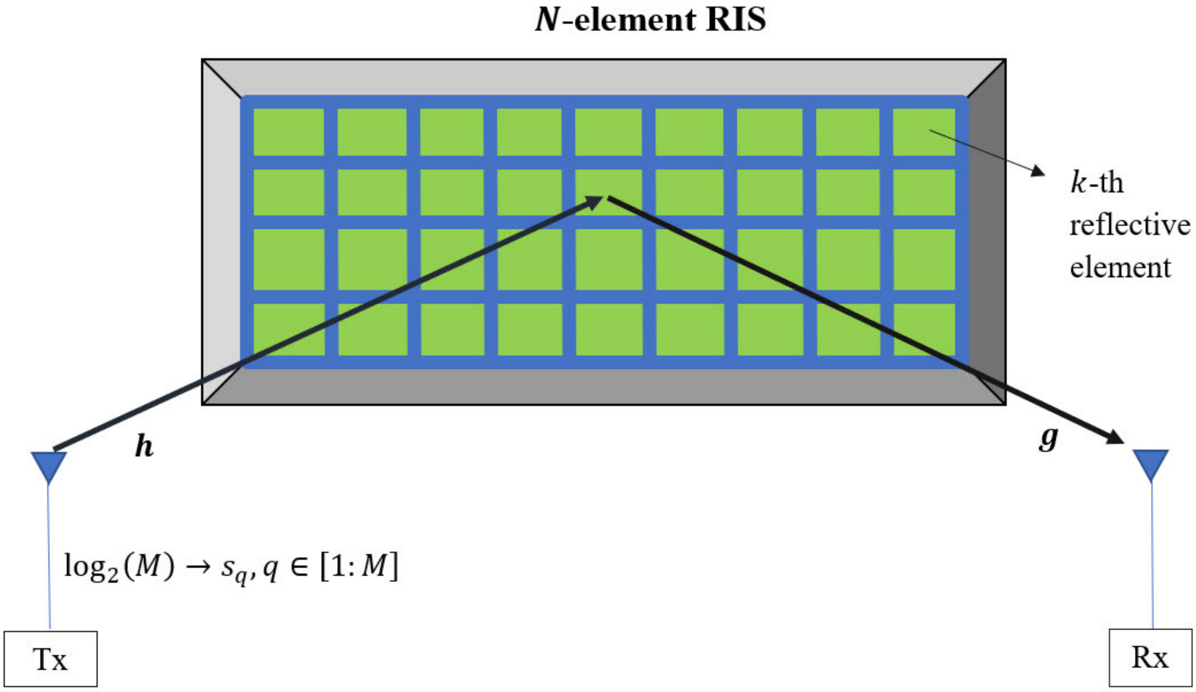

Figure 6.2.1: Diagram illustrating the system model of the RIS-aided non-AP scheme

Consider Figure 6.2.1. The N-element RIS is positioned inside the wireless channel, where it acts as an intelligent reflector of the incoming signal from the transmitter.

As described in Chapter 2, information bits of length $\log_2(M)$ bits are mapped onto an M-QAM or M-PSK symbol denoted by s_q, where $q \in [1:M]$, and where M is the size of the QAM or PSK constellation. The symbol s_q is then transmitted towards the RIS, where the signal is intelligently reflected towards the receiver.

The Rician fading channel vectors are denoted by $\boldsymbol{h}$ and $\boldsymbol{g}$, where $\boldsymbol{h}, \boldsymbol{g} \in \mathbb{C}^{1\times N} \sim CN(0,1)$. The fading vector $\boldsymbol{h}$ occurs in the Tx-RIS path, and $\boldsymbol{g}$ occurs in the RIS-Rx path. The AWGN present in the channel is denoted by $n \sim CN(0,1)$.

It is worth noting that a Rician fading sample is computed as [134]:

$$h = (t_2 X_1 + t_1) + j(t_2 X_2 + t_1), \tag{6.1}$$

where $t_1 = \sqrt{\frac{K}{2(K+1)}}$, $t_2 = \sqrt{\frac{1}{2(K+1)}}$, K denotes the Rician K-factor, and X_1 and X_2 are RVs taken from the standard normal distribution $N(0,1)$. It is important to note that a Rayleigh fading sample is obtained from (6.1) for $K = 0$.

Hence, for a given SNR denoted by ρ, the receive signal can be written as [48]:

$$y = \sqrt{\rho}\mathrm{A}s_q + n, \tag{6.2}$$

where $\mathrm{A} = \sum_{k=1}^{N} h_k g_k e^{j\theta_k}$. The phases θ_k denotes the optimized phase shift of the k-th reflective element such that the SNR is maximized. The phase shift of each reflective element man be optimized by rewriting the fading vectors in polar form as $h_k = \alpha_k e^{j\phi_k}$ and $g_k = \beta_k e^{j\varphi_k}$, thereby optimizing the k-th phase shift as $\theta_k = -(\phi_k + \varphi_k)$. By doing so, the phase shifts may be completely eliminated, and the resultant channel is rewritten as $\mathrm{A} = \sum_{k=1}^{N} \alpha_k \beta_k$.

The ML detector for (6.2) is given, assuming full channel knowledge, as:

$$\hat{s}_q = \underset{q\in[1:M]}{\operatorname{argmin}} \left| y - \sqrt{\rho}\mathrm{A}s_q \right|^2. \tag{6.3}$$

6.3 RIS AP system model

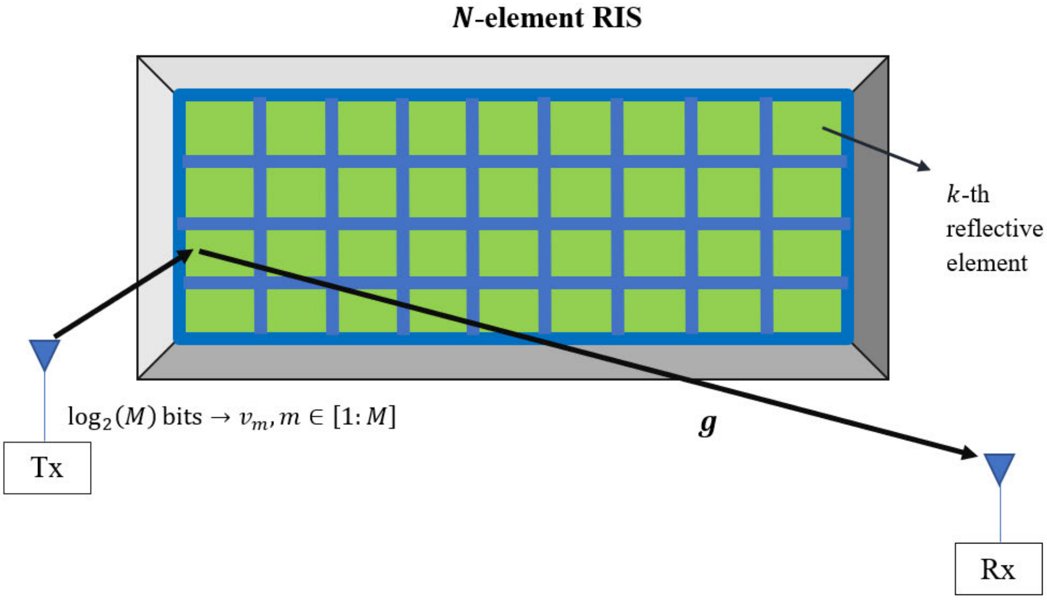

Figure 6.3.1: Diagram illustrating the system model of the RIS-aided AP scheme

Consider Figure 6.3.1. As described previously in Chapter 2, the RIS is positioned close to the transmitter in the RIS AP scheme, creating an innovative scheme in which the RIS virtually transmits the wireless signal.

Notably in this scheme, only $\boldsymbol{g}$ is present, defined in the previous subsection, and AWGN denoted by $n \sim CN(0,1)$.

The RIS AP scheme considers the transmission of an unmodulated carrier. Hence, the receive signal may be written as [48]:

$$y = \sqrt{\rho}\left(\sum_{k=1}^{N} g_k e^{j\theta_k}\right) + n. \tag{6.4}$$

The phase adjustment θ_k is computed by the selection of a common additional phase term given by $v_m, m \in [1:M]$ according to input bits of $\log_2(M)$ bits per interval [48]. Therefore, the reflector elements are adjusted as $\theta_k = -(\varphi_k + v_m)$.

Therefore, the receive signal in (6.4) can be simplified as follows [48]:

$$y = \sqrt{\rho}\left(\sum_{k=1}^{N} \beta_k\right) e^{j v_m} + n = \sqrt{\rho}\mathrm{B}s_m + n, \tag{6.5}$$

where s_m is a virtual M-PSK symbol, where M is the size of the PSK constellation. In other words, the model of the scheme simplifies to the transmission of an M-PSK symbol according to input bits of $\log_2(M)$ bits in length through a fading channel given by $\mathrm{B} = \sum_{k=1}^{N} \beta_k$.

The ML detector is given, assuming full channel knowledge, as:

$$\hat{s}_m = \underset{m \in [1:M]}{\operatorname{argmin}} \left| y - \sqrt{\rho}\mathrm{B}s_m \right|^2. \tag{6.6}$$

6.4 Performance Analysis of RIS-aided schemes

The instantaneous received SNR of the RIS non-AP and RIS AP schemes, for their respective settings, is given as:

$$\gamma_{nAP} = \rho \mathrm{A}^2, \tag{6.7.1}$$

$$\gamma_{AP} = \rho \mathrm{B}^2. \tag{6.7.2}$$

An arbitrary Rician RV denoted by Y has the following mean, second moment and variance, respectively, as [15]:

$$\mu = E[Y] = \sigma\sqrt{\frac{\pi}{2}}\left[(1+K)I_0\left(\frac{K}{2}\right) + KI_1\left(\frac{K}{2}\right)\right] e^{-\frac{K}{2}}, \tag{6.8.1}$$

$$\mathcal{M}_2 = E[Y^2] = (1+K)2\sigma^2, \tag{6.8.2}$$

$$Var(Y) = \mathcal{M}_2 - \mu^2, \tag{6.8.3}$$

where, for our analyses based on (6.1), $\sigma = t_2 = \sqrt{\frac{1}{2(K+1)}}$.

It is also worth noting that the MBF of the first kind is written as [15]:

$$I_z(r) = \sum_{k=0}^{\infty} \frac{\left(\frac{r}{2}\right)^{2k+z}}{(k!)\Gamma(k+z+1)}, \quad r \geq 0, \tag{6.9}$$

where z represents an arbitrary order of the MBF. Of particular importance in the SEP analyses is the zero and first order of the MBF, which are written as [15]:

$$I_0(r) = \sum_{k=0}^{\infty}\left(\frac{r^k}{k!\,2^k}\right)^2, \tag{6.10}$$

$$I_1(r) = \sum_{k=0}^{\infty}\frac{\left(\frac{r}{2}\right)^{2k+1}}{(k!)\Gamma(k+2)}. \tag{6.11}$$

Some important results to note is $I_0(0) = 1$ and $I_1(0) = 0$. Hence for $K = 0$, the statistics in (6.8.1) – (6.8.3) is equivalent to those of Rayleigh statistics.

6.4.1 SEP of RIS non-AP scheme

In the non-AP scheme, the channel magnitudes α_k and β_k are i.i.d Rician RVs, each with means and variances given by (6.8.1) – (6.8.3). The mean and variance of A may then be computed by applying the CLT by assuming high values of N.

Hence, the statistics of A may be computed as:

$$\mu_{\mathrm{A}} = E[\mathrm{A}] = E\left[\sum_{k=1}^{N}\alpha_k\beta_k\right] \cong NE[\alpha_k]E[\beta_k], \tag{6.12.1}$$

$$Var(\mathrm{A}) = Var\left(\sum_{k=1}^{N}\alpha_k\beta_k\right) \cong NVar(\alpha_k\beta_k) = N\left(E\left[\alpha_k^2\right]E\left[\beta_k^2\right] - (E[\alpha_k])^2(E[\beta_k])^2\right). \tag{6.12.2}$$

Based on the above, the final mean and variance of A are computed as:

$$\mu_{\mathrm{A}} = E[\mathrm{A}] = N\mu^2, \tag{6.13.1}$$

$$\sigma_{\mathrm{A}}^2 = \ Var(\mathrm{A}) = N(\mathcal{M}_2^2 - \mu^4). \tag{6.13.2}$$

It may be observed that γ_{nAP} is a non-central chi-squared RV with one degree-of-freedom with an MGF given as:

$$\mathrm{M}_{\gamma_{nAP}}(x) = \frac{1}{\sqrt{1 - 2\rho\sigma_{\mathrm{A}}^2 x}}e^{\left(\frac{\mu_{\mathrm{A}}^2\rho x}{1-2\sigma_{\mathrm{A}}^2\rho x}\right)}. \tag{6.14}$$

Hence, the SEP of the RIS non-AP scheme for M-QAM data is computed as [48]:

$$P_e = \frac{4}{\pi}b\int_0^{\frac{\pi}{2}}\mathrm{M}_{\gamma_{nAP}}\left(-\frac{3}{2(M-1)\sin^2\chi}\right)d\chi - \frac{4}{\pi}b^2\int_0^{\frac{\pi}{4}}\mathrm{M}_{\gamma_{nAP}}\left(-\frac{3}{2(M-1)\sin^2\chi}\right)d\chi, \tag{6.15}$$

where $b = \left(1 - \frac{1}{\sqrt{M}}\right)$. For M-PSK data, the SEP is formulated as [48]:

$$P_e = \frac{1}{\pi}\int_0^{\frac{(M-1)\pi}{M}}\mathrm{M}_{\gamma_{nAP}}\left(-\frac{\sin^2\left(\frac{\pi}{M}\right)}{\sin^2\chi}\right)d\chi. \tag{6.16}$$

6.4.2 SEP of RIS AP scheme

In the AP scheme, only the channel magnitude β_k is considered, with a mean and variance given by (6.8.1) – (6.8.3). The mean and variance of B can be computed by applying the CLT assuming high values of N.

Hence, the statistics of B may be computed as:

$$\mu_{\mathrm{B}} = E[\mathrm{B}] = E\left[\sum_{k=1}^{N} \beta_k\right] \cong NE[\beta_k], \tag{6.17.1}$$

$$\sigma_{\mathrm{B}}^2 = Var(\mathrm{B}) = Var\left(\sum_{k=1}^{N} \beta_k\right) \cong NVar(\beta_k) = N\left(E\left[\beta_k^2\right] - (E[\beta_k])^2\right). \tag{6.17.2}$$

Based on the above, the final mean and variance of B can be computed as:

$$\mu_{\mathrm{B}} = N\mu, \tag{6.18.1}$$

$$\sigma_{\mathrm{B}}^2 = \ Var(\mathrm{B}) = N(\mathcal{M}_2 - \mu^2). \tag{6.18.2}$$

Having derived these statistics, it can be observed that γ_{AP} is a non-central chi-squared RV with one degree of freedom with an MGF as:

$$\mathrm{M}_{\gamma_{AP}}(x) = \frac{1}{\sqrt{1 - 2\rho\sigma_{\mathrm{B}}^2 x}} e^{\left(\frac{\mu_{\mathrm{B}}^2 \rho x}{1 - 2\sigma_{\mathrm{B}}^2 \rho x}\right)}. \tag{6.19}$$

Hence, the SEP of the RIS AP scheme is computed as [48]:

$$P_e = \frac{1}{\pi} \int_0^{\frac{(M-1)\pi}{M}} \mathrm{M}_{\gamma_{AP}}\left(-\frac{\sin^2\left(\frac{\pi}{M}\right)}{\sin^2 \chi}\right) d\chi. \tag{6.20}$$

6.5 RIS M-QAM AP scheme for low N

6.5.1 RIS M-QAM AP system model

The authors of [78], presented the ABEP analysis of the RIS M-QAM AP scheme for low numbers of reflective elements, assuming Rayleigh fading. They used a PDF-based approach to formulate the ABEP and demonstrated that the proposed ABEP matched well for a variety of N values.

Motivated by this, the ABEP analysis of the RIS M-QAM AP scheme for low numbers of reflective elements, assuming Rician fading, is presented.

In the system model, the transmission of an M-QAM symbol denoted by $x_q, q \in [1{:}M]$ is assumed, where M is the size of the QAM constellation with $E\left[\left|x_q\right|^2\right] = 1$. The scheme also utilizes an N-element RIS in the AP configuration, similar to Figure 6.3.1, under Rician fading with AWGN.

Based on this, the receive signal is given as:

$$r = \left(\sum_{k=1}^{N} h_k e^{j\theta_k} \right) x_q + n, \tag{6.21}$$

where $h_k = |h_k| e^{j\psi_k}$ represents the RV distributed as $CN(0, 1)$, with magnitude $|h_k|$ and phase ψ_k denoting the fading channel between the k-th RIS element and the receiver, $\theta_k = -\psi_k$ is the k-th intelligent phase shift of the k-th reflective element of the RIS, and $n \sim CN\left(0, \frac{1}{\rho}\right)$ denotes the AWGN, where ρ denotes the average SNR.

6.5.2 SEP of RIS M-QAM AP scheme

The CLT allows us to assume that the PDF of the sum of RVs given by $\mathrm{Z} = \sum_{k=1}^{N} |h_k|$ follows a Gaussian distribution, in other words, the CLT assumes:

$$\mathrm{E[Z]} = E\left[\sum_{k=1}^{N} |h_k| \right] \cong NE[|h_k|], \tag{6.22}$$

$$Var(Z) = Var\left(\sum_{k=1}^{N} |h_k| \right) \cong NVar(|h_k|). \tag{6.23}$$

This approach is documented in [48]. However, this approach fails when N is considerably low, as already observed in previous chapters. The PDF of the sum of RVs following a Rician distribution has been given in [133], such that the ABEP may be formulated for low N values.

The ABEP of the RIS M-QAM AP scheme is given as [78]:

$$P_e = \omega \int_0^{\infty} \left\{ Q\left(\sqrt{\xi x^2}\right) - aQ^2\left(\sqrt{\xi x^2}\right) \right\} f_{\mathrm{Z}}(x)\, dx, \tag{6.24}$$

where $\xi = \frac{3N\rho}{M-1}$, $a = 1 - \frac{1}{\sqrt{M}}$, $\omega = \frac{4a}{\log_2(M)}$ and $f_{\mathrm{Z}}(x)$ is the PDF given in [133] as:

$$f_{\mathrm{Z}}(x) = \frac{x^N}{c_2^2} \left(\frac{c_1}{c_2 b} \right)^{N-1} \exp\left[-\frac{1}{2} \left(\frac{x^2}{c_2^2} + \frac{b^2}{c_1^2} \right) \right] I_{N-1}\left(\frac{xb}{c_1 c_2} \right), \tag{6.25}$$

where $b = \sqrt{\frac{NK\Omega}{K+1}}$, where, as defined in Chapter 1, Section 1.1.2.2, K denotes the Rician K-factor, $I_z(r)$ denotes the MBF of the first kind given in (6.10), and c_1 and c_2 are constants derived using the interior-reflective Newton method depending on the corresponding values of K and N given in Table 6.5.2.1 [133].

Table 6.5.2.1: Table of Coefficients for Approximation of Rician PDF [133]

N	$K = 1\text{dB}$		$K = 3\text{dB}$		$K = 5\text{dB}$		$K = 7\text{dB}$	
	c_1	c_2	c_1	c_2	c_1	c_2	c_1	c_2
2	0.5194	0.4746	0.4395	0.4131	0.3657	0.3509	0.2992	0.2914
3	0.5411	0.4770	0.4518	0.4150	0.3726	0.3524	0.3027	0.2922
4	0.5507	0.4772	0.4580	0.4157	0.3761	0.3530	0.3048	0.2928
5	0.5589	0.4783	0.4621	0.4165	0.3782	0.3534	0.3058	0.2931
6	0.5634	0.4786	0.4646	0.4168	0.3796	0.3537	0.3066	0.2933
7	0.5675	0.4791	0.4668	0.4172	0.3806	0.3539	0.3073	0.2935
8	0.5699	0.4793	0.4680	0.4173	0.3815	0.3541	0.3076	0.2936

The well-known Q-function approximations $Q(u) \cong \frac{1}{12}e^{-\frac{u^2}{2}} + \frac{1}{4}e^{-\frac{2u^2}{3}}$ and $Q^2(u) \cong \frac{1}{8}e^{-u^2}$ are employed to rewrite (6.25) as:

$$P_e \approx \omega \int_0^\infty \left\{\frac{1}{12}e^{-\frac{\xi x^2}{2}} + \frac{1}{4}e^{-\frac{2\xi x^2}{3}} - \frac{a}{8}e^{-\xi x^2}\right\}\left(\frac{x^N}{c_2^2}\left(\frac{c_1}{c_2 b}\right)^{N-1} \exp\left[-\frac{1}{2}\left(\frac{x^2}{c_2^2} + \frac{b^2}{c_1^2}\right)\right] I_{N-1}\left(\frac{xb}{c_1 c_2}\right)\right) dx, \tag{6.26}$$

which simplifies to:

$$P_e \approx L\left(\beta_{11}^{-N}\Omega\left(\frac{A}{2\sqrt{\beta_{11}}}\right) + 3\beta_{12}^{-N}\Omega\left(\frac{A}{2\sqrt{\beta_{12}}}\right) - \frac{3a}{2}\beta_{13}^{-N}\Omega\left(\frac{A}{2\sqrt{\beta_{13}}}\right)\right), \tag{6.27}$$

where $L = \frac{\omega}{24c_2^2}\left(\frac{c_1 A}{2c_2 b}\right)^{N-1} \exp\left(-\frac{b^2}{2c_1^2}\right)$, $A = \frac{b}{c_1 c_2}$, $\beta_{11} = \frac{1}{2}\left(\xi + \frac{1}{c_2^2}\right)$, $\beta_{12} = \left(\frac{2}{3}\xi + \frac{1}{2c_2^2}\right)$, $\beta_{13} = \left(\xi + \frac{1}{2c_2^2}\right)$ and $\Omega(x) = \sum_{k=0}^{\infty}\frac{x^{2k}}{k!}$.

The full derivation of (6.27) may be found in Appendix G.

6.6 Numerical Results

In this section, the EP of the RIS non-AP and AP schemes is investigated under slow frequency-flat Rician fading channels in the form of SER/BER vs SNR graphs. The theoretical graphs are also provided to validate the tightness between the simulation and analytical results. For the RIS-non-AP scheme, M-QAM data is assumed to be transmitted, whereas for the RIS-AP scheme, M-PSK data is transmitted. Therefore, all theoretical results are based on (6.15), (6.20) and (6.27).

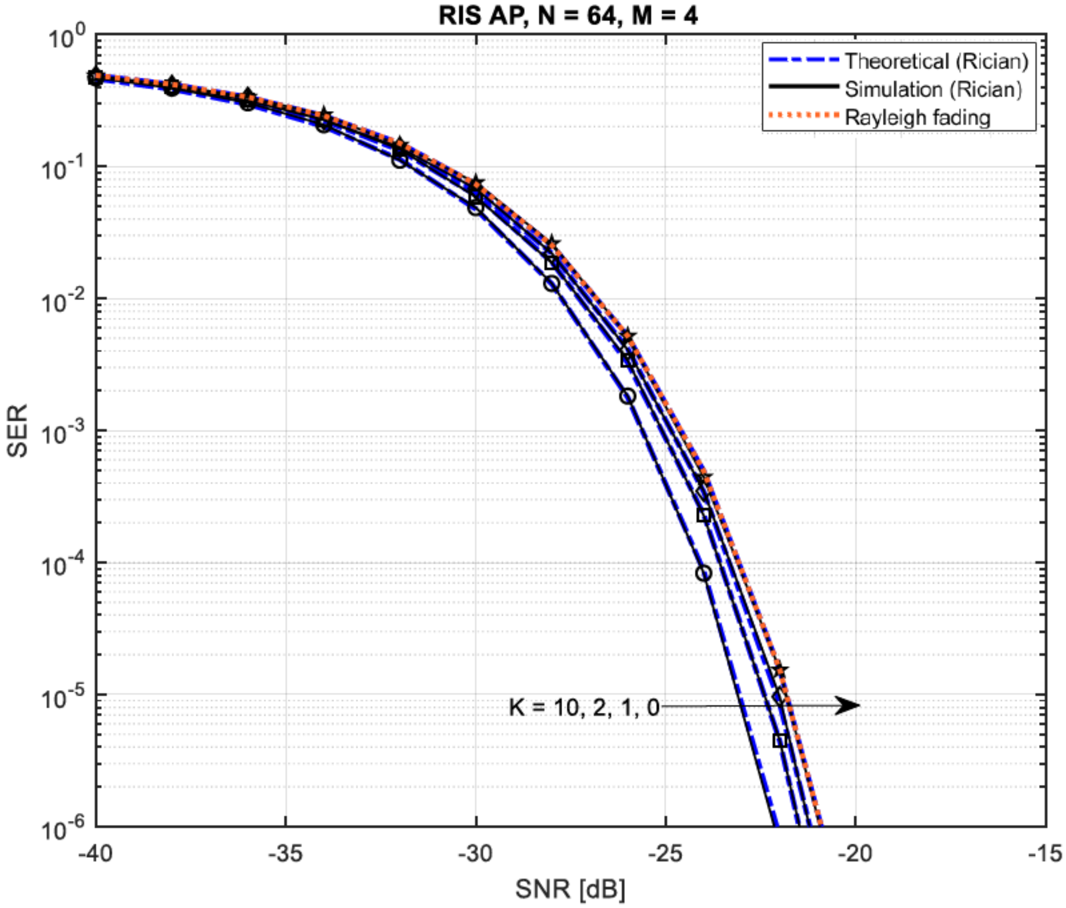

Figure 6.6.1: SER vs SNR graphs of the RIS AP scheme, $M = 4, N = 64$, varying K

Figure 6.6.1 shows the EP of the RIS AP scheme for $M = 4, N = 64$ and varying $K \in \{0, 1, 2, 10\}$. The curve of the RIS AP under Rayleigh fading is also shown to observe that for $K = 0$, the fading channel is equivalent to a Rayleigh fading channel, as already seen in Chapter 2. It is observed that as K increases, the EP improves, as there is a greater degree of LOS. The setting $K = 0$ (Rayleigh fading) produces the worst EP as the path becomes a NLOS.

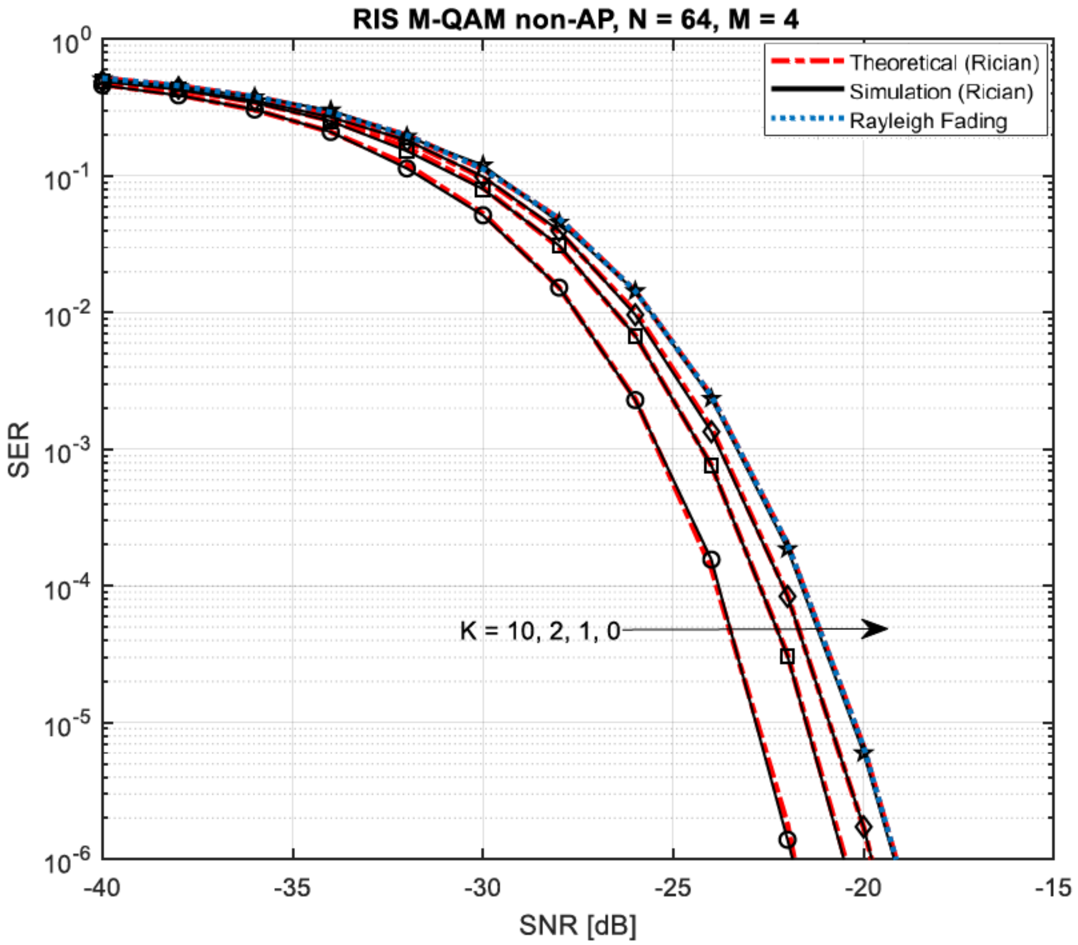

Figure 6.6.2: SER vs SNR graphs of the RIS M-QAM non-AP scheme, $N = 64, M = 4$, varying K

Figure 6.6.2 shows the EP of the RIS non-AP scheme for $M = 4$, $N = 64$ and varying $K \in \{0, 1, 2, 10\}$. Similar to Figure 6.6.1, the curve for the RIS non-AP scheme under Rayleigh fading is shown to match the curve for Rician fading at $K = 0$. It is observed that there is a much greater improvement in EP when increasing K for the non-AP scheme than in the AP scheme. When comparing Figure 6.6.1 with Figure 6.6.2, it is also observed that the AP scheme performs better than the non-AP scheme when there is a very low degree of LOS, in other words, for low K. This demonstrates that the non-AP scheme produces better EPs at higher degrees of LOS.

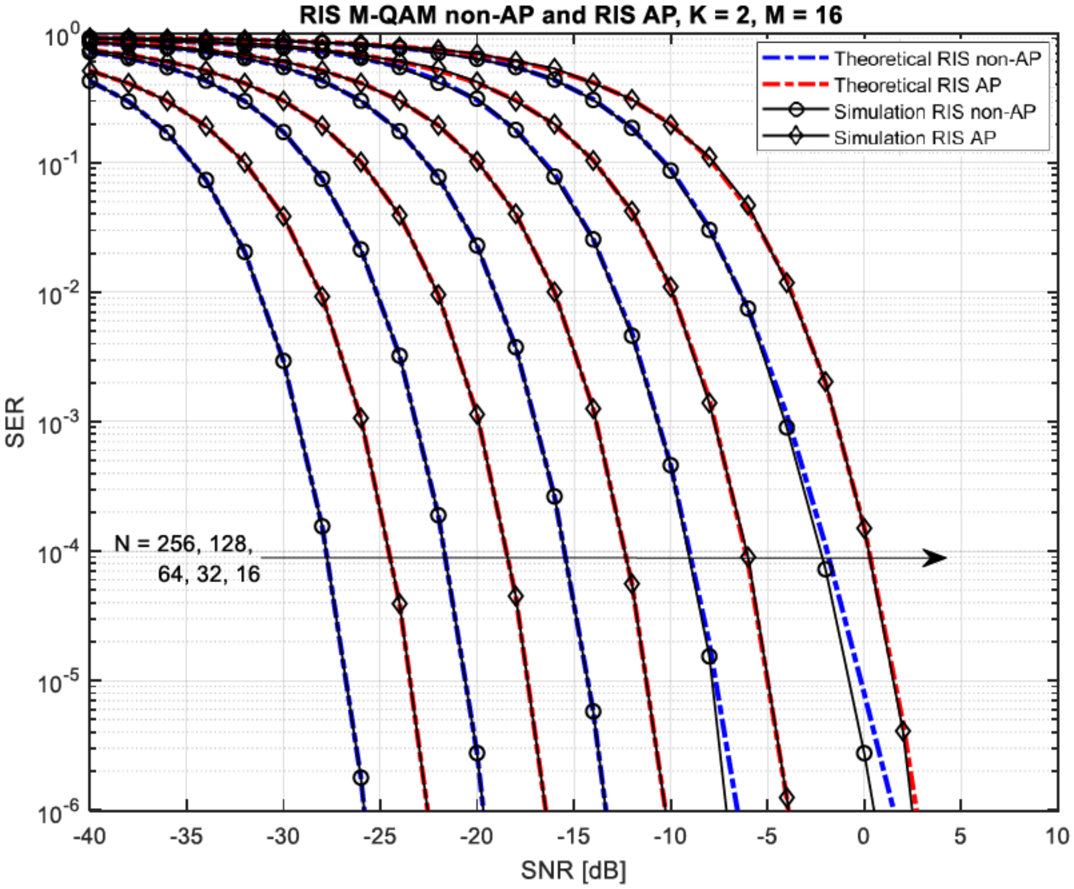

Figure 6.6.3: SER vs SNR graphs of the RIS M-QAM non-AP and RIS AP schemes, $K = 2, N = 64$*, varying* N

Figure 6.6.3 shows the EP of the RIS M-QAM non-AP and RIS AP schemes for $M = 16, K = 2$, and varying $N \in \{16, 32, 64, 128, 256\}$. It can be observed that when doubling the reflective elements for each scheme, the EP improves by 6-7dB. It is also observed that for the non-AP scheme, the theoretical and simulation graphs match for $N \in \{64, 128, 256\}$, but not for $N \in \{16, 32\}$. This is due to the CLT being assumed for high N, hence for high N, the theoretical and simulation graphs match, but for lower N, error floors form as shown. This is expected, as it has been observed in Chapter 2 already. However, this phenomenon is not as prominent in the RIS AP scheme, with the theoretical and simulation graphs matching for $N \in \{32, 64, 128, 256\}$, and only a very small error floor at $N = 16$.

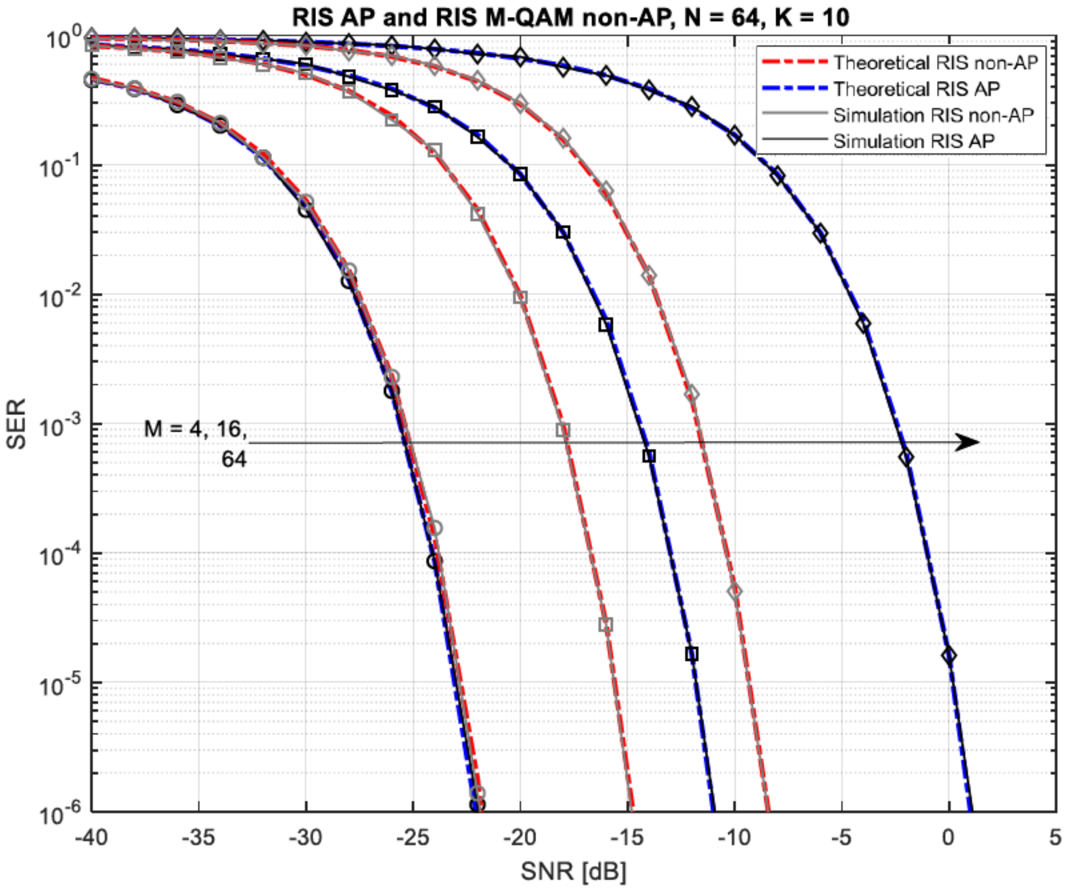

Figure 6.6.4: SER vs SNR graphs of the RIS M-QAM non-AP and RIS AP schemes, $K = 10, N = 64$, varying M

Figure 6.6.4 shows the EP of the RIS non-AP and RIS AP schemes for $K = 10$, $N = 64$ and varying $M \in \{4, 16, 64\}$. It is observed that for the RIS non-AP system, a change of 7.5dB is seen as M increases, whereas for the RIS AP scheme, a change of 12dB is seen, indicating a greater deterioration in EP in the RIS AP scheme compared to the RIS non-AP scheme. This is due to the greater SNR loss for M-PSK transmission over M-QAM transmission.

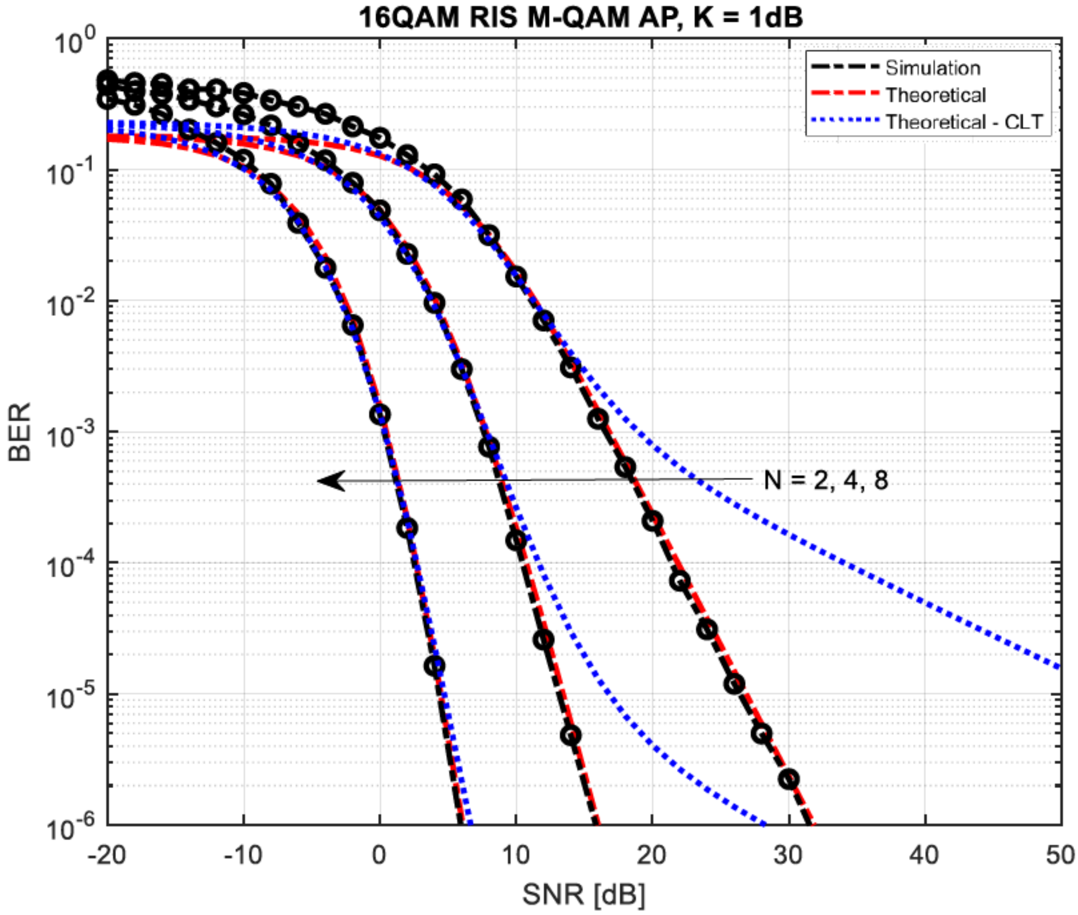

Figure 6.6.5: BER vs SNR graphs of the RIS M-QAM AP scheme, $K = 1dB, M = 16$, varying N

Figure 6.6.5 shows the EP of the RIS M-QAM AP scheme for $K = 1$dB, $M = 16$ and varying $N \in \{2, 4, 8\}$. It is observed that the theoretical result given in (6.27) produces a tight fit with the simulation graphs. It can also be observed that there is a great difference between the CLT approach and the exact ABEP for low N, with large error floors for $N = 2$ and 4 and a small error floor for $N = 8$, which further demonstrates the accuracy and the necessity of the PDF-based approach for low N. For $N = 2, 4$ and 8, SNRs of 31dB, 16dB and 5dB are seen, respectively.

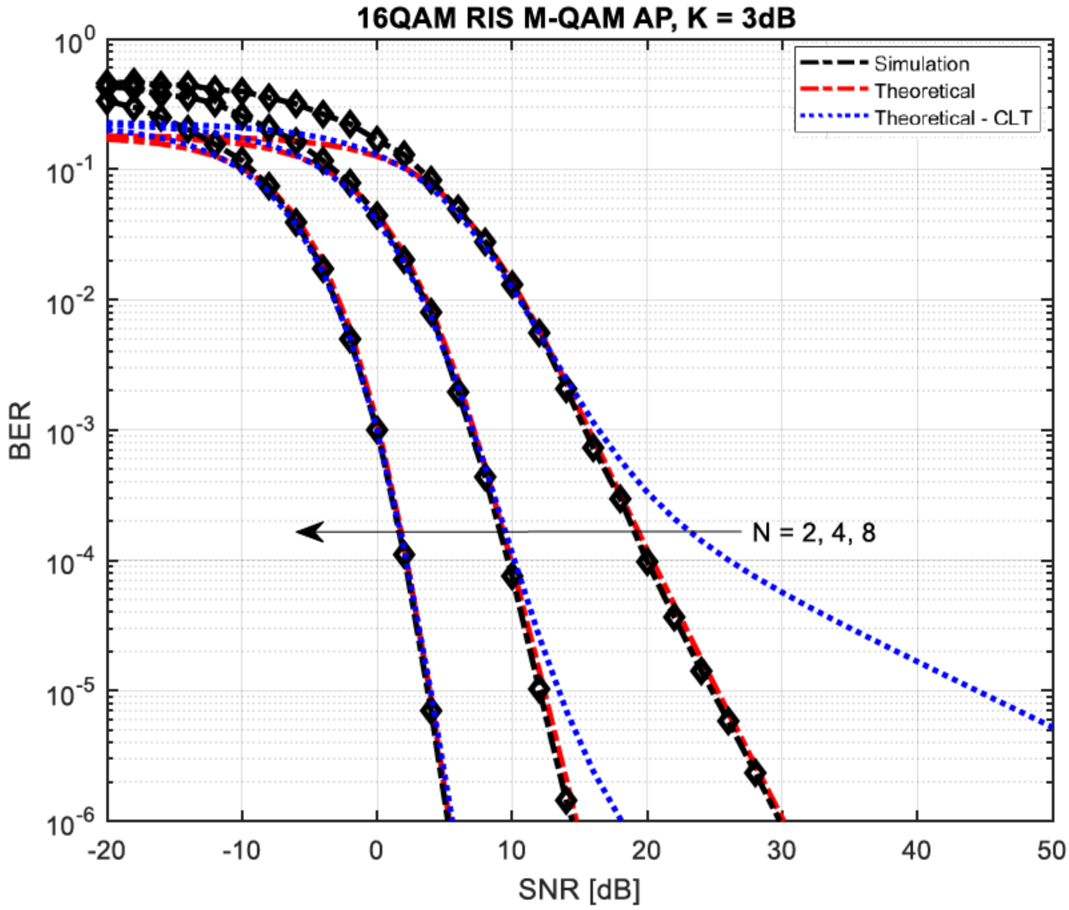

Figure 6.6.6: BER vs SNR graphs of the RIS M-QAM AP scheme, $K = 3\text{dB}, M = 16$, varying N

Figure 6.6.6 shows the EP of the RIS M-QAM AP scheme for $K = 3\text{dB}$, $M = 16$ and varying $N \in \{2, 4, 8\}$. Similar observations in Figure 6.6.5 may be seen in Figure 6.6.6, with large error floors forming for $N = 2$ and 4. However, it is observed that for $N = 8$, the CLT theoretical result closely matches the PDF-based result. When comparing the same case in Figure 6.6.5, it suggests that for increasing K, the CLT matches the PDF-based ABEP for an appropriately-sized N. Here, SNRs of $30\text{dB}, 14\text{dB}$ and 4.5dB for $N = 2, 4$ and 8, respectively, are observed.

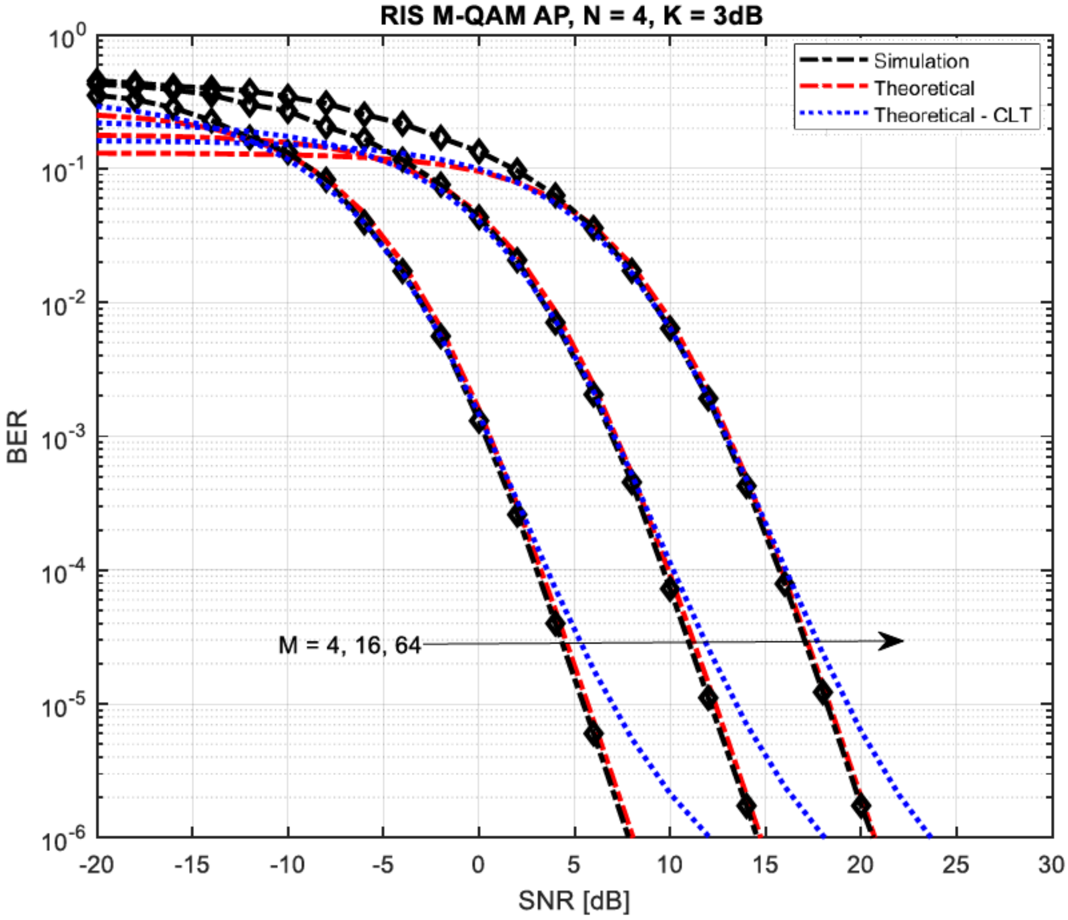

Figure 6.6.7: BER vs SNR graphs of the RIS M-QAM AP scheme, $K = 3$dB, $N = 4$, varying M

Figure 6.6.7 shows the EP of the RIS M-QAM AP scheme for $K = 3$dB, $\mathrm{N} = 4$ and varying $M \in \{4, 16, 64\}$. It is observed that the PDF-based theoretical result fits tightly with the simulation results, as opposed to the CLT approach which produces sizeable error floors. It is also observed that increasing the modulation order deteriorates the EP by 7.5dB per M value.

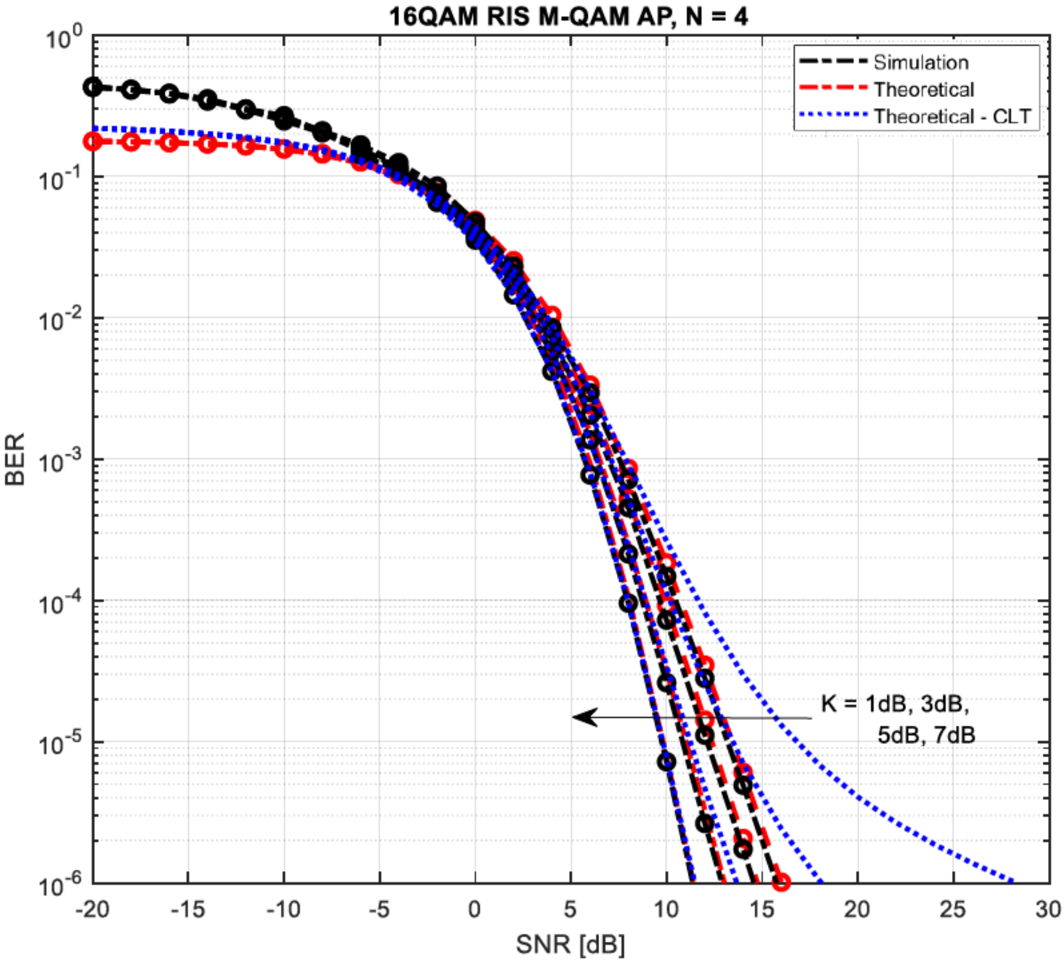

Figure 6.6.8: BER vs SNR graphs of the RIS M-QAM AP scheme, $N = 4, M = 16$, varying K

Figure 6.6.8 shows the EP of the RIS M-QAM AP scheme for $M = 16, \mathrm{N} = 4$ and varying $K \in \{1, 3, 5, 7\}$ dB. It is observed that increasing K produces an improvement of 1.4dB. It is also observed that for increasing K, the CLT tends towards the PDF-based theoretical curve, which confirms our earlier observation that for high K, the CLT theoretical result matches the PDF-based theoretical result.

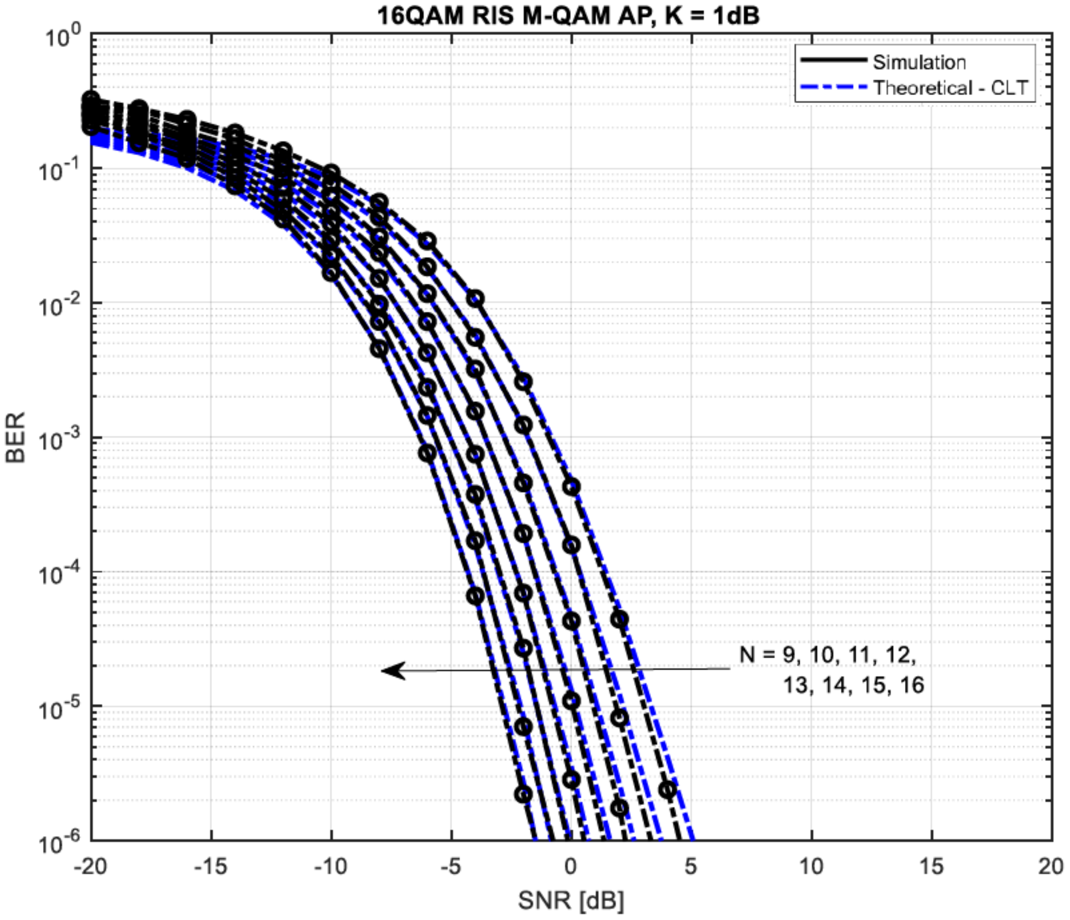

Figure 6.6.9: BER vs SNR graphs of the RIS M-QAM AP scheme - CLT analysis

Figure 6.6.9 shows the EP of the RIS M-QAM AP scheme for $K = 1\text{dB}, \text{M} = 16$ and varying $N \in \{9{:}\,16\}$. It is observed that the extent of the usefulness of the CLT result lies within the range of N values $N \in \{13{:}\,16\}$, and the accuracy begins to drop off at $N = 11$ and 12. A drawback of the PDF-based approach given in (6.28) is that it is only defined for specific N values, hence this comparison sheds some light on exactly which values the CLT does not work for, such that future research may fill in the research and analysis gaps found in this study.

Chapter Summary

In this chapter, the system models of the RIS non-AP and RIS AP schemes in Rician fading channels were presented, and the performance analysis of each scheme was described. Additionally, the system model of the RIS M-QAM AP scheme in Rician fading channels for low values of N was presented, and the formulation of the ABEP of the scheme was also provided. Simulation results in the form of SER vs SNR graphs were provided for the RIS non-AP and RIS AP scheme, and BER vs SNR graphs were presented for the RIS M-QAM AP scheme, and observations are drawn based on the results. for the RIS non-AP and RIS AP schemes, the theoretical framework has been shown to fit tightly with the simulation graphs for high values of N, with error floors present for low values of N, which was similarly observed in Chapter 2. It was also observed that for increasing K, a greater improvement in EP is seen in the RIS non-AP scheme in comparison to the RIS AP scheme, suggesting that the RIS non-AP scheme may outperform the RIS AP scheme if the degree of LOS is high enough. For the RIS M-QAM AP scheme, it was observed that the theoretical framework fits tightly with simulation results for low values of N. However, a weakness of the PDF derived is that it only works for specific vales of K and N. More work needs to be done to derive a closed form of the Rician distribution such that the approximated PDF may be applied for general values of K and N.

7 CONCLUSION

In this dissertation, RISs-aided schemes were investigated from an EP and SE perspective. The conventional RIS schemes were covered in both Rayleigh and Rician fading channels, and the mathematical frameworks of the SEPs and ABEPs of the respective schemes were derived. Simulation results have been provided to validate the system models and theoretical results of the RIS schemes, as well as evaluate the impact of the LOS component in RIS-aided systems. Then, an analysis was provided of the RIS-aided KCS GC modulation scheme and its ABEP, and simulation results were provided to validate these results. The concept of HRM was discussed, and simulation results were provided to justify the study of this concept with respect to EP, achievable rate and EE. Further, novel HRM-aided schemes were investigated to improve upon the EP and SE of conventional RIS-aided schemes, and their ABEP expressions derived and documented in this dissertation. Simulation results were provided to evaluate the improvements in EP and SE over existing schemes and validate the theoretical results.

Some of the challenges/future research directions in this work are as follows. Firstly, the HRM schemes were investigated for high values of N. However, the investigation of the schemes for low N is necessary, as deployment is theoretically easier and more practical than considering very large RISs. Hence, the derivation and formulation of the ABEPs of the HRM-aided schemes assuming low N is required for future work. Secondly, when considering the RIS M-QAM AP scheme under Rician fading, it would be useful to derive a general PDF-based ABEP expression for all N values, as the PDF used only considers a finite series of RVs for specific values of K. Thirdly, considering the potential of the RIS-aided KCS GC modulation scheme to provide significant EP gains at high SEs, it would be of interest to integrate the HRM concept with this scheme. It is envisioned that the computational complexity will be very high in this case, so a novel low complexity detection scheme may be required to lower the computational complexity of this scheme.

Future work includes the following.

1. The consideration of the RIS-aided and HRM-aided schemes in other types of fading channels, for example, Nakagami-m or Nakagami-q fading.
2. The EP of the RIS schemes assuming partial CSI or absence of CSI may be investigated.
3. In all scenarios, a perfect RIS is assumed. It is worth investigating the EP assuming an imperfect RIS.
4. An investigation into the EP considering discrete phase shifts of the reflective elements of the RISs is an interesting research direction, where the phases of the reflective elements are quantised to satisfy practical hardware requirements.
5. The exploration of multiple-antenna nodes in the documented RIS schemes.
6. The effect of hardware impairments on the EP of RIS-aided schemes may be explored.

The EP gains of the HRM schemes are summarized in Table 7.1.

Table 7.1: Table summarizing EP gains of HRM schemes over conventional schemes

EP gains of HRM schemes over conventional schemes at BER = 10^{-6}						
Schemes:	RIS non-AP		RIS AP		HRM	
	4 bits/s/Hz	8 bits/s/Hz	4 bits/s/Hz	8 bits/s/Hz	4 bits/s/Hz	8 bits/s/Hz
HRM non-AP	12dBm	12dBm	–	–	12dBm	57dBm
HRM AP	–	–	11dBm	13dBm	72dBm	116dBm

The key findings of Chapter 6, the study of RIS-aided systems in Rician fading channels, are summarised as follows:

1. In Figures 6.6.1 and 6.6.2, it was observed that the RIS non-AP scheme showed greater improvements in EP as K increased in comparison to the RIS AP scheme. This may suggest that if K is large enough, the RIS non-AP scheme may produce the same EP as the RIS AP scheme.
2. In Figure 6.6.3, it was observed that for the RIS non-AP scheme, applying the CLT approximation assuming high N yielded accurate SEP results in a range of $N = \{64, 128, 256\}$, whereas error floors form in the range $N = \{16, 32\}$. For the RIS AP scheme, this was accurate for $N = \{32, 64, 128, 256\}$, and a very small error floor was present at $N = 16$. This demonstrated the CLT approximation is far more accurate for the RIS AP scheme than the RIS non-AP scheme.
3. In Figures 6.6.5 – 6.6.8, it was observed that the PDF approximation given in [133] proved to be accurate for low values of N in comparison to the CLT method for $N = \{2, 4, 8\}, M = \{4, 16, 64\}$ and $K = \{1, 3, 5, 7\}$ dB. However, a limitation observed in the PDF is that it was only accurate for particular values of N and K. More work would need to be done to derive a closed-form Rician distribution to generate accurate results for arbitrary N and K values.
4. In Figure 6.6.9, it was observed that the CLT approximation was viable for $N \geq 13$. Therefore, it may be useful if the work performed in [133] may be extended to approximate the Rician PDF for $N = [9{:}12]$, as the PDF in [133] has only been derived for $N = [2{:}8]$ as shown in Table 6.5.2.1.
5. Considering the observations made in Figures 6.6.1 and 6.6.2, it may be of use to investigate the EP of the RIS non-AP scheme in Rician fading channels assuming low N.

REFERENCES

[1] L. J. Vora, "Evolution of mobile generation technology: 1G to 5G and review of upcoming wireless technology 5G," *International Journal of Modern Trends in Engineering and Research,* vol. 2, no. 10, pp. 281-290, 2015.

[2] J. A. d. Peral-Rosado, R. Raulefs, J. A. López-Salcedo and G. Seco-Granados, "Survey of Cellular Mobile Radio Localization," *IEEE Communications Surveys & Tutorials,* vol. 20, no. 2, pp. 1124 - 1148, 2018.

[3] A. U. Gawas, "An Overview on Evolution of Mobile Wireless Communication Networks: 1G-6G," *International Journal on Recent and Innovation Trends in Computing and Communication,* vol. 3, no. 5, p. 3130 – 3133, 2015.

[4] A. A. A. Solyman and K. Yahya, "Evolution of wireless communication networks: from 1G to 6G and future perspective," *International Journal of Electrical and Computer Engineering (IJECE),* vol. 12, no. 4, pp. 3943-3950, 2022.

[5] H. Mehta, D. Patel, B. Joshi and H. Modi, "0G to 5G Mobile Technology: A Survey," *Journal of Basic and Applied Engineering Research,* vol. 1, no. 6, pp. 56-60, 2014.

[6] L. Yi, K. Miao and A. Liu, "A comparative study of WiMAX and LTE as the next generation mobile enterprise network," in *13th International Conference on Advanced Communication Technology (ICACT),* Gangwon, Korea (South), 2011.

[7] S. Chen, Y.-C. Liang, S. Sun, S. Kang, W. Cheng and M. Peng, "Vision, Requirements, and Technology Trend of 6G: How to Tackle the Challenges of System Coverage, Capacity, User Data-Rate and Movement Speed," *IEEE Wireless Communications,* vol. 27, no. 2, pp. 218 - 228, 2020.

[8] R. Y. Mesleh, H. Haas, S. Sinanovic, C. W. Ahn and S. Yun, "Spatial Modulation," *IEEE Transactions on Vehicular Technology,* vol. 57, no. 4, pp. 2228 - 2241, 2008.

[9] A. K. Khandani, "Media-based modulation: A new approach to wireless transmission," in *2013 IEEE International Symposium on Information Theory,* Istanbul, Turkey, 2013.

[10] J.-C. Belfiore, G. Rekaya and E. Viterbo, "The golden code: a 2 x 2 full-rate space-time code with non-vanishing determinants," in *International Symposium on Information Theory, 2004. ISIT 2004. Proceedings.*, Chicago, IL, USA, 2004.

[11] W. Cheng, W. Zhang, H. Jing, S. Gao and H. Zhang, "Orbital Angular Momentum for Wireless Communications," *IEEE Wireless Communications,* vol. 26, no. 1, pp. 100 - 107, 2019.

[12] A. b. Idris, R. F. b. Rahim and D. b. M. Ali, "The Effect of Additive White Gaussian Noise and Multipath Rayleigh Fading On BER Statistic in Digital Cellular Network," in *2006 International RF and Microwave Conference,* Putra Jaya, Malaysia, 2006.

[13] A. Goldsmith, Wireless Communications, New York: Cambridge University Press, 2005.

[14] R. T. Tsvaki, "Double Spaced Media Based Modulation," *ResearchSpace,* 2019. [Online]. Available: https://researchspace.ukzn.ac.za/handle/10413/18856.

[15] J. G. Proakis and M. Salehi, Digital Communications, 5th ed., vol. 95, New York: McGraw-Hill, 2005.

[16] E. Basar, M. D. Renzo, J. D. Rosny, M. Debbah, M.-S. Alouini and R. Zhang, "Wireless Communications Through Reconfigurable Intelligent Surfaces," *IEEE Access*, vol. 7, pp. 116753-116773, 2019.

[17] M. A. ElMossallamy, H. Zhang, L. Song, K. G. Seddik, Z. Han and G. Y. Li, "Reconfigurable Intelligent Surfaces for Wireless Communications: Principles, Challenges, and Opportunities," *IEEE Transactions on Cognitive Communications and Networking*, vol. 6, no. 3, pp. 990 - 1002, 2020.

[18] Y. Liu, X. Liu, X. Mu, T. Hou, J. Xu, M. D. Renzo and N. Al-Dhahir, "Reconfigurable Intelligent Surfaces: Principles and Opportunities," *IEEE Communications Surveys & Tutorials (Volume: 23, Issue: 3, thirdquarter 2021)*, vol. 23, no. 3, pp. 1546 - 1577, 2021.

[19] S. V. Hum and J. Perruisseau-Carrier, "Reconfigurable Reflectarrays and Array Lenses for Dynamic Antenna Beam Control: A Review," *IEEE Transactions on Antennas and Propagation*, vol. 62, no. 1, pp. 183 - 198, 2014.

[20] V. Arun and H. Balakrishnan, "RFocus: Practical beamforming for Small Devices," *arXiv:1905.05130*, 2019. [Online]. Available: https://www.arxiv.org/abs/1905.05130.

[21] H.-T. Chen, A. J. Taylor and N. Yu, "A review of metasurfaces: physics and applications," *Reports on Progress in Physics*, vol. 79, no. 7, 2016.

[22] F. Liu, O. Tsilipakos, A. Pitilakis, A. C. Tasolamprou, M. S. Mirmoosa, N. V. Kantartzis, D.-H. Kwon, J. Georgiou, K. Kossifos, M. A. Antoniades, M. Kafesaki, C. M. Soukoulis and S. A. Tretyakov, "Intelligent Metasurfaces with Continuously Tunable Local Surface Impedance for Multiple Reconfigurable Functions," *Phys. Rev. Applied*, vol. 11, no. 4, 2019.

[23] H. Lin, W. Yu, R. Tang, J. Jin, Y. Wang, J. Xiong, Y. Wu and J. Zhao, "A dual-band reconfigurable intelligent metasurface with beam steering," *Journal of Physics D: Applied Physics*, vol. 55, no. 24, pp. 1-9, 2022.

[24] C. Huang, A. Zappone, G. C. Alexandropoulos, M. Debbah and C. Yuen, "Reconfigurable Intelligent Surfaces for Energy Efficiency in Wireless Communication," *IEEE Transactions on Wireless Communications*, vol. 18, no. 8, pp. 4157-4170, 17 October 2019.

[25] Z. Yang, M. Chen, W. Saad, W. Xu, M. Shikh-Bahaei, H. V. Poor and S. Cui, "Energy-Efficient Wireless Communications With Distributed Reconfigurable Intelligent Surfaces," *IEEE Transactions on Wireless Communications*, vol. 21, no. 1, pp. 665 - 679, 2022.

[26] Y. Zhang, B. Di, H. Zhang, J. Lin, C. Xu, D. Zhang, Y. Li and L. Song, "Beyond Cell-Free MIMO: Energy Efficient Reconfigurable Intelligent Surface Aided Cell-Free MIMO Communications," *IEEE Transactions on Cognitive Communications and Networking*, vol. 7, no. 2, pp. 412 - 426, 2021.

[27] Z. Li, M. Chen, Z. Yang, J. Zhao, Y. Wang, J. Shi and C. Huang, "Energy Efficient Reconfigurable Intelligent Surface Enabled Mobile Edge Computing Networks with NOMA," *IEEE Transactions on Cognitive Communications and Networking*, vol. 7, no. 2, pp. 427 - 440, 2021.

[28] G. Lee, M. Jung, A. T. Z. Kasgari, W. Saad and M. Bennis, “Deep Reinforcement Learning for Energy-Efficient Networking with Reconfigurable Intelligent Surfaces,” in *ICC 2020 - 2020 IEEE International Conference on Communications (ICC)*, Dublin, Ireland, 2020.

[29] Y.-C. Liang, J. Chen, R. Long, Z.-Q. He, X. Lin, C. Huang, S. Liu, S. Shen and M. D. Renzo, “Reconfigurable Intelligent Surfaces for Smart Wireless Environments: Channel Estimation, System Design, and Applications in 6G Networks,” *Science China Information Sciences,* 64, 200301 (2021). https://doi.org/10.1007/s11432-020-3261-5.

[30] A. L. Swindlehurst, G. Zhou, R. Liu, C. Pan and M. Li, “Channel Estimation with Reconfigurable Intelligent,” *Proceedings of the IEEE,* vol. 110, no. 9, pp. 1312 - 1338, 2022.

[31] J. Chen, Y.-C. Liang, H. V. Cheng and W. Yu, “Channel Estimation for Reconfigurable Intelligent Surface Aided Multi-User mmWave MIMO Systems,” *arXiv:1912.03619,* 2023. [Online]. Available: https://www.arxiv.org/abs/1912.03619.

[32] C. Hu, L. Dai, S. Han and X. Wang, “Two-Timescale Channel Estimation for Reconfigurable Intelligent Surface Aided Wireless Communications,” *IEEE Transactions on Communications,* vol. 69, no. 11, pp. 7736 - 7747, 2021.

[33] H. Liu, X. Yuan and Y.-J. A. Zhang, “Matrix-Calibration-Based Cascaded Channel Estimation for Reconfigurable Intelligent Surface Assisted Multiuser MIMO,” *arXiv:1912.09025,* 2020. [Online]. Available: https://www.arxiv.org/abs/1912.09025.

[34] Y. Jin, J. Zhang, X. Zhang, H. Xiao, B. Ai and D. W. K. Ng, “Channel Estimation for Semi-Passive Reconfigurable Intelligent Surfaces With Enhanced Deep Residual Networks,” *IEEE Transactions on Vehicular Technology,* vol. 70, no. 10, pp. 11083 - 11088, 2021.

[35] N. K. Kundu and M. R. McKay, “Channel Estimation for Reconfigurable Intelligent Surface Aided MISO Communications: From LMMSE to Deep Learning Solutions,” *IEEE Open Journal of the Communications Society,* vol. 2, pp. 471 - 487, 2021.

[36] S. Ellingson, “Path Loss in Reconfigurable Intelligent Surface-Enabled Channels,” in *2021 IEEE 32nd Annual International Symposium on Personal, Indoor and Mobile Radio Communications (PIMRC)*, Helsinki, Finland, 2021.

[37] J. Jeong, J. H. Oh, S. Y. Lee, Y. Park and S.-H. Wi, “An Improved Path-Loss Model for Reconfigurable-Intelligent-Surface-Aided Wireless Communications and Experimental Validation,” *IEEE Access,* vol. 10, pp. 98065 - 98078, 2022.

[38] W. Tang, M. Z. Chen, X. Chen, J. Y. Dai, Y. Han, M. D. Renzo, Y. Zeng, S. Jin, Q. Cheng and T. J. Cui, “Wireless Communications with Reconfigurable Intelligent Surface: Path Loss Modeling and Experimental Measurement,” *arXiv:1911.05326,* 2020. [Online]. Available: https://www.arxiv.org/abs/1911.05326.

[39] W. Tang, X. Chen, M. Z. Chen, J. Y. Dai, Y. Han, M. D. Renzo, S. Jin, Q. Cheng and T. J. Cui, “Path Loss Modeling and Measurements for Reconfigurable Intelligent Surfaces in the Millimeter-Wave Frequency Band,” *IEEE Transactions on Communications,* vol. 70, no. 9, pp. 6259 - 6276, 2022.

[40] M. D. Renzo, F. H. Danufane, X. Xi, J. d. Rosny and S. Tretyakov, “Analytical Modeling of the Path-Loss for Reconfigurable Intelligent Surfaces – Anomalous Mirror or Scatterer?,” in *2020*

IEEE 21st International Workshop on Signal Processing Advances in Wireless Communications (SPAWC), Atlanta, GA, USA, 2020.

[41] F. H. Danufane, M. D. Renzo, J. d. Rosny and S. Tretyakov, “On the Path-Loss of Reconfigurable Intelligent Surfaces: An Approach Based on Green's Theorem Applied to Vector Fields,” *arXiv:2007.13158,* 2020. [Online]. Available: https://www.arxiv.org/abs/2007.13158.

[42] J. Zhang, H. Du, Q. Sun, B. Ai and D. W. K. Ng, “Physical Layer Security Enhancement With Reconfigurable Intelligent Surface-Aided Networks,” *arXiv:2012.00269,* 2021. [Online]. Available: https://www.arxiv.org/abs/2012.00269.

[43] H. Long, M. Chen, Z. Yang, B. Wang, Z. Li, X. Yun and M. Shikh-Bahaei, “Reflections in the Sky: Joint Trajectory and Passive Beamforming Design for Secure UAV Networks with Reconfigurable Intelligent Surface,” *arXiv:2005.10559,* 2020. [Online]. Available: https://www.arxiv.org/abs/2005.10559.

[44] S. Li, B. Duo, M. D. Renzo, M. Tao and X. Yuan, “Robust Secure UAV Communications With the Aid of Reconfigurable Intelligent Surfaces,” *IEEE Transactions on Wireless Communications,* vol. 20, no. 10, pp. 6402 - 6417, 2021.

[45] A. U. Makarfi, K. M. Rabie, O. Kaiwartya, X. Li and R. Kharel, “Physical Layer Security in Vehicular Networks with Reconfigurable Intelligent Surfaces,” in *2020 IEEE 91st Vehicular Technology Conference (VTC2020-Spring),* Antwerp, Belgium, 2020.

[46] A. U. Makarfi, K. M. Rabie, O. Kaiwartya, K. Adhikari, X. Li, M. Quiroz-Castellanos and R. Kharel, “Reconfigurable Intelligent Surfaces-Enabled Vehicular Networks: A Physical Layer Security Perspective,” *arXiv:2004.11288,* 2020. [Online]. Available: https://www.arxiv.org/abs/2004.11288.

[47] Z. Zhang, C. Zhang, C. Jiang, F. Jia, J. Ge and F. Gong, “Improving Physical Layer Security for Reconfigurable Intelligent Surface Aided NOMA 6G Networks,” *IEEE Transactions on Vehicular Technology,* vol. 70, no. 5, pp. 4451 - 4463, 2021.

[48] E. Basar, “Transmission Through Large Intelligent Surfaces: A New Frontier in Wireless Communications,” in *2019 European Conference on Networks and Communications (EuCNC),* Valencia, Spain, 2019.

[49] E. Basar, “Reconfigurable Intelligent Surface-Based Index Modulation: A New Beyond MIMO Paradigm for 6G,” *IEEE Transactions on Communications,* vol. 68, no. 5, pp. 3187 - 3196, 2020.

[50] Y. Yan, Y. Cao and T. Lv, “Enabling Media-Based Modulation for Reconfigurable Intelligent Surface Communications,” in *Wireless Communications and Networking Conference (WCNC),* Nanjing, China, 2021.

[51] S. Saini, V. S. Bhat and A. Chockalingam, “RIS-aided Media Based Modulation,” in *2023 IEEE 97th Vehicular Technology Conference (VTC2023-Spring),* Florence, Italy, 2023.

[52] B. A. Ozden, E. Aydin and F. Cogen, “Reconfigurable Intelligent Surface Aided Spatial Media-Based Modulation,” *arXiv:2211.07720,* 2022. [Online]. Available: https://arxiv.org/abs/2211.07720.

[53] T. Hou, Y. Liu, Z. Song, X. Sun, Y. Chen and L. Hanzo, “Reconfigurable Intelligent Surface Aided NOMA Networks,” *IEEE Journal on Selected Areas in Communications,* vol. 38, no. 11, pp. 2575 - 2588, 2020.

[54] N. Pillay and H. Xu, “Large intelligent surfaces: Random waypoint mobility and two-way relaying,” *Int J Commun Syst.,* 2020;33:e4505. https://doi.org/10.1002/dac.4505.

[55] S. Althunibat and R. Mesleh, “Performance analysis of quadrature spatial modulation in two-way relaying cooperative networks,” *IET Communications,* vol. 12, no. 4, pp. 466-472, 2018.

[56] S. E. Zegrar, L. Afeef and H. Arslan, “A General Framework for RIS-Aided mmWave Communication Networks: Channel Estimation and Mobile User Tracking,” *arXiv:2009.01180,* 2020. [Online]. Available: https://www.arxiv.org/abs/2009.01180.

[57] A. Khaleel and E. Basar, “Reconfigurable Intelligent Surface-Empowered MIMO Systems,” *IEEE Systems Journal,* vol. 15, no. 3, pp. 4358 - 4366, 2021.

[58] A. A. Puspitasari and B. M. Lee, “A Survey on Reinforcement Learning for Reconfigurable Intelligent Surfaces in Wireless Communications,” *Sensors,* 2023, 23, 2554. https://doi.org/10.3390/s23052554.

[59] S. Zhang, M. Li, M. Jian, Y. Zhao and F. Gao, “AIRIS: Artificial Intelligence Enhanced Signal Processing in Reconfigurable Intelligent Surface Communications,” *arXiv:2106.00171,* 2021. [Online]. Available: https://www.arxiv.org/abs/2106.00171.

[60] Z. Ding, L. Lv, F. Fang, O. A. Dobre, G. K. Karagiannidis, N. Al-Dhahir, R. Schober and H. V. Poor, “A State-of-the-Art Survey on Reconfigurable Intelligent Surface-Assisted Non-Orthogonal Multiple Access Networks,” *Proceedings of the IEEE,* vol. 110, no. 9, pp. 1358 - 1379, 2022.

[61] J. Zhao and Y. Liu, “A Survey of Intelligent Reflecting Surfaces (IRSs): Towards 6G Wireless Communication Networks,” *arXiv:1907.04789,* 2019. [Online]. Available: https://www.arxiv.org/abs/1907.04789.

[62] S. Hassouna, M. A. Jamshed, J. Rains, J. u. R. Kazim, M. U. Rehman, M. Abualhayja, L. Mohjazi, T. J. Cui, M. A. Imran and Q. H. Abbasi, “A survey on reconfigurable intelligent surfaces: Wireless communication perspective,” *IET Communications,* vol. 17, p. 497–537, 2023. https://doi.org/10.1049/cmu2.12571.

[63] R. Alghamdi, R. Alhadrami, D. Alhothali, H. Almorad, A. Faisal, S. Helal, R. Shalabi, R. Asfour, N. Hammad, A. Shams, N. Saeed, H. Dahrouj, T. Y. Al-Naffouri and M.-S. Alouini, “Intelligent Surfaces for 6G Wireless Networks: A Survey of Optimization and Performance Analysis Techniques,” *IEEE Access,* vol. 8, pp. 202795 - 202818, 2020.

[64] K. M. Faisal and W. Choi, “Machine Learning Approaches for Reconfigurable Intelligent Surfaces: A Survey,” *IEEE Access,* vol. 10, pp. 27343 - 27367, 2022.

[65] G. C. Alexandropoulos, K. Stylianopoulos, C. Huang, C. Yuen, M. Bennis and M. Debbah, “Pervasive Machine Learning for Smart Radio Environments Enabled by Reconfigurable Intelligent Surfaces,” *Proceedings of the IEEE,* vol. 110, no. 9, pp. 1494 - 1525, 2022.

[66] A. Almohamed, A. M. Tahir, A. Al-Kababji, H. M. Furqan, T. Khattab, M. O. Hasna and H. Arslan, “Smart and Secure Wireless Communications via Reflecting Intelligent Surfaces: A Short Survey,” *IEEE Open Journal of the Communications Society,* vol. 1, pp. 1442-1456, 2020.

[67] R. Chen, M. Liu, Y. Hui, N. Cheng and J. Li, “Reconfigurable Intelligent Surfaces for 6G IoT Wireless Positioning: A Contemporary Survey,” *IEEE Internet of Things Journal,* vol. 9, no. 23, pp. 23570 - 23582, 2022.

[68] M. Munochiveyi, A. C. Pogaku, D.-T. Do, A.-T. Le, M. Voznak and N. D. Nguyen, “Reconfigurable Intelligent Surface Aided Multi-User Communications: State-of-the-Art Techniques and Open Issues,” *IEEE Access,* vol. 9, pp. 118584 - 118605, 2021.

[69] T. Ma, Y. Xiao, X. Lei, L. Zhang, Y. Niu and G. K. Karagiannidis, “Reconfigurable Intelligent Surface-Assisted Localization: Technologies, Challenges, and the Road Ahead,” *IEEE Open Journal of the Communications Society,* vol. 4, pp. 1430 - 1451, 2023.

[70] S. Kisseleff, S. Chatzinotas and B. Ottersten, “Reconfigurable Intelligent Surfaces in Challenging Environments: Underwater, Underground, Industrial and Disaster,” *IEEE Access,* vol. 9, pp. 150214 - 150233, 2021.

[71] M. Dajer, Z. Ma, L. Piazzi, N. Prasad, X.-F. Qi, B. Sheen, J. Yang and G. Yue, “Reconfigurable intelligent surface: design the channel – a new opportunity for future wireless networks,” *Digital Communications and Networks,* vol. 8, p. 87–104, 2022.

[72] G. C. Alexandropoulos, N. Shlezinger and P. d. Hougne, “Reconfigurable Intelligent Surfaces for Rich Scattering Wireless Communications: Recent Experiments, Challenges, and Opportunities,” *IEEE Communications Magazine,* vol. 59, no. 6, pp. 28 - 34, 2021.

[73] A. Habib, A. E. Falou, C. Langlais and M. Berbineau, “Reconfigurable Intelligent Surface Assisted Railway Communications: A survey,” in *2023 IEEE 97th Vehicular Technology Conference (VTC2023-Spring),* Florence, Italy, 2023.

[74] S. Balgabay, S. Arzykulov and G. Nauryzbayev, “Semi-Passive Reconfigurable Intelligent Surfaces Enabled Communications: A Comprehensive Survey,” *TechRxiv. Preprint.,* 2022. https://doi.org/10.36227/techrxiv.19904335.v1.

[75] V. Tapio, I. Hemadeh, A. Mourad, A. Shojaeifard and M. Juntti, “Survey on reconfgurable intelligent surfaces below 10 GHz,” *Journal on Wireless Communications and Networking,* vol. 1, pp. 1-18, 2021.

[76] A. S. Abdalla, T. F. Rahman and V. Marojevic, “UAVs with Reconfigurable Intelligent Surfaces: Applications, Challenges, and Opportunities,” *arXiv:2012.04775* , 2020. [Online]. Available: https://www.arxiv.org/abs/2012.04775.

[77] R. Long, Y.-C. Liang, Y. Pei and E. G. Larsson, “Active Reconfigurable Intelligent Surface-Aided Wireless Communications,” *IEEE Transactions on Wireless Communications,* vol. 20, no. 8, pp. 4962 - 4975, 2021.

[78] N. Pillay and H. Xu, “Reconfigurable Intelligent Surface-aided Single-Input Single-Output K-Complex Symbol Golden Codeword-based Modulation,” *IEEE Access,* vol. 9, pp. 71849 - 71855, 2021.

[79] Z. Yigit, E. Basar, M. Wen and I. Altunbas, “Hybrid Reflection Modulation,” *IEEE Transactions on Wireless Communications,* vol. 22, no. 6, pp. 4106 - 4116, 2023.

[80] Z. Zhang, L. Dai, X. Chen, C. Liu, F. Yang, R. Schobar and H. V. Poor, “Active RIS vs. Passive RIS: Which Will Prevail in 6G?,” *IEEE Transactions on Communications,* vol. 71, no. 3, pp. 1707 - 1725, 2023.

[81] W. Lyu, Y. Xiu, S. Yang, C. Yuen and Z. Zhang, “Energy-Efficient Cell-Free Network Assisted by Hybrid RISs,” *IEEE Wireless Communications Letters,* vol. 12, no. 4, pp. 718 - 722, 2023.

[82] N. T. Nguyen, J. He, V.-D. Nguyen, H. Wymeersch, D. W. K. Ng, R. Schober, S. Chatzinotas and M. Juntti, “Hybrid Relay-Reflecting Intelligent Surface-Aided Wireless Communications: Opportunities, Challenges, and Future Perspectives,” *arXiv:2104.02039,* 2021. [Online]. Available: https://www.arxiv.org/abs/2104.02039.

[83] N. T. Nguyen, V.-D. Nguyen, Q. Wu, A. Totti, S. Chatzinotas and M. Juntti, “Hybrid Active-Passive Reconfigurable Intelligent Surface-Assisted Multi-User MISO Systems,” in *2022 IEEE 23rd International Workshop on Signal Processing Advances in Wireless Communication (SPAWC),* Oulu, Finland, 2022.

[84] S. Zeng, H. Zhang, B. Di, Y. Tan, Z. Han, H. V. Poor and L. Son, “Reconfigurable Intelligent Surfaces in 6G: Reflective, Transmissive, or Both?,” *IEEE Communication Letters,* vol. 25, no. 6, pp. 2063 - 2067, 2021.

[85] C. Singh and C. H. Lin, “Reconfigurable Intelligent Surfaces Aided Communication: Capacity and Performance Analysis Over Rician Fading Channel,” *arXiv:2107.10937,* 2021. [Online]. Available: https://www.arxiv.org/abs/2107.10937.

[86] A. M. Salhab and M. H. Samuh, “Accurate Performance Analysis of Reconfigurable Intelligent Surfaces over Rician Fading Channels,” *IEEE Wireless Communications Letters,* vol. 10, no. 5, pp. 1051-1055, 2021.

[87] L. Subrt and P. Pechac, “Controlling propagation environments using Intelligent Walls,” in *Proc. 2012 6th European Conf. Antennas Propag.(EUCAP),* Prague, Czech Republic, 2012.

[88] X. Tan, Z. Sun, J. M. Jornet and D. Pados, “Increasing Indoor Spectrum Sharing Capacity using Smart Reflect-Array,” in *Proc. 2016 IEEE Int. Conf. Commun. (ICC),* Kuala Lumpur, Malaysia, 2016.

[89] S. Hu, F. Rusek and O. Edfors, “Beyond Massive-MIMO: The Potential of Data-Transmission with Large Intelligent Surfaces,” *IEEE Transactions on Signal Processing,* vol. 66, no. 10, p. 2746–2758, 2018.

[90] S. Hu, F. Rusek and O. Edfors, “Beyond Massive-MIMO: The Potential of Positioning with Large Intelligent Surfaces,” *IEEE Transactions on Signal Processing,* vol. 66, no. 7, p. 1761–1774, 19 May 2018.

[91] M. Jung, W. Saad, Y. Jang, G. Kong and S. Choi, “Performance Analysis of Large Intelligent Surfaces (LISs): Asymptotic Data Rate and Channel Hardening Effects,” *IEEE Transactions on Wireless Communications,* vol. 19, no. 3, pp. 2052 - 2065, 26 December 2020.

[92] M. Jung, W. Saad and G. Kong, "Performance Analysis of Active Large Intelligent Surfaces (LISs): Uplink SE and Pilot Training," *IEEE Transactions on Communications,* vol. 69, no. 5, pp. 3379 - 3394, 31 March 2021.

[93] M. Jung, W. Saad, Y. Jang and G. Kong, "Uplink Data Rate in Large Intelligent Surfaces: Asymptotic Analysis under Channel Estimation Errors," ResearchGate, 2018. [Online]. Available: https://www.researchgate.net/publication/328827179_Uplink_Data_Rate_in_Large_Intelligent_Surfaces_Asymptotic_Analysis_under_Channel_Estimation_Errors. [Accessed 7 September 2023].

[94] M. Jung, W. Saad, Y. Jang, G. Kong and S. Choi, "Reliability Analysis of Large Intelligent Surfaces (LISs): Rate Distribution and Outage Probability," *IEEE Wireless Communications Letters,* vol. 8, no. 6, pp. 1662 - 1666, 2019.

[95] C. Huang, A. Zappone, M. Debbah and C. Yuen, "Achievable Rate Maximization by Passive Intelligent Mirrors," in *2018 IEEE International Conference on Acoustics, Speech and Signal Processing (ICASSP),* Calgary, AB, Canada, 2018.

[96] C. Huang, G. C. Alexandropoulos, A. Zappone, M. Debbah and C. Yuen, "Energy Efficient Multi-User MISO Communication Using Low Resolution Large Intelligent Surfaces," in *2018 IEEE Globecom Workshops (GC Wkshps),* Abu Dhabi, UAE, 2018.

[97] Q. Wu and R. Zhang, "Intelligent Reflecting Surface Enhanced Wireless Network: Joint Active and Passive Beamforming Design," in *2018 IEEE Global Communications Conference (GLOBECOM),* Abu Dhabi, UAE, 2018.

[98] Q. Wu and R. Zhang, "Beamforming Optimization for Intelligent Reflecting Surface with Discrete Phase Shifts," in *ICASSP 2019 - 2019 IEEE International Conference on Acoustics, Speech and Signal Processing (ICASSP),* Brighton, UK, 2019.

[99] N. Pillay and H. Xu, "Golden codeword–based modulation schemes for single-input multiple-output systems," *Int J Commun Syst.,* 2019;32:e3963. https://doi.org/10.1002/dac.3963.

[100] N. Pillay and H. Xu, "The Component-Interleaved Golden Code and Its Low-Complexity Detection," *IEEE Access,* vol. 8, pp. 59550 - 59558, 2020.

[101] N. Pillay and H. Xu, "An Alternative Encoding of the Golden Code and its Low Complexity Detection," *IEEE Access,* vol. 10, pp. 30147 - 30156, 2022.

[102] G. O. Otieno, "Generalised Differential Golden Code Modulation: EP Analysis and Bandwidth Efficiency," *ResearchSpace@UKZN,* 2022. [Online]. Available: https://ukzn-dspace.ukzn.ac.za/handle/10413/20809.

[103] N. Pillay, H. Xu and X. Jin, "Golden Codeword Based Generalized Differential Alamouti Modulation," *IEEE Access,* vol. 8, pp. 65649 - 65657, 2020.

[104] N. Pillay, H. Xu and N. Sibanda, "Golden codeword-based generalized spatial modulation," *Int J Commun Syst.,* 2022;35(10):e5144. doi:10.1002/dac.5144.

[105] N. Pillay and H. Xu, "RF Mirror Media-based Modulation for Golden Codes," *Journal of Telecommunication, Electronic and Computer Engineering,* vol. 10, no. 3, pp. 21-24, 2018.

[106] N. Pillay and H. Xu, “Single-Input Multiple-Output K-Complex Symbol Golden Codeword Media-Based Modulation,” *IEEE Access,* vol. 11, pp. 81828 - 81837, 2023.

[107] A. J. Bamisaye and T. Quazi, “Using of Golden Code Orthogonal Super-Symbol in Media-Based Modulation for Single-Input Multiple-Output Schemes,” *Journal of Telecommunications and Information Technology,* vol. 1, no. 2, pp. 43-48, 2022.

[108] N. Pillay and H. Xu, “Uplink Non-Orthogonal Multiple Access With Golden Codeword Constellation,” *IEEE Access,* vol. 9, pp. 150966 - 150974, 2021.

[109] N. Pillay, H. Xu and F. Yang, “Rotated Golden Codewords Based Space-Time Line Code Systems,” *IEEE Access,* vol. 10, pp. 54784 - 54793, 2022.

[110] M. O. Sinnokrot and J. R. Barry, “Fast maximum-likelihood decoding of the golden code,” *IEEE Transactions on Wireless Communications,* vol. 9, no. 1, pp. 26-31, 2010.

[111] N. Pillay and H. Xu, “Reduced Complexity Detection Schemes for Golden Code Systems,” *IEEE Access,* vol. 7, pp. 139140 - 139149, 2019.

[112] N. Pillay and H. Xu, “Multiple Complex Symbol Golden Code,” *IEEE Access,* vol. 8, pp. 103576 - 103584, 2020.

[113] N. Pillay and H. Xu, “Intelligent reflecting surface-assisted single-input single-output Golden codeword-based modulation schemes,” *IET Communications,* pp. 1-15, 2020.

[114] B. M. Hochwald and S. t. Brink, “Achieving near-capacity on a multiple-antenna channel,” *IEEE Transactions on Communications,* vol. 51, no. 3, pp. 389-399, 2003.

[115] M. Schwartz, W. R. Bennett and S. Stein, Communication Systems and Techniques, New York: McGraw-Hill, 1966.

[116] Z. Yang, M. Chen, W. Saad, W. Xu, M. Shikh-Bahaei, H. V. Poor and S. Cui, “Energy-Efficient Wireless Communications with Distributed Reconfigurable Intelligent Surfaces,” *IEEE Transactions on Wireless Communications,* vol. 21, no. 1, pp. 665 - 679, 2022.

[117] J. Zhang, J. Liu, S. Ma, C.-K. Wen and S. Jin, “Large System Achievable Rate Analysis of RIS-Assisted MIMO Wireless Communication with Statistical CSIT,” *IEEE Transactions on Wireless Communications,* vol. 20, no. 9, pp. 5572 - 5585, 2021.

[118] B. Di, H. Zhang, L. Song, Y. Li, Z. Han and H. V. Poor, “Hybrid Beamforming for Reconfigurable Intelligent Surface based Multi-user Communications: Achievable Rates with limited Discrete Phase Shifts,” *IEEE Journal on Selected Areas in Communications,* vol. 38, no. 8, pp. 1809 - 1822, 2020.

[119] N. S. Perovic, L.-N. Tran, M. D. Renzo and M. F. Flanagan, “On the Maximum Achievable Sum-Rate of the RIS-aided MIMO Broadcast Channel,” in *2021 IEEE 22nd International Workshop on Signal Processing Advances in Wireless Communications (SPAWC),* Lucca, Italy, 2021.

[120] E. Basar, M. Wen, R. Mesleh, M. D. Renzo, Y. Xiao and H. Haas, “Index-Modulation Techniques for Next-Generation Wireless Networks,” *IEEE Access,* vol. 5, pp. 16693 - 16746, 2017.

[121] X. Cheng, M. Zhang, M. Wen and L. Yang, “Index Modulation for 5G: Striving to do More with Less,” *IEEE Wireless Communications,* vol. 25, no. 2, pp. 126 - 132, 2018.

[122] S. Guo, S. Lv, H. Zhang, J. Ye and P. Zhang, “Reflecting Modulation,” *arXiv:1912.08428*, 2020. [Online]. Available: https://arxiv.org/abs/1912.08428.

[123] S. Lin, B. Zheng, G. C. Alexandropoulos, M. Wen, M. D. Renzo and F. Chen, “Reconfigurable Intelligent Surfaces with Reflection Pattern Modulation: Beamforming Design and Performance Analysis,” *IEEE Transactions on Wireless Communications,* vol. 20, no. 2, pp. 741 - 754, 2021.

[124] S. Lin, M. Wen, M. D. Renzo and F. Chen, “Reconfigurable Intelligent Surface-Based Quadrature Reflection Modulation,” in *ICC 2021 - IEEE International Conference on Communications*, Montreal, QC, Canada, 2021.

[125] E. Basar and H. V. Poor, “Present and Future of Reconfigurable Intelligent Surface-Empowered Communications [Perspectives],” *IEEE Signal Processing Magazine,* vol. 38, no. 6, pp. 146 - 152, 2021.

[126] N. T. Nguyen, Q.-D. Vu, K. Lee and M. Juntti, “Hybrid Relay-Reflecting Intelligent Surface-Assisted Wireless Communications,” *IEEE Transactions on Vehicular Technology,* vol. 71, no. 6, pp. 6228-6244, 2022.

[127] G. C. Alexandropoulos, N. Shlezinger, I. Alamzadeh, M. F. Imani, H. Zhang and Y. C. Eldar, “Hybrid Reconfigurable Intelligent Metasurfaces: Enabling Simultaneous Tunable Reflections and Sensing for 6G Wireless Communications,” *arXiv.2104.04690,* 10 April 2021. [Online]. Available: https://arxiv.org/abs/2104.04690.

[128] H. Zhang, N. Shlezinger, G. C. Alexandropoulos, A. Shultzman, I. Alamzadeh, M. F. Imani and Y. C. Eldar, “Channel Estimation with Hybrid Reconfigurable Intelligent Metasurfaces,” *IEEE Transactions on Communications,* vol. 71, no. 4, pp. 2441 - 2456, 8 June 2023.

[129] R. Ghazalian, H. Chen, G. C. Alexandropoulos, G. Seco-Granados, H. Wymeersch and R. Jäntti, “Joint User Localization and Location Calibration of A Hybrid Reconfigurable Intelligent Surface,” *IEEE Transactions on Vehicular Technology (Early Access),* pp. 1-6, 2023.

[130] N. R. Naidoo, H. Xu and T. Quazi, “Spatial modulation: optimal detector asymptotic performance and multiple-stage detection,” *IET Communications,* vol. 5, no. 10, pp. 1368-1376, 2011.

[131] K.-T. Nguyen, T.-H. Vu and S. Kim, “Exploiting Reconfigurable Intelligent Surfaces-Based Uplink/Downlink Wireless Systems,” *IEEE Access,* vol. 10, pp. 91059-91072, 2022.

[132] I. Yildirim, A. Uyrus and E. Basar, “Modeling and Analysis of Reconfigurable Intelligent Surfaces for Indoor and Outdoor Applications in Future Wireless Networks,” *IEEE Transactions on Communications,* vol. 69, no. 2, pp. 1290 - 1301, 2021.

[133] J. Hu and N. C. Beaulieu, “Accurate Closed-form Approximations to Ricean Sum Distributions and Densities,” *IEEE Communications Letters,* vol. 9, no. 2, pp. 133-135, 2005.

[134] M. Viswanathan, Wireless Communications Systems in Matlab, Independently published, 2020.

[135] I. S. Gradshteyn and I. M. Ryzhik, Table of Integrals, Series and Products, 7th ed., California, USA: Elsevier, 2007.

APPENDIX

Appendix A

RIS AP theory derivation

System Model:

$$r_{AP} = \sqrt{\frac{E_s}{N_\Upsilon}}\beta e^{j\vartheta_l} + n \tag{A1}$$

where $\beta = \sum_{k=1}^{N} g_k e^{j\theta_k}$.

We assume transmitted symbol l is erroneously detected as $\hat{l}$. $n \sim CN(0,1)$

Hence, the PEP can be expressed as:

$$P(x \to \hat{x}|\beta) = P\left(\left|r_{AP} - \sqrt{\frac{E_s}{N_\Upsilon}}\beta e^{j\vartheta_l}\right|^2 > \left|r_{AP} - \sqrt{\frac{E_s}{N_\Upsilon}}\beta e^{j\vartheta_{\hat{l}}}\right|^2\right). \tag{A2}$$

Substitute $r_{AP} = \sqrt{\frac{E_s}{N_\Upsilon}}\beta e^{j\vartheta_l} + n$.

Then we have:

$$\begin{aligned} P(x \to \hat{x}|\beta) &= P\left(\left|\sqrt{\frac{E_s}{N_\Upsilon}}\beta e^{j\vartheta_l} + n - \sqrt{\frac{E_s}{N_\Upsilon}}\beta e^{j\vartheta_l}\right|^2 \right. \\ &\qquad \left. > \left|\sqrt{\frac{E_s}{N_\Upsilon}}\beta e^{j\vartheta_l} + n - \sqrt{\frac{E_s}{N_\Upsilon}}\beta e^{j\vartheta_{\hat{l}}}\right|^2\right) \\ &= P\left(|n|^2 > \left|\sqrt{\frac{E_s}{N_\Upsilon}}\beta\left(e^{j\vartheta_l} - e^{j\vartheta_{\hat{l}}}\right) + n\right|^2\right). \end{aligned} \tag{A3}$$

We employ theorem 1, which says that:

$$Theorem\ 1: |a_1 + a_2|^2 = |a_1|^2 + |a_2|^2 + 2Re\{a_1 a_2^*\}. \tag{A4}$$

The proof of theorem 1 is found at the end of the derivation.

Continue as:

$$= P\left(|n|^2 > \left| \sqrt{\frac{E_s}{N_\Upsilon}} \beta\left(e^{j\vartheta_l} - e^{j\vartheta_{\hat{l}}}\right) \right|^2 + |n|^2 \right.$$

$$\left. + 2Re\left\{ \left(\sqrt{\frac{E_s}{N_\Upsilon}} \beta\left(e^{j\vartheta_l} - e^{j\vartheta_{\hat{l}}}\right) \right) (n)^* \right\} \right)$$

$$= P\left(0 > \frac{E_s \beta^2 \left|e^{j\vartheta_l} - e^{j\vartheta_{\hat{l}}}\right|^2}{2N_\Upsilon} + Re\left\{ \left(\sqrt{\frac{E_s}{N_\Upsilon}} \beta\left(e^{j\vartheta_l} - e^{j\vartheta_{\hat{l}}}\right) \right) (n)^* \right\} \right). \tag{A5}$$

At this stage, we note that $\frac{\left|e^{j\vartheta_l} - e^{j\vartheta_{\hat{l}}}\right|^2}{2} = 1 - \cos(\vartheta_l - \vartheta_{\hat{l}})$.

For convenience, we can write (A6) as:

$$= P\left(0 < -\frac{E_s}{N_\Upsilon} \beta^2 (1 - \cos(\vartheta_l - \vartheta_{\hat{l}})) - Re\left\{ \left(\sqrt{\frac{E_s}{N_\Upsilon}} \beta\left(e^{j\vartheta_l} - e^{j\vartheta_{\hat{l}}}\right) \right) (n)^* \right\} \right). \tag{A6}$$

At this point in the derivation, we can note that for a RV denoted by $X \sim CN(\mu, \sigma^2)$, the Q-function can be written according to Theorem 2, which states that:

$$Theorem\ 2: P(X > c) = P\left(\frac{X}{\sqrt{\sigma^2}} > \frac{c}{\sqrt{\sigma^2}}\right) = Q\left(\frac{c}{\sqrt{\sigma^2}}\right). \tag{A7}$$

Let $Re\left\{ \left(\sqrt{\frac{E_s}{N_\Upsilon}} \beta\left(e^{j\vartheta_l} - e^{j\vartheta_{\hat{l}}}\right) \right) (n)^* \right\} = X$, where $X \sim CN(\mu, \sigma^2)$ is a RV.

Need to find σ^2:

$$\sigma^2 = E[|X|^2] = E\left[\left| Re\left\{ \left(\sqrt{\frac{E_s}{N_\Upsilon}} \beta\left(e^{j\vartheta_l} - e^{j\vartheta_{\hat{l}}}\right) \right) (n)^* \right\} \right|^2 \right], \tag{A8}$$

which can be continued as:

$$Re\left\{ E\left[\left| \left(\sqrt{\frac{E_s}{N_\Upsilon}} \beta\left(e^{j\vartheta_l} - e^{j\vartheta_{\hat{l}}}\right) \right) (n)^T \right|^2 \right] \right\} = Re\left\{ \frac{E_s}{N_\Upsilon} \beta^2 \left|e^{j\vartheta_l} - e^{j\vartheta_{\hat{l}}}\right|^2 E[|n|^2] \right\}$$

$$= \frac{E_s \beta^2 \left|e^{j\vartheta_l} - e^{j\vartheta_{\hat{l}}}\right|^2}{2N_\Upsilon} = \frac{E_s}{N_\Upsilon} \beta^2 (1 - \cos(\vartheta_l - \vartheta_{\hat{l}})). \tag{A9}$$

Therefore:

$$= P\left(Re\left\{ \left(\sqrt{\frac{E_s}{N_\Upsilon}} \beta\left(e^{j\vartheta_l} - e^{j\vartheta_{\hat{l}}}\right) \right) (n)^T \right\} < \frac{E_s}{N_\Upsilon} \beta^2 (1 - \cos(\vartheta_l - \vartheta_{\hat{l}})) \right). \tag{A10}$$

According to Theorem 3:

$$Theorem\,3 \colon P(X < -a) = P(X > a). \tag{A11}$$

Therefore, we have that (A10) is:

$$= P\left(X > \frac{E_s}{N_\Upsilon}\beta^2(1 - \cos(\vartheta_l - \vartheta_{\hat{l}}))\right). \tag{A12}$$

Now we can use Theorem 2 in (A7) as follows:

$$= P\left(\frac{X}{\sqrt{\frac{E_s}{N_\Upsilon}\beta^2(1 - \cos(\vartheta_l - \vartheta_{\hat{l}}))}} > \frac{\frac{E_s}{N_\Upsilon}\beta^2(1 - \cos(\vartheta_l - \vartheta_{\hat{l}}))}{\sqrt{\frac{E_s}{N_\Upsilon}\beta^2(1 - \cos(\vartheta_l - \vartheta_{\hat{l}}))}}\right)$$

$$= Q\left(\frac{\frac{E_s}{N_\Upsilon}\beta^2(1 - \cos(\vartheta_l - \vartheta_{\hat{l}}))}{\sqrt{\frac{E_s}{N_\Upsilon}\beta^2(1 - \cos(\vartheta_l - \vartheta_{\hat{l}}))}}\right). \tag{A13}$$

Simplifying, we get:

$$= Q\left(\frac{\sqrt{E_s}\beta\sqrt{(1 - \cos(\vartheta_l - \vartheta_{\hat{l}}))}}{\sqrt{N_\Upsilon}}\right)$$

$$= Q\left(\sqrt{\frac{E_s\beta^2(1 - \cos(\vartheta_l - \vartheta_{\hat{l}}))}{N_\Upsilon}}\right). \tag{A14}$$

The term $(1 - \cos(\vartheta_l - \vartheta_{\hat{l}}))$ can be minimized by assuming uniform phases of $\vartheta_l = \frac{2\pi(l-1)}{M}, l \in [1 \colon M]$.

Proof of Theorem 1:

Given two matrices $\boldsymbol{A}_1$ *and* $\boldsymbol{A}_2$*:*

$$\|\boldsymbol{A}_1 + \boldsymbol{A}_2\|^2 = (\boldsymbol{A}_1 + \boldsymbol{A}_2)(\boldsymbol{A}_1 + \boldsymbol{A}_2)^H$$

$$= (\boldsymbol{A}_1 + \boldsymbol{A}_2)(\boldsymbol{A}_1^H + \boldsymbol{A}_2^H)$$

$$= \boldsymbol{A}_1\boldsymbol{A}_1^H + \boldsymbol{A}_1\boldsymbol{A}_2^H + \boldsymbol{A}_2\boldsymbol{A}_1^H + \boldsymbol{A}_2\boldsymbol{A}_2^H$$

Now $\boldsymbol{A}_1\boldsymbol{A}_1^H = \|\boldsymbol{A}_1\|^2, \boldsymbol{A}_2\boldsymbol{A}_2^H = \|\boldsymbol{A}_2\|^2$

$$= \|\boldsymbol{A}_1\|^2 + \|\boldsymbol{A}_2\|^2 + \boldsymbol{A}_1\boldsymbol{A}_2^H + \boldsymbol{A}_2\boldsymbol{A}_1^H$$

We can write $\boldsymbol{A}_2\boldsymbol{A}_1^H$ *as* $(\boldsymbol{A}_1\boldsymbol{A}_2^H)^H$

$$= \|\boldsymbol{A}_1\|^2 + \|\boldsymbol{A}_2\|^2 + \boldsymbol{A}_1\boldsymbol{A}_2^H + (\boldsymbol{A}_1\boldsymbol{A}_2^H)^H$$

Now $\boldsymbol{A}_1\boldsymbol{A}_2^H + (\boldsymbol{A}_1\boldsymbol{A}_2^H)^H = (Re\{\boldsymbol{A}_1\boldsymbol{A}_2^H\} + jIm\{\boldsymbol{A}_1\boldsymbol{A}_2^H\}) + (Re\{\boldsymbol{A}_1\boldsymbol{A}_2^H\} + jIm\{\boldsymbol{A}_1\boldsymbol{A}_2^H\})^H$

$$= (Re\{\boldsymbol{A}_1\boldsymbol{A}_2^H\} + jIm\{\boldsymbol{A}_1\boldsymbol{A}_2^H\}) + (Re\{\boldsymbol{A}_1\boldsymbol{A}_2^H\} - jIm\{\boldsymbol{A}_1\boldsymbol{A}_2^H\})$$

$$= 2Re\{\boldsymbol{A}_1\boldsymbol{A}_2^H\}$$

Hence,

$$\|\boldsymbol{A}_1 + \boldsymbol{A}_2\|^2 = \|\boldsymbol{A}_1\|^2 + \|\boldsymbol{A}_2\|^2 + 2Re\{\boldsymbol{A}_1\boldsymbol{A}_2^H\}$$

For scalar complex values a_1 *and* a_2, $|a_1 + a_2|^2 = |a_1|^2 + |a_2|^2 + 2Re\{a_1 a_2^*\}$

Appendix B

Proof of Matrices $\boldsymbol{H}$ and ε_k for $K \in \{2, 4, 8\}$.

Proof of $\boldsymbol{H}$ for $K = 2$:

Assume $n = 1, K = 2, k \in \{1{:}n\}, l \in \{1{:}\,2^{n-1}\}$

Golden Codewords:

$$x_{1,1} = \frac{\alpha}{\sqrt{5}}\left(x_{0,1} + x_{0,2}\theta\right), \tag{B1.1}$$

$$x_{1,2} = \frac{\bar{\alpha}}{\sqrt{5}}\left(x_{0,1} + x_{0,2}\bar{\theta}\right). \tag{B1.2}$$

Receive Signals:

$$r_1 = t_1 x_{1,1} + \eta_1, \tag{B2.1}$$

$$r_2 = t_2 x_{1,2} + \eta_2. \tag{B2.2}$$

Rearranging in terms of $\boldsymbol{x} = \begin{bmatrix} x_{0,1} \\ x_{0,2} \end{bmatrix}$ and substitute (B1.1) into (B2.1) and (B1.2) into (B2.2), we get the following:

$$\begin{aligned} r_1 &= t_1\left(\frac{\alpha}{\sqrt{5}}\left(x_{0,1} + x_{0,2}\theta\right)\right) + \eta_1 \\ &= t_1\frac{\alpha}{\sqrt{5}}x_{0,1} + t_1\frac{\alpha}{\sqrt{5}}x_{0,2}\theta + \eta_1. \end{aligned} \tag{B3}$$

Using a similar process for r_2, we get:

$$\begin{aligned} r_2 = t_2 x_{1,2} + \eta_2 &= t_2\left(\frac{\bar{\alpha}}{\sqrt{5}}\left(x_{0,1} + x_{0,2}\bar{\theta}\right)\right) + \eta_2 \\ &= t_2\frac{\bar{\alpha}}{\sqrt{5}}x_{0,1} + t_2\frac{\bar{\alpha}}{\sqrt{5}}x_{0,2}\bar{\theta} + \eta_2. \end{aligned} \tag{B4}$$

We now write in vector notation:

$$\boldsymbol{r} = \begin{bmatrix} r_1 \\ r_2 \end{bmatrix} = \begin{bmatrix} t_1\frac{\alpha}{\sqrt{5}}x_{0,1} + t_1\frac{\alpha}{\sqrt{5}}x_{0,2}\theta + \eta_1 \\ t_2\frac{\bar{\alpha}}{\sqrt{5}}x_{0,1} + t_2\frac{\bar{\alpha}}{\sqrt{5}}x_{0,2}\bar{\theta} + \eta_2 \end{bmatrix}. \tag{B5}$$

Letting $\boldsymbol{\eta} = \begin{bmatrix} \eta_1 \\ \eta_2 \end{bmatrix}$, we get:

$$\boldsymbol{r} = \begin{bmatrix} r_1 \\ r_2 \end{bmatrix} = \begin{bmatrix} t_1\frac{\alpha}{\sqrt{5}}x_{0,1} + t_1\frac{\alpha}{\sqrt{5}}x_{0,2}\theta \\ t_2\frac{\bar{\alpha}}{\sqrt{5}}x_{0,1} + t_2\frac{\bar{\alpha}}{\sqrt{5}}x_{0,2}\bar{\theta} \end{bmatrix} + \boldsymbol{\eta}. \tag{B6}$$

We may now decompose the matrix $\boldsymbol{Y} = \begin{bmatrix} t_1 \frac{\alpha}{\sqrt{5}} x_{0,1} + t_1 \frac{\alpha}{\sqrt{5}} x_{0,2}\theta \\ t_2 \frac{\bar{\alpha}}{\sqrt{5}} x_{0,1} + t_2 \frac{\bar{\alpha}}{\sqrt{5}} x_{0,2}\bar{\theta} \end{bmatrix}$ in terms of $\boldsymbol{x}$ as follows:

$$\begin{aligned} \boldsymbol{Y} &= \begin{bmatrix} t_1 \frac{\alpha}{\sqrt{5}} x_{0,1} + t_1 \frac{\alpha}{\sqrt{5}} x_{0,2}\theta \\ t_2 \frac{\bar{\alpha}}{\sqrt{5}} x_{0,1} + t_2 \frac{\bar{\alpha}}{\sqrt{5}} x_{0,2}\bar{\theta} \end{bmatrix} \\ &= \begin{bmatrix} t_1 \frac{\alpha}{\sqrt{5}} \\ t_2 \frac{\bar{\alpha}}{\sqrt{5}} \end{bmatrix} x_{0,1} + \begin{bmatrix} t_1 \frac{\alpha}{\sqrt{5}} \theta \\ t_2 \frac{\bar{\alpha}}{\sqrt{5}} \bar{\theta} \end{bmatrix} x_{0,2} \\ &= \begin{bmatrix} t_1 \frac{\alpha}{\sqrt{5}} & t_1 \frac{\alpha}{\sqrt{5}} \theta \\ t_2 \frac{\bar{\alpha}}{\sqrt{5}} & t_2 \frac{\bar{\alpha}}{\sqrt{5}} \bar{\theta} \end{bmatrix} \boldsymbol{x}, \end{aligned} \tag{B7}$$

where $\boldsymbol{H} = \begin{bmatrix} t_1 \frac{\alpha}{\sqrt{5}} & t_1 \frac{\alpha}{\sqrt{5}} \theta \\ t_2 \frac{\bar{\alpha}}{\sqrt{5}} & t_2 \frac{\bar{\alpha}}{\sqrt{5}} \bar{\theta} \end{bmatrix} = \frac{1}{\sqrt{5}} \begin{bmatrix} t_1 \alpha & t_1 \alpha\theta \\ t_2 \bar{\alpha} & t_2 \bar{\alpha}\bar{\theta} \end{bmatrix}$.

ABEP matrix

When considering the ABEP, we assume only $x_{0,1}$ is detected correctly.

Hence, we may write the receive signal as:

$$\boldsymbol{r} = \boldsymbol{E} x_{0,1} + \boldsymbol{\eta}, \tag{B8}$$

where $\boldsymbol{E} = \frac{1}{\sqrt{5}} \begin{bmatrix} t_1 \frac{\alpha}{\sqrt{5}} & t_2 \frac{\bar{\alpha}}{\sqrt{5}} \end{bmatrix}^T$ is the resultant matrix corresponding to symbol $x_{0,1}$.

We may now rewrite the signal as:

$$\begin{aligned} \boldsymbol{r} = \begin{bmatrix} r_1 \\ r_2 \end{bmatrix} &= \begin{bmatrix} t_1 \frac{\alpha}{\sqrt{5}} + \eta_1 \\ t_2 \frac{\bar{\alpha}}{\sqrt{5}} + \eta_2 \end{bmatrix} \\ &= \begin{bmatrix} t_1 \frac{\alpha}{\sqrt{5}} \\ t_2 \frac{\bar{\alpha}}{\sqrt{5}} \end{bmatrix} x_{0,1} + \begin{bmatrix} \eta_1 \\ \eta_2 \end{bmatrix} \\ &= \begin{bmatrix} \frac{\alpha}{\sqrt{5}} & \frac{\bar{\alpha}}{\sqrt{5}} \end{bmatrix} \begin{bmatrix} t_1 \\ t_2 \end{bmatrix} x_{0,1} + \begin{bmatrix} \eta_1 \\ \eta_2 \end{bmatrix}, \end{aligned} \tag{B9}$$

where ε_k for $K = 2$ is defined as:

$$\begin{aligned} \varepsilon_k &= \begin{bmatrix} \frac{\alpha}{\sqrt{5}} & \frac{\bar{\alpha}}{\sqrt{5}} \end{bmatrix} \\ &= \frac{1}{\sqrt{5}} [\alpha \quad \bar{\alpha}]. \end{aligned} \tag{B10}$$

Proof of $\boldsymbol{H}$ for $K = 4$:

$$\text{Assume } n = 2, K = 4, p \in \{1:2\}, l \in \{1:2\}$$

Golden Codewords:

1st Encoding:

$$x_{1,1} = \frac{\alpha}{\sqrt{5}}\left(x_{0,1} + x_{0,3}\theta\right), \tag{B11.1}$$

$$x_{1,2} = \frac{\bar{\alpha}}{\sqrt{5}}\left(x_{0,1} + x_{0,3}\bar{\theta}\right), \tag{B11.2}$$

$$x_{1,3} = \frac{\alpha}{\sqrt{5}}\left(x_{0,2} + x_{0,4}\theta\right), \tag{B11.3}$$

$$x_{1,4} = \frac{\bar{\alpha}}{\sqrt{5}}\left(x_{0,2} + x_{0,4}\bar{\theta}\right). \tag{B11.4}$$

2nd Encoding:

$$\left\{x_{2,1}, x_{2,2}\right\} = \left\{\frac{\alpha}{\sqrt{5}}\left(x_{1,1} + x_{1,3}\theta\right), \frac{\bar{\alpha}}{\sqrt{5}}\left(x_{1,1} + x_{1,3}\bar{\theta}\right)\right\}, \tag{B12.1}$$

$$\left\{x_{2,3}, x_{2,4}\right\} = \left\{\frac{\alpha}{\sqrt{5}}\left(x_{1,2} + x_{1,4}\theta\right), \frac{\bar{\alpha}}{\sqrt{5}}\left(x_{1,2} + x_{1,4}\bar{\theta}\right)\right\}. \tag{B12.2}$$

Receive Signals:

$$r_1 = t_1 x_{2,1} + \eta_1, \tag{B13.1}$$

$$r_2 = t_2 x_{2,2} + \eta_2, \tag{B13.2}$$

$$r_3 = t_3 x_{2,3} + \eta_3, \tag{B13.3}$$

$$r_4 = t_4 x_{2,4} + \eta_4. \tag{B13.4}$$

Rearrange in terms of $\boldsymbol{x} = [x_{0,1} \quad x_{0,2} \quad x_{0,3} \quad x_{0,4}]^T$ and substitute (B11.1) - (B11.4) into (B12.1) - (B12.2), we get:

$$\begin{aligned} x_{2,1} = \frac{\alpha}{\sqrt{5}}\left(x_{1,1} + x_{1,3}\theta\right) &= \frac{\alpha}{\sqrt{5}}\left(\left(\frac{\alpha}{\sqrt{5}}\left(x_{0,1} + x_{0,3}\theta\right)\right) + \left(\frac{\alpha}{\sqrt{5}}\left(x_{0,2} + x_{0,4}\theta\right)\right)\theta\right) \\ &= \frac{\alpha^2}{5}\left(x_{0,1} + x_{0,3}\theta\right) + \frac{\alpha^2}{5}\theta\left(x_{0,2} + x_{0,4}\theta\right). \end{aligned} \tag{B14}$$

Multiplying out, we get:

$$\begin{aligned} x_{2,1} &= \frac{\alpha^2}{5}x_{0,1} + \frac{\alpha^2}{5}\theta x_{0,3} + \frac{\alpha^2}{5}\theta x_{0,2} + \frac{\alpha^2}{5}\theta^2 x_{0,4} \\ &= \frac{\alpha^2}{5}x_{0,1} + \frac{\alpha^2}{5}\theta x_{0,2} + \frac{\alpha^2}{5}\theta x_{0,3} + \frac{\alpha^2}{5}\theta^2 x_{0,4.} \end{aligned} \tag{B15}$$

Using a similar procedure, we obtain:

$$x_{2,2} = \frac{\bar{\alpha}}{\sqrt{5}}\left(x_{1,1} + x_{1,3}\bar{\theta}\right) = \frac{\bar{\alpha}}{\sqrt{5}}\left(\left(\frac{\alpha}{\sqrt{5}}\left(x_{0,1} + x_{0,3}\theta\right)\right) + \left(\frac{\alpha}{\sqrt{5}}\left(x_{0,2} + x_{0,4}\theta\right)\right)\bar{\theta}\right)$$

$$= \frac{\alpha\bar{\alpha}}{5} x_{0,1} + \frac{\alpha\bar{\alpha}\bar{\theta}}{5} x_{0,2} + \frac{\alpha\bar{\alpha}\theta}{5} x_{0,3} + + \frac{\alpha\bar{\alpha}\theta\bar{\theta}}{5} x_{0,4}, \tag{B16}$$

$$x_{2,3} = \frac{\alpha}{\sqrt{5}}\left(x_{1,2} + x_{1,4}\theta\right) = \frac{\alpha}{\sqrt{5}}\left(\left(\frac{\bar{\alpha}}{\sqrt{5}}\left(x_{0,1} + x_{0,3}\bar{\theta}\right)\right) + \left(\frac{\bar{\alpha}}{\sqrt{5}}\left(x_{0,2} + x_{0,4}\bar{\theta}\right)\right)\theta\right)$$

$$= \frac{\alpha\bar{\alpha}}{5} x_{0,1} + \frac{\alpha\bar{\alpha}\theta}{5} x_{0,2} + \frac{\alpha\bar{\alpha}\bar{\theta}}{5} x_{0,3} + \frac{\alpha\bar{\alpha}\theta\bar{\theta}}{5} x_{0,4}, \tag{B17}$$

$$x_{2,4} = \frac{\bar{\alpha}}{\sqrt{5}}\left(x_{1,2} + x_{1,4}\bar{\theta}\right) = \frac{\bar{\alpha}}{\sqrt{5}}\left(\left(\frac{\bar{\alpha}}{\sqrt{5}}\left(x_{0,1} + x_{0,3}\bar{\theta}\right),\right) + \left(\frac{\bar{\alpha}}{\sqrt{5}}\left(x_{0,2} + x_{0,4}\bar{\theta}\right)\right)\bar{\theta}\right)$$

$$= \frac{\bar{\alpha}^2}{5} x_{0,1} + \frac{\bar{\alpha}^2\bar{\theta}}{5} x_{0,2} + \frac{\bar{\alpha}^2\bar{\theta}}{5} x_{0,3} + \frac{\bar{\alpha}^2\bar{\theta}^2}{5} x_{0,4}. \tag{B18}$$

Substituting these results into the receive signals, we get:

$$r_1 = t_1 x_{2,1} + \eta_1 = t_1\left(\frac{\alpha^2}{5} x_{0,1} + \frac{\alpha^2}{5}\theta x_{0,2} + \frac{\alpha^2}{5}\theta x_{0,3} + \frac{\alpha^2}{5}\theta^2 x_{0,4}\right) + \eta_1, \tag{B19.1}$$

$$r_2 = t_2 x_{2,2} + \eta_2 = t_2\left(\frac{\alpha\bar{\alpha}}{5} x_{0,1} + \frac{\alpha\bar{\alpha}\bar{\theta}}{5} x_{0,2} + \frac{\alpha\bar{\alpha}\theta}{5} x_{0,3} + + \frac{\alpha\bar{\alpha}\theta\bar{\theta}}{5} x_{0,4}\right) + \eta_2, \tag{B19.2}$$

$$r_3 = t_3 x_{2,3} + \eta_3 = t_3\left(\frac{\alpha\bar{\alpha}}{5} x_{0,1} + \frac{\alpha\bar{\alpha}\theta}{5} x_{0,2} + \frac{\alpha\bar{\alpha}\bar{\theta}}{5} x_{0,3} + \frac{\alpha\bar{\alpha}\theta\bar{\theta}}{5} x_{0,4}\right) + \eta_3, \tag{B19.3}$$

$$r_4 = t_4 x_{2,4} + \eta_4 = t_4\left(\frac{\bar{\alpha}^2}{5} x_{0,1} + \frac{\bar{\alpha}^2\bar{\theta}}{5} x_{0,2} + \frac{\bar{\alpha}^2\bar{\theta}}{5} x_{0,3} + \frac{\bar{\alpha}^2\bar{\theta}^2}{5} x_{0,4}\right) + \eta_4. \tag{B19.4}$$

Multiplying out, we get:

$$r_1 = t_1\frac{\alpha^2}{5} x_{0,1} + t_1\frac{\alpha^2}{5}\theta x_{0,2} + t_1\frac{\alpha^2}{5}\theta x_{0,3} + t_1\frac{\alpha^2}{5}\theta^2 x_{0,4} + \eta_1, \tag{B20.1}$$

$$r_2 = t_2\frac{\alpha\bar{\alpha}}{5} x_{0,1} + t_2\frac{\alpha\bar{\alpha}\bar{\theta}}{5} x_{0,2} + t_2\frac{\alpha\bar{\alpha}\theta}{5} x_{0,3} + t_2\frac{\alpha\bar{\alpha}\theta\bar{\theta}}{5} x_{0,4} + \eta_2, \tag{B20.2}$$

$$r_3 = t_3\frac{\alpha\bar{\alpha}}{5} x_{0,1} + t_3\frac{\alpha\bar{\alpha}\theta}{5} x_{0,2} + t_3\frac{\alpha\bar{\alpha}\bar{\theta}}{5} x_{0,3} + t_3\frac{\alpha\bar{\alpha}\theta\bar{\theta}}{5} x_{0,4} + \eta_3, \tag{B20.3}$$

$$r_4 = t_4\frac{\bar{\alpha}^2}{5} x_{0,1} + t_4\frac{\bar{\alpha}^2\bar{\theta}}{5} x_{0,2} + t_4\frac{\bar{\alpha}^2\bar{\theta}}{5} x_{0,3} + t_4\frac{\bar{\alpha}^2\bar{\theta}^2}{5} x_{0,4} + \eta_4. \tag{B20.4}$$

Let $\boldsymbol{r} = [r_1 \quad r_2 \quad r_3 \quad r_4]^T, \boldsymbol{\eta} = [\eta_1 \quad \eta_2 \quad \eta_3 \quad \eta_4]^T$ and $\boldsymbol{x} = [x_{0,1} \quad x_{0,2} \quad x_{0,3} \quad x_{0,4}]^T$, we may rewrite the receive signals to obtain:

$$\boldsymbol{r} = \begin{bmatrix} t_1\frac{\alpha^2}{5} & t_1\frac{\alpha^2}{5}\theta & t_1\frac{\alpha^2}{5}\theta & t_1\frac{\alpha^2}{5}\theta^2 \\ t_2\frac{\alpha\bar{\alpha}}{5} & t_2\frac{\alpha\bar{\alpha}\bar{\theta}}{5} & t_2\frac{\alpha\bar{\alpha}\theta}{5} & t_2\frac{\alpha\bar{\alpha}\theta\bar{\theta}}{5} \\ t_3\frac{\alpha\bar{\alpha}}{5} & t_3\frac{\alpha\bar{\alpha}\theta}{5} & t_3\frac{\alpha\bar{\alpha}\bar{\theta}}{5} & t_3\frac{\alpha\bar{\alpha}\theta\bar{\theta}}{5} \\ t_4\frac{\bar{\alpha}^2}{5} & t_4\frac{\bar{\alpha}^2\bar{\theta}}{5} & t_4\frac{\bar{\alpha}^2\bar{\theta}}{5} & t_4\frac{\bar{\alpha}^2\bar{\theta}^2}{5} \end{bmatrix}\boldsymbol{x} + \boldsymbol{\eta}, \tag{B21}$$

where:

$$\boldsymbol{H} = \begin{bmatrix} t_1\frac{\alpha^2}{5} & t_1\frac{\alpha^2}{5}\theta & t_1\frac{\alpha^2}{5}\theta & t_1\frac{\alpha^2}{5}\theta^2 \\ t_2\frac{\alpha\bar{\alpha}}{5} & t_2\frac{\alpha\bar{\alpha}\bar{\theta}}{5} & t_2\frac{\alpha\bar{\alpha}\theta}{5} & t_2\frac{\alpha\bar{\alpha}\theta\bar{\theta}}{5} \\ t_3\frac{\alpha\bar{\alpha}}{5} & t_3\frac{\alpha\bar{\alpha}\theta}{5} & t_3\frac{\alpha\bar{\alpha}\bar{\theta}}{5} & t_3\frac{\alpha\bar{\alpha}\theta\bar{\theta}}{5} \\ t_4\frac{\bar{\alpha}^2}{5} & t_4\frac{\bar{\alpha}^2\bar{\theta}}{5} & t_4\frac{\bar{\alpha}^2\bar{\theta}}{5} & t_4\frac{\bar{\alpha}^2\bar{\theta}^2}{5} \end{bmatrix} = \frac{1}{5}\begin{bmatrix} t_1\alpha^2 & t_1\alpha^2\theta & t_1\alpha^2\theta & t_1\alpha^2\theta^2 \\ t_2\alpha\bar{\alpha} & t_2\alpha\bar{\alpha}\bar{\theta} & t_2\alpha\bar{\alpha}\theta & t_2\alpha\bar{\alpha}\theta\bar{\theta} \\ t_3\alpha\bar{\alpha} & t_3\alpha\bar{\alpha}\theta & t_3\alpha\bar{\alpha}\bar{\theta} & t_3\alpha\bar{\alpha}\theta\bar{\theta} \\ t_4\bar{\alpha}^2 & t_4\bar{\alpha}^2\bar{\theta} & t_4\bar{\alpha}^2\bar{\theta} & t_4\bar{\alpha}^2\bar{\theta}^2 \end{bmatrix}. \qquad \text{(B22)}$$

Hence:

$$\boldsymbol{H} = \frac{1}{5}\begin{bmatrix} t_1\alpha^2 & t_1\alpha^2\theta & t_1\alpha^2\theta & t_1\alpha^2\theta^2 \\ t_2\alpha\bar{\alpha} & t_2\alpha\bar{\alpha}\bar{\theta} & t_2\alpha\bar{\alpha}\theta & t_2\alpha\bar{\alpha}\theta\bar{\theta} \\ t_3\alpha\bar{\alpha} & t_3\alpha\bar{\alpha}\theta & t_3\alpha\bar{\alpha}\bar{\theta} & t_3\alpha\bar{\alpha}\theta\bar{\theta} \\ t_4\bar{\alpha}^2 & t_4\bar{\alpha}^2\bar{\theta} & t_4\bar{\alpha}^2\bar{\theta} & t_4\bar{\alpha}^2\bar{\theta}^2 \end{bmatrix}, \text{ for } K = 4. \qquad \text{(B23)}$$

<u>**ABEP matrix for $\boldsymbol{K = 4}$:**</u>

Assume only $x_{0,1}$ detected correctly.

Hence, only consider 1st column of $\boldsymbol{H}$.

Hence, given for $K = 4$:

$$\boldsymbol{r} = \boldsymbol{E}x_{0,1} + \boldsymbol{\eta}, \qquad \text{(B24)}$$

where $\boldsymbol{E}$ is the vector $\boldsymbol{E} = \frac{1}{5}[t_1\alpha^2 \quad t_2\alpha\bar{\alpha} \quad t_3\alpha\bar{\alpha} \quad t_4\bar{\alpha}^2]^T$.

We may the rewrite the receive signal as:

$$\boldsymbol{r} = \frac{1}{5}\begin{bmatrix} t_1\alpha^2 \\ t_2\alpha\bar{\alpha} \\ t_3\alpha\bar{\alpha} \\ t_4\bar{\alpha}^2 \end{bmatrix} x_{0,1} + \boldsymbol{\eta}$$

$$= \frac{1}{5}[\alpha^2 \quad \alpha\bar{\alpha} \quad \alpha\bar{\alpha} \quad \bar{\alpha}^2]\begin{bmatrix} t_1 \\ t_2 \\ t_3 \\ t_4 \end{bmatrix} x_{0,1} + \boldsymbol{\eta}, \qquad \text{(B25)}$$

where ε_k for $K = 4$ is defined as:

$$\varepsilon_k = \frac{1}{5}[\alpha^2 \quad \alpha\bar{\alpha} \quad \alpha\bar{\alpha} \quad \bar{\alpha}^2]. \qquad \text{(B26)}$$

<u>Proof of $\boldsymbol{H}$ for $K = 8$:</u>

Assume $n = 3, K = 8, p \in \{1{:}\,3\}, l \in \{1{:}\,4\}$

1st encoding:

$$\{x_{1,1}, x_{1,2}\} = \left\{\frac{\alpha}{\sqrt{5}}\left(x_{0,1} + x_{0,5}\theta\right), \frac{\bar{\alpha}}{\sqrt{5}}\left(x_{0,1} + x_{0,5}\bar{\theta}\right)\right\}, \qquad \text{(B27.1)}$$

$$\{x_{1,3}, x_{1,4}\} = \left\{\frac{\alpha}{\sqrt{5}}\left(x_{0,2} + x_{0,6}\theta\right), \frac{\bar{\alpha}}{\sqrt{5}}\left(x_{0,2} + x_{0,6}\bar{\theta}\right)\right\}, \tag{B27.2}$$

$$\{x_{1,5}, x_{1,6}\} = \left\{\frac{\alpha}{\sqrt{5}}\left(x_{0,3} + x_{0,7}\theta\right), \frac{\bar{\alpha}}{\sqrt{5}}\left(x_{0,3} + x_{0,7}\bar{\theta}\right)\right\}, \tag{B27.3}$$

$$\{x_{1,7}, x_{1,8}\} = \left\{\frac{\alpha}{\sqrt{5}}\left(x_{0,4} + x_{0,8}\theta\right), \frac{\bar{\alpha}}{\sqrt{5}}\left(x_{0,4} + x_{0,8}\bar{\theta}\right)\right\}. \tag{B27.4}$$

2nd encoding:

$$\{x_{2,1}, x_{2,2}\} = \left\{\frac{\alpha}{\sqrt{5}}\left(x_{1,1} + x_{1,5}\theta\right), \frac{\bar{\alpha}}{\sqrt{5}}\left(x_{1,1} + x_{1,5}\bar{\theta}\right)\right\}, \tag{B28.1}$$

$$\{x_{2,3}, x_{2,4}\} = \left\{\frac{\alpha}{\sqrt{5}}\left(x_{1,2} + x_{1,6}\theta\right), \frac{\bar{\alpha}}{\sqrt{5}}\left(x_{1,2} + x_{1,6}\bar{\theta}\right)\right\}, \tag{B28.2}$$

$$\{x_{2,5}, x_{2,6}\} = \left\{\frac{\alpha}{\sqrt{5}}\left(x_{1,3} + x_{1,7}\theta\right), \frac{\bar{\alpha}}{\sqrt{5}}\left(x_{1,3} + x_{1,7}\bar{\theta}\right)\right\}, \tag{B28.3}$$

$$\{x_{2,7}, x_{2,8}\} = \left\{\frac{\alpha}{\sqrt{5}}\left(x_{1,4} + x_{1,8}\theta\right), \frac{\bar{\alpha}}{\sqrt{5}}\left(x_{1,4} + x_{1,8}\bar{\theta}\right)\right\}. \tag{B28.4}$$

3rd encoding:

$$\{x_{3,1}, x_{3,2}\} = \left\{\frac{\alpha}{\sqrt{5}}\left(x_{2,1} + x_{2,5}\theta\right), \frac{\bar{\alpha}}{\sqrt{5}}\left(x_{2,1} + x_{2,5}\bar{\theta}\right)\right\}, \tag{B29.1}$$

$$\{x_{3,3}, x_{3,4}\} = \left\{\frac{\alpha}{\sqrt{5}}\left(x_{2,2} + x_{2,6}\theta\right), \frac{\bar{\alpha}}{\sqrt{5}}\left(x_{2,2} + x_{2,6}\bar{\theta}\right)\right\}, \tag{B29.2}$$

$$\{x_{3,5}, x_{3,6}\} = \left\{\frac{\alpha}{\sqrt{5}}\left(x_{2,3} + x_{2,7}\theta\right), \frac{\bar{\alpha}}{\sqrt{5}}\left(x_{2,3} + x_{2,7}\bar{\theta}\right)\right\}, \tag{B29.3}$$

$$\{x_{3,7}, x_{3,8}\} = \left\{\frac{\alpha}{\sqrt{5}}\left(x_{2,4} + x_{2,8}\theta\right), \frac{\bar{\alpha}}{\sqrt{5}}\left(x_{2,4} + x_{2,8}\bar{\theta}\right)\right\}. \tag{B29.4}$$

Receive Signals:

$$\boldsymbol{r} = \boldsymbol{t}\boldsymbol{x}_3 + \boldsymbol{\eta}, \tag{B30}$$

where $\boldsymbol{r} = [r_1 \quad r_2 \quad r_3 \quad r_4 \quad r_5 \quad r_6 \quad r_7 \quad r_8]^T$, $\boldsymbol{t} = [t_1 \quad t_2 \quad t_3 \quad t_4 \quad t_5 \quad t_6 \quad t_7 \quad t_8]^T$, $\boldsymbol{x}_3 = [x_{3,1} \quad x_{3,2} \quad x_{3,3} \quad x_{3,4} \quad x_{3,5} \quad x_{3,6} \quad x_{3,7} \quad x_{3,8}]^T$ and $\boldsymbol{\eta} = [\eta_1 \quad \eta_2 \quad \eta_3 \quad \eta_4 \quad \eta_5 \quad \eta_6 \quad \eta_7 \quad \eta_8]^T$.

Back substitute all encoded GCs into the k-th receive signal.

For 1st receive signal:

$$\begin{aligned} r_1 &= t_1 x_{3,1} + \eta_1 \\ &= t_1\left(\frac{\alpha}{\sqrt{5}}\left(x_{2,1} + x_{2,5}\theta\right)\right) + \eta_1 \\ &= t_1\left(\frac{\alpha}{\sqrt{5}}\left(\left(\frac{\alpha}{\sqrt{5}}\left(x_{1,1} + x_{1,5}\theta\right)\right) + \left(\frac{\alpha}{\sqrt{5}}\left(x_{1,3} + x_{1,7}\theta\right)\right)\theta\right)\right) + \eta_1 \end{aligned}$$

$$
\begin{aligned}
&= t_1\left(\frac{\alpha}{\sqrt{5}}\left(\left(\frac{\alpha}{\sqrt{5}}\left(\left(\frac{\alpha}{\sqrt{5}}\left(x_{0,1}+x_{0,5}\theta\right)\right)+\left(\frac{\alpha}{\sqrt{5}}\left(x_{0,3}+x_{0,7}\theta\right)\right)\theta\right)\right)\right.\right.\\
&\qquad\left.\left.+\left(\frac{\alpha}{\sqrt{5}}\left(\left(\frac{\alpha}{\sqrt{5}}\left(x_{0,2}+x_{0,6}\theta\right)\right)+\left(\frac{\alpha}{\sqrt{5}}\left(x_{0,4}+x_{0,8}\theta\right)\right)\theta\right)\right)\theta\right)\right)\\
&\qquad+\eta_1.
\end{aligned}
\tag{B31}
$$

Multiplying out and simplifying, we get:

$$
\begin{aligned}
r_1 = t_1\Bigg(&\frac{\alpha^3}{5\sqrt{5}}x_{0,1}+\frac{\alpha^3\theta}{5\sqrt{5}}x_{0,2}+\frac{\alpha^3\theta}{5\sqrt{5}}x_{0,3}+\frac{\alpha^3\theta^2}{5\sqrt{5}}x_{0,4}+\frac{\alpha^3\theta}{5\sqrt{5}}x_{0,5}+\frac{\alpha^3\theta^2}{5\sqrt{5}}x_{0,6}\\
&+\frac{\alpha^3\theta^2}{5\sqrt{5}}x_{0,7}+\frac{\alpha^3\theta^3}{5\sqrt{5}}x_{0,8}\Bigg)+\eta_1.
\end{aligned}
\tag{B32}
$$

Applying the same method to all the receive signals, we get the following:

2nd receive signal:

$$
\begin{aligned}
r_2 &= t_2x_{3,2}+\eta_2\\
&= t_2\left(\frac{\bar{\alpha}}{\sqrt{5}}\left(\left(\frac{\alpha}{\sqrt{5}}\left(\left(\frac{\alpha}{\sqrt{5}}\left(x_{0,1}+x_{0,5}\theta\right)\right)+\left(\frac{\alpha}{\sqrt{5}}\left(x_{0,3}+x_{0,7}\theta\right)\right)\theta\right)\right)\right.\right.\\
&\qquad+\left(\frac{\alpha}{\sqrt{5}}\left(\left(\frac{\alpha}{\sqrt{5}}\left(x_{0,2}+x_{0,6}\theta\right)\right)\right.\right.\\
&\qquad\left.\left.\left.\left.+\left(\frac{\alpha}{\sqrt{5}}\left(x_{0,4}+x_{0,8}\theta\right)\right)\theta\right)\right)\bar{\theta}\right)\right)+\eta_2\\
&= t_2\Bigg(\frac{\alpha^2\bar{\alpha}}{5\sqrt{5}}x_{0,1}+\frac{\alpha^2\bar{\alpha}\bar{\theta}}{5\sqrt{5}}x_{0,2}+\frac{\alpha^2\bar{\alpha}\theta}{5\sqrt{5}}x_{0,3}+\frac{\alpha^2\bar{\alpha}\theta\bar{\theta}}{5\sqrt{5}}x_{0,4}+\frac{\alpha^2\bar{\alpha}\theta}{5\sqrt{5}}x_{0,5}\\
&\qquad+\frac{\alpha^2\bar{\alpha}\theta\bar{\theta}}{5\sqrt{5}}x_{0,6}+\frac{\alpha^2\bar{\alpha}\theta^2}{5\sqrt{5}}x_{0,7}+\frac{\alpha^2\bar{\alpha}\theta^2\bar{\theta}}{5\sqrt{5}}x_{0,8}\Bigg)+\eta_2.
\end{aligned}
\tag{B33}
$$

3rd receive signal:

$$
\begin{aligned}
&r_3 = t_3x_{3,3}+\eta_3\\
r_3 = t_3\Bigg(&\frac{\alpha^2\bar{\alpha}}{5\sqrt{5}}x_{0,1}+\frac{\alpha^2\bar{\alpha}\theta}{5\sqrt{5}}x_{0,2}+\frac{\alpha^2\bar{\alpha}\bar{\theta}}{5\sqrt{5}}x_{0,3}+\frac{\alpha^2\bar{\alpha}\theta\bar{\theta}}{5\sqrt{5}}x_{0,4}+\frac{\alpha^2\bar{\alpha}\theta}{5\sqrt{5}}x_{0,5}\\
&+\frac{\alpha^2\bar{\alpha}\theta^2}{5\sqrt{5}}x_{0,6}+\frac{\alpha^2\bar{\alpha}\theta\bar{\theta}}{5\sqrt{5}}x_{0,7}+\frac{\alpha^2\bar{\alpha}\theta^2\bar{\theta}}{5\sqrt{5}}x_{0,8}\Bigg)+\eta_3.
\end{aligned}
\tag{B34}
$$

4th receive signal:

$$r_4 = t_4 x_{3,4} + \eta_4$$

$$\begin{aligned} r_4 = t_4 \Bigg(& \frac{\alpha\bar{\alpha}^2}{5\sqrt{5}} x_{0,1} + \frac{\alpha\bar{\alpha}^2\bar{\theta}}{5\sqrt{5}} x_{0,2} + \frac{\alpha\bar{\alpha}^2\bar{\theta}}{5\sqrt{5}} x_{0,3} + \frac{\alpha\bar{\alpha}^2\bar{\theta}^2}{5\sqrt{5}} x_{0,4} + \frac{\alpha\bar{\alpha}^2\theta}{5\sqrt{5}} x_{0,5} \\ & + \frac{\alpha\bar{\alpha}^2\theta\bar{\theta}}{5\sqrt{5}} x_{0,6} + \frac{\alpha\bar{\alpha}^2\theta\bar{\theta}}{5\sqrt{5}} x_{0,7} + \frac{\alpha\bar{\alpha}^2\theta\bar{\theta}^2}{5\sqrt{5}} x_{0,8} \Bigg) + \eta_4. \end{aligned} \tag{B35}$$

5th receive signal:

$$r_5 = t_5 x_{3,5} + \eta_5$$

$$\begin{aligned} r_5 = t_5 \Bigg(& \frac{\alpha^2\bar{\alpha}}{5\sqrt{5}} x_{0,1} + \frac{\alpha^2\bar{\alpha}\theta}{5\sqrt{5}} x_{0,2} + \frac{\alpha^2\bar{\alpha}\theta}{5\sqrt{5}} x_{0,3} + \frac{\alpha^2\bar{\alpha}\theta^2}{5\sqrt{5}} x_{0,4} + \frac{\alpha^2\bar{\alpha}\bar{\theta}}{5\sqrt{5}} x_{0,5} \\ & + \frac{\alpha^2\bar{\alpha}\theta\bar{\theta}}{5\sqrt{5}} x_{0,6} + \frac{\alpha^2\bar{\alpha}\theta\bar{\theta}}{5\sqrt{5}} x_{0,7} + \frac{\alpha^2\bar{\alpha}\theta^2\bar{\theta}}{5\sqrt{5}} x_{0,8} \Bigg) + \eta_5. \end{aligned} \tag{B36}$$

6th receive signal:

$$r_6 = t_6 x_{3,6} + \eta_6$$

$$\begin{aligned} r_6 = t_6 \Bigg(& \frac{\alpha\bar{\alpha}^2}{5\sqrt{5}} x_{0,1} + \frac{\alpha\bar{\alpha}^2\bar{\theta}}{5\sqrt{5}} x_{0,2} + \frac{\alpha\bar{\alpha}^2\theta}{5\sqrt{5}} x_{0,3} + \frac{\alpha\bar{\alpha}^2\theta\bar{\theta}}{5\sqrt{5}} x_{0,4} + \frac{\alpha\bar{\alpha}^2\bar{\theta}}{5\sqrt{5}} x_{0,5} \\ & + \frac{\alpha\bar{\alpha}^2\bar{\theta}^2}{5\sqrt{5}} x_{0,6} + \frac{\alpha\bar{\alpha}^2\theta\bar{\theta}}{5\sqrt{5}} x_{0,7} + \frac{\alpha\bar{\alpha}^2\theta\bar{\theta}^2}{5\sqrt{5}} x_{0,8} \Bigg) + \eta_6. \end{aligned} \tag{B37}$$

7th receive signal:

$$r_7 = t_7 x_{3,7} + \eta_7$$

$$\begin{aligned} r_7 = t_7 \Bigg(& \frac{\alpha\bar{\alpha}^2}{5\sqrt{5}} x_{0,1} + \frac{\alpha\bar{\alpha}^2\theta}{5\sqrt{5}} x_{0,2} + \frac{\alpha\bar{\alpha}^2\bar{\theta}}{5\sqrt{5}} x_{0,3} + \frac{\alpha\bar{\alpha}^2\theta\bar{\theta}}{5\sqrt{5}} x_{0,4} + \frac{\alpha\bar{\alpha}^2\bar{\theta}}{5\sqrt{5}} x_{0,5} \\ & + \frac{\alpha\bar{\alpha}^2\theta\bar{\theta}}{5\sqrt{5}} x_{0,6} + \frac{\alpha\bar{\alpha}^2\bar{\theta}^2}{5\sqrt{5}} x_{0,7} + \frac{\alpha\bar{\alpha}^2\theta\bar{\theta}^2}{5\sqrt{5}} x_{0,8} \Bigg) + \eta_7. \end{aligned} \tag{B38}$$

8th receive signal:

$$r_8 = t_8 x_{3,8} + \eta_8$$

$$\begin{aligned} r_8 = t_8 \Bigg(& \frac{\bar{\alpha}^3}{5\sqrt{5}} x_{0,1} + \frac{\bar{\alpha}^3\bar{\theta}}{5\sqrt{5}} x_{0,2} + \frac{\bar{\alpha}^3\bar{\theta}}{5\sqrt{5}} x_{0,3} + \frac{\bar{\alpha}^3\bar{\theta}^2}{5\sqrt{5}} x_{0,4} + \frac{\bar{\alpha}^3\bar{\theta}}{5\sqrt{5}} x_{0,5} \\ & + \frac{\bar{\alpha}^3\bar{\theta}^2}{5\sqrt{5}} x_{0,6} + \frac{\bar{\alpha}^3\bar{\theta}^2}{5\sqrt{5}} x_{0,7} + \frac{\bar{\alpha}^3\bar{\theta}^3}{5\sqrt{5}} x_{0,8} \Bigg) + \eta_8. \end{aligned} \tag{B39}$$

Let $\boldsymbol{x} = [x_{0,1} \quad x_{0,2} \quad x_{0,3} \quad x_{0,4} \quad x_{0,5} \quad x_{0,6} \quad x_{0,7} \quad x_{0,8}]^T$.

We may rewrite the receive signals in vector form as:

$$\boldsymbol{r} = \frac{1}{5\sqrt{5}} \begin{bmatrix} \alpha^3 & \alpha^3\theta & \alpha^3\theta & \alpha^3\theta^2 & \alpha^3\theta & \alpha^3\theta^2 & \alpha^3\theta^2 & \alpha^3\theta^3 \\ \alpha^2\bar{\alpha} & \alpha^2\bar{\alpha}\bar{\theta} & \alpha^2\bar{\alpha}\theta & \alpha^2\bar{\alpha}\theta\bar{\theta} & \alpha^2\bar{\alpha}\theta & \alpha^2\bar{\alpha}\theta\bar{\theta} & \alpha^2\bar{\alpha}\theta^2 & \alpha^2\bar{\alpha}\theta^2\bar{\theta} \\ \alpha^2\bar{\alpha} & \alpha^2\bar{\alpha}\theta & \alpha^2\bar{\alpha}\bar{\theta} & \alpha^2\bar{\alpha}\theta\bar{\theta} & \alpha^2\bar{\alpha}\theta & \alpha^2\bar{\alpha}\theta^2 & \alpha^2\bar{\alpha}\theta\bar{\theta} & \alpha^2\bar{\alpha}\theta^2\bar{\theta} \\ \alpha\bar{\alpha}^2 & \alpha\bar{\alpha}^2\bar{\theta} & \alpha\bar{\alpha}^2\bar{\theta} & \alpha\bar{\alpha}^2\bar{\theta}^2 & \alpha\bar{\alpha}^2\theta & \alpha\bar{\alpha}^2\theta\bar{\theta} & \alpha^2\bar{\alpha}\theta\bar{\theta} & \alpha\bar{\alpha}^2\theta\bar{\theta}^2 \\ \alpha^2\bar{\alpha} & \alpha^2\bar{\alpha}\theta & \alpha^2\bar{\alpha}\theta & \alpha^2\bar{\alpha}\theta^2 & \alpha^2\bar{\alpha}\bar{\theta} & \alpha^2\bar{\alpha}\theta\bar{\theta} & \alpha^2\bar{\alpha}\theta\bar{\theta} & \alpha^2\bar{\alpha}\theta^2\bar{\theta} \\ \alpha\bar{\alpha}^2 & \alpha\bar{\alpha}^2\bar{\theta} & \alpha\bar{\alpha}^2\theta & \alpha\bar{\alpha}^2\theta\bar{\theta} & \alpha\bar{\alpha}^2\bar{\theta} & \alpha\bar{\alpha}^2\bar{\theta}^2 & \alpha\bar{\alpha}^2\theta\bar{\theta} & \alpha\bar{\alpha}^2\theta\bar{\theta}^2 \\ \alpha\bar{\alpha}^2 & \alpha\bar{\alpha}^2\theta & \alpha\bar{\alpha}^2\bar{\theta} & \alpha\bar{\alpha}^2\theta\bar{\theta} & \alpha\bar{\alpha}^2\bar{\theta} & \alpha\bar{\alpha}^2\theta\bar{\theta} & \alpha\bar{\alpha}^2\bar{\theta}^2 & \alpha\bar{\alpha}^2\theta\bar{\theta}^2 \\ \bar{\alpha}^3 & \bar{\alpha}^3\bar{\theta} & \bar{\alpha}^3\bar{\theta} & \bar{\alpha}^3\bar{\theta}^2 & \bar{\alpha}^3\bar{\theta} & \bar{\alpha}^3\bar{\theta}^2 & \bar{\alpha}^3\bar{\theta}^2 & \bar{\alpha}^3\bar{\theta}^3 \end{bmatrix} \boldsymbol{x} + \boldsymbol{\eta}, \tag{B40}$$

where:

$$\boldsymbol{H} = \frac{1}{5\sqrt{5}}\begin{bmatrix} \alpha^3 & \alpha^3\theta & \alpha^3\theta & \alpha^3\theta^2 & \alpha^3\theta & \alpha^3\theta^2 & \alpha^3\theta^2 & \alpha^3\theta^3 \\ \alpha^2\bar{\alpha} & \alpha^2\bar{\alpha}\bar{\theta} & \alpha^2\bar{\alpha}\theta & \alpha^2\bar{\alpha}\theta\bar{\theta} & \alpha^2\bar{\alpha}\theta & \alpha^2\bar{\alpha}\theta\bar{\theta} & \alpha^2\bar{\alpha}\theta^2 & \alpha^2\bar{\alpha}\theta^2\bar{\theta} \\ \alpha^2\bar{\alpha} & \alpha^2\bar{\alpha}\theta & \alpha^2\bar{\alpha}\bar{\theta} & \alpha^2\bar{\alpha}\theta\bar{\theta} & \alpha^2\bar{\alpha}\theta & \alpha^2\bar{\alpha}\theta^2 & \alpha^2\bar{\alpha}\theta\bar{\theta} & \alpha^2\bar{\alpha}\theta^2\bar{\theta} \\ \alpha\bar{\alpha}^2 & \alpha\bar{\alpha}^2\bar{\theta} & \alpha\bar{\alpha}^2\bar{\theta} & \alpha\bar{\alpha}^2\bar{\theta}^2 & \alpha\bar{\alpha}^2\theta & \alpha\bar{\alpha}^2\theta\bar{\theta} & \alpha^2\bar{\alpha}\theta\bar{\theta} & \alpha\bar{\alpha}^2\theta\bar{\theta}^2 \\ \alpha^2\bar{\alpha} & \alpha^2\bar{\alpha}\theta & \alpha^2\bar{\alpha}\theta & \alpha^2\bar{\alpha}\theta^2 & \alpha^2\bar{\alpha}\bar{\theta} & \alpha^2\bar{\alpha}\theta\bar{\theta} & \alpha^2\bar{\alpha}\theta\bar{\theta} & \alpha^2\bar{\alpha}\theta^2\bar{\theta} \\ \alpha\bar{\alpha}^2 & \alpha\bar{\alpha}^2\bar{\theta} & \alpha\bar{\alpha}^2\theta & \alpha\bar{\alpha}^2\theta\bar{\theta} & \alpha\bar{\alpha}^2\bar{\theta} & \alpha\bar{\alpha}^2\bar{\theta}^2 & \alpha\bar{\alpha}^2\theta\bar{\theta} & \alpha\bar{\alpha}^2\theta\bar{\theta}^2 \\ \alpha\bar{\alpha}^2 & \alpha\bar{\alpha}^2\theta & \alpha\bar{\alpha}^2\bar{\theta} & \alpha\bar{\alpha}^2\theta\bar{\theta} & \alpha\bar{\alpha}^2\bar{\theta} & \alpha\bar{\alpha}^2\theta\bar{\theta} & \alpha\bar{\alpha}^2\bar{\theta}^2 & \alpha\bar{\alpha}^2\theta\bar{\theta}^2 \\ \bar{\alpha}^3 & \bar{\alpha}^3\bar{\theta} & \bar{\alpha}^3\bar{\theta} & \bar{\alpha}^3\bar{\theta}^2 & \bar{\alpha}^3\bar{\theta} & \bar{\alpha}^3\bar{\theta}^2 & \bar{\alpha}^3\bar{\theta}^2 & \bar{\alpha}^3\bar{\theta}^3 \end{bmatrix}, \text{ for } K = 8. \quad \text{(B41)}$$

ABEP matrix for $K = 8$:

Assume only $x_{0,1}$ detected correctly.

Hence, only consider 1st column of $\boldsymbol{H}$.

Hence, given for $K = 8$:

$$\boldsymbol{r} = \boldsymbol{E}x_{0,1} + \boldsymbol{\eta}, \qquad \text{(B42)}$$

where the matrix $\boldsymbol{E} = \frac{1}{5\sqrt{5}}[\alpha^3 \quad \alpha^2\bar{\alpha} \quad \alpha^2\bar{\alpha} \quad \alpha\bar{\alpha}^2 \quad \alpha^2\bar{\alpha} \quad \alpha\bar{\alpha}^2 \quad \alpha\bar{\alpha}^2 \quad \bar{\alpha}^3]^T$.

Hence:

$$\varepsilon_k = \frac{1}{5\sqrt{5}}[\alpha^3 \quad \alpha^2\bar{\alpha} \quad \alpha^2\bar{\alpha} \quad \alpha\bar{\alpha}^2 \quad \alpha^2\bar{\alpha} \quad \alpha\bar{\alpha}^2 \quad \alpha\bar{\alpha}^2 \quad \bar{\alpha}^3], \text{ for } K = 8. \qquad \text{(B43)}$$

MGF Derivation

We start with:

$$\begin{aligned} \mathrm{M}_{\rho_k}(s) &= \int_0^\infty f_{\rho_k}(\rho_k)e^{\rho_k s}d\rho_k = \int_0^\infty \frac{\rho_k^{N-1}\exp\left(-\frac{\rho_k}{2bN\bar{\rho}|\varepsilon_k|^2}\right)}{(2bN|\varepsilon_k|^2\bar{\rho})^N(N-1)!}\exp(\rho_k s)\,d\rho_k \\ &= \frac{1}{(2bN|\varepsilon_k|^2\bar{\rho})^N(N-1)!}\int_0^\infty \rho_k^{N-1}\exp\left(-\frac{\rho_k}{2bN\bar{\rho}|\varepsilon_k|^2} + \rho_k s\right)d\rho_k \\ &= \frac{1}{(2bN|\varepsilon_k|^2\bar{\rho})^N(N-1)!}\int_0^\infty \rho_k^{N-1}\exp\left(-\rho_k\left[\frac{1}{2bN\bar{\rho}|\varepsilon_k|^2} - s\right]\right)d\rho_k. \end{aligned} \qquad \text{(B44)}$$

Now we let $A = \frac{1}{2bN\bar{\rho}|\varepsilon_k|^2} - \frac{2bN\bar{\rho}|\varepsilon_k|^2 s}{2bN\bar{\rho}|\varepsilon_k|^2} = \frac{1-2bN\bar{\rho}|\varepsilon_k|^2 s}{2bN\bar{\rho}|\varepsilon_k|^2}$.

We continue as:

$$\mathrm{M}_{\rho_k}(s) = \frac{1}{(2bN|\varepsilon_k|^2\bar{\rho})^N(N-1)!}\int_0^\infty \rho_k^{N-1}\exp(-A\rho_k)\,d\rho_k. \qquad \text{(B45)}$$

But $\int_0^\infty x^n e^{-ax}dx = \frac{n!}{a^{n+1}} = \frac{\Gamma(n+1)}{a^{n+1}}$ found in Equation 3.326.2 in [135].

So:

$$\int_0^{\infty} \rho_k^{N-1} \exp(-A\rho_k)\, d\rho_k = \frac{\Gamma(N)}{A^N}. \tag{B46}$$

Therefore, the final MGF is found as:

$$\begin{aligned}\int_0^{\infty} f_{\rho_k}(\rho_k) e^{\rho_k s} d\rho_k &= \frac{\Gamma(N)}{(2bN|\varepsilon_k|^2\bar{\rho})^N (N-1)!} \frac{(2bN\bar{\rho}|\varepsilon_k|^2)^N}{(1-2bN\bar{\rho}|\varepsilon_k|^2 s)^N} \\ &= \frac{\Gamma(N)}{(N-1)!\,(1-2bN\bar{\rho}|\varepsilon_k|^2 s)^N}.\end{aligned} \tag{B47}$$

Appendix C

<u>HRM Theory derivation</u>

System model:

$$r = \sqrt{\mathrm{P}_{tx}} H_{\ell_a} + \eta. \tag{C1}$$

We assume transmitted index ℓ_a is erroneously detected as $\hat{\ell}_a$. Correspondingly, the number of active elements $N_a = \ell_a S_G$ is erroneously detected as $\widehat{N}_a = \hat{\ell}_a S_G$.

Applying the CLT, we have:

$$\eta \sim CN\left(0, N_{\Upsilon}^2\right). \tag{C2}$$

Therefore, we express the CPEP as:

$$P\left(\ell_a \to \hat{\ell}_a | \boldsymbol{h}, \boldsymbol{g}, \boldsymbol{\phi}, \boldsymbol{\psi}\right) = P\left(\left|r - \sqrt{\mathrm{P}_{tx}} H_{\ell_a}\right|^2 > \left|r - \sqrt{\mathrm{P}_{tx}} H_{\hat{\ell}_a}\right|^2\right). \tag{C3}$$

Substitute $r = \sqrt{\mathrm{P}_{tx}} H_{\ell_a} + \eta$.

Then we have:

$$\begin{aligned} P\left(\ell_a \to \hat{\ell}_a | \boldsymbol{h}, \boldsymbol{g}, \boldsymbol{\phi}, \boldsymbol{\psi}\right) &= P\left(\left|\sqrt{\mathrm{P}_{tx}} H_{\ell_a} + \eta - \sqrt{\mathrm{P}_{tx}} H_{\ell_a}\right|^2 > \left|\sqrt{\mathrm{P}_{tx}} H_{\ell_a} + \eta - \sqrt{\mathrm{P}_{tx}} H_{\hat{\ell}_a}\right|^2\right) \\ &= P\left(|\eta|^2 > \left|\sqrt{\mathrm{P}_{tx}} H_{\ell_a} + \eta - \sqrt{\mathrm{P}_{tx}} H_{\hat{\ell}_a}\right|^2\right) \\ &= P\left(|\eta|^2 > \left|\sqrt{\mathrm{P}_{tx}}\left(H_{\ell_a} - H_{\hat{\ell}_a}\right) + \eta\right|^2\right). \end{aligned} \tag{C4}$$

We employ Theorem 1 given in Appendix A, Equation (A4).

Therefore, we continue as:

$$\begin{aligned} = P\Big(|\eta|^2 > &\left|\sqrt{\mathrm{P}_{tx}}\left(H_{\ell_a} - H_{\hat{\ell}_a}\right)\right|^2 + |\eta|^2 \\ &+ 2Re\left\{\left(\sqrt{\mathrm{P}_{tx}}\left(H_{\ell_a} - H_{\hat{\ell}_a}\right)\right)(\eta)^H\right\}\Big). \end{aligned} \tag{C5}$$

Note that $(\eta)^H = \eta^*$ as η is a scalar quantity.

We cancel out the term $|\eta|^2$ on both sides. Hence, we have:

$$= P\left(0 > \left|\sqrt{\mathrm{P}_{tx}}\left(H_{\ell_a} - H_{\hat{\ell}_a}\right)\right|^2 + 2Re\left\{\left(\sqrt{\mathrm{P}_{tx}}\left(H_{\ell_a} - H_{\hat{\ell}_a}\right)\right)(\eta)^*\right\}\right). \tag{C6}$$

For convenience, (C6) can be written as:

$$\begin{aligned} &= P\left(0 < -\left(\left|\sqrt{\mathrm{P}_{tx}}\left(H_{\ell_a} - H_{\hat{\ell}_a}\right)\right|^2 + 2Re\left\{\left(\sqrt{\mathrm{P}_{tx}}\left(H_{\ell_a} - H_{\hat{\ell}_a}\right)\right)(\eta)^*\right\}\right)\right) \\ &= P\left(0 < -\mathrm{P}_{tx}\left|\left(H_{\ell_a} - H_{\hat{\ell}_a}\right)\right|^2 - 2Re\left\{\left(\sqrt{\mathrm{P}_{tx}}\left(H_{\ell_a} - H_{\hat{\ell}_a}\right)\right)(\eta)^*\right\}\right). \end{aligned} \tag{C7}$$

At this point in the derivation, we can note that for a RV denoted by $X \sim CN(\mu, \sigma^2)$, the Q-function can be written according to Theorem 2 given in Appendix A, Equation (A7).

We can write the next step as:

$$= P\left(Re\left\{\left(\sqrt{\mathrm{P}_{tx}}\left(H_{\ell_a} - H_{\hat{\ell}_a}\right)\right)(\eta)^*\right\} < -\frac{1}{2}\mathrm{P}_{tx}\left|\left(H_{\ell_a} - H_{\hat{\ell}_a}\right)\right|^2\right). \tag{C8}$$

Let $Re\left\{\left(\sqrt{\mathrm{P}_{tx}}\left(H_{\ell_a} - H_{\hat{\ell}_a}\right)\right)(\eta)^*\right\} = X \sim CN(\mu, \sigma^2)$.

Use Theorem 3 in Appendix A, Equation (A11). Therefore, (C8) is written as:

$$= P\left(X > \frac{1}{2}\mathrm{P}_{tx}\left|\left(H_{\ell_a} - H_{\hat{\ell}_a}\right)\right|^2\right). \tag{C9}$$

Need to find σ^2:

$$\sigma^2 = E\left[Re\left\{\left|\left(\sqrt{\mathrm{P}_{tx}}\left(H_{\ell_a} - H_{\hat{\ell}_a}\right)\right)(\eta)^*\right|^2\right\}\right] = Re\left\{E\left[\left|\left(\sqrt{\mathrm{P}_{tx}}\left(H_{\ell_a} - H_{\hat{\ell}_a}\right)\right)(\eta)^*\right|^2\right]\right\}$$

$$= \frac{1}{2}\left(\mathrm{P}_{tx}\left(\left|H_{\ell_a} - H_{\hat{\ell}_a}\right|^2\right)\right)E[|\eta^*|^2]. \tag{C10}$$

But $E[|\eta^*|^2] = E[|\eta|^2] = N_{\mathrm{Y}}^2$, hence (C10) simplifies to:

$$= \frac{1}{2}\left(\left(\mathrm{P}_{tx}\left(\left|H_{\ell_a} - H_{\hat{\ell}_a}\right|^2\right)\right)N_{\mathrm{Y}}^2\right). \tag{C11}$$

Hence, we can continue the derivation as follows:

$$P\left(\frac{X}{\sqrt{\sigma^2}} > \frac{\frac{1}{2}\mathrm{P}_{tx}\left|\left(H_{\ell_a} - H_{\hat{\ell}_a}\right)\right|^2}{\sqrt{\sigma^2}}\right).$$

$$= P\left(\frac{X}{\sqrt{\frac{1}{2}\mathrm{P}_{tx}\left(\left|H_{\ell_a} - H_{\hat{\ell}_a}\right|^2\right)(N_{\mathrm{Y}}^2)}} > \frac{\frac{1}{2}\mathrm{P}_{tx}\left|\left(H_{\ell_a} - H_{\hat{\ell}_a}\right)\right|^2}{\sqrt{\frac{1}{2}\mathrm{P}_{tx}\left(\left|H_{\ell_a} - H_{\hat{\ell}_a}\right|^2\right)(N_{\mathrm{Y}}^2)}}\right)$$

$$= Q\left(\frac{\frac{1}{2}\mathrm{P}_{tx}\left|\left(H_{\ell_a} - H_{\hat{\ell}_a}\right)\right|^2}{\sqrt{\frac{1}{2}\mathrm{P}_{tx}\left(\left|H_{\ell_a} - H_{\hat{\ell}_a}\right|^2\right)(N_{\mathrm{Y}}^2)}}\right). \tag{C12}$$

This can be simplified as follows:

$$Q\left(\frac{\frac{1}{2}\mathrm{P}_{tx}\left|\left(H_{\ell_a} - H_{\hat{\ell}_a}\right)\right|^2}{\sqrt{\frac{1}{2}}\sqrt{N_{\mathrm{Y}}^2}\sqrt{\mathrm{P}_{tx}}\left|H_{\ell_a} - H_{\hat{\ell}_a}\right|}\right)$$

$$\begin{aligned} &Q\left(\frac{\frac{1}{\sqrt{2}}\sqrt{\mathrm{P}_{tx}}\left|\left(H_{\ell_a} - H_{\hat{\ell}_a}\right)\right|}{\sqrt{N_{\Upsilon}^{2}}}\right) \\ &= Q\left(\sqrt{\frac{\mathrm{P}_{tx}\left|\left(H_{\ell_a} - H_{\hat{\ell}_a}\right)\right|^{2}}{2N_{\Upsilon}^{2}}}\right). \end{aligned} \tag{C13}$$

Appendix D

HRM statistics derivation

Given that $H_{\ell_a} = \alpha \sum_{k=1}^{N_a} |h_k||g_k| + \sum_{k=N_a+1}^{N} |h_k||g_k|$ and $H_{\hat{\ell}_a} = \alpha \sum_{k=1}^{\hat{N}_a} |h_k||g_k| + \sum_{k=\hat{N}_a+1}^{N} |h_k||g_k|$. Channel magnitudes $|h_k|$ and $|g_k|$ are i.i.d. Rayleigh RVs with means of $E[|h_k|] = \sqrt{\mathcal{L}_t}\sqrt{\frac{\pi}{4}}$ and $E[|g_k|\,] = \sqrt{\mathcal{L}_r}\sqrt{\frac{\pi}{4}}$ respectively; and variances of $\sigma^2_{|h_k|} = \mathcal{L}_t\left(1 - \frac{\pi}{4}\right)$ and $\sigma^2_{|g_k|} = \mathcal{L}_r\left(1 - \frac{\pi}{4}\right)$. The second moment of $|h_k|$ and $|g_k|$ can be found as follows: $Var(|h_k|) = E[|h_k|^2] - (E[|h_k|])^2, \therefore\ E[|h_k|^2] = Var(|h_k|) + (E[|h_k|])^2 = \mathcal{L}_t\left(1 - \frac{\pi}{4}\right) + \left(\sqrt{\mathcal{L}_t}\sqrt{\frac{\pi}{4}}\right)^2 = \mathcal{L}_t - \mathcal{L}_t\frac{\pi}{4} + \mathcal{L}_t\frac{\pi}{4} = \mathcal{L}_t$. A similar procedure can be used to determine that $E[|g_k|^2] = \mathcal{L}_r$.

The mean of T is:

$$\begin{aligned}
\mu_{\mathrm{T}} &= E[\mathrm{T}] \\
&= E[H_{\ell_a} - H_{\hat{\ell}_a}] \\
&= E\left[\alpha \sum_{k=1}^{N_a} |h_k||g_k| + \sum_{k=N_a+1}^{N} |h_k||g_k| - \alpha \sum_{k=1}^{\hat{N}_a} |h_k||g_k| - \sum_{k=\hat{N}_a+1}^{N} |h_k||g_k|\right] \\
&= E\left[\alpha \sum_{k=1}^{N_a} |h_k||g_k|\right] + E\left[\sum_{k=N_a+1}^{N} |h_k||g_k|\right] + E\left[-\alpha \sum_{k=1}^{\hat{N}_a} |h_k||g_k|\right] \\
&\quad + E\left[-\sum_{k=\hat{N}_a+1}^{N} |h_k||g_k|\right] \\
&= \alpha E\left[\sum_{k=1}^{N_a} |h_k||g_k|\right] + E\left[\sum_{k=N_a+1}^{N} |h_k||g_k|\right] - \alpha E\left[\sum_{k=1}^{\hat{N}_a} |\mathfrak{h}_k||\mathcal{G}_k|\right] \\
&\quad - E\left[\sum_{k=\hat{N}_a+1}^{N} |h_k||g_k|\right] \\
&= \alpha \sum_{k=1}^{N_a} E[|h_k|]E[\,|g_k|] + \sum_{k=N_a+1}^{N} E[|h_k|]E[\,|g_k|] - \alpha \sum_{k=1}^{\hat{N}_a} E[|h_k|]E[\,|g_k| \\
&\quad - \sum_{k=\hat{N}_a+1}^{N} E[|h_k|]E[\,|g_k|].
\end{aligned} \tag{D1}$$

Substituting all statistics in, we get:

$$\begin{aligned}
&= \alpha\sqrt{\mathcal{L}_t}\sqrt{\frac{\pi}{4}}\sqrt{\mathcal{L}_r}\sqrt{\frac{\pi}{4}} \textstyle\sum_{k=1}^{N_a}(1) + \sqrt{\mathcal{L}_t}\sqrt{\frac{\pi}{4}}\sqrt{\mathcal{L}_r}\sqrt{\frac{\pi}{4}} \textstyle\sum_{k=N_a+1}^{N}(1) - \\
&\alpha\sqrt{\mathcal{L}_t}\sqrt{\frac{\pi}{4}}\sqrt{\mathcal{L}_r}\sqrt{\frac{\pi}{4}} \textstyle\sum_{k=1}^{\hat{N}_a}(1) - \sqrt{\mathcal{L}_t}\sqrt{\frac{\pi}{4}}\sqrt{\mathcal{L}_r}\sqrt{\frac{\pi}{4}} \textstyle\sum_{k=\hat{N}_a+1}^{N}(1).
\end{aligned} \tag{D2}$$

Now $\sum_{k=a}^{b} 1 = b - (a - 1)$. Hence, we have:

$$= \alpha\sqrt{\mathcal{L}_t\mathcal{L}_r}\frac{\pi}{4}\, N_a - \alpha\sqrt{\mathcal{L}_t\mathcal{L}_r}\frac{\pi}{4}\, \hat{N}_a + \alpha\sqrt{\mathcal{L}_t\mathcal{L}_r}\frac{\pi}{4}\,(N - N_a) - \sqrt{\mathcal{L}_t\mathcal{L}_r}\frac{\pi}{4}\,(N - N_a)$$

$$\begin{aligned} &= \alpha\sqrt{\mathcal{L}_t\mathcal{L}_r}\frac{\pi}{4}\, N_a - \alpha\sqrt{\mathcal{L}_t\mathcal{L}_r}\frac{\pi}{4}\, \widehat{N}_a + \sqrt{\mathcal{L}_t\mathcal{L}_r}\frac{\pi}{4}N - (\sqrt{\mathcal{L}_t\mathcal{L}_r}\frac{\pi}{4}N_a) \\ &\quad - \sqrt{\mathcal{L}_t\mathcal{L}_r}\frac{\pi}{4}N + (\sqrt{\mathcal{L}_t\mathcal{L}_r}\frac{\pi}{4}\widehat{N}_a) \\ &= \alpha\sqrt{\mathcal{L}_t\mathcal{L}_r}\frac{\pi}{4}\, N_a - \alpha\sqrt{\mathcal{L}_t\mathcal{L}_r}\frac{\pi}{4}\, \widehat{N}_a - \left((\sqrt{\mathcal{L}_t\mathcal{L}_r}\frac{\pi}{4}\, N_a) - (\sqrt{\mathcal{L}_t\mathcal{L}_r}\frac{\pi}{4}\, \widehat{N}_a)\right) \\ &= \sqrt{\mathcal{L}_t\mathcal{L}_r}\frac{\pi}{4}\left(\alpha\left(N_a - \widehat{N}_a\right) - \left(N_a - \widehat{N}_a\right)\right). \end{aligned} \tag{D3}$$

Channel magnitudes $|h_k|$ and $|g_k|$ are i.i.d. Rayleigh RVs with means of $E[|h_k|] = \sqrt{\mathcal{L}_t}\sqrt{\frac{\pi}{4}}$ and $E[|g_k|\,] = \sqrt{\mathcal{L}_r}\sqrt{\frac{\pi}{4}}$ respectively; and variances of $\sigma^2_{|h_k|} = \mathcal{L}_t\left(1 - \frac{\pi}{4}\right)$ and $\sigma^2_{|g_k|} = \mathcal{L}_r\left(1 - \frac{\pi}{4}\right)$. The second moment of $|h_k|$ and $|g_k|$ can be found as follows: $Var(|h_k|) = E[|h_k|^2] - (E[|h_k|])^2, \therefore$ $E[|h_k|^2] = Var(|h_k|) + (E[|h_k|])^2 = \mathcal{L}_t\left(1 - \frac{\pi}{4}\right) + \left(\sqrt{\mathcal{L}_t}\sqrt{\frac{\pi}{4}}\right)^2 = \mathcal{L}_t - \mathcal{L}_t\frac{\pi}{4} + \mathcal{L}_t\frac{\pi}{4} = \mathcal{L}_t.$ A similar procedure can be used to determine that $E[|g_k|^2] = \mathcal{L}_r$.

$$\begin{aligned} \sigma_{\mathrm{T}}^2 &= Var(T) \\ &= Var\left(H_{\ell_a} - H_{\hat{\ell}_a}\right) \\ &= Var\left(\alpha\sum_{k=1}^{N_a}|h_k||g_k| + \sum_{k=N_a+1}^{N}|h_k||g_k| - \alpha\sum_{k=1}^{\widehat{N}_a}|h_k||g_k| - \sum_{k=\widehat{N}_a+1}^{N}|h_k||g_k|\right) \\ &= Var\left(\alpha\sum_{k=1}^{N_a}|h_k||g_k| - \alpha\sum_{k=1}^{\widehat{N}_a}|h_k||g_k| + \sum_{k=N_a+1}^{N}|h_k||g_k| - \sum_{k=\widehat{N}_a+1}^{N}|h_k||g_k|\right). \end{aligned} \tag{D4}$$

We can rearrange and use the properties of the variance operator as $Var(X_1 + X_2 + \cdots + X_n) = Var(X_1) + Var(X_2) + \cdots + Var(X_n)$, and $Var(aX) = a^2Var(X)$.

Hence, we continue as follows:

$$\begin{aligned} &= Var\left(\alpha\sum_{k=1}^{N_a}|h_k||g_k| - \alpha\sum_{k=1}^{\widehat{N}_a}|h_k||g_k|\right) + Var\left(\sum_{k=N_a+1}^{N}|h_k||g_k| - \sum_{k=\widehat{N}_a+1}^{N}|h_k||g_k|\right) \\ &= \alpha^2 Var\left(\sum_{k=1}^{N_a}|h_k||g_k| - \sum_{k=1}^{\widehat{N}_a}|h_k||g_k|\right) + Var\left(\sum_{k=N_a+1}^{N}|h_k||g_k| - \sum_{k=\widehat{N}_a+1}^{N}|h_k||g_k|\right). \end{aligned} \tag{D5}$$

Now, applying the CLT assuming high N:

$$\begin{aligned} Var\left(\sum_{k=1}^{N_a}|h_k||g_k| - \sum_{k=1}^{\widehat{N}_a}|h_k||g_k|\right) &\cong \sum_{k=1}^{N_a}Var(|h_k||g_k|) - \sum_{k=1}^{\widehat{N}_a}Var(|h_k||g_k|) \\ &\cong \left(N_a - 1 - \left(\widehat{N}_a - 1\right)\right)Var(|h_k||g_k|) = \left(N_a - \widehat{N}_a\right)Var(|h_k||g_k|). \end{aligned} \tag{D6}$$

Therefore, we continue as follows:

$$= \alpha^2 \left(\sum_{k=1}^{N_a} Var(|h_k||g_k|) - \sum_{k=1}^{\widehat{N}_a} Var(|h_k||g_k|) \right) + \left(\sum_{k=N_a+1}^{N} Var(|h_k||g_k|) - \sum_{k=\widehat{N}_a+1}^{N} Var(|h_k||g_k|) \right). \tag{D7}$$

Simplifying, we get:

$$\begin{aligned} &= \alpha^2 \left(N_a - \widehat{N}_a\right) Var(|h_k||g_k|) + \left(N_a - \widehat{N}_a\right) Var(|h_k||g_k|) \\ &= \mathcal{L}_t \mathcal{L}_r \left(1 - \frac{\pi^2}{16}\right) \left[\alpha^2 \left(N_a - \widehat{N}_a\right) + \left(N_a - \widehat{N}_a\right)\right]. \end{aligned} \tag{D8}$$

Appendix E

Achievable Rate derivation

We have that:

$$A_r(H;\ \boldsymbol{R}) = \int_{-\infty}^{\infty} p\left(r|H_{\ell_a}\right) p\left(H_{\ell_a}\right) \log_2\left(\frac{p\left(r|H_{\ell_a}\right)}{\sum_{\hat{\ell}_a} p\left(r|H_{\hat{\ell}_a}\right) p\left(H_{\ell_a}\right)}\right) dr, \tag{E1}$$

with

$$p\left(r|H_{\ell_a}\right) = \frac{1}{\pi N_\Upsilon^2} \exp\left(-\frac{\left|r - \sqrt{\mathrm{P}_{tx}} H_{\ell_a}\right|^2}{N_\Upsilon^2}\right), \tag{E2}$$

and

$$p\left(H_{\ell_a}\right) = {}^{1}\!/_{G}. \tag{E3}$$

Substituting, we get:

$$A_r(H;\ \boldsymbol{R})$$

$$= \int_{-\infty}^{\infty} \frac{1}{\pi N_\Upsilon^2} \exp\left(-\frac{\left|r - \sqrt{\mathrm{P}_{tx}} H_{\ell_a}\right|^2}{N_\Upsilon^2}\right) \left({}^{1}\!/_{G}\right) \log_2\left(\frac{\frac{1}{\pi N_\Upsilon^2} \exp\left(-\frac{\left|r - \sqrt{\mathrm{P}_{tx}} H_{\ell_a}\right|^2}{N_\Upsilon^2}\right)}{\sum_{\hat{\ell}_a} \frac{1}{\pi N_\Upsilon^2} \exp\left(-\frac{\left|r - \sqrt{\mathrm{P}_{tx}} H_{\hat{\ell}_a}\right|^2}{N_\Upsilon^2}\right) {}^{1}\!/_{G}}\right) dr$$

$$= \frac{1}{\pi N_\Upsilon^2} \int_{-\infty}^{\infty} \exp\left(-\frac{\left|r - \sqrt{\mathrm{P}_{tx}} H_{\ell_a}\right|^2}{N_\Upsilon^2}\right) \left({}^{1}\!/_{G}\right) \log_2\left(G\, \frac{\exp\left(-\frac{\left|r - \sqrt{\mathrm{P}_{tx}} H_{\ell_a}\right|^2}{N_\Upsilon^2}\right)}{\sum_{\hat{\ell}_a} \exp\left(-\frac{\left|r - \sqrt{\mathrm{P}_{tx}} H_{\hat{\ell}_a}\right|^2}{N_\Upsilon^2}\right)}\right) dr. \tag{E4}$$

We can manipulate the logarithmic term in (D4) as:

$$\log_2\left(\frac{G}{\sum_{\hat{\ell}_a} \exp\left(\frac{\left|r - \sqrt{\mathrm{P}_{tx}} H_{\ell_a}\right|^2}{N_\Upsilon^2} - \frac{\left|r - \sqrt{\mathrm{P}_{tx}} H_{\hat{\ell}_a}\right|^2}{N_\Upsilon^2}\right)}\right). \tag{E5}$$

Expanding the logarithmic term using the additive logarithmic law:

$$= \frac{1}{\pi N_\Upsilon^2} \int_{-\infty}^{\infty} \exp\left(-\frac{\left|r - \sqrt{\mathrm{P}_{tx}} H_{\ell_a}\right|^2}{N_\Upsilon^2}\right) {}^{1}\!/_{G} \Bigg(\log_2 G$$

$$- \log_2\left(\sum_{\hat{\ell}_a} \exp\left(\frac{\left|r - \sqrt{\mathrm{P}_{tx}} H_{\ell_a}\right|^2}{N_\Upsilon^2} - \frac{\left|r - \sqrt{\mathrm{P}_{tx}} H_{\hat{\ell}_a}\right|^2}{N_\Upsilon^2}\right)\right)\Bigg) dr. \tag{E6}$$

Factor out $\frac{1}{G}$ and distribute the exponential term:

$$
\begin{aligned}
&= \frac{1}{\pi N_{\Upsilon}^{2}} \frac{1}{G} \int_{-\infty}^{\infty} \log_2(G) \exp\left(-\frac{\left| r - \sqrt{\mathrm{P}_{tx}} H_{\ell_a} \right|^2}{N_{\Upsilon}^{2}} \right) \\
&- \exp\left(-\frac{\left| r - \sqrt{\mathrm{P}_{tx}} H_{\ell_a} \right|^2}{N_{\Upsilon}^{2}} \right) \log_2\left(\sum_{\hat{\ell}_a} \exp\left(\frac{\left| r - \sqrt{\mathrm{P}_{tx}} H_{\ell_a} \right|^2}{N_{\Upsilon}^{2}} \right.\right. \\
&\left.\left. - \frac{\left| r - \sqrt{\mathrm{P}_{tx}} H_{\hat{\ell}_a} \right|^2}{N_{\Upsilon}^{2}} \right) \right) dr. \qquad \text{(E7)}
\end{aligned}
$$

The receive signal space $\boldsymbol{R}$ spans over the different values of ℓ_a. Hence, we can express the integral from $-\infty$ to ∞ as the sum of ℓ_a integrals over $\boldsymbol{R}$ with respect to the HRM symbol H_{ℓ_a}.

Hence, we can write (D7) as follows:

$$
\begin{aligned}
&= \frac{1}{\pi N_{\Upsilon}^{2}} \frac{1}{G} \sum_{\ell_a} \int \log_2(G) \exp\left(-\frac{\left| r - \sqrt{\mathrm{P}_{tx}} H_{\ell_a} \right|^2}{N_{\Upsilon}^{2}} \right) dr \\
&- \frac{1}{\pi N_{\Upsilon}^{2}} \frac{1}{G} \sum_{\ell_a} \int \exp\left(-\frac{\left| r - \sqrt{\mathrm{P}_{tx}} H_{\ell_a} \right|^2}{N_{\Upsilon}^{2}} \right) \\
&\times \log_2\left(\sum_{\hat{\ell}_a} \exp\left(\frac{\left| r - \sqrt{\mathrm{P}_{tx}} H_{\ell_a} \right|^2 - \left| r - \sqrt{\mathrm{P}_{tx}} H_{\hat{\ell}_a} \right|^2}{N_{\Upsilon}^{2}} \right) \right) dr. \qquad \text{(E8)}
\end{aligned}
$$

$Theorem$ 4: The total area over a PDF is equal to 1, that is for $f(x|y)$ being a conditional PDF, when we integrate over the real domain, we have that:

$$
Theorem\ 4\text{:} \int f(x|y)\, dx = 1. \qquad \text{(E9)}
$$

We have G number of index values ℓ_a, therefore:

$$
\begin{aligned}
\frac{1}{\pi N_{\Upsilon}^{2}} \frac{1}{G} \sum_{\ell_a} \int \exp\left(-\frac{\left| r - \sqrt{\mathrm{P}_{tx}} H_{\ell_a} \right|^2}{N_{\Upsilon}^{2}} \right) dr &= \frac{1}{G} \sum_{\ell_a} \int \frac{1}{\pi N_{\Upsilon}^{2}} \exp\left(-\frac{\left| r - \sqrt{\mathrm{P}_{tx}} H_{\ell_a} \right|^2}{N_{\Upsilon}^{2}} \right) dr \\
&= \frac{1}{G} \sum_{\ell_a} \int p\left(r | H_{\ell_a}\right) dr = \frac{1}{G} \times G(1) = 1. \qquad \text{(E10)}
\end{aligned}
$$

Hence:

$$A_r(H;\, \boldsymbol{R}) = \log_2(G) - \frac{1}{\pi N_\Upsilon^2}\frac{1}{G}\sum_{\ell_a}\int \exp\left(-\frac{\left|r-\sqrt{\mathrm{P}_{tx}}H_{\ell_a}\right|^2}{N_\Upsilon^2}\right) \times \log_2\left(\sum_{\hat{\ell}_a}\exp\left(\frac{\left|r-\sqrt{\mathrm{P}_{tx}}H_{\ell_a}\right|^2-\left|r-\sqrt{\mathrm{P}_{tx}}H_{\hat{\ell}_a}\right|^2}{N_\Upsilon^2}\right)\right)dr. \tag{E11}$$

We substitute $r=\sqrt{\mathrm{P}_{tx}}H_{\ell_a}+\eta$ into the second exponential term. The first exponential term can be manipulated such that we can use Theorem 4 to simplify it.

$$A_r(H;\, \boldsymbol{R})$$

$$= \log_2(G) - \frac{1}{G}\frac{1}{\pi N_\Upsilon^2}\sum_{\ell_a}\int \exp\left(-\frac{\left|r-\sqrt{\mathrm{P}_{tx}}H_{\ell_a}\right|^2}{N_\Upsilon^2}\right) \times \log_2\left(\sum_{\hat{\ell}_a}\exp\left(\frac{\left|\sqrt{\mathrm{P}_{tx}}H_{\ell_a}+\eta-\sqrt{\mathrm{P}_{tx}}H_{\ell_a}\right|^2-\left|\sqrt{\mathrm{P}_{tx}}H_{\ell_a}+\eta-\sqrt{\mathrm{P}_{tx}}H_{\hat{\ell}_a}\right|^2}{N_\Upsilon^2}\right)\right)dr$$

$$= \log_2(G) - \frac{1}{G}\frac{1}{\pi N_\Upsilon^2}\sum_{\ell_a}\int \exp\left(-\frac{\left|r-\sqrt{\mathrm{P}_{tx}}H_{\ell_a}\right|^2}{N_\Upsilon^2}\right) \times \log_2\left(\sum_{\hat{\ell}_a}\exp\left(\frac{|\eta|^2-\left|\sqrt{\mathrm{P}_{tx}}\left(H_{\ell_a}-H_{\hat{\ell}_a}\right)+\eta\right|^2}{N_\Upsilon^2}\right)\right)dr. \tag{E12}$$

We can factor out an exponential constant term from the logarithmic term as follows:

$$= \log_2(G) - \frac{1}{G}\frac{1}{\pi N_\Upsilon^2}\sum_{\ell_a}\int \exp\left(-\frac{\left|r-\sqrt{\mathrm{P}_{tx}}H_{\ell_a}\right|^2}{N_\Upsilon^2}\right) \times \log_2\left(\exp\left(\frac{|\eta|^2}{N_\Upsilon^2}\right)\sum_{\hat{\ell}_a}\exp\left(\frac{-\left|\sqrt{\mathrm{P}_{tx}}\left(H_{\ell_a}-H_{\hat{\ell}_a}\right)+\eta\right|^2}{N_\Upsilon^2}\right)\right)dr. \tag{E13}$$

Use the additive logarithmic law:

$$= \log_2(G) - \frac{1}{G}\frac{1}{\pi N_\Upsilon^2}\sum_{\ell_a}\left(\int \exp\left(-\frac{\left|r-\sqrt{\mathrm{P}_{tx}}H_{\ell_a}\right|^2}{N_\Upsilon^2}\right)\times\log_2\left(\exp\left(\frac{|\eta|^2}{N_\Upsilon^2}\right)\right)dr + \exp\left(\left(-\frac{\left|r-\sqrt{\mathrm{P}_{tx}}H_{\ell_a}\right|^2}{N_\Upsilon^2}\right)\right)\log_2\left(\sum_{\hat{\ell}_a}\exp\left(\frac{-\left|\sqrt{\mathrm{P}_{tx}}\left(H_{\ell_a}-H_{\hat{\ell}_a}\right)+\eta\right|^2}{N_\Upsilon^2}\right)\right)dr\right). \tag{E14}$$

Because we have introduced the RV η, we now need to evaluate over the mean with respect to η. We can achieve this by taking the expectation over the expression as follows:

$$
\begin{aligned}
&= \log_2(G) \\
&- E\left\{\log_2\left(\exp\left(\frac{|\,\eta\,|^2}{N_\Upsilon^2}\right)\right)\frac{1}{G}\,\frac{1}{\pi N_\Upsilon^2}\sum_{\ell_a}\int \exp\left(\left(-\frac{\left|\,r-\sqrt{\mathrm{P}_{tx}}H_{\ell_a}\right|^2}{N_\Upsilon^2}\right)\right)dr\right. \\
&\left.+\frac{1}{G}\,\frac{1}{\pi N_\Upsilon^2}\sum_{\ell_a}\int \exp\left(\left(-\frac{\left|\,r-\sqrt{\mathrm{P}_{tx}}H_{\ell_a}\right|^2}{N_\Upsilon^2}\right)\right)\log_2\left(\sum_{\hat{\ell}_a}\exp\left(\frac{-\left|\sqrt{\mathrm{P}_{tx}}\left(H_{\ell_a}-H_{\hat{\ell}_a}\right)+\,\eta\,\right|^2}{N_\Upsilon^2}\right)\right)dr\right\}.
\end{aligned}
\tag{E15}
$$

We can see that Theorem 4 can be applied in the first term again:

$$
\begin{aligned}
\frac{1}{\pi N_\Upsilon^2}\frac{1}{G}\sum_{\ell_a}\int \exp\left(-\frac{\left|r-\sqrt{\mathrm{P}_{tx}}H_{\ell_a}\right|^2}{N_\Upsilon^2}\right)dr &= \frac{1}{G}\sum_{\ell_a}\int \frac{1}{\pi N_\Upsilon^2}\exp\left(-\frac{\left|r-\sqrt{\mathrm{P}_{tx}}H_{\ell_a}\right|^2}{N_\Upsilon^2}\right)dr \\
&= \frac{1}{G}\sum_{\ell_a}\int p\left(r|H_{\ell_a}\right)dr = \frac{1}{G}\times G(1) = 1.
\end{aligned}
\tag{E16}
$$

Therefore, we continue as:

$$
\begin{aligned}
&= \log_2(G) \\
&- E\left\{\log_2\left(\exp\left(\frac{|\,\eta\,|^2}{N_\Upsilon^2}\right)\right)\right. \\
&\left.+\frac{1}{G}\sum_{\ell_a}\frac{1}{\pi N_\Upsilon^2}\int \exp\left(\left(-\frac{\left|\,r-\sqrt{\mathrm{P}_{tx}}H_{\ell_a}\right|^2}{N_\Upsilon^2}\right)\right)\log_2\left(\sum_{\hat{\ell}_a}\exp\left(\frac{-\left|\sqrt{\mathrm{P}_{tx}}\left(H_{\ell_a}-H_{\hat{\ell}_a}\right)+\,\eta\,\right|^2}{N_\Upsilon^2}\right)\right)dr\right\}.
\end{aligned}
\tag{E17}
$$

We can distribute the expectation operator over η in the first term, and over the entirety of the second term:

$$
\begin{aligned}
&= \log_2(G) \\
&- \log_2\left(\exp\left(\frac{E\{|\,\eta\,|^2\}}{N_\Upsilon^2}\right)\right) \\
&- E\left\{\frac{1}{G}\sum_{\ell_a}\frac{1}{\pi N_\Upsilon^2}\int \exp\left(\left(-\frac{\left|\,r-\sqrt{\mathrm{P}_{tx}}H_{\ell_a}\right|^2}{N_\Upsilon^2}\right)\right)\log_2\left(\sum_{\hat{\ell}_a}\exp\left(\frac{-\left|\sqrt{\mathrm{P}_{tx}}\left(H_{\ell_a}-H_{\hat{\ell}_a}\right)+\,\eta\,\right|^2}{N_\Upsilon^2}\right)\right)dr\right\}.
\end{aligned}
\tag{E18}
$$

We substitute $E\{|\ \eta\ |^2\} = N_\Upsilon^2$ as:

$$= \log_2(G) - \log_2(\exp(1))$$
$$-\frac{1}{G}\sum_{\ell_a} E\left\{\log_2\left(\sum_{\hat{\ell}_a}\exp\left(\frac{-\left|\sqrt{\mathrm{P}_{tx}}\left(H_{\ell_a} - H_{\hat{\ell}_a}\right) +\ \eta\ \right|^2}{N_\Upsilon^2}\right)\right)\frac{1}{\pi N_\Upsilon^2}\int \exp\left(\left(-\frac{\left|\ r - \sqrt{\mathrm{P}_{tx}}H_{\ell_a}\right|^2}{N_\Upsilon^2}\right)\right)dr\right\}. \tag{E19}$$

Once again, $Theorem$ 4 can be used again:

$$\frac{1}{\pi N_\Upsilon^2}\int \exp\left(\left(-\frac{\left|\ r - \sqrt{\mathrm{P}_{tx}}H_{\ell_a}\right|^2}{N_\Upsilon^2}\right)\right)dr = \int p\left(r|H_{\ell_a}\right)dr = 1. \tag{E20}$$

Hence, we can write (D18) as:

$$= \log_2(G) - \log_2(e) - \frac{1}{G}\sum_{\ell_a} E\left\{\log_2\left(\sum_{\hat{\ell}_a}\exp\left(\frac{-\left|\sqrt{\mathrm{P}_{tx}}\left(H_{\ell_a} - H_{\hat{\ell}_a}\right) +\ \eta\ \right|^2}{N_\Upsilon^2}\right)\right)\right\}. \tag{E21}$$

Finally, we can factor out -1 to simplify the final expression as:

$$= \log_2(G) - \left(\log_2(e) + \frac{1}{G}\sum_{\ell_a} E\left\{\log_2\left(\sum_{\hat{\ell}_a}\exp\left(\frac{-\left|\sqrt{\mathrm{P}_{tx}}\left(H_{\ell_a} - H_{\hat{\ell}_a}\right) +\ \eta\ \right|^2}{N_\Upsilon^2}\right)\right)\right\}\right). \tag{E22}$$

Appendix F

HRM non-AP Theory derivations

Given receive signal: $r = \sqrt{P_{tx}} H_{l_a} x_q + n$, where $E[|n|^2] = N_v$

First assume transmitted symbol x_q is erroneously detected as $\hat{x}_q$, and l_a is detected correctly.

We express the CPEP as:

$$P\left(x_q \to \hat{x}_q | H_{l_a}, l_a\right) = P\left(\left|r - \sqrt{P_{tx}} H_{l_a} x_q\right|^2 > \left|r - \sqrt{P_{tx}} H_{l_a} \hat{x}_q\right|^2\right). \tag{F1}$$

Substitute $r = \sqrt{P_{tx}} H_{l_a} x_q + n$.

Then we have:

$$\begin{aligned} P\left(x_q \to \hat{x}_q | l_a, H_{l_a}\right) \\ &= P\left(\left|\sqrt{P_{tx}} H_{l_a} x_q + n - \sqrt{P_{tx}} H_{l_a} x_q\right|^2 > \left|\sqrt{P_{tx}} H_{l_a} x_q + n - \sqrt{P_{tx}} H_{l_a} \hat{x}_q\right|^2\right) \\ &= P\left(|n|^2 > \left|\sqrt{P_{tx}} H_{l_a}\left(x_q - \hat{x}_q\right) + n\right|^2\right). \end{aligned} \tag{F2}$$

We employ Theorem 1 from Appendix A, Equation (A4). Hence, continue as:

$$= P\left(|n|^2 > \left|\sqrt{P_{tx}} H_{l_a}\left(x_q - \hat{x}_q\right)\right|^2 + |n|^2 + 2Re\left\{\left(\sqrt{P_{tx}} H_{l_a}\left(x_q - \hat{x}_q\right)\right)(n)^*\right\}\right). \tag{F3}$$

Now, $(n)^H = n^*$ because n is scalar.

We cancel out $|n|^2$ on both sides. Hence, we can simplify and rearrange as follows:

$$\begin{aligned} &= P\left(0 > \left|\sqrt{P_{tx}} H_{l_a}\left(x_q - \hat{x}_q\right)\right|^2 + 2Re\left\{\left(\sqrt{P_{tx}} H_{l_a}\left(x_q - \hat{x}_q\right)\right)(n)^*\right\}\right) \\ &= P\left(0 < -\left|\sqrt{P_{tx}} H_{l_a}\left(x_q - \hat{x}_q\right)\right|^2 - 2Re\left\{\left(\sqrt{P_{tx}} H_{l_a}\left(x_q - \hat{x}_q\right)\right)(n)^*\right\}\right). \end{aligned} \tag{F4}$$

At this point in the derivation, we can note that for a RV denoted by $X \sim CN(\mu, \sigma^2)$, the Q-function can be written using Theorem 2 in Appendix A, Equation (A7).

Let $Re\left\{\left(\sqrt{P_{tx}} H_{l_a}\left(x_q - \hat{x}_q\right)\right)(n)^*\right\} = X \sim CN(\mu, \sigma^2)$.

Need the variance σ^2:

$$\begin{aligned} \sigma^2 = Re\left\{E\left[\left|\left(\sqrt{P_{tx}} H_{l_a}\left(x_q - \hat{x}_q\right)\right)(n)^*\right|^2\right]\right\} &= Re\left\{\left(P_{tx}\left|H_{l_a}\right|^2\left|x_q - \hat{x}_q\right|^2\right) E\left[|n|^2\right]\right\} \\ &= \frac{1}{2} P_{tx} N_0 \left|H_{l_a}\right|^2 \left|x_q - \hat{x}_q\right|^2. \end{aligned} \tag{F5}$$

Hence, we can write by substituting X in as:

$$\begin{aligned} P\left(0 < -\left|\sqrt{P_{tx}} H_{l_a}\left(x_q - \hat{x}_q\right)\right|^2 - 2Re\left\{\left(\sqrt{P_{tx}} H_{l_a}\left(x_q - \hat{x}_q\right)\right)(n)^*\right\}\right) \\ = P\left(X > \frac{1}{2} P_{tx}\left|H_{l_a}\right|^2 \left|\left(x_q - \hat{x}_q\right)\right|^2\right). \end{aligned} \tag{F6}$$

We can now write in terms of the Q-function using Theorem 2 as:

$$P\left(\frac{X}{\frac{1}{2}P_{tx}N_v\left|H_{l_a}\right|^2\left|x_q-\hat{x}_q\right|^2}>\frac{\frac{1}{2}P_{tx}\left|H_{l_a}\right|^2\left|\left(x_q-\hat{x}_q\right)\right|^2}{\frac{1}{2}P_{tx}N_v\left|H_{l_a}\right|^2\left|x_q-\hat{x}_q\right|^2}\right)$$
$$=Q\left(\frac{\frac{1}{2}P_{tx}\left|H_{l_a}\right|^2\left|\left(x_q-\hat{x}_q\right)\right|^2}{\sqrt{\frac{1}{2}P_{tx}N_v\left|H_{l_a}\right|^2\left|x_q-\hat{x}_q\right|^2}}\right), \tag{F7}$$

which may be simplified to:

$$=Q\left(\sqrt{\frac{P_{tx}\left|H_{l_a}\right|^2\left|\left(x_q-\hat{x}_q\right)\right|^2}{2N_v}}\right). \tag{F8}$$

Next, assume transmitted index l_a is erroneously detected as $\hat{l}_a$, and x_q is detected correctly.

$$P\left(l_a\to\hat{l}_a|H_{l_a},H_{\hat{l}_a},x_q\right)=P\left(\left|r-\sqrt{P_{tx}}H_{l_a}x_q\right|^2>\left|r-\sqrt{P_{tx}}H_{\hat{l}_a}x_q\right|^2\right). \tag{F9}$$

Substitute $r=\sqrt{P_{tx}}H_{l_a}x_q+n$ in:

Then we have:

$$=P\left(\left|\sqrt{P_{tx}}H_{l_a}x_q+n-\sqrt{P_{tx}}H_{l_a}x_q\right|^2>\left|\sqrt{P_{tx}}H_{l_a}x_q+n-\sqrt{P_{tx}}H_{\hat{l}_a}x_q\right|^2\right)$$
$$=P\left(|n|^2>\left|\sqrt{P_{tx}}x_q\left(H_{l_a}-H_{\hat{l}_a}\right)+n\right|^2\right). \tag{F10}$$

We use Theorem 1 from Appendix A, Equation (A4).

Continue as:

$$=P\left(|n|^2>\left|\sqrt{P_{tx}}x_q\left(H_{l_a}-H_{\hat{l}_a}\right)\right|^2+|n|^2+2Re\left\{\left(\sqrt{P_{tx}}x_q\left(H_{l_a}-H_{\hat{l}_a}\right)\right)(n)^*\right\}\right)$$
$$=P\left(0>\left|\sqrt{P_{tx}}x_q\left(H_{l_a}-H_{\hat{l}_a}\right)\right|^2+2Re\left\{\left(\sqrt{P_t}x_q\left(H_{l_a}-H_{\hat{l}_a}\right)\right)(n)^*\right\}\right)$$
$$=P\left(0>P_{tx}\left|x_q\right|^2\left|\left(H_{l_a}-H_{\hat{l}_a}\right)\right|^2+2Re\left\{\left(\sqrt{P_{tx}}x_q\left(H_{l_a}-H_{\hat{l}_a}\right)\right)(n)^*\right\}\right). \tag{F11}$$

Noting that for M-PSK symbols, $\left|x_q\right|^2=1$, we have:

$$=P\left(0>P_{tx}\left|\left(H_{l_a}-H_{\hat{l}_a}\right)\right|^2+2Re\left\{\left(\sqrt{P_{tx}}x_q\left(H_{l_a}-H_{\hat{l}_a}\right)\right)(n)^*\right\}\right). \tag{F12}$$

For convenience, the above expression can be written as:

$$=P\left(0<-\left|\left(H_{l_a}-H_{\hat{l}_a}\right)\right|^2-2Re\left\{\left(\sqrt{P_{tx}}\left(H_{l_a}-H_{\hat{l}_a}\right)\right)(\eta)^*\right\}\right). \tag{F13}$$

At this point in the derivation, we can note that for a RV denoted by $X\sim CN(\mu,\sigma^2)$, the Q-function can be written using Theorem 2 from Appendix A, Equation (A7).

Let $Re\left\{\left(\sqrt{P_{tx}}\left(H_{l_a}-H_{\hat{l}_a}\right)\right)(\eta)^*\right\}=X\sim CN(\mu,\sigma^2)$.

Variance of $Re\{X\}$:

$$\begin{aligned}\sigma^2 &= E\left[Re\left\{\left(\sqrt{P_{tx}}x_q\left(H_{l_a} - H_{\hat{l}_a}\right)\right)(n)^*\right\}\right]\\ &= Re\left\{E\left[\left|\left(\sqrt{P_{tx}}x_q\left(H_{l_a} - H_{\hat{l}_a}\right)\right)(n)^*\right|^2\right]\right\}\\ &= Re\left\{P_{tx}N_0\left|H_{l_a} - H_{\hat{l}_a}\right|^2\right\}\\ &= \frac{1}{2}P_{tx}N_0\left|H_{l_a} - H_{\hat{l}_a}\right|^2. \end{aligned} \tag{F14}$$

Using theorem 2, we rearrange and substitute X in as follows:

$$\begin{aligned} &= P\left(0 > P_{tx}\left|\left(H_{l_a} - H_{\hat{l}_a}\right)\right|^2 + 2X\right)\\ &= P\left(-2X > P_{tx}\left|\left(H_{l_a} - H_{\hat{l}_a}\right)\right|^2\right)\\ &= P\left(X < -\frac{1}{2}P_{tx}\left|\left(H_{l_a} - H_{\hat{l}_a}\right)\right|^2\right). \end{aligned} \tag{F15}$$

Now, $P(X < -a) = P(X > a)$. Hence, we can rearrange (F15) as:

$$= P\left(X > \frac{1}{2}P_{tx}\left|\left(H_{l_a} - H_{\hat{l}_a}\right)\right|^2\right). \tag{F16}$$

Now use Theorem 2:

$$\begin{aligned} &P\left(\frac{X}{\sqrt{\frac{1}{2}P_{tx}N_v\left|H_{l_a} - H_{\hat{l}_a}\right|^2}} > \frac{\frac{1}{2}P_{tx}\left|\left(H_{l_a} - H_{\hat{l}_a}\right)\right|^2}{\sqrt{\frac{1}{2}P_{tx}N_v\left|H_{l_a} - H_{\hat{l}_a}\right|^2}}\right)\\ &\quad = Q\left(\frac{\frac{1}{2}P_{tx}\left|\left(H_{l_a} - H_{\hat{l}_a}\right)\right|^2}{\sqrt{\frac{1}{2}P_{tx}N_v\left|H_{l_a} - H_{\hat{l}_a}\right|^2}}\right). \end{aligned} \tag{F17}$$

Simplify (F17) as:

$$= Q\left(\sqrt{\frac{P_{tx}\left|\left(H_{l_a} - H_{\hat{l}_a}\right)\right|^2}{2N_v}}\right). \tag{F18}$$

Note that Equations (F8) and (F18) are also the results obtained for the HRM AP theory derivations with simple changes in variable notation described throughout Chapter 5.

Statistics of non-AP HRM symbol:

The channel magnitudes $|h_k|$ and $|g_k|$ are i.i.d. Rayleigh RVs with modes of $\sigma_{|h_k|} = \sqrt{\frac{L_t}{2}}$ and $\sigma_{|g_k|} = \sqrt{\frac{L_r}{2}}$. These RVs have means of $E[|h_k|] = \sigma_{|h_k|}\sqrt{\frac{\pi}{2}} = \sqrt{L_t}\sqrt{\frac{\pi}{4}}$ and $E[|g_k|\,] = \sigma_{|g_k|}\sqrt{\frac{\pi}{2}} = \sqrt{L_r}\sqrt{\frac{\pi}{4}}$ respectively; and variances of $Var(|h_k|) = \sigma^2_{|h_k|}\left(2 - \frac{\pi}{2}\right) = L_t\left(1 - \frac{\pi}{4}\right)$ and $Var(|g_k|) = \sigma^2_{|g_k|}\left(2 - \frac{\pi}{2}\right) = L_r\left(1 - \frac{\pi}{4}\right)$.

Mean of HRM symbol:

$$\begin{aligned}\mu_\epsilon &= E\left[H_{l_a}\right]\\ &= E\left[\alpha\sum_{k=1}^{N_a}|h_k||g_k| + \sum_{k=N_a+1}^{N}|h_k||g_k|\right]\\ &= \alpha E\left[\sum_{k=1}^{N_a}|h_k||g_k|\right] + E\left[\sum_{k=N_a+1}^{N}|h_k||g_k|\right]\\ &= \alpha\sum_{k=1}^{N_a}E[|h_k||g_k|] + \sum_{k=N_a+1}^{N}E[|h_k||g_k|].\end{aligned} \tag{F19}$$

Now, $E[AB] = E[A]E[B]$. Substituting all statistics in, we get:

$$\begin{aligned}&= \alpha N_a\sqrt{L_t}\sqrt{\frac{\pi}{4}}\sqrt{L_r}\sqrt{\frac{\pi}{4}} + (N - N_a)\sqrt{L_t}\sqrt{\frac{\pi}{4}}\sqrt{L_r}\sqrt{\frac{\pi}{4}}\\ &= \sqrt{L_tL_r}\left(\frac{\pi}{4}\right)(\alpha N_a + N - N_a).\end{aligned} \tag{F20}$$

Variance of HRM symbol:

$$\begin{aligned}\sigma_\epsilon^2 &= E\left[\left|H_{l_a}\right|^2\right]\\ &= E\left[\left|\alpha\sum_{k=1}^{N_a}|h_k||g_k| + \sum_{k=N_a+1}^{N}|h_k||g_k|\right|^2\right]\\ &= E\left[\left|\alpha\sum_{k=1}^{N_a}|h_k||g_k|\right|^2\right] + E\left[\left|\sum_{k=N_a+1}^{N}|h_k||g_k|\right|^2\right].\end{aligned} \tag{F21}$$

Substituting all statistics in, we get:

$$\begin{aligned}&= \alpha^2N_aL_tL_r\left(1-\frac{\pi^2}{16}\right) + (N-N_a)L_tL_r\left(1-\frac{\pi^2}{16}\right)\\ &= \alpha^2N_aL_tL_r\left(1-\frac{\pi^2}{16}\right) + (N-N_a)L_tL_r\left(1-\frac{\pi^2}{16}\right)\\ &= \alpha^2N_aL_tL_r\left(1-\frac{\pi^2}{16}\right) + (N-N_a)L_tL_r\left(1-\frac{\pi^2}{16}\right)\\ &= L_tL_r\left(1-\frac{\pi^2}{16}\right)(\alpha^2N_a + N - N_a).\end{aligned} \tag{F22}$$

Statistics of AP HRM symbol:

The channel magnitude $|g_k|$ is an independent Rayleigh RV with mode of $\sigma_{|g_k|} = \sqrt{\frac{L_r}{2}}$. These RVs can be expressed in terms of the mode, with a mean of $E[|g_k|] = \sigma_{|g_k|}\sqrt{\frac{\pi}{2}} = \sqrt{L_r}\sqrt{\frac{\pi}{4}}$ respectively; and variance $Var(|g_k|) = \sigma_{|g_k|}^2\left(2-\frac{\pi}{2}\right) = L_r\left(1-\frac{\pi}{4}\right)$.

The second moment is derived as $E[|g_k|^2] = Var(|g_k|) + E[|g_k|]^2 = L_r\left(1-\frac{\pi}{4}\right) + \left(\sqrt{L_r}\sqrt{\frac{\pi}{4}}\right)^2 = L_r$.

Mean of AP HRM symbol:

$$\begin{aligned}\mu_\epsilon &= E\left[\alpha\sum_{k=1}^{N_a}|g_k| + \sum_{k=N_a+1}^{N}|g_k|\right]\\ &= \alpha\sum_{k=1}^{N_a}E[|g_k|] + \sum_{k=N_a+1}^{N}E[|g_k|]\\ &= \sqrt{L_r}\sqrt{\frac{\pi}{4}}(\alpha N_a + N - N_a).\end{aligned} \tag{F23}$$

Variance of AP HRM symbol:

$$\sigma_\epsilon^2 = E\left[\left|\alpha\sum_{k=1}^{N_a}|g_k| + \sum_{k=N_a+1}^{N}|g_k|\right|^2\right]$$

$$\begin{aligned}&= \alpha^2\sum_{k=1}^{N_a}E\left[||g_k||^2\right] + \sum_{k=N_a+1}^{N}E\left[||g_k||^2\right]\\ &= L_r\left(1-\frac{\pi}{4}\right)(\alpha^2 N_a + N - N_a).\end{aligned} \tag{F24}$$

Appendix G

Derivation of ABEP of RIS M-QAM AP scheme for low N

We have that $\xi = \frac{3N\rho}{M-1}$, $a = 1 - \frac{1}{\sqrt{M}}$, $\omega = \frac{4a}{\log_2(M)}$, and the PDF of Rician RVs is given by [133]:

$$f_{\mathrm{Z}}(x) = \frac{x^N}{c_2^2}\left(\frac{c_1}{c_2 b}\right)^{N-1} \exp\left[-\frac{1}{2}\left(\frac{x^2}{c_2^2} + \frac{b^2}{c_1^2}\right)\right] I_{N-1}\left(\frac{xb}{c_1 c_2}\right), \tag{G1}$$

where $b = \sqrt{\frac{NK\Omega}{K+1}}$, c_1 and c_2 are constants, and $I_{N-1}(\,\cdot\,)$ is the MBF of the first kind, described in Chapter 6, Section 6.4, Equation (6.9). Note that for this analysis, $\Omega = 1$.

The ABEP is given by [78]:

$$P_e = \omega \int_0^\infty \left\{Q\left(\sqrt{\xi x^2}\right) - aQ^2\left(\sqrt{\xi x^2}\right)\right\} f_{\mathrm{Z}}(x)\, dx. \tag{G2}$$

Using Q-function approximations $Q(u) \cong \frac{1}{12}e^{-\frac{u^2}{2}} + \frac{1}{4}e^{-\frac{2u^2}{3}}$ and $Q^2(u) \cong \frac{1}{8}e^{-u^2}$, we get:

$$\begin{aligned} P_e \approx \omega \int_0^\infty &\left\{\frac{1}{12}\exp\left(-\frac{\xi x^2}{2}\right) + \frac{1}{4}\exp\left(-\frac{2\xi x^2}{3}\right)\right. \\ &\left. - \frac{a}{8}\exp(-\xi x^2)\right\}\left(\frac{x^N}{c_2^2}\left(\frac{c_1}{c_2 b}\right)^{N-1} \exp\left[-\frac{1}{2}\left(\frac{x^2}{c_2^2} + \frac{b^2}{c_1^2}\right)\right] I_{N-1}\left(\frac{xb}{c_1 c_2}\right)\right) dx. \end{aligned} \tag{G3}$$

Now, letting $C = \frac{1}{c_2^2}\left(\frac{c_1}{c_2 b}\right)^{N-1} \exp\left[-\frac{1}{2}\left(\frac{b^2}{c_1^2}\right)\right]$, and $A = \frac{b}{c_1 c_2}$ we then have:

$$\begin{aligned} P_e \approx \omega C \int_0^\infty &\left\{\frac{1}{12}\exp\left(-\frac{\xi x^2}{2}\right) + \frac{1}{4}\exp\left(-\frac{2\xi x^2}{3}\right)\right. \\ &\left. - \frac{a}{8}\exp(-\xi x^2)\right\}\left(x^N \exp\left[-\frac{1}{2}\left(\frac{x^2}{c_2^2}\right)\right] I_{N-1}(Ax)\right) dx. \end{aligned} \tag{G4}$$

Taking a common denominator of 24, we get:

$$\begin{aligned} P_e \approx \frac{\omega C}{24} \int_0^\infty &\left\{2\exp\left(-\frac{\xi x^2}{2}\right) + 6\exp\left(-\frac{2\xi x^2}{3}\right)\right. \\ &\left. - 3a\exp(-\xi x^2)\right\}\left(x^N \exp\left[-\frac{1}{2}\left(\frac{x^2}{c_2^2}\right)\right] I_{N-1}(Ax)\right) dx. \end{aligned} \tag{G5}$$

Now, multiplying out and combining all exponential terms, we get:

$$\begin{aligned} P_e \approx F \int_0^\infty &\left\{2\exp\left(\left[-\frac{\xi}{2} - \frac{1}{2c_2^2}\right]x^2\right) + 6\exp\left(\left[-\frac{2\xi}{3} - \frac{1}{2c_2^2}\right]x^2\right)\right. \\ &\left. - 3a\exp\left(\left[-\xi - \frac{1}{2c_2^2}\right]x^2\right)\right\}\left(x^N I_{N-1}(Ax)\right) dx, \end{aligned} \tag{G6}$$

where $F = \frac{\omega C}{24}$.

By further simplification of the exponential terms, we may define $\beta_{11} = \frac{\xi c_2^2+1}{2c_2^2}$,$\beta_{12} = \frac{4\xi c_2^2+3}{6c_2^2}$, and $\beta_{13} = \frac{2\xi c_2^2+1}{2c_2^2}$, we may write:

$$\begin{aligned} P_e \approx F \int_0^\infty &\{2\exp([-\beta_{11}]x^2) + 6\exp([-\beta_{12}]x^2) \\ &- 3a\exp([-\beta_{13}]x^2)\}\big(x^N I_{N-1}(Ax)\big)\, dx. \end{aligned} \tag{G7}$$

Now, we may expand the MBF as follows:

$$I_{N-1}(Ax) = \sum_{k=0}^{\infty} \frac{\left(\frac{A}{2}x\right)^{2k+N-1}}{(k!)\Gamma(k+N)}. \tag{G8}$$

We now use the principle that the integral of the sum is the sum of the integral as follows:

$$\begin{aligned} P_e &\approx F \int_0^\infty \{2\exp([-\beta_{11}]x^2) + 6\exp([-\beta_{12}]x^2) \\ &\qquad - 3a\exp([-\beta_{13}]x^2)\}\big(x^N I_{N-1}(Ax)\big)\, dx \\ &\approx F \int_0^\infty x^N\{2\exp([-\beta_{11}]x^2) + 6\exp([-\beta_{12}]x^2) \\ &\qquad - 3a\exp([-\beta_{13}]x^2)\}\left(\sum_{k=0}^{\infty} \frac{\left(\frac{A}{2}x\right)^{2k+N-1}}{(k!)\Gamma(k+N)}\right) dx \\ &\approx F \sum_{k=0}^{\infty} \frac{\left(\frac{A}{2}\right)^{2k+N-1}}{(k!)\Gamma(k+N)} \int_0^\infty x^{2N+2k-1}\{2\exp([-\beta_{11}]x^2) + 6\exp([-\beta_{12}]x^2) \\ &\qquad - 3a\exp([-\beta_{13}]x^2)\}\, dx. \end{aligned} \tag{G9}$$

Now, we use the integral property given in Equation 3.326.2 in [135] stated as follows:

$$\int_0^\infty r^m \exp(-\alpha r^n)\, dr = \frac{\Gamma(\varphi)}{n\alpha^{\varphi}}, \varphi = \frac{m+1}{n}, \tag{G10}$$

assuming $Re\{\alpha\} > 0, Re\{m\} > 0, Re\{n\} > 0$.

This property may be used to evaluate each of the integrals to produce:

$$\begin{aligned} P_e &\approx F \sum_{k=0}^{\infty} \frac{\left(\frac{A}{2}\right)^{2k+N-1}}{(k!)\Gamma(k+N)} \int_0^\infty x^{2N+2k-1}\{2\exp([-\beta_{11}]x^2) + 6\exp([-\beta_{12}]x^2) \\ &\qquad - 3a\exp([-\beta_{13}]x^2)\}\, dx \\ P_e &\approx F \sum_{k=0}^{\infty} \frac{\left(\frac{A}{2}\right)^{2k+N-1}}{(k!)\Gamma(k+N)} \left[\frac{\Gamma(N+k)}{\beta_{11}^{(N+k)}} + 3\frac{\Gamma(N+k)}{\beta_{12}^{(N+k)}} - \frac{3a\Gamma(N+k)}{2\beta_{13}^{(N+k)}}\right] \\ P_e &\approx F\left(\frac{A}{2}\right)^{N-1} \sum_{k=0}^{\infty} \frac{\left(\frac{A}{2}\right)^{2k}}{(k!)} \left[\beta_{11}^{-(N+k)} + 3\beta_{12}^{-(N+k)} - \left(\frac{3a}{2}\right)\beta_{13}^{-(N+k)}\right]. \end{aligned} \tag{G11}$$

We now define $L = F\left(\frac{A}{2}\right)^{N-1}$, and separate the sums as follows:

$$P_e \approx L\left(\sum_{k=0}^{\infty}\frac{\left(\frac{A}{2}\right)^{2k}}{(k!)}\beta_{11}^{-(N+k)} + 3\sum_{k=0}^{\infty}\frac{\left(\frac{A}{2}\right)^{2k}}{(k!)}\beta_{12}^{-(N+k)} - \frac{3a}{2}\sum_{k=0}^{\infty}\frac{\left(\frac{A}{2}\right)^{2k}}{(k!)}\beta_{13}^{-(N+k)}\right)$$

$$\approx L\left(\beta_{11}^{-N}\sum_{k=0}^{\infty}\frac{\left(\frac{A}{2}\right)^{2k}}{(k!)}\beta_{11}^{-k} + 3\beta_{12}^{-N}\sum_{k=0}^{\infty}\frac{\left(\frac{A}{2}\right)^{2k}}{(k!)}\beta_{12}^{-k} - \frac{3a}{2}\beta_{13}^{-N}\sum_{k=0}^{\infty}\frac{\left(\frac{A}{2}\right)^{2k}}{(k!)}\beta_{13}^{-k}\right). \qquad \text{(G12)}$$

Now $a^{-b} = \left(\frac{1}{a}\right)^{b} = \left(\frac{1}{a}\right)^{\frac{2b}{2}} = \left(\frac{1}{\sqrt{a}}\right)^{2b}$. Hence, we can write:

$$P_e \approx L\left(\beta_{11}^{-N}\sum_{k=0}^{\infty}\frac{\left(\frac{A}{2}\right)^{2k}}{(k!)}\beta_{11}^{-k} + 3\beta_{12}^{-N}\sum_{k=0}^{\infty}\frac{\left(\frac{A}{2}\right)^{2k}}{(k!)}\beta_{12}^{-k} - \frac{3a}{2}\beta_{13}^{-N}\sum_{k=0}^{\infty}\frac{\left(\frac{A}{2}\right)^{2k}}{(k!)}\beta_{13}^{-k}\right)$$

$$\approx L\left(\beta_{11}^{-N}\sum_{k=0}^{\infty}\frac{\left(\frac{A}{2\sqrt{\beta_{11}}}\right)^{2k}}{(k!)} + 3\beta_{12}^{-N}\sum_{k=0}^{\infty}\frac{\left(\frac{A}{2\sqrt{\beta_{12}}}\right)^{2k}}{(k!)} - \frac{3a}{2}\beta_{13}^{-N}\sum_{k=0}^{\infty}\frac{\left(\frac{A}{2\sqrt{\beta_{13}}}\right)^{2k}}{(k!)}\right)$$

$$\approx L\left(\beta_{11}^{-N}\Omega\left(\frac{A}{2\sqrt{\beta_{11}}}\right) + 3\beta_{12}^{-N}\Omega\left(\frac{A}{2\sqrt{\beta_{12}}}\right) - \frac{3a}{2}\beta_{13}^{-N}\Omega\left(\frac{A}{2\sqrt{\beta_{13}}}\right)\right), \qquad \text{(G13)}$$

where $\Omega(x) = \sum_{k=0}^{\infty}\frac{x^{2k}}{k!}$, $L = \frac{\omega}{24c_2^2}\left(\frac{c_1 A}{2c_2 b}\right)^{N-1}\exp\left(-\frac{b^2}{2c_1^2}\right)$, $A = \frac{b}{c_1 c_2}$, $\beta_{11} = \frac{\xi c_2^2+1}{2c_2^2}$, $\beta_{12} = \frac{4\xi c_2^2+3}{6c_2^2}$, $\beta_{13} = \frac{2\xi c_2^2+1}{2c_2^2}$, $\xi = \frac{3N\rho}{M-1}$, $a = 1 - \frac{1}{\sqrt{M}}$, and $\omega = \frac{4a}{\log_2(M)}$.